A New Crystal Plasticity Model for Steels Exhibiting Transformation Induced Plasticity with Application to Quenched and Partitioned Steel

by

Daniel Sean Connolly

A thesis
presented to the University of Waterloo
in fulfillment of the
thesis requirement for the degree of
Doctor of Philosophy
in
Mechanical and Mechatronics Engineering

Waterloo, Ontario, Canada, 2021

Examining Committee Membership

The following served on the Examining Committee for this thesis. The decision of the Examining Committee is by majority vote.

Supervisor:	Kaan Inal, PhD NSERC/General Motors Industrial Research Chair in "Integrated Computational Mechanics for Mass Efficient Automotive Structures"; Professor, University of Waterloo
External Examiner:	Farhang Pourboghrat, PhD Professor, Ohio State University
Internal Examiner:	Étienne Martin, PhD Adjunct Associate Professor, University of Waterloo Associate Professor, École Polytechnique de Montréal
Internal Examiner:	Adrian Gerlich, PhD, PEng NSERC/TransCanada Industrial Research Chair in "Welding for Energy Infrastructure"; Associate Associate Professor, University of Waterloo
Internal-External Examiner:	Robert Gracie, PhD Professor, University of Waterloo

Author's Declaration

This thesis consists of material of which I authored or co-authored: see Statement of Contributions included in this thesis. This is a true copy of the thesis, including any required final revisions, as accepted by my examiners.

I understand that my thesis may be made electronically available to the public.

Statement of Contributions

Chapter 4 of this thesis is adapted from a paper that was co-authored by myself, Dr. Kohar, Dr. Muhammad, Dr. Hector Jr., Dr. Mishra, and Prof. Inal. Dr. Kohar provided the initial implicit user defined material for crystal plasticity in LS-Dyna. Prof. Inal and Dr. Kohar provided valuable discussions during model development and results analysis. Dr. Muhammad provided the initial EBSD data for QP1180. Dr. Hector Jr. provided the in-situ HEXRD tensile test data, and provided valuable discussion regarding data analysis and expected transformation behaviour. Dr. Kohar, Dr. Hector Jr., Dr. Mishra, and Prof. Inal assisted the authors with editing parts of the work. The balance of the work was my own.

Chapter 5 of this thesis is adapted from a paper that was co-authored by myself, Dr. Kohar and Prof. Inal. Prof. Inal and Dr. Kohar provided valuable discussions during model development and results analysis. Dr. Kohar, and Prof. Inal assisted the authors with editing parts of the work. Dr. Poling provided the raw EBSD data for the QP3Mn material published in her thesis. The balance of the work was my own.

Abstract

This thesis outlines the development of a constitutive model and the modelling techniques required to accurately model steels that exhibit transformation induced plasticity over a wide range of strain-rates and temperatures. A novel thermodynamically consistent rate-dependent crystal plasticity formulation incorporating stress-induced transformation is first developed from the existing models in the literature. In this baseline model, plastic slip and martensitic transformation are governed by thermodynamically derived driving forces that account for various physical mechanism (e.g. temperature, crystal orientation, stress, and martensite surface energy). Thermodynamic arguments are used to derive a physics driven temperature evolution law. Both plastic slip and transformation kinetics are described by power law type rate-dependent evolution. Homogenization of retained austenite (RA) and transformed martensite is considered implicitly using the plastic slip kinetics law. The constitutive model is implemented into a thermo-mechanical Crystal Plasticity (CP) Finite Element Method (FEM) formulation to study the bulk material properties of QP1180 steel. The initial material microstructure is characterized using Electron Backscatter Diffraction (EBSD) and Scanning Electron Microscope (SEM) data. A new method for incorporating thermal boundary conditions in CPFEM models is proposed. The constitutive model is calibrated using experimental stress-strain and martensite evolution measurements characterized using in-situ High Energy X-Ray Diffraction (HEXRD) uniaxial tension experiments. Numerical experiments are conducted to study the effect of thermal and mechanical boundary conditions. Results are presented for a range of temperatures, strain-rates and thermal boundary conditions.

Building on the the initial framework, a generalized constitutive model is proposed that avoids several limiting assumptions of the baseline model. Thermodynamic arguments are again used to derive plastic slip and transformation driving forces that account for various physical mechanisms, as well as a constitutive law governing temperature evolution. Homogenization of RA and transformed martensite is considered explicitly using a modified Taylor homogenization law to determine strain partitioning while accounting for transformation. The mechanical thermo-elasto-viscoplastic behaviour is explicitly and separately modelled in RA and transformed martensite. The model is calibrated and validated for a QP3Mn alloy over a large range of temperatures ($-10\,^{\circ}\mathrm{C}$ – $70\,^{\circ}\mathrm{C}$) and strain-rates ($5 \times 10^{-4}\,\mathrm{s}^{-1}$ – $200\,\mathrm{s}^{-1}$). The fully calibrated model is compared to a model recalibrated without strain-rate dependent transformation, demonstrating that capturing strain-rate dependent transformation may be necessary even for materials where no direct experimental strain-rate dependence. The calibrated model is used to conduct plane strain and equibiaxial tension simulations, showing that increasing triaxiality results in increased transformation.

Acknowledgements

I would like to thank Professor Kaan Inal for his excellent supervision in the completion of my doctoral studies. I would not have been able to complete this thesis without the funding, industrial support and collaborations established through him. I would like to thank the members of my committee: Professor Étienne Martin (U. Waterloo & Montréal Polytéchnique), Professor Adrian Gerlich (U. Waterloo), Professor Robert Gracie (U. Waterloo) and Professor Farhang Pourboghrat (Ohio State U.) for all of their contributions to ensure the thesis is of high caliber. I would like to thank Dr. Raja K. Mishra and Dr. Louis G. Hector Jr. of General Motors Research & Development Center in Warren, Michigan for their mentorship in bridging the needs of the automotive industry to the scientific community. I would also like to thank Dr. Abhijit Brahme at the University of Waterloo for his assistance in textural and microstructural analysis. I am deeply grateful to Dr. Christopher Kohar for his support and guidance throughout my research at the Computational Mechanics Research Group. I would like to acknowledge Dr. Waqas Muhammad at the University of Waterloo for performing Electron Backscatter Diffraction tests for material characterization. I would like to acknowledge Dr. Whitney Poling of General Motors Research & Development Center in Warren, Michigan for providing Electron Backscatter Diffraction test data. Financial support for this work was provided by: Natural Sciences and Engineering Research Council of Canada – Industrial Research Chair Automotive Partnership of Canada (NSERC-APC) under Grant number IRCPJ-503185-2016, General Motors of Canada, Ontario Graduate Scholarship (OGS), President's Graduate Scholarship of Waterloo, and the University of Waterloo - Engineering Doctoral Domestic Student Award. I would like to thank all of those who were part of the Computational Mechanics Research Group during my tenure. I would like to thank all those who kept me company throughout the late nights of work, conferences and extra-curricular activities. Special acknowledgements go to: Prusodman Sathananthan for the ever-interesting conversations and for being there for a much needed break; David Booth for late nights at the the office, juggling, rubik's cubes and playing pool; Samira Wettasinghe for climbing and skiing; Owen Linton who provided valuable computer science related advice; Larry Li for useful theoretical discussions; and Dr. Christopher Kohar for the late-night crunch time company, the enjoyable walks, and the fun times together. Of course, I want to thank my lovely wife Laura Linton, who put up with the stress and frustration of graduate school and helped me to push through it. Finally, I would like to thank my family. To my father, Brook, whose sword-making hobby sparked my interest in mechanical engineering. To my mother, Rosslynn, whose intelligence, efficiency and hard work was a constant inspiration. To John, Miriam and Richard, who sparked the intellectual curiosity, determination and resilience that led me to complete my graduate studies.

Table of Contents

List of Figures

List of Tables

1 Introduction

Government mandates for greenhouse gas emissions have been a driving factor for recent improvements in fuel economy standards across the automotive industry [1]. Vehicle lightweighting has been a proven strategy that automakers have employed to reduce fuel consumption and energy requirements during the operation of a vehicle. This requires automakers to develop innovations in design technologies [2, 3] and lightweight materials (e.g. aluminum [4–6], magnesium alloys [7, 8], and advanced high strength steels [9–13]) to accomplish this goal. However, these lightweight structures must also satisfy the evolving standards in vehicle performance and safety. In particular, new requirements for anti-intrusion protection present a unique challenge to automakers to minimize entry into the occupant cell using these lightweight solutions.

The utilization of advanced high strength steels (AHSS) in these critical components is a solution that has been employed by the automotive sector [12]. In particular, Quenched and Partitioned (QP) steels are a new generation of AHSS that show promise in anti-intrusion applications due to their high strength and ductility with relatively low alloying cost [12, 14, 15]. This high strength and ductility are achieved through alloy composition and the quench and partitioning heat treatment process that partially stabilizes austenite at room temperature [16]. As the material deforms, this retained austenite (RA) transforms to martensite, which adds significant hardenability and ductility [17]; this is known as transformation-induced plasticity (TRIP) phenomenon. Martensitic transformation during deformation depends on temperature [18], stress-state [19, 20], strain-rate [21] and crystal orientation [22]. The temperature rise due to latent heat released during transformation has a suppressing effect on martensitic transformation at elevated strain-rates [23]. Dependence on crystal orientation suggests that material texture may cause anisotropy in the transformation behaviour. As such, designs incorporating QP steels must account for martensitic transformation and its dependence on temperature, stress-state, strain-rate and orientation.

Automakers strive to complete the design process primarily in a virtual environment using computer simulations to reduce the time and cost of bringing their product to market. This includes simulation of forming processes to determine the manufacturability of the vehicle [24, 25], and performance during normal operation and crash events [4, 26]. Experimental measurements and testing are then used to provide initial material parameters and validate the final design iterations. These computer simulations require a constitutive model that can accurately describe the deformation behaviour of the material. Therefore, the successful implementation of QP steel into future automotive structures requires a constitutive model that captures the material's complexities mentioned above. Furthermore, forming and crashworthiness simulation require the constitutive model to be accurate over

a wide range of temperatures and strain-rates with varying dynamic conditions.

Constitutive models can be divided into two broad categories: phenomenological and mechanistic models. Phenomenological models aim to describe the deformation behaviour of the material without needing to capture the underlying deformation mechanisms. These models are often appropriate for a crash and forming simulations due to low computational time and ease of use. However, some accuracy is sacrificed due to an inability to capture evolving anisotropy from microstructural evolution at large strains [27]. Mechanistic models aim to capture the deformation mechanisms of the material of interest directly. For metallic materials, crystal plasticity provides a good balance between capturing underlying physical mechanisms while retaining predictive capability for bulk material properties [28]. This is achieved by modelling the crystal deformation kinematics while neglecting the underlying atomic interactions that govern plasticity. The composite behaviour of polycrystalline metals is then calculated from the behaviour of the constituent crystals using a numerical method or homogenization scheme to handle inter-grain interactions. Using a representative sample of the crystals in metals, crystal plasticity can reproduce the material's bulk properties with high accuracy and fewer calibration experiments than required for phenomenological models [29], at the cost of increased simulation time. For use in engineering applications, each model category's advantages can be combined using crystal plasticity models as an intermediate step to calibrate phenomenological models [29].

This thesis aims to develop a crystal plasticity constitutive model and the supporting technologies required to simulate steels with deformation-induced martensitic transformation, including QP steels, over a wide range of temperatures and strain-rates. This constitutive model will capture the various aspects of martensitic transformation, such as stress and strain-induced transformation, along with a numerical scheme to accurately partition the deformation components. While various models exist in the literature that captures relevant physical mechanics individually, no model has yet been presented that captures all of the mechanics necessary to achieve this objective. This new model will explore the various properties of martensite transformation on bulk deformation of QP steels for these different loading conditions. As part of this work, a novel method will be proposed for incorporating thermal boundary conditions into representative volume element crystal plasticity simulations that allow the proper representation of thermal conditions under realistic loading situations. The ability to incorporate thermal boundary conditions is essential for designers to understand how the material can behave during forming operations. By tailoring and optimizing their thermal boundaries, this constitutive model and accompanying modelling technologies can serve as a numerical tool to allow these designers to achieve next-generation lightweight QP steel structures.

The thesis is structured in the following manner: in Chapter 2, the current understand-

ing of QP steel mechanical behaviour and modelling is presented. A literature review is presented summarizing the motivation for developing QP steels and the associated manufacturing process. A review on the experimental understanding of the thermo-mechanical deformation behaviour of steels exhibiting the TRIP effect is presented. A review of the state-of-the-art constitutive modelling methods is presented. Chapter 3 presents the research strategy employed throughout this work. Chapter 4 and Chapter 5 present the research results of this thesis. These chapters are derived from a published and under-review peer-reviewed manuscript, respectively. Each of these chapters will introduce the problem, method of solution, predicted results, discussion, and conclusions. Chapter 6 presents a summary of the key contributions and conclusions. Future work to improve on this constitutive framework is presented.

2 Literature Review

2.1 Advanced High Strength Steels

Figure 2.1 shows the tensile strength vs. uniform elongation for several classes of steel [17]. Conventional steels, such as mild and high strength low alloy (HSLA) steels, have relatively low strength. First-generation AHSS uses more complex chemical compositions and processing technologies to achieve fine control of phase properties. These include transformation-induced plasticity (TRIP), dual-phase (DP) and complex-phase (CP) steels and have improved strength and ductility relative to conventional steels. Second-generation AHSS, such as the austenitic stainless and twinning induced plasticity (TWIP) steels, employ significant alloying elements to improve material properties at greatly increased costs. QP steels are considered a third-generation AHSS, with material properties and cost between first and second-generation AHSS.

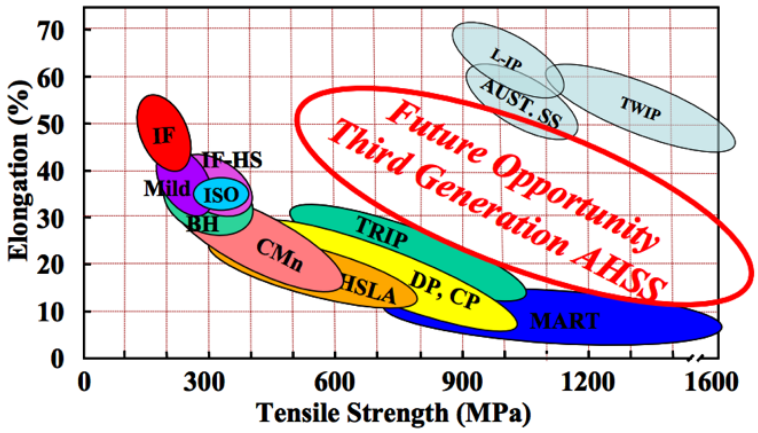

Fig. 2.1: Tensile strength vs. uniform elongation for various classes of steel [17].

2.2 Processing of QP Steel

The quenching and partitioning heat treatment premise, first introduced by Speer et al. [16], is to partially form martensite using an initial quenching step followed by carbon enrichment of the remaining austenite using a partitioning step. This carbon enrichment improves austenite stability at room temperature. Figure 2.2 shows a schematic of a full austenization, two-step QP process. In general, the QP process can begin with either

intercritical annealing or full austenization (i.e. temperature greater than AC_3). If full austenization does not occur, then some ferrite will remain in the final microstructure [17]. Next, the material is quenched to a temperature (T_{QT}) between the martensite start (M_s) and martensite finish (M_f) temperatures, such that the austenite partially transforms to martensite with a volume fraction of M_{QT}. Then, a partitioning step is used to allow carbon to diffuse from martensite to the RA, tempering the martensite phase. In a single-step QP process, the partitioning temperature is T_{QT}, whereas, in a two-step process, the temperature is raised to T_{PT}. Lastly, a final quench is conducted to bring the material to room temperature. If T_{QT} is relatively high, then M_{QT} will be too low to contain sufficient carbon to stabilize the RA phase fully. In this case, the final quench will form fresh martensite. Additionally, the QP process can be tailored to produce bainitic phases.

When first developed, QP steels used TRIP steel chemistries as a base composition. This included Si and Al to suppress carbide formation and C and Mn to promote austenite stability [30–32]. However, carbide formation in QP steels must be suppressed with alloying elements that maximize the diffusion of C into the RA phase [33]. Si effectively suppresses the formation of carbides, and Mo effectively increases the retained austenite volume fraction (RAVF) [34]. While Al effectively suppresses carbide formation, it also reduces the RAVF [34]. Finally, Mn significantly enhances austenite stability and suppresses the formation of ferrite, bainite and pearlite [35]. Overall, the phases in QP steels generally include ferrite, lower-carbon tempered martensite, and relatively high-carbon RA [36].

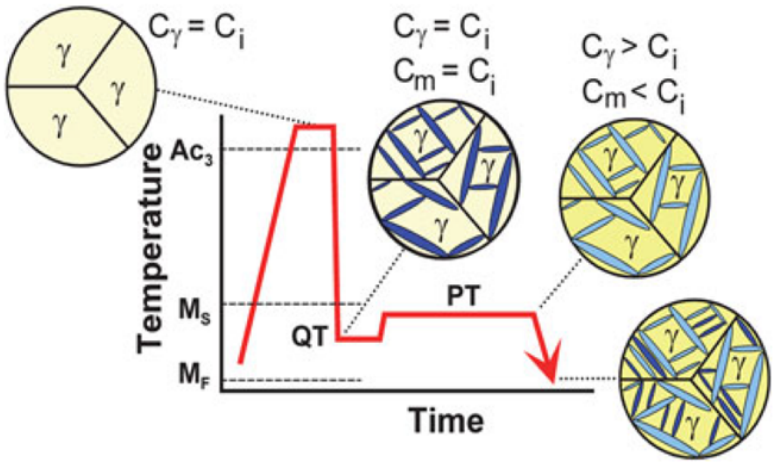

Fig. 2.2: Schematic of QP process [17]

2.3 QP Steel Mechanical Behaviour

The bulk deformation properties of QP steel are a consequence of the microstructural morphology and each crystal's deformation properties. The microstructural morphology encompasses statistical information regarding the grain sizes, shapes, and crystal orientations of the grains within each phase of the material and the relative spatial distribution of each phase. This is generally characterized using one of two methods. The first method is X-Ray diffraction (XRD), wherein the material acts as a 3D diffraction grating for X-Ray light directed at it. In the simplest version, this only allows for the characterization of the orientation distribution of each phase [15]. Recently proposed advanced versions allow for characterization of all microstructural information throughout a volume of material if the material's grain size is sufficiently large [37]. The second technique is electron backscatter diffraction (EBSD), wherein the surface of a material is polished and bombarded with electrons using a scanning electron microscope (SEM). The diffraction pattern generated by the backscattered electrons is sufficiently specific to identify both the phase and orientation of a specific point on the polished surface. Repeating the procedure across many points on the surface generates a 2D map of the crystal phases and orientations [38]. In practice, the simple XRD is used to characterize bulk properties, such as phase and orientation distribution, and EBSD is used to characterize general microstructural information. For single-phase materials, a 3D representative microstructure can be reconstructed using EBSD images taken on three orthogonal planes [39]. The mechanical behaviour of individual crystals in QP steels results from two distinct deformation mechanisms: crystallographic slip in all phases and martensitic transformation in austenite.

2.3.1 Crystallographic Slip

Each crystal in a metal is composed of repeating arrangements of atoms called a crystal lattice. Figure 2.3 shows common crystal lattices of engineering metals: hexagonal close-packed (HCP), face-centred cubic (FCC), body-centred cubic (BCC) and body-centred tetragonal (BCT). Each of the crystal structures shown in Figure 2.3 is invariant to certain symmetries: for example, BCC and FCC are invariant to 90° rotations and mirroring along each axis as well as central inversion. QP steels generally consist of FCC austenite (γ), BCC ferrite and BCT martensite (α') [40], where the c/a ratio of BCT martensite is a function of carbon content [41]. In QP steel, the c/a ratio of tempered martensite is very close to one due to reduced carbon content [41]. The tempered martensite can, therefore, be approximated as a BCC phase. In general, it is difficult to distinguish between BCC ferrite and BCT martensite in steels using only an EBSD because of the similarity in

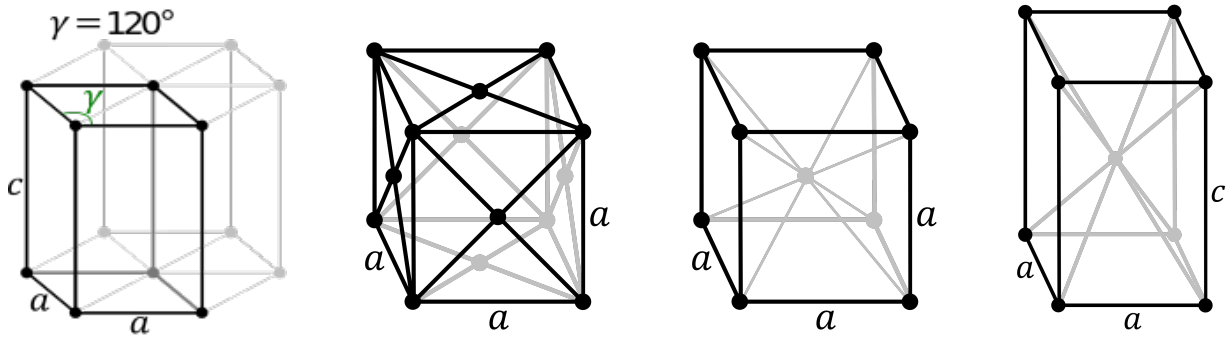

(a) HCP [44] (b) FCC [45] (c) BCC [46] (d) BCT [47]

Fig. 2.3: Schematic crystal lattice unit cells.

the crystal structures and consequent diffraction patterns [40]. Some steels exhibiting the TRIP effect also contain HCP ϵ-martensite [20, 42]. Figure 2.4, taken from Hu et al. 2017 [40], shows a representative example of a QP steel microstructure with ferrite (α), tempered α' martensite (α'_T), and austenite (γ) present. As is common in QP steel [40, 43], the austenite is observed in both blocky (γ_B) and film-like (γ_L) morphologies. Blocky austenite is generally equiaxed with a grain size greater than 1 µm and is often surrounded by proto-eutectic ferrite [43]. In contrast, film-like austenite generally has a thickness on the order of 100 nm, a very high length to thickness ratio, and is surrounded by laths of tempered martensite [43].

In most engineering metals, plastic deformation occurs primarily via crystallographic slip, defined as the aggregate motion of dislocations along specific planes and directions [48]. These are called the slip planes and slip directions and are collectively called slip systems. Dislocations are a type of line defect in a crystal lattice and can be either edge, screw or mixed type [48]. Edge dislocations can be visualized as an insertion of a half-plane of atoms relative to a perfect lattice, as shown in Figure 2.5(a). Screw dislocations are instead represented by a shift in atomic alignment along a half-plane, forming a helical path about the line defect, as shown in Figure 2.5(b). Mixed dislocations are a combination of both dislocation types [48]. The vector required to close a loop around the dislocation is called the Burger's vector and gives both the direction and magnitude of dislocation motion [48]. Bulk plastic deformation is initiated when there is sufficient stress to create or move a significant number of dislocations through the crystal. In general, the critical resolved shear stress to cause dislocation motion is governed by the mean free path of dislocation motion before interference with a pinning obstacle, such as a solute atom, grain boundary, particle, or second dislocation. As such, hardening occurs primarily due to increased dislocation

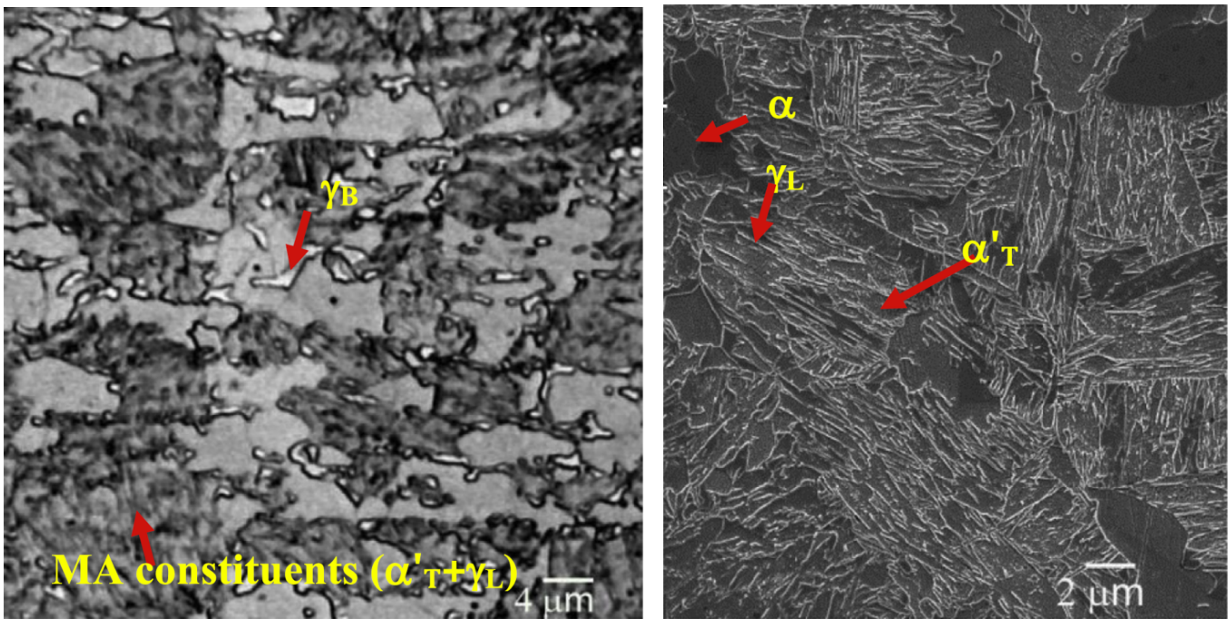

(a) Optical micrograph

(b) SEM micrograph

Fig. 2.4: Example QP steel microstructure [40].

density causing a reduction in the dislocation mean free path. Since dislocation motion is thermally activated [49], the stress required to activate dislocation motion must depend significantly on temperature and strain-rate [50].

For low strain-rates or high temperatures, the diffusion rate of solute atoms can be similar to the dislocation velocity. This dynamic strain ageing (DSA) effect causes repeated pinning and unpinning of dislocations, manifesting as significant serrated flow in the stress vs. strain curve. In severe cases, this can result in propagative instabilities known as Portevin-Le Châtelier (PLC) bands. In Fe-Mn-C steels such as QP, this is driven by C-Mn pair reorientation [51] and has been observed for several different alloys [51, 52] including QP steels [53]. At high temperatures and low strain-rates, the movement of dislocations near a grain boundary can allow adjacent grains to move relative to each other. This grain boundary sliding is important for accurate modelling of creep and creep fracture [54, 55]. When strain gradients are present, additional dislocations are necessary to accommodate the geometry change. These geometrically necessary dislocations (GNDs) act as additional dislocation obstacles that contribute to the inverse correlation between material strength and grain size [56].

Plane normals and directions in a crystal are denoted using Miller indices $(hk\ell)$ and

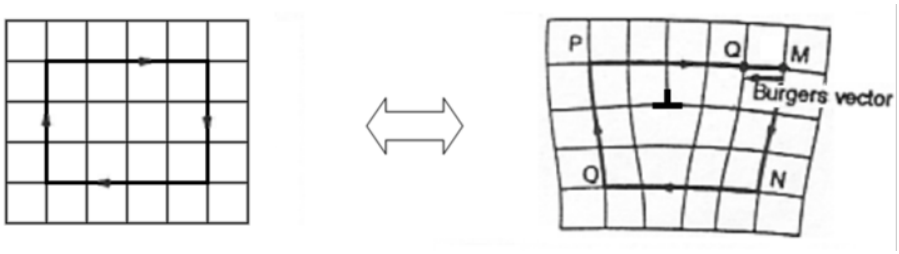

(a) Edge type

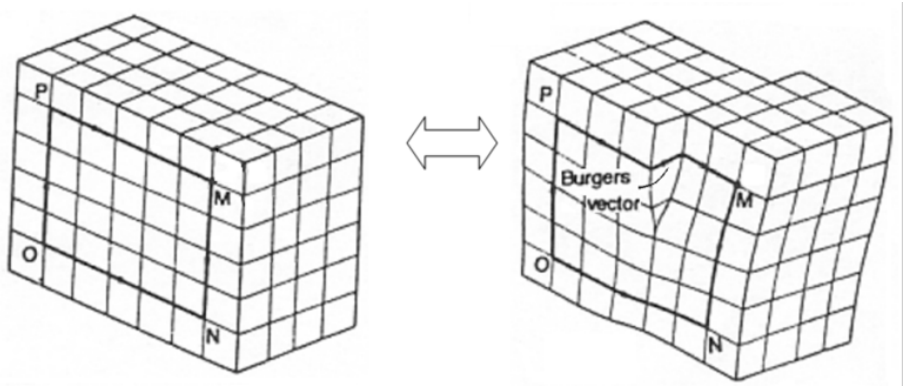

(b) Screw type

Fig. 2.5: Schematic of crystal lattice containing dislocations [57].

$[hk\ell]$, where h, k, and ℓ are translated into a vector using the crystallographic basis of the lattice $\mathbf{b}_1$, $\mathbf{b}_2$, and $\mathbf{b}_3$, which is shown below as

$$\mathbf{g}_{hkl} = h\mathbf{b}_1 + k\mathbf{b}_2 + \ell\mathbf{b}_3 \tag{2.1}$$

An overbar is used to indicate a negative value of h, k, or l. The family of all planes and directions, which are equivalent to $(hk\ell)$ and $[hk\ell]$ using the crystal symmetry, are denoted by $\{hk\ell\}$ and $\langle hk\ell\rangle$. Slip systems along which the majority of dislocations move are called active slip systems. In FCC, the active slip system family is $\{111\}\langle 110\rangle$ [48]. In BCC, $\{110\}\langle 111\rangle$ and $\{112\}\langle 111\rangle$ [48] are active at room temperature and $\{123\}\langle 111\rangle$ becomes active at elevated temperatures [58]. Figure 2.6 illustrates the dominant slip family in FCC materials, where blue planes are the slip planes, the red arrows normal to the planes are the slip normals, and the red arrows along the planes are the slip directions.

Two methods can be used to measure the slip resistance of the material directly. The first method is to measure elastic crystal lattice strains from XRD measurements and

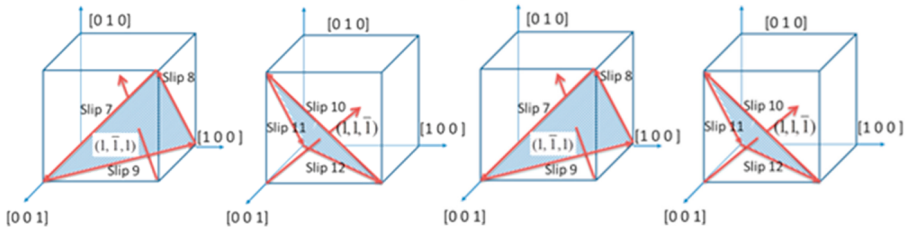

Fig. 2.6: FCC slip planes and directions [59].

convert the measurement to crystal lattice stress using crystal elasticity assumptions. Hu et al. [15] used this technique in conjunction with numerical experiments to show that some plastic slip must occur in transformed martensite to match the lattice strains correctly. A second method is a nano-indentation test where a nano-indenter impact a micropillar created using ion beam milling. Recordings of impact force, grain orientation, slip plane angle, and the number of active slip planes is then used to characterize the slip resistance of individual slip systems [60].

2.3.2 Martensitic Transformation

Figure 2.7(a) shows Gibb's free energies of austenite and martensite. Figure 2.7(b) shows a schematic of the critical stress required for martensitic transformation as a function of temperature [61]. Below the M_s temperature, the difference in Gibb's free energy between austenite and martensite ($\Delta G^{(\gamma \to \alpha')}$) provides a sufficient driving force for martensite to form spontaneously at pre-existing nucleation sites in the austenite. Above the M_s temperature, an additional mechanical driving force (U') is needed to initiate transformation. Stress-assisted transformation occurs between M_s and M_s^σ and is initiated by stress from elastic deformations. Strain-induced transformation occurs between M_s^σ and M_d, where the stress required to initiate transformation is larger than the yield stress. Transformation in this regime occurs due to stress-assisted transformation at existing martensite nucleation sites and spontaneous transformation at potent nucleation sites at the intersection of deformation-induced shear bands [18]. Stress-assisted and strain-induced martensitic transformation are collectively called deformation-induced martensitic transformation (DIMT). Above the M_d temperature, austenite is stable against martensitic transformation because the stress is too low to induce transformation before fracture.

Martensitic transformation is an athermal process for most steels, wherein transformation occurs as soon as the driving force exceeds a critical value [32]. Figure 2.8 shows

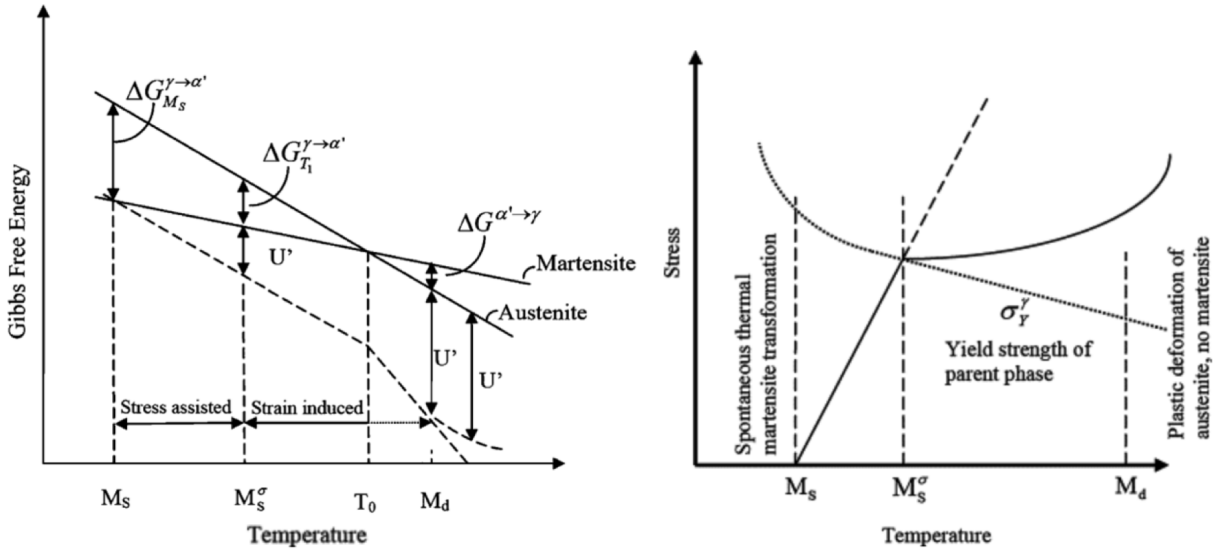

(a) Austenite and martensite Gibb's free energy (b) Critical austenite transformation stress

Fig. 2.7: Temperature dependence of transformation properties [61].

the microstructure of a Fe-1.8C steel alloy as a cooling-driven transformation process progresses. In this figure, the light background is the austenite phase, and the dark needle-like shapes are transformed martensite structures. The martensitic transformation is accompanied by a lattice rotation, plastic dilation and plastic shear [62], with specific values varying depending on alloy and heat treatment [62]. This deformation occurs because the interface between austenite and martensite, called the habit plane, is left undeformed and unrotated [62]. Due to the induced plasticity, DIMT is also known as the transformation induced plasticity (TRIP) effect. The deformation due to transformation is often conceptualized with two components: an unconstrained transformation strain and the strain required to maintain the undeformed and unrotated habit plane. Figure 2.9 shows a schematic of this transformation process, where the dashed lines represent the habit plane: (a) represents the undeformed crystal, (b) represents the free transformation deformation, and (c) and (d) show two different physical modes for accommodating the strain to maintain the habit plane [32]. These two modes (plastic slip and deformation twinning) correspond to martensite formation with lath and twinned type morphologies, respectively [32]. The twinned martensite morphology is known as plate martensite because it tends to form in a plate-like shape. Richman [63] and Roberts and Owen [64] showed that the morphology type is dependent on the initial carbon content of the parent austenite. They showed that low carbon steel (less than 0.4wt%C) formed lath martensite, whereas high carbon

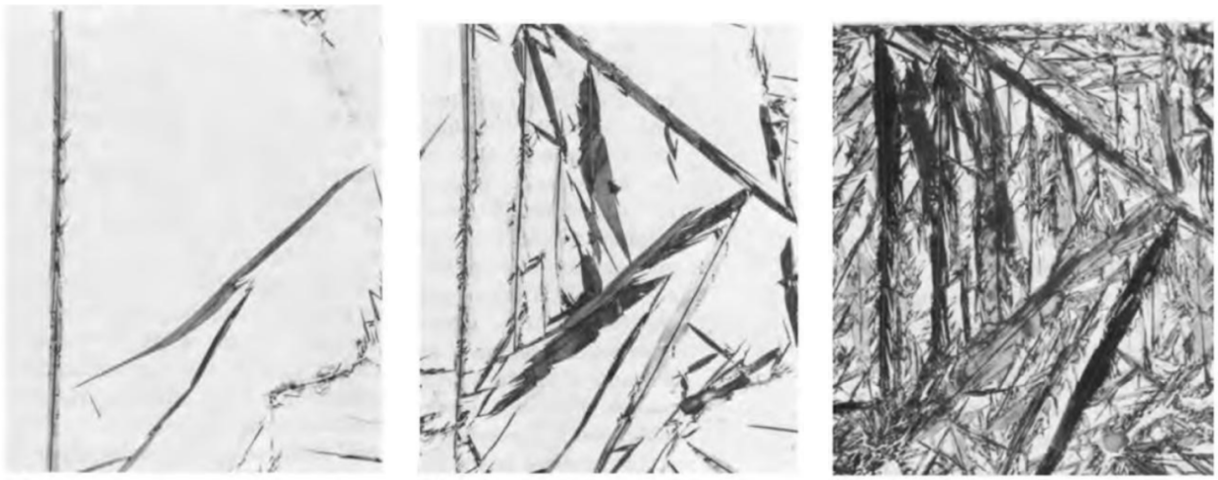

(a) (b) (c)

Fig. 2.8: Cooling driven athermal transformation in Fe-1.8C alloy after cooling to (a) 24 °C, (b) −60 °C and (c) −100 °C. Reproduced from Krauss [32].

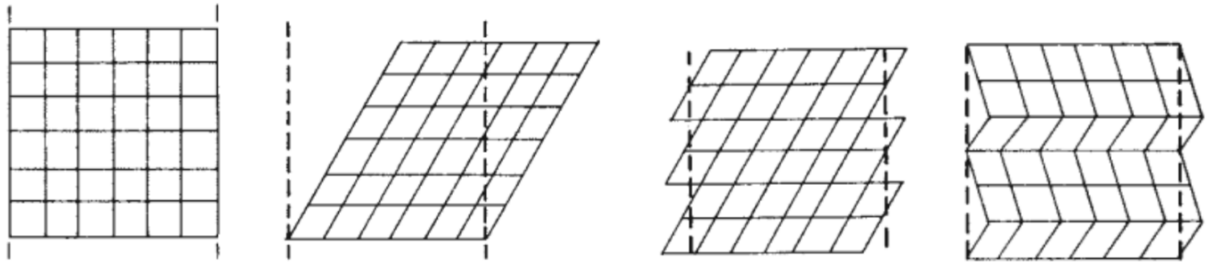

(a) (b) (c) (d)

Fig. 2.9: Schematic of (a) initial austenite, (b) freely transformed martensite, and (c) slipped and (d) twinned constrained martensite lattices. Modified from Krauss [32].

steel formed twinned morphology. In QP steels, the initial martensite is primarily of lath type [65] whereas the transformed martensite primarily develops a twinned morphology [40, 43, 65].

Table 2.1 summarizes a selection of common orientation relationships (OR) used to describe lattice rotations. The notation $\{hk\ell\}\gamma//\{h'k'\ell'\}\alpha'$ means that the $\{hk\ell\}$ family of planes in the initial austenite crystal is parallel to $\{h'k'\ell'\}$ family in the martensite crystal.

Table 2.1: Common orientation relationships.

	Number of Variants	Orientation Relationship	
Bain and Dunkirk [66]	3	$\{001\}\gamma//\{001\}\alpha'$	$\langle 100\rangle\gamma//\langle 110\rangle\alpha'$
K-S [67]	24	$\{111\}\gamma//\{110\}\alpha'$	$\langle 110\rangle\gamma//\langle 111\rangle\alpha'$
N-W [68, 69]	12	$\{111\}\gamma//\{110\}\alpha'$	$\langle 112\rangle\gamma//\langle 110\rangle\alpha'$
Pitsch [70]	12	$\{100\}\gamma//\{100\}\alpha'$	$\langle 011\rangle\gamma//\langle 111\rangle\alpha'$

Similarly, the notation $\langle uvw\rangle\gamma//\langle u'v'w'\rangle\alpha'$ indicates the $\langle uvw\rangle\gamma$ family of directions in the initial austenite crystal is parallel to the $\langle u'v'w'\rangle$ family of directions in the martensite crystal. This means that parent austenite could transform into several distinct martensite variants, each with different orientations. Bain and Dunkirk [66] first proposed an OR based on the theoretical transformation between the FCC and BCT lattice structures of austenite and martensite. However, experimental observations by Kurdjumov and Sachs [67] (K-S) on mild steel and by Nishiyama [68] and Wassermann [69] (N-W) on Fe30%Ni showed significant deviations from Bain's theory. Their works suggested that the mesoscopic OR is governed by effects other than the atom-level austenite to martensite lattice transformation. To avoid the confounding influence of the surrounding matrix on transformation OR in bulk metals, Pitsch [70] used X-Ray diffraction on thin-film austenite to determine another OR. Figure 2.10 summarizes these OR as a stereographic pole figure of $\{100\}\alpha'$ projected onto the $\{111\}\gamma$ [71].

DIMT results in significant work hardening caused by the increased yield stress of transformed martensite relative to austenite [17], local compatibility constraints inducing plastic strain in both the matrix and the transformed martensite [72], and reductions in effective austenite grain size. This enhancement in the work hardening rate increases uniform elongation and thereby improving formability. Additionally, the TRIP effect improves fracture toughness due to delayed crack initiation and reduced crack propagation [14]. Studies have shown that insufficiently stable RA will lower formability and fracture resistance due to premature transformation exhausting the RA. In contrast, RA that is too stable will also lead to lower fracture toughness due to lower microcracking resistance [14] and easier void formation [73].

Due to its significant effect on mechanical behaviour, the RA evolution's characterization is paramount for understanding QP steel. Several methods have been proposed for characterizing this evolution, including the use of electron backscatter diffraction (EBSD) [74] measurements and X-Ray diffraction [53]. Recently, in-situ high-energy X-ray diffrac-

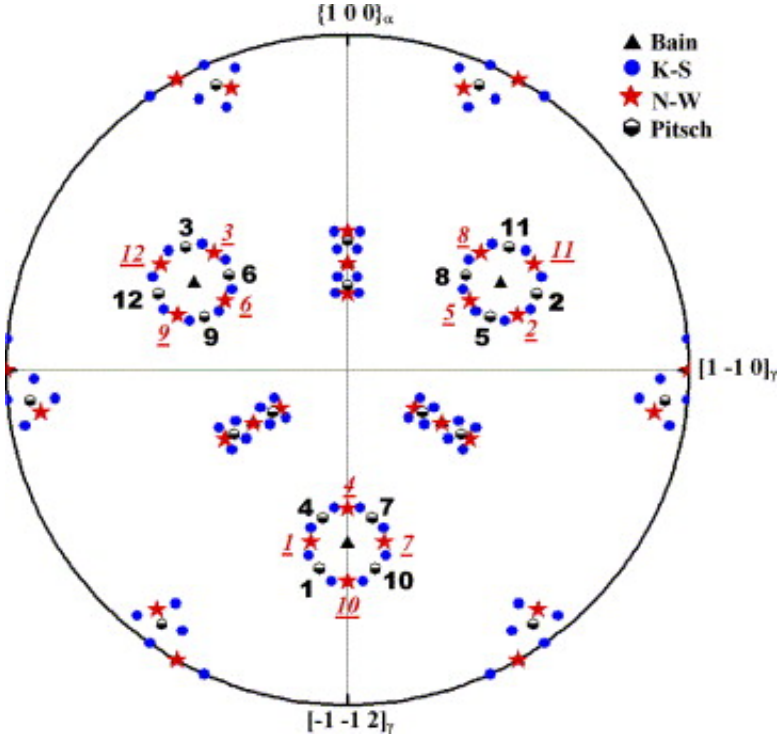

Fig. 2.10: Stereographic pole figure of $\{100\}\alpha'$ poles projected onto $\{111\}\gamma$ plane for Bain and Dunkirk, K-S, N-W and Pitsch OR [71].

tion (HEXRD) uniaxial tension tests have been used to simultaneously capture both stress and RA evolution responses during mechanical testing. Extensive research has been conducted on the mechanical stability of austenite in steels. Serri [75] showed that higher triaxiality resulted in higher transformation rates in TRIP steel because the plastic dilational strain of transformation must do work against hydrostatic pressure, independent of the level of deviatoric stress. Wu et al. [12] stamped a T-shaped component using a medium manganese TRIP steel, observing a more complicated strain path dependence wherein uniaxial tension had the most transformation followed by biaxial then plane strain. Yang and Bhadeshia [76] concluded that decreasing austenite grain size increases the stability of austenite against DIMT. Xiong et al. [43] studied the effects of austenite morphology in QP steel. They found that despite lower carbon content (0.64wt%C vs. 1.14wt%C), film type austenite was significantly more stable than blocky austenite against DIMT. They suggested two possible explanations for this: (1) that the high strength martensite surrounding the film austenite reduces the strain acting on it, or (2) the residual stress in the surrounding martensite exerts a hydrostatic pressure on the film austenite, thereby

suppressing transformation. Oliver et al. [22] studied TRIP steel and observed a preference for transformation along the $\langle 100 \rangle$ family of directions.

Particular focus has been placed on studying the effect of strain-rate and temperature on RA stability. Dan et al. [77] and Durrenberger et al. [78] studied uniaxial deformation of room temperature TRIP800 steel at several strain rates, demonstrating that increasing strain-rate reduces the transformation rate while increasing the overall stress. Rusinek and Klepaczko [79] studied quasi-static uniaxial deformation of TRIP800 steel at several temperatures, finding that overall stress is reduced as the temperature is increased. They conducted an additional room temperature test at $10\,\mathrm{s}^{-1}$ where a temperature rise of nearly $50\,\mathrm{K}$ was recorded at the ultimate tensile strength (UTS). Additional analysis showed that the latent heating of transformation contributed significantly to this heating. Olson and Cohen [18] studied 304 stainless steel, demonstrating that temperature increases significantly suppressed austenite transformation. Poling [53] conducted a detailed experimental analysis of QP3Mn and TRIP7Mn over a wide range of strain rates and temperatures. Figure 2.11 shows martensite transformation results of Poling [53] for QP3Mn and Dan et al. [77] for TRIP 800 steel for several strain-rates. Unlike TRIP800, no clear correlation is observed between transformation rates and the applied strain-rate in QP3Mn steel. Figure 2.12 shows the stress response of Poling for QP3Mn and Durrenberger et al. [78] for TRIP 800 steel for several strain rates. As before, the QP3Mn steel does not exhibit the strain-rate dependence observed in TRIP 800. As in Rusinek and Klepaczko [79], Poling observed a significant temperature rise when QP3Mn was deformed at moderate strain-rates. The impact of strain-rate on transformation is hypothesized to be due to its effect on shear band evolution [21, 80, 81].

Figure 2.13 shows results from Poling for QP3Mn and TRIP7Mn for several temperatures. As in austenitic stainless [18] and TRIP steels [9, 53], increasing temperature heavily suppressed DIMT. Figure 2.14 shows the stress vs. strain results from Poling for QP3Mn and TRIP7Mn for the same temperatures. Despite having similar DIMT temperature dependence in both alloys, the stress response of the QP3Mn shows significantly less temperature dependence than in TRIP7Mn. This suggests that the martensitic transformation in QP3Mn causes significantly less bulk hardening than the transformation in TRIP7Mn. The temperature dependence of transformation is proposed to be due to its impact on chemical stability and shear band evolution [18, 53, 82]. The observed temperature dependence of DIMT in QP3Mn combined with the increased temperature rise at high strain-rate should act to suppress martensitic transformation. Since this is not observed, increasing strain-rate for a fixed temperature would probably promote transformation.

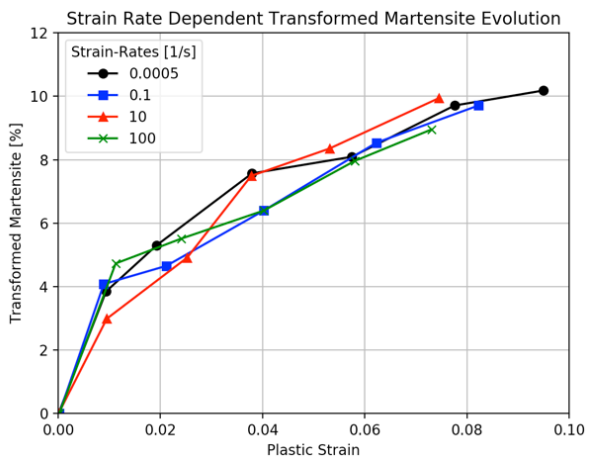

(a) QP3Mn [53]

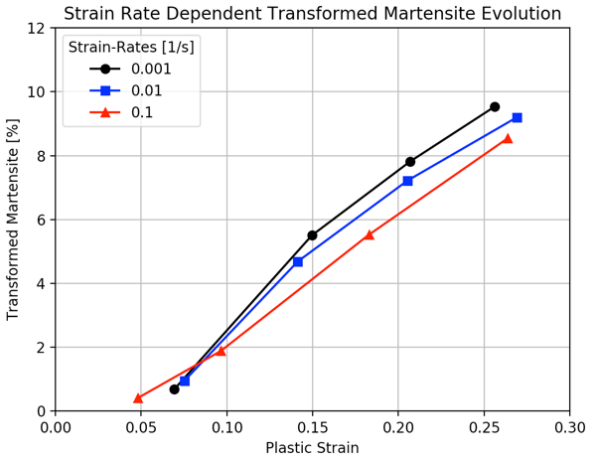

(b) TRIP 800 [77]

Fig. 2.11: Experimental strain-rate dependent martensite transformation (adapted from Poling [53] and Dan et al. [77]).

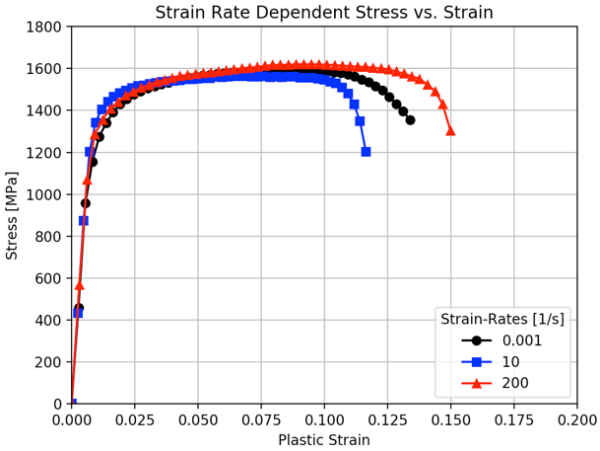

(a) QP3Mn [53]

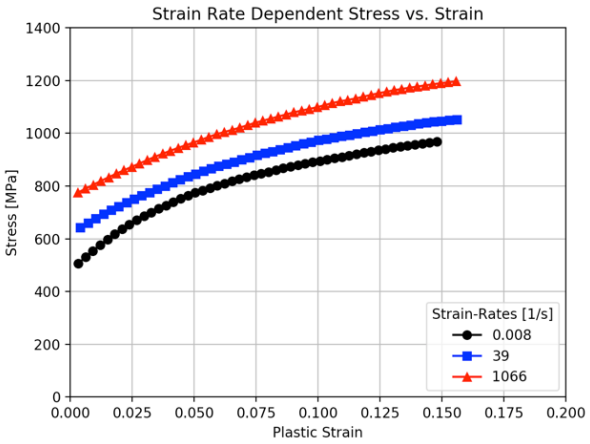

(b) TRIP 800 [78]

Fig. 2.12: Experimental strain-rate dependent stress vs. strain (adapted from Poling [53] and Durrenberger et al. [78]).

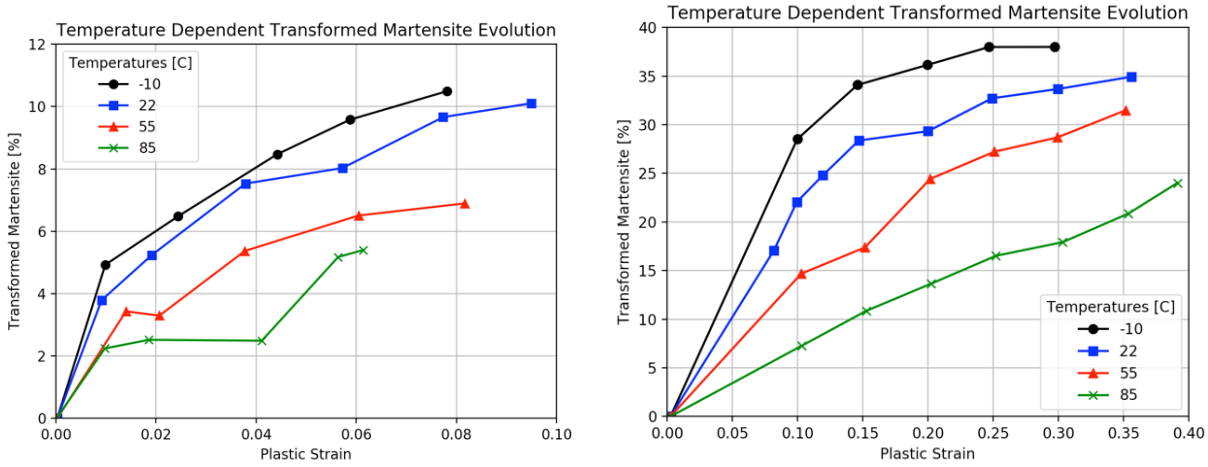

(a) QP3Mn [53] (b) TRIP7Mn [53]

Fig. 2.13: Experimental temperature dependent martensite transformation (adapted from Poling [53]).

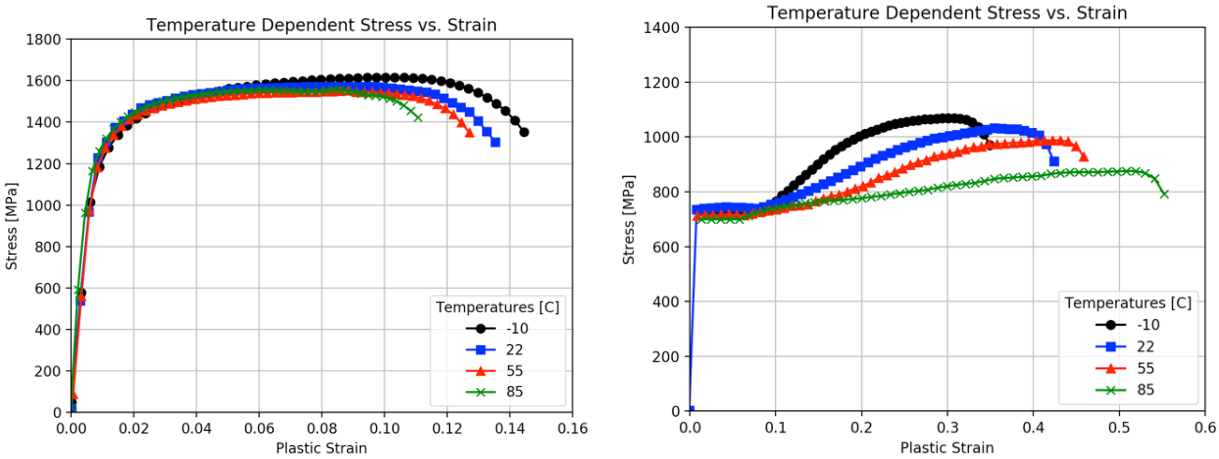

(a) QP3Mn [53] (b) TRIP7Mn [53]

Fig. 2.14: Experimental temperature dependent stress vs. strain. (adapted from Poling [53]).

2.4 Constitutive Modelling

Modelling of QP steel requires the incorporation of both plastic slip and the TRIP effect. These effects can be modelled using either phenomenological or mechanistic models. Phenomenological models capture macroscopically observed physical behaviour without capturing the underlying mechanics and are frequently used to model austenitic stainless [83–86] and TRIP steels [9, 85, 87]. These models are used in lab-scale component analysis [9, 83–87], due to improved computational efficiency relative to mechanistic models. However, phenomenological models require a relatively large number of calibration experiments to characterize the material behaviour. In contrast, mechanistic models focus on incorporating the underlying physics to enable higher modelling accuracy with fewer required experiments, with a proportional reduction in computational efficiency. This high accuracy is essential for crash and forming simulations, where significant sensitivity to material anisotropy is observed [88, 89]. Recently, mechanistic models have received considerable attention [27, 29, 90] for applications in multiscale modelling, where mechanistic models are used to generate calibration data for phenomenological models. This mitigates both models' disadvantages because fewer experiments are required for calibration, but the final model has the desired computational efficiency for lab-scale components. This work will focus on mechanistic models due to (1) higher accuracy, (2) fewer calibration experiments and (3) necessity as the first step of multi-scaling models.

Several types of mechanistic models can be used to model the behaviour of QP steel. Molecular dynamics (MD) uses numerical approximations to model the atomic-level interactions within a unit cell [91]. Discrete dislocation dynamics (DDD) directly models dislocations as an elastic inclusion embedded in an elastic medium. Crystal plasticity (CP) is a model that attempts to capture the aggregate motion of dislocations on the crystal's slip systems. Figure 2.15 shows the length and time scales that are achievable with current computational capabilities for each of these mechanistic models [92]. MD and DD cannot capture the length and time scales needed to simulate bulk material properties, leaving only crystal plasticity suitable for this work. However, the crystal plasticity constitutive laws only capture a single crystal. Modelling techniques must be used to aggregate the behaviour of many single crystals to capture a polycrystalline metal's material behaviour.

2.4.1 Polycrystalline Modelling

Two general approaches exist for aggregating polycrystalline behaviour from single-crystal responses: direct numerical solution and homogenization. In direct numerical so-

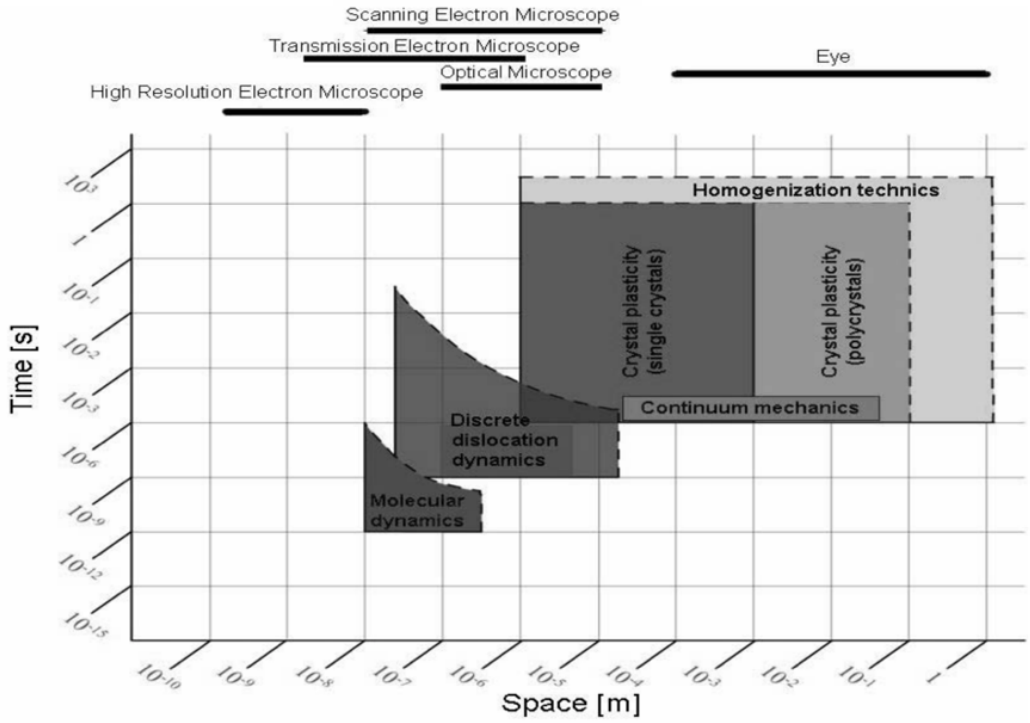

Fig. 2.15: Achievable length and time scales of mechanistic models [92].

lution, a solution to the partial differential equations (PDEs) that govern the interaction between grains is approximated numerically using the finite element method (FEM)[93], or fast Fourier transforms (FFT)[94]. In either case, boundary conditions are applied to a representative volume element (RVE) that is assumed to repeat in an infinite tessellation in all three directions. As such, the RVE boundary conditions must be periodic, and the RVE must be a representative sample of the real material orientation distribution, phase volume fraction and phase morphology. FEM with CP has been used frequently for QP steels [40, 41, 95] with most assuming that the material is isothermal [40, 41]. In the work of Lee et al. [95], the temperature was assumed to vary adiabatically with different strain rates producing different heating rates by modifying the ratio of plastic work to heat generation. This simplification does not allow for the incorporation of general thermal boundary conditions, which can significantly affect formability in TRIP steel alloys [10]. No work has proposed a method for incorporating general thermal boundary conditions in RVE models, as may be necessary for QP steel.

In homogenization, inter-grain interactions are solved analytically for a limited case,

which is used to approximate the homogenous bulk material response. The simplest models for polycrystalline materials are the Taylor [96], and Sachs [97] models that assume all crystals in a material have the same applied strain or stress, respectively. The Taylor model has often been used to predict bulk properties and localization in aluminum, magnesium and steel alloys [98–100]. However, care must be taken to ensure that the stress differential between grains is not too large, as the Taylor model does not rigorously enforce stress equilibrium. The Sachs model is rarely used because it does not enforce strain compatibility. To account for both strain compatibility and stress equilibrium, Eshelby [101] determined a homogenous analytical response for an elastic material with small, diffuse elastic inclusions embedded inside. This is useful for materials with a small volume fraction of inclusions, where the inter-inclusion interactions can be neglected. For the case of polycrystals, where no matrix phase can be directly defined, Hill [102] proposed the self-consistent (SC) scheme. In this scheme, all grains are modelled as inclusions within a matrix phase that behaves identically to the homogenized material. Molinari et al. [103] generalized the SC scheme to viscoplastic behaviour by proposing linearization of the material response over a time increment. Lebensohn et al. [104] showed that the specific choice of linearization scheme has a significant effect on homogenized material properties. They then derived a second-order self-consistent scheme that accounts for stress variations within each grain that produced more accurate results and reduced sensitivity to the chosen linearization scheme. Self-consistent schemes have often been used to model QP steels under isothermal conditions [15, 40]. For non-isothermal conditions, there has been little work using homogenization schemes because the self-consistent does not account for the variation of temperature and thermal strains throughout the material.

2.4.2 Slip Plasticity

Rate-independent crystal plasticity was first proposed by Asaro and Rice [105] to model localization in single crystals. Slip was assumed to occur on a subset of the possible active slip families with the amount of slip governed by a hardening law. In this model, slip rates could only be uniquely defined if exactly five slip systems were active. Based on physical principles, Bishop and Hill [106] proposed using the set of slip systems leading to maximum plastic work. Asaro and Needleman [107] proposed a visco-plastic rate-dependent crystal plasticity wherein the slip rate on all possible slip systems is governed by the ratio of resolved shear stress to a critical resolved shear stress (CRSS), a viscosity and a rate exponent. This CRSS was assumed to evolve with increasing strain. This model had the additional advantage of not requiring any assumption regarding the choice of active slip systems. Recently, there has been significant interest in temperature-dependent and

thermodynamically consistent crystal plasticity-based constitutive models to better simulate materials where the temperature has a significant effect on the underlying physics and deformation mechanisms [108, 109]. The first such model for plastic slip was Clayton [108] who proposed modifications to the kinematics such that the deformation gradient is decomposed into elastic ($\mathbf{F}_e$), thermal ($\mathbf{F}_\theta$) and plastic ($\mathbf{F}_p$) components

$$\mathbf{F} = \mathbf{F}_e\mathbf{F}_\theta\mathbf{F}_p \tag{2.2}$$

where deformation and rigid body rotation from the plastic slip are contained in $\mathbf{F}_p$, thermal expansion is contained in $\mathbf{F}_\theta$ and elastic deformation and all other rigid body rotation is contained in $\mathbf{F}_e$. The velocity gradient is decomposed additively

$$\mathbf{L} = \dot{\mathbf{F}}\mathbf{F}^{-1} = \dot{\mathbf{F}}_e\mathbf{F}_e^{-1} + \mathbf{F}_e\dot{\mathbf{F}}_\theta\mathbf{F}_\theta^{-1}\mathbf{F}_e^{-1} + \mathbf{F}_e\mathbf{F}_\theta\dot{\mathbf{F}}_p\mathbf{F}_p^{-1}\mathbf{F}_\theta^{-1}\mathbf{F}_\theta^{-1} \tag{2.3}$$

The strain-rate ($\mathbf{D}$) and spin-rate ($\mathbf{\Omega}$) tensors are decomposed into elastic, thermal and plastic parts

$$\mathbf{D} = \frac{\mathbf{L}+\mathbf{L}^T}{2} = \mathbf{D}_e + \mathbf{D}_\theta + \mathbf{D}_p \tag{2.4}$$

$$\mathbf{\Omega} = \frac{\mathbf{L}-\mathbf{L}^T}{2} = \mathbf{\Omega}_e + \mathbf{\Omega}_\theta + \mathbf{\Omega}_p \tag{2.5}$$

where the thermal spin-rate ($\mathbf{\Omega}_\theta$) is zero, and the thermal strain-rate is given by

$$\mathbf{D}_\theta = A\dot{\theta}\mathbf{I} \tag{2.6}$$

where A is the linear thermal expansion coefficient, $\dot{\theta}$ is the rate of change of temperature and $\mathbf{I}$ is the second-order identity tensor. Plasticity occurs by slip on each slip system. These slip systems are assumed to deform and rotate with the elastic and thermal deformation gradients, such that

$$\mathbf{s}_e^{(\alpha)} = \mathbf{F}_e\mathbf{F}_\theta\mathbf{s}^{(\alpha)} \tag{2.7}$$

$$\mathbf{m}_e^{(\alpha)} = \mathbf{m}^{(\alpha)}\mathbf{F}_\theta^{-1}\mathbf{F}_e^{-1} \tag{2.8}$$

where $\mathbf{s}_e^{(\alpha)}$ and $\mathbf{m}_e^{(\alpha)}$ are the deformed slip direction and slip system normal on slip system α and $\mathbf{s}^{(\alpha)}$ and $\mathbf{m}^{(\alpha)}$ are the slip direction and slip system normal on slip system α at the beginning of the simulation. The plastic strain-rate and spin rate tensors are calculated as a function of the slip rate ($\dot{\gamma}^{(\alpha)}$) on each slip system α using

$$\mathbf{D}_p = \sum_{\alpha=1}^{N_p} \dot{\gamma}^{(\alpha)}\mathbf{P}_p^{(\alpha)} \tag{2.9}$$

$$\mathbf{\Omega}_p = \sum_{\alpha=1}^{N_p} \dot{\gamma}^{(\alpha)}\mathbf{W}_p^{(\alpha)} \tag{2.10}$$

where N_p is the number of slip systems and $\mathbf{P}_p^{(\alpha)}$ and $\mathbf{W}_p^{(\alpha)}$ are symmetric and antisymmetric slip system tensors given by

$$\mathbf{P}_p^{(\alpha)} = \frac{\mathbf{s}_e^{(\alpha)} \otimes \mathbf{m}_e^{(\alpha)} + \mathbf{m}_e^{(\alpha)} \otimes \mathbf{s}_e^{(\alpha)}}{2} \quad (2.11) \qquad \mathbf{W}_p^{(\alpha)} = \frac{\mathbf{s}_e^{(\alpha)} \otimes \mathbf{m}_e^{(\alpha)} - \mathbf{m}_e^{(\alpha)} \otimes \mathbf{s}_e^{(\alpha)}}{2} \quad (2.12)$$

The overall stress is calculated using a hyper-elastic law as given below

$$\overset{\triangledown}{\tau}_{ij} = F_{e(ia)} F_{e(jb)} F_{e(kc)} F_{e(ld)} \mathbb{C}_{abcd} D_{e(kl)} = \left[\mathbf{F}_e \cdot \mathbf{F}_e \cdot \mathbb{C} \cdot \mathbf{F}_e^T \cdot \mathbf{F}_e^T\right] : \mathbf{D}_e \quad (2.13)$$

where $\overset{\triangledown}{\tau}$ is any objective stress rate of the Kirchoff stress, $\mathbb{C}$ is an elastic tensor that is generally calculated using crystal elasticity [107, 110]. In crystal elasticity, the specific form of $\mathbb{C}$ is dependent on the symmetry of the crystal lattice of the material. For materials with cubic symmetry (e.g. FCC and BCC), the crystal elasticity $\mathbb{C}$ is given in Voigt form by

$$\{\mathbb{C}\} = \left\{ \begin{bmatrix} \kappa_1 & \kappa_2 & \kappa_2 & 0 & 0 & 0 \\ \kappa_2 & \kappa_1 & \kappa_2 & 0 & 0 & 0 \\ \kappa_2 & \kappa_2 & \kappa_1 & 0 & 0 & 0 \\ 0 & 0 & 0 & \kappa_3 & 0 & 0 \\ 0 & 0 & 0 & 0 & \kappa_3 & 0 \\ 0 & 0 & 0 & 0 & 0 & \kappa_3 \end{bmatrix} \right\} \quad (2.14)$$

where κ_1, κ_2 and κ_3 are independent material constants. To calculate the slip rates, most rate-dependent crystal plasticity models assume that dislocation motion occurs according to the Schmid law [107], where slip occurs when the resolved stress on a slip system exceeds a critical resolved shear stress (CRSS). Mathematically, this is given by

$$\dot{\gamma}^{(\alpha)} = f(\tau^{(\alpha)}, g^{(\alpha)}, \mathbf{c}, \mathbf{d}) \quad (2.15) \qquad \tau^{(\alpha)} = \mathbf{P}_p^{(\alpha)} : \boldsymbol{\tau} \quad (2.16)$$

where f is a kinetics function that determines the magnitude of slip, $\tau^{(\alpha)}$ and $g^{(\alpha)}$ are the resolved and critical resolved shear stress on slip system α, $\mathbf{c}$ is a vector of material parameters, and $\mathbf{d}$ is a vector of other state variables. Various functions have been proposed for use as f, including primarily power-law type behaviour [27, 29, 107] and exponential behaviour inspired by dislocation kinetics theory [111]. Power-law behaviour, due to its simplicity and history, is the most commonly used and is given by

$$\dot{\gamma}^{(\alpha)} = f(\tau^{(\alpha)}, g^{(\alpha)}, \dot{a}_0, m) = \dot{a}_0 \text{ sign } \left(\tau^{(\alpha)}\right) \left|\frac{\tau^{(\alpha)}}{g^{(\alpha)}}\right|^{\frac{1}{m}} \quad (2.17)$$

where $\dot{a}_0$ is a reference slip rate, and m is a parameter determining the strain-rate dependence of the material. The evolution of $g^{(\alpha)}$ is then described by

$$\dot{g}^{(\alpha)} = \sum_{\beta=1}^{N_p} h\left(\gamma_a\right) q_{\alpha\beta} \dot{\gamma}^{(\beta)} \tag{2.18}$$

$$\gamma_a = \sum_{\alpha=1}^{N_p} \int_0^t \left|\dot{\gamma}^{(\alpha)}\right| \, \mathrm{d}t \tag{2.19}$$

where $h(\star)$ is the hardening function, $q_{\alpha\beta}$ is the latent hardening matrix, and γ_a is the total absolute shear. Common models for $h(\star)$ and $q_{\alpha\beta}$ include Chang-Asaro [112] and Asaro-Needleman [107]. To ensure that the model is thermodynamically consistent, it is assumed that Helmholtz free energy follows the form $\Psi = \Psi\left(\mathbf{E}_e, \theta, \beta\right)$ where $\mathbf{E}_e$ is the elastic Green-Lagrange strain, θ is the temperature, and β is a measure of the stored strain-energy surrounding dislocations. The first and second laws of thermodynamics are then given in the forms

$$\rho \dot{e} + \boldsymbol{\nabla} \cdot \mathbf{q} - \boldsymbol{\sigma} : \mathbf{D} = \rho r \tag{2.20}$$

$$\rho \dot{\eta} \geq -\boldsymbol{\nabla} \cdot \left(\frac{\mathbf{q}}{\theta}\right) + \frac{\rho r}{\theta} \tag{2.21}$$

where ρ is the density, $\dot{e}$ is the rate of change of internal energy, $\mathbf{q}$ is the heat flux vector, $\dot{\eta}$ is the rate of change of entropy, and r is the volumetric heat generation rate. Using the Legendre transformation $\Psi = e - \theta\eta$ and using the results of Coleman and Noll [113] regarding irreversible thermodynamic systems, the following Helmholtz free energy function

$$\rho\Psi = \frac{1}{2}\mathbf{E}_e : \mathbb{C} : \mathbf{E}_e + \frac{1}{2}\kappa\mu\beta^2 - \hat{c}\theta \ln\left(\frac{\theta}{\theta_0}\right) \tag{2.22}$$

where κ is a dimensionless scalar relating internal energy to the internal microstrain metric, μ is the shear modulus, $\hat{c}$ is the specific heat capacity, and θ_0 is a reference temperature. This is then used in combination with the above equations to derive the temperature evolution law

$$\rho\hat{c}\dot{\theta} = \sum_{\alpha=1}^{N_p} \tau^{(\alpha)}\dot{\gamma}^{(\alpha)} - \rho\left(\frac{\partial\Psi}{\partial\beta} - \theta\frac{\partial^2\Psi}{\partial\theta\partial\beta}\right)\dot{\beta} + \rho\theta\frac{\partial^2\Psi}{\partial\theta\partial\mathbf{E}_e} : \dot{\mathbf{E}}_e - \boldsymbol{\nabla}\cdot\mathbf{q} + \rho r \tag{2.23}$$

Several numerical formulations have been proposed for integrating the crystal plasticity equations. Asaro and Needleman [107] used the rate tangent scheme, a type of forward gradient integration algorithm, which produced good results. Raphanel et al. [114] proposed a Runge-Kutta scheme for use with crystal plasticity. Rossiter et al. [7] proposed an explicit Euler integration algorithm for use with explicit dynamic finite element models.

2.4.3 Martensitic Transformation

Whether used with phenomenological or mechanistic plastic slip models, most TRIP models proposed in literature follow a mechanistic formulation. This is due to the difficulty of capturing the material behaviour without including the underlying physics. Significant work has been conducted on mechanistic modelling of the TRIP effect, which will be summarized in the next subsections. The following model lineages will be summarized:

- Stringfellow et al. Model Lineage [9, 10, 18, 19, 21, 83]
- Cherkaoui et al. Model Lineage [42, 115–117]
- Turteltaub et al. Model Lineage [109, 110, 118, 119]
- Lee et al. Model Lineage [18, 83, 95]
- Ma and Hartmaier Model Lineage [91, 120, 121]
- Park et al. Model Lineage [41, 122, 123]

To avoid confusion, variables defined in each subsection are specific to the subsection and do not overlap with the other models.

2.4.3.1 Stringfellow et al. Model Lineage

Mechanistic modelling of martensitic transformation originated with the work of Olson and Cohen [18], who observed that martensite nucleated at shear band intersection sites. This was later extended by Stringfellow et al. [83], Tomita and Iwamoto [21], and Iwamoto et al. [19] to better account for strain-rate, stress state and temperature. In this model, the rate of transformation of martensite ($f_{\alpha'}$) is given by

$$\dot{f}_{\alpha'} = f_{\gamma}\left[p\dot{f}^{i}_{sb} + f^{i}_{sb}\dot{p}H(\dot{p})\right] \tag{2.24}$$

where f_{γ} is the RAVF, p is the probability of a shear band intersection site transforming, f^{i}_{sb} is the volume fraction of shear band intersection sites and $H(\star)$ is a Heaviside function. The shear band intersection volume fraction is related to the volume fraction of shear bands (f_{sb}) and an effective slip rate in the austenite ($\dot{\bar{\varepsilon}}^{pslip}_{\gamma}$) using

$$f_{sb}^{i} = \eta \left(f_{sb}\right)^{n} \qquad (2.25) \qquad \dot{f}_{sb} = a_m \left(1 - f_{sb}\right) \dot{\bar{\varepsilon}}_{\gamma}^{pslip} \qquad (2.26)$$

where η and n are calibration constants and a_m is given by

$$a_m = \left(a_{m,1} + a_{m,1}T + a_{m,1}T^2 - a_{m,1}\Sigma\right)\left(1 - a_{m,1}\left(\frac{\dot{\bar{\varepsilon}}}{\dot{\varepsilon}_0}\right)\right) \qquad (2.27)$$

$$\Sigma = \frac{\mathrm{tr}(\boldsymbol{\sigma})}{3\bar{\sigma}} \qquad (2.28)$$

where $a_{m,1} - a_{m,6}$ are calibration parameters, T is temperature, Σ is stress triaxiality, $\dot{\bar{\varepsilon}}$ is an effective strain rate, $\dot{\varepsilon}_0$ is a strain-rate normalization factor, and $\bar{\sigma}$ is the von Mises equivalent stress. The probability of transformation is given by

$$p = \frac{1}{\sqrt{2\pi}\sigma_s} \int_{-\infty}^{g} \exp\left(-\frac{\left(g' - g_0\right)^2}{2\sigma_s^2}\right) \mathrm{d}g' \qquad (2.29)$$

$$g = -T + g_1\Sigma \qquad (2.30)$$

where g_0 and σ_s are the mean and standard deviation of the distribution of critical driving forces required to cause transformation at a shear band intersection site, g is the transformation driving force g_1 is the dependence of the driving force triaxiality. Hardening due to transformation is handled by homogenization of stresses in austenite and transformed martensite.

This model was used by Kohar et al. [9] with an advanced phenomenological slip plasticity model to analyze TRIP800 crush behaviour. They showed that adiabatic heating at high strain-rates suppressed martensite generation, thereby limiting the energy absorption capacity of TRIP 800 steel. The model was then used by Connolly et al. [10] to study the formability of TRIP 800 steel, showing that temperature had a significant impact on formability and that thermal boundary condition control could result in significantly improved formability.

2.4.3.2 Cherkaoui et al. Model Lineage

Cherkaoui et al. [115, 116] and Kubler et al. [117] proposed the first constitutive model incorporating transformation within a crystal plasticity framework. In their work, each martensite variant was modelled as an ellipsoidal inclusion in an austenitic matrix. The macroscopic strain rate ($\dot{\mathbf{E}}$) is decomposed according to

$$\dot{\mathbf{E}} = \dot{\mathbf{E}}_e + \dot{\mathbf{E}}_p + \dot{\mathbf{E}}_{tr} = \langle \dot{\boldsymbol{\varepsilon}}_e \rangle + \langle \dot{\boldsymbol{\varepsilon}}_p \rangle + \langle \dot{\boldsymbol{\varepsilon}}_{tr} \rangle \tag{2.31}$$

where $\dot{\mathbf{E}}_e$, $\dot{\mathbf{E}}_p$ and $\dot{\mathbf{E}}_{tr}$ are the macroscopic elastic, plastic slip and transformation induced strains and $\dot{\boldsymbol{\varepsilon}}_e$, $\dot{\boldsymbol{\varepsilon}}_p$ and $\dot{\boldsymbol{\varepsilon}}_{tr}$ are the corresponding local strains, and $\langle \star \rangle = \frac{1}{V}\int_V (\star)\ \mathrm{d}V$ indicates a volume average. The macroscopic strains are given by

$$\dot{\mathbf{E}}_e = \left[\mathbb{C}^A\right]^{-1} : \overset{\triangledown}{\boldsymbol{\Sigma}} \tag{2.32}$$

$$\dot{\mathbf{E}}_p = (1-f)\,\dot{\bar{\varepsilon}}_p^A + \sum_{I=1}^{N_T} f_I \dot{\bar{\varepsilon}}_p^{M_I} \tag{2.33}$$

$$\dot{\mathbf{E}}_{tr} = \sum_{I=1}^{N_T} \dot{f}^I \boldsymbol{\varepsilon}_T^I \tag{2.34}$$

where $\mathbb{C}^A$ is the austenitic elasticity tensor, $\overset{\triangledown}{\boldsymbol{\Sigma}}$ is the macroscopic Jaumann stress rate, $f = \sum_{I=1}^{N_T} f_I$ is the total volume fraction of martensite, f^I, ε_T^I and $\dot{\bar{\varepsilon}}_p^{M_I}$ are the volume fraction, total transformation strain and average local plastic strain rate of martensite variant I, $\dot{\bar{\varepsilon}}_p^A$ is the average local strain rate in the austenite phase, and N_T is the number of active martensite variants. The macroscopic rotation rate ($\dot{\boldsymbol{\Omega}}$) is decomposed using

$$\dot{\boldsymbol{\Omega}} = \dot{\boldsymbol{\Omega}}_e + \dot{\boldsymbol{\Omega}}_p + \dot{\boldsymbol{\Omega}}_{tr} = \langle \dot{\boldsymbol{\omega}}_e \rangle + \langle \dot{\boldsymbol{\omega}}_p \rangle + \langle \dot{\boldsymbol{\omega}}_{tr} \rangle \tag{2.35}$$

where $\dot{\boldsymbol{\Omega}}_e$, $\dot{\boldsymbol{\Omega}}_p$ and $\dot{\boldsymbol{\Omega}}_{tr}$ are the macroscopic elastic, plastic slip and transformation induced rotation rates and $\dot{\boldsymbol{\omega}}_e$, $\dot{\boldsymbol{\omega}}_p$ and $\dot{\boldsymbol{\omega}}_{tr}$ are the corresponding local rotation rates. The inelastic rotation rates are given by

$$\dot{\boldsymbol{\Omega}}_p = \dot{\bar{\boldsymbol{\omega}}}_p^A - \sum_{I=1}^{N_T} f_I \mathbb{T}^I : \mathbb{C}^A : \left(\dot{\bar{\varepsilon}}_p^{M_I} - \dot{\bar{\varepsilon}}_p^A\right) \tag{2.36}$$

$$\dot{\boldsymbol{\Omega}}_{tr} = \sum_{I=1}^{N_T} \dot{f}_I \omega_T^I \tag{2.37}$$

where $\dot{\bar{\boldsymbol{\omega}}}_p^A$ is the average local plastic rotation rate of the austenite, and T^I and ω_T^I are the antisymmetric Eshelby tensor and the total transformation rotation of martensite variant I. The elastic rotation rates are determined from the applied macroscopic rotation rate and the inelastic rotation rates. The plastic slip strain and rotation rates are given by

$$\dot{\bar{\varepsilon}}_p^A = \sum_{\alpha=1}^{N_s^A} \dot{\gamma}_A^\alpha \mathbf{P}_A^{(\alpha)} \qquad (2.38) \qquad\qquad \dot{\boldsymbol{\omega}}_p^A = \sum_{\alpha=1}^{N_s^A} \dot{\gamma}_A^\alpha \mathbf{W}_A^{(\alpha)} \qquad (2.39)$$

$$f_I \dot{\bar{\varepsilon}}_p^{M_I} = \sum_{\alpha=1}^{N_s^{M_I}} \dot{\gamma}_{M_I}^\alpha \mathbf{P}_{M_I}^{(\alpha)} + \dot{f}_I \left(\bar{\varepsilon}_p^A - \bar{\varepsilon}_p^{M_I}\right) \qquad (2.40)$$

where $\dot{\gamma}_A^\alpha$ are the austenite slip rates, $\mathbf{P}_A^{(\alpha)}$ and $\mathbf{W}_A^{(\alpha)}$ are the symmetric and antisymmetric austenite Schmid tensors, $\dot{\gamma}_{M_I}^\alpha$ and $\mathbf{P}_{M_I}^{(\alpha)}$ are the slip rates and symmetric Schmid tensors of martensite variant I, and N_s^A and $N_s^{M_I}$ are the number of slip systems in the austenite phase and martensite variant I. The Schmid tensors are defined by slip systems as in standard crystal plasticity. The stresses in austenite (σ^A) and martensite variant I (σ^{M_I}) are given by

$$\boldsymbol{\sigma}^A = \boldsymbol{\Sigma} - \sum_{I=1}^{N_T} f_I \mathbb{C}^A : (\mathbb{I} - \mathbb{S}_I) : \left(\bar{\boldsymbol{\varepsilon}}_p^A - \bar{\boldsymbol{\varepsilon}}_T^I - \bar{\boldsymbol{\varepsilon}}_p^{M_I}\right) \qquad (2.41)$$

$$\boldsymbol{\sigma}^{M_I} = \boldsymbol{\sigma}^A \sum_{I=1}^{N_T} f_I \mathbb{C}^A : (\mathbb{I} - \mathbb{S}_I) : \left(\bar{\boldsymbol{\varepsilon}}_p^A - \bar{\boldsymbol{\varepsilon}}_T^I - \bar{\boldsymbol{\varepsilon}}_p^{M_I}\right) \qquad (2.42)$$

where $\mathbb{I}$ is the fourth-order identity tensor and $\mathbb{S}_I$ is the symmetric Eshelby tensor for martensite variant I. Finally, the Coleman and Noll [113] procedure is used to derive driving forces for plasticity in austenite ($F_p^{A(\alpha)}$) and martensite variant I plasticity ($F_p^{M_I(\alpha)}$) and transformation (F^I)

$$F_p^{A(\alpha)} = \boldsymbol{\sigma}^A : \mathbf{P}_A^{(\alpha)} \qquad (2.43) \qquad\qquad F_p^{M_I(\alpha)} = \boldsymbol{\sigma}^{M_I} : \mathbf{P}_{M_I}^{(\alpha)} \qquad (2.44)$$

$$\begin{aligned} F^I = {} & \boldsymbol{\sigma}^A : \boldsymbol{\varepsilon}_T^I - B(T - T_0) - \frac{1}{2}(\boldsymbol{\varepsilon}_T^I : \mathbb{C}^A : (\mathbb{I} - \mathbb{S}_I) : \boldsymbol{\varepsilon}_T^I \\ & + \kappa \sum_{\alpha=1}^{N_s^A} \boldsymbol{\varepsilon}_T^I : \mathbb{C}^A : (\mathbb{S}_I - \mathbb{S}_d) : \mathbf{P}_A^{(\alpha)} \gamma_A^{(\alpha)} + \frac{1}{2}\frac{\dot{f}_I}{f_I}(\boldsymbol{\varepsilon}_T^I : \mathbb{C}^A : \dot{\mathbb{S}}_I : \boldsymbol{\varepsilon}_T^I) \end{aligned} \qquad (2.45)$$

where T and T_0 are current and reference temperature, B is the dependence of energy on temperature, κ is a calibration constant, and $\mathbb{S}_d$ is the symmetric Schmid tensor for a transforming plastic defect. A consistency rule is then established from the driving force and a hardening law, giving a complete set of equations for slip and transformation rates. This model was used to model 304 stainless steel by Petit et al. [42], showing that with

a suitable choice of transformation system, the stress vs. strain curve and transformation kinetics can be captured accurately. However, this work also showed that to capture the texture evolution properly, it was necessary to account for the formation of ϵ martensite plates as an intermediary to the formation of α' martensite.

2.4.3.3 Turteltaub et al. Model Lineage

Turteltaub and Suiker [110, 118] proposed a stress-based transformation model for use with shape memory alloys and with some steel applications. Tjahjanto et al. [119] and Yadegari et al. [109] extended the model to include thermal and plastic slip deformation modes. The deformation kinematics are given by a multiplicative decomposition of the deformation gradient

$$\mathbf{F} = \mathbf{F}_e \mathbf{F}_\theta \mathbf{F}_p \mathbf{F}_{tr} \tag{2.46}$$

where $\mathbf{F}_e$, $\mathbf{F}_\theta$, $\mathbf{F}_p$ and $\mathbf{F}_{tr}$ are the elastic, thermal, plastic slip and TRIP deformation gradients. The thermal, plastic slip and TRIP components are defined by

$$\mathbf{F}_\theta = \mathbf{I} + \frac{1}{\det\left(\mathbf{F}_{tr}\right)} \left(\xi_A \mathbf{A}_A + (1+\delta_T) \sum_{\alpha=1}^{N_T} \xi^{(\alpha)} \mathbf{A}^{(\alpha)} \right) (\theta - \theta_0) \tag{2.47}$$

$$\dot{\mathbf{F}}_p = \left[\sum_{i=1}^{N_s} \dot{\gamma}^{(i)} \mathbf{s}^{(i)} \otimes \mathbf{m}^{(i)} \right] \mathbf{F}_p \tag{2.48}$$

$$\dot{\mathbf{F}}_{tr} = \left[\sum_{\alpha=1}^{N_T} \dot{\xi}^{(\alpha)} \mathbf{b}^{(\alpha)} \otimes \mathbf{d}^{(\alpha)} \right] \tag{2.49}$$

where $\mathbf{I}$ is the identity tensor, ξ_A and $\mathbf{A}_A$ are the volume fraction and thermal expansion tensor of austenite, $\xi^{(\alpha)}$ and $\mathbf{A}^{(\alpha)}$ are the volume fraction and thermal expansion tensor of martensite variant α, N_T and N_s are the number of variants and slip systems, θ and θ_0 are the current and reference temperatures, $\dot{\gamma}^{(i)}$, $\mathbf{s}^{(i)}$ and $\mathbf{m}^{(i)}$ are the slip rate, direction and normal vectors for slip system i, and $b^{(\alpha)}$ and $d^{(\alpha)}$ are the transformation direction and habit plane normal for transformation system α, and $\delta_T = \mathbf{b}^{(\alpha)} \cdot \mathrm{d}^{(\alpha)}$ is the volumetric expansion during transformation for all martensite variants. The entropy density (η) is decomposed additively, according to

$$\eta = \eta_e + \eta_m + \eta_p + \eta_{tr} \tag{2.50}$$

where η_e, η_m, η_p and η_{tr} are the thermal, thermo-mechanical coupling, plastic and transformation induced parts of the entropy density. These are defined by

$$\eta_e = \left(\xi_A h_A + \sum_{\alpha=1}^{N_T} \dot{\xi}^{(\alpha)}\right) \ln\left(\frac{\theta}{\theta_T}\right) + \eta_T \tag{2.51}$$

$$\dot{\eta}_p = \det\left(\mathbf{F}_{tr}\right) \sum_{i=1}^{N_s} \dot{\gamma}^{(i)} \phi^{(i)} \tag{2.52}$$

$$\dot{\eta}_{tr} = \sum_{\alpha=1}^{N_T} \dot{\xi}^{(\alpha)} \frac{\lambda_T^{(\alpha)}}{\theta_T} \tag{2.53}$$

$$\eta_m = \frac{1}{\rho_0} \det\left(\mathbf{F}_\theta\right) \mathbf{F}_\theta^T \mathbf{F}_\theta \mathbf{S} \mathbf{F}_\theta^{-1} : \left(\xi_A h_A + (1+\delta_T) \sum_{\alpha=1}^{N_T} \xi^{(\alpha)} \mathbf{A}^{(\alpha)}\right) \tag{2.54}$$

where h_A and $h^{(\alpha)}$ are the specific heat capacities of austenite and the martensite variant α, θ_T and η_T are the temperature and transformation entropy density where transformation occurs spontaneously without applied stress, $\phi^{(i)}$ is the entropy per unit slip in slip system i, ρ_0 is the initial density, S is the second Piola-Kirchoff stress, and $\lambda_T^{(\alpha)}$ is the latent heat of transformation for martensite variant α. Stress is updated according to

$$\mathbf{S} = \left(J_\theta^A \mathbb{C}_A - \sum_{\alpha=1}^{N_T} J_\theta^{(\alpha)} (1+\delta_T) \mathbb{C}^{(\alpha)}\right) : \mathbf{E}_e \tag{2.55}$$

where $\mathbb{C}_A$ and J_θ^A are the elasticity tensor and volumetric thermal expansion of the austenite phase, $C^{(\alpha)}$ and $J_\theta^{(\alpha)}$ are the elasticity tensor and volumetric thermal expansion of martensite variant α and $\mathbf{E}_e = (\mathbf{F}_e^T \mathbf{F}_e - \mathbf{I})/2$ is the elastic Green-Lagrange strain. A microstrain metric (β) is then defined as

$$\dot{\beta} = \sum_{i=1}^{N_s} w^{(i)} \dot{\gamma}^{(i)} \tag{2.56}$$

$$w^{(i)} = \frac{1}{c_A \mu_A N_s} \sum_{j=1}^{N_s} H_A^{(j,i)} \tag{2.57}$$

where c_A is a dimensionless scaling factor, μ_A is the elastic shear modulus of the austenite, and $H_A^{(j,i)}$ is the hardening matrix of the austenite. The initial microstrain is given by β_0. Using the Coleman and Noll [113] procedure, the following slip and transformation driving forces are derived

$$
\begin{aligned}
F_{tr}^{(\alpha)} = & \det\left(\mathbf{F}_\theta \mathbf{F}_{tr}\right)\left[\mathbf{F}_p^T \mathbf{F}_\theta^T \mathbf{F}_e^T \mathbf{S} \mathbf{F}_\theta^{-T} \mathbf{F}_p^{-T} \mathbf{F}_{tr}^{-T}\right] : \left(\mathbf{b}^{(\alpha)} \otimes \mathbf{d}^{(\alpha)}\right) + \rho_0 \frac{\lambda_T^{(\alpha)}}{\theta_T}\left(\theta - \theta_T\right) \\
& + \rho_0\left(h_A - h^{(\alpha)}\right)\left(\theta - \theta_T - \theta \ln\left(\frac{\theta}{\theta_T}\right)\right) + \frac{\chi}{\ell_0}\left(2\xi^{(\alpha)} - 1\right) \\
& + \det\left(\mathbf{F}_{tr}\right) \mathbf{F}_e^T \mathbf{F}_e \mathbf{S} \mathbf{F}_\theta^{-T} : \left(\left(1 + \delta_T\right) \mathbf{A}^{(\alpha)} - \mathbf{A}_A\right)\left(\theta - \theta_0\right) \\
& + \frac{1}{2} \mathbf{E}_e : \left(J_\theta^A \mathbb{C}_A - J_\theta^{(\alpha)}\left(1 + \delta_T\right) \mathbb{C}^{(\alpha)}\right) : \mathbf{E}_e \\
& + \frac{\omega_A}{2}\left(J_\theta^A \mu_A - \left(1 + \delta_T\right) J_\theta^{(\alpha)} \mu^{(\alpha)}\right) \beta^2
\end{aligned} \tag{2.58}
$$

$$
F_p^{(i)} = \det\left(\mathbf{F}_\theta\right) \mathbf{F}_\theta^T \mathbf{F}_e^T \mathbf{S} \mathbf{F}_\theta^{-T} : \left(\mathbf{s}^{(i)} \otimes \mathbf{m}^{(i)}\right) + \rho_0 \theta \phi^{(i)} - \omega_A \mu_A \beta w^{(i)} \tag{2.59}
$$

where ω_A relates the internal energy to the microstrain metric, χ is the interface energy between martensite and austenite per unit are and ℓ_0 a length scale for the martensitic interface. The transformation and slip rates are then given by

$$
\dot{\xi}^{(\alpha)} = \begin{cases} \dot{\xi}_0 \tanh\left(\frac{F_{tr}^{(\alpha)} - f_{cr}^{(\alpha)}}{\nu f_{cr}^{(\alpha)}}\right) & F_{tr}^{(\alpha)} > f_{cr}^{(\alpha)} \\ 0 & F_{tr}^{(\alpha)} \leq f_{cr}^{(\alpha)} \end{cases} \tag{2.60}
$$

$$
\dot{\gamma}^{(i)} = \begin{cases} \dfrac{\dot{\gamma}_0 \xi^{(0)}}{\det\left(\mathbf{F}_{tr}\right)}\left(\left(\frac{F_p^{(i)}}{s_A^{(i)}}\right)^{\frac{1}{n}} - 1\right) & F_p^{(\alpha)} > s_A^{(i)} \\ 0 & F_p^{(\alpha)} \leq s_A^{(i)} \end{cases} \tag{2.61}
$$

where $\dot{\xi}_0$ is the maximum transformation rate, $f_{cr}^{(\alpha)}$ is the critical transformation force, ν is a dimensionless parameter, $\dot{\gamma}_0$ is a reference slip rate, $\xi^{(0)}$ is the current RAVF, $s_A^{(i)}$ is a critically resolved shear stress and n is a dimensionless rate exponent.

2.4.3.4 Lee et al. Model Lineage

Lee et al. [95] proposed a strain-induced transformation model with applications to 204M stainless steel sheet. Transformation was modelled as a shear-band intersection mediated process, building on the work of Olson and Cohen [18] and Stringfellow et al. [83]. The shear band (f_{sb}) and shear band intersection (f_{sb}^i) volume fraction rates are

$$\dot{f}_{sb}^{i} = \alpha C f_{sb}^{r-1}\left(1-f_{sb}\right)\dot{\bar{\varepsilon}}_{aus} \qquad (2.62) \qquad \dot{f}_{sb} = \alpha\left(1-f_{sb}\right)\dot{\bar{\varepsilon}}_{aus} \qquad (2.63)$$

$$\dot{\bar{\varepsilon}}_{aus} = \frac{\sum_{i=1}^{N_s}\tau^{(i)}\gamma^{(i)}}{\bar{\sigma}_{aus}} \qquad (2.64)$$

where α determines shear band evolution, C and r represent the relationship between shear band and shear band intersection volume fraction, $\dot{\bar{\varepsilon}}_{aus}$ and $\bar{\sigma}_{aus}$ are the effective von Mises strain-rate and stress of the austenite phase. The initial shear band fraction is zero, and the initial shear band intersection volume fraction ($f_{sb,0}^{i}$) is a calibrated parameter. The transformation rate is given by

$$\begin{aligned}\dot{f}^{\beta} = f_A\frac{\alpha_{KM}\alpha\delta r f_{sb}^{r-1}\left(1-f_{sb}\right)\left(\Delta G+U^{\beta}\right)}{N_T\Delta S}\dot{\bar{\varepsilon}}_{aus} - f_A\frac{0.011\left(1+\delta f_{sb}^{r}\right)}{N_T\Delta S}\left[\frac{\mathrm{d}}{\mathrm{d}t}\left(\Delta G+U^{\beta}\right)\right] \\ \times\left[H\left(-\frac{\mathrm{d}}{\mathrm{d}t}\left(\Delta G+U^{\beta}\right)\right)\right]\left[H\left(\Delta G_C-\Delta G-U^{\beta}\right)\right]\end{aligned} \qquad (2.65)$$

where f_A and f^{β} are the volume fractions of austenite and martensite variant β, α_{KM} is a calibrated constant, ΔG is the chemical driving force for transformation, $U^{\beta} = \sigma_A : \varepsilon_T^{\beta}$ is the mechanical driving force of transformation, σ_A is the austenite Cauchy stress, ε_T^{β} is the transformation strain of martensite variant β, N_T is the number of transformation systems, ΔS is the entropy change of transformation, $H(\star)$ is a Heaviside function, ΔG_C is the critical driving force of transformation and $\delta = C/f_{sb,0}^{i}$. The two terms in the transformation rate represent strain-induced and stress-induced transformation, respectively. Thermal dependence is then accounted for using

$$\alpha = K\exp\left(-bT\right) \qquad (2.66) \qquad \Delta G = \Delta G_C + \Delta S\left(T-M_s\right) \qquad (2.67)$$

where K and b are empirical parameters, T is the current temperature, and M_s is the martensite start temperature. The deformation kinematics are given by

$$\mathbf{F} = \mathbf{F}_e\mathbf{F}_p \qquad (2.68) \qquad \dot{\mathbf{F}}_p\mathbf{F}_p^{-1} = f_A\bar{\mathbf{L}}_p \qquad (2.69) \qquad \bar{\mathbf{L}}_p = \bar{\mathbf{L}}_p^{A} + \bar{\mathbf{L}}_p^{M} \qquad (2.70)$$

where $\mathbf{F}_e$ and $\mathbf{F}_p$ are the elastic and plastic deformation gradients, $\bar{\mathbf{L}}_p$ is the normalized plastic velocity gradient, $\bar{\mathbf{L}}_p^{A}$ and $\bar{\mathbf{L}}_p^{M}$ are the plastic velocity gradients in the austenite and martensite phases. Standard rate-dependent crystal plasticity is used to calculate $\bar{\mathbf{L}}_p^{A}$ from $\boldsymbol{\sigma}_A$. The martensite plastic velocity gradient is given by

$$\bar{\mathbf{L}}_p^{M} = \sum_{\beta=1}^{N_T}\mathbf{R}^{\beta}\left[\frac{\dot{f}_{sb}^{\beta}}{f^{\beta}}\mathbf{I}+\dot{f}^{\beta}\mathbf{M}\right]\left[\mathbf{R}^{\beta}\right]^{-1} \qquad (2.71)$$

where R^β represents the rotation between the FCC and martensite variant bases and M is the transformation deformation in the variant basis. The stress update is then given by

$$\mathbf{S}_A = \mathbb{C}^A : \mathbf{E}_e \qquad (2.72) \qquad \mathbf{S}^\beta = \mathbb{C}^\beta : \mathbf{E}_e \qquad (2.73)$$

$$\boldsymbol{\sigma} = f_A \boldsymbol{\sigma}_A + \sum_{\beta=1}^{N_T} f^\beta \boldsymbol{\sigma}^\beta \qquad (2.74)$$

where σ is the bulk Cauchy stress, $\mathbf{S}_A$ and $\mathbb{C}^A$ are the second Piola-Kirchoff stress and elasticity tensor of austenite, $\boldsymbol{\sigma}^\beta$, $\mathbf{S}^\beta$ and $\mathbb{C}^\beta$ are the Cauchy stress, second Piola-Kirchoff stress and elasticity tensor of martensite variant β and $\mathbf{E}_e = (\mathbf{F}_e^T \mathbf{F}_e - \mathbf{I})/2$ is the elastic Green-Lagrange strain.

This model accurately captures martensite volume fraction, stress and temperature evolution of 204M stainless steel under uniaxial tension for several strain rates. Instead of applying thermal boundary conditions, a coefficient was specified for each strain-rate to control the ratio of work to temperature change to match the temperature evolution. The transformation strain rate dependence was shown to be a consequence of temperature dependence, given different temperature evolution profiles for each strain rate.

2.4.3.5 Ma and Hartmaier Model Lineage

Ma and Hartmaier [120] proposed a second mechanistic model based on shear band intersection kinetics. The kinetics law for transformation includes strain-based nucleation and stress-based growth of martensite, inspired by the work of Sinclair and Hoagland [91] on martensitic nucleation. This work used MD to investigate the nucleation mechanism proposed by Olson and Cohen [121], wherein martensite nucleates at the intersection of $\langle 121 \rangle \{111\}$ type fault bands. This MD analysis shows that the transformation OR is close to NW. Decomposition of the deformation gradient and variant I martensite volume fraction (η_I) is given by

$$\mathbf{F} = \mathbf{F}_e \mathbf{F}_{tr} \mathbf{F}_p \qquad (2.75) \qquad \eta_I = \eta_I^0 + \eta_I^{strain} + \eta_I^{stress} \qquad (2.76)$$

where $\mathbf{F}_e$, $\mathbf{F}_{tr}$ and $\mathbf{F}_p$ are the elastic, transformation and plastic deformation gradient and η_I^0, η_I^{strain} and η_I^{stress} are the initial, strain-induced and stress-induced martensite volume fractions for martensite variant I. The plastic and transformation deformation gradients are then given by

$$\dot{\mathbf{F}}_{tr}\mathbf{F}_{tr}^{-1} = \sum_{I=1}^{N_T} \dot{\eta}_I^{stress} \left(\mathbf{b}_I \otimes \mathbf{d}_I\right) \qquad (2.77) \qquad\qquad \dot{\mathbf{F}}_{p}\mathbf{F}_{p}^{-1} = \sum_{\alpha=1}^{N_s} \dot{\gamma}^{(\alpha)} \left(\mathbf{s}_\alpha \otimes \mathbf{m}_\alpha\right) \qquad (2.78)$$

where $\mathbf{b}_I$ and $\mathbf{d}_I$ are the initial configuration transformation direction and habit plane for martensite variant I, $\mathbf{s}_\alpha$, $\mathbf{m}_\alpha$ are the initial configuration slip direction and normal of slip system α, and $\dot{\gamma}^{(\alpha)}$ is the slip rate on slip system α. The stress update is then given by

$$\mathbf{S} = \left[\right] \left(1 - \sum_{I=1}^{N_T} \eta_I\right) \mathbb{C}_A + \sum_{I=1}^{N_T} \eta_I \mathbb{C}_I \Bigg] : \frac{\left(\mathbf{F}_e^T \mathbf{F}_e - \mathbf{I}\right)}{2} \qquad (2.79)$$

where $\mathbb{C}_A$ and $\mathbb{C}_I$ are the elastic tensors of austenite and martensite variant I. Using energy methods, the plastic slip driving force ($\zeta_p^{(\alpha)}$) is given by

$$\zeta_p^{(\alpha)} = \tau^{(\alpha)} - \left(\tau_p^{(\alpha)} + \tau_t^{(\alpha)}\right) \text{sign}\left(\tau^{(\alpha)}\right) \qquad (2.80)$$

$$\dot{\tau}_t^{(\alpha)} = c_{mhd}\, \mu \sum_{I=1}^{N_T} \dot{\eta}_I \qquad (2.81)$$

where $\tau^{(\alpha)}$ and $\tau_p^{(\alpha)}$ are the resolved and critical resolved shear stresses calculated using the Schmid tensor and a hardening law as in standard crystal plasticity. Lamellar hardening ($\tau_t^{(\alpha)}$) is incorporated to handle transformation hardening, where c_{mhd} is a calibrated constant, and μ is a shear modulus. The rate-dependent equation then gives the plastic slip rate is

$$\dot{\gamma}^{(\alpha)} = \dot{\gamma}_0 \left| \frac{\zeta_p^{(\alpha)}}{\tau_0} \right| \text{sign}\left(\tau^{(\alpha)}\right) \qquad (2.82)$$

where τ_0 is the initial yield stress. The strain-induced transformation driving force is derived using energy methods as

$$\zeta_I^{strain} = -\left[c_{dwp}\left(2\eta_I - 6\eta_I^2 + 4\eta_I^3\right)\right] - \left[12\Delta G\left(\eta_I^2 - \eta_I^3\right)\right] \qquad (2.83)$$

where c_{dwp} is a calibrated parameter. The strain-induced transformation rate is given by

$$\dot{\eta}_I^{strain} = c_{nuc} \left(1 - \sum_{J=1}^{N_T}\right) H''_{I\beta} H'_{\beta\alpha} \zeta_I^{strain} \dot{\gamma}^{(\alpha)} \qquad (2.84)$$

where c_{nuc} is a calibrated parameter, $H'_{\beta\alpha}$ projects slip onto shear bands and $H''_{I\beta}$ calculates the shear band intersection from the shear bands. The stress-induced transformation driving force is derived using the energy method as

$$\zeta_I^{stress} = \det(\mathbf{F})\,\boldsymbol{\sigma} : \frac{\mathbf{F}_e\mathbf{b}_I \otimes \mathbf{d}_I\mathbf{F}_e^{-1} + \mathbf{F}_e^{-T}\mathbf{d}_I \otimes \mathbf{b}_I\mathbf{F}_e^{T}}{2} + \zeta_I^{strain} \tag{2.85}$$

The stress-induced transformation rate is given by

$$\dot{\eta}_I^{stress} = c_{gro}\left(\eta_I^0 + \eta_I^{strain}\right)\left(1 - \sum_{J=1}^{N_T}\eta_J\right)\zeta_I^{stress} \tag{2.86}$$

where c_{gro} is a calibration parameter.

This was then used to simulate an artificially generated microstructure containing ferrite and austenite under tension and compression. This showed significant tension-compression asymmetry in both the transformation and stress vs. strain curves.

2.4.3.6 Park et al. Model Lineage

Park et al. [41] modelled QP steel using a novel constitutive model. The RA and transformed martensite phase are considered separately, with a Taylor approximation used to determine strain partitioning. This is given by

$$\dot{\boldsymbol{\varepsilon}}_{\alpha'}^{k} = \dot{\boldsymbol{\varepsilon}}_{\gamma} \tag{2.87}$$

where $\dot{\boldsymbol{\varepsilon}}_{\alpha'}^{k}$ and $\dot{\boldsymbol{\varepsilon}}_{\gamma}$ are the local transformed martensite variant k and RA strain-rate tensors expressed in the lattice coordinate system. This work uses the K-S orientation relationship, giving 24 possible martensite variants. Additive decomposition of these strain-rates gives

$$\dot{\boldsymbol{\varepsilon}}_{\alpha'}^{k} = \dot{\boldsymbol{\varepsilon}}_{\alpha'}^{k(e)} + \dot{\boldsymbol{\varepsilon}}_{\alpha'}^{k(slip)} \tag{2.88}$$

$$\dot{\boldsymbol{\varepsilon}}_{\gamma} = \dot{\boldsymbol{\varepsilon}}_{\gamma}^{e} + \dot{\boldsymbol{\varepsilon}}_{\gamma}^{slip} + \dot{\boldsymbol{\varepsilon}}_{\gamma}^{MT} \tag{2.89}$$

where $\dot{\boldsymbol{\varepsilon}}_{\alpha'}^{k(e)}$ and $\dot{\boldsymbol{\varepsilon}}_{\alpha'}^{k(slip)}$ are the elastic and plastic slip components of martensite variant k, and $\dot{\boldsymbol{\varepsilon}}_{\gamma}^{e}$, $\dot{\boldsymbol{\varepsilon}}_{\gamma}^{slip}$ and $\dot{\boldsymbol{\varepsilon}}_{\gamma}^{MT}$ are the elastic, plastic slip and transformation components of the RA strain-rate. This work therefore assumes that all transformation strain is accommodated within the austenite phase. As in rate-dependent crystal plasticity, the plastic slip strain-rates for all local phases are governed by

$$\dot{\boldsymbol{\varepsilon}}^{slip} = \mathbf{D}^{slip} = \sum_{\alpha=1}^{N} \dot{\gamma}^{(\alpha)} \mathbf{P}^{(\alpha)} \tag{2.90}$$

where $\dot{\gamma}^{(\alpha)}$ and $\mathbf{P}^{(\alpha)}$ are the slip rates and symmetric Schmid tensor for the phase in question. Using the results of Zamiri and Pourboghrat [122], a plastic yield potential $f(\boldsymbol{\sigma})$ is defined such that the plastic slip strain-rates are defined by

$$\mathbf{D}^{slip} = \lambda \frac{\partial f(\boldsymbol{\sigma})}{\partial \boldsymbol{\sigma}} \tag{2.91}$$

where λ is a plastic multiplier defining the amount of strain and $\boldsymbol{\sigma}$ is the Cauchy stress tensor. The plastic yield potential is given by

$$f(\boldsymbol{\sigma}) = \frac{1}{\rho} \ln \left\{ \sum_{\alpha=1}^{N} \exp \left[\frac{\rho}{m} \left(\frac{\left| \boldsymbol{\sigma} : \mathbf{P}^{(\alpha)} \right|}{\tau_y^{(\alpha)}} - 1 \right) \right] \right\} \tag{2.92}$$

where ρ and m are calibration coefficients defining the closeness of the yield condition and the yield surface shape, and $\tau_y^{(\alpha)}$ is the critical resolved shear stress for slip system α. Using this equation, the slip-rates are given by

$$\dot{\gamma}^{(\alpha)} = \lambda \frac{\frac{\text{sign}\left(\boldsymbol{\sigma}:\mathbf{P}^{(\alpha)}\right)}{\tau_y^{(\alpha)}} \exp \left[\frac{\rho}{m} \left(\frac{\left|\boldsymbol{\sigma}:\mathbf{P}^{(\alpha)}\right|}{\tau_y^{(\alpha)}} - 1 \right) \right]}{m \sum_{\alpha=1}^{N} \exp \left[\frac{\rho}{m} \left(\frac{\left|\boldsymbol{\sigma}:\mathbf{P}^{(\alpha)}\right|}{\tau_y^{(\alpha)}} - 1 \right) \right]} \tag{2.93}$$

The plastic multiplier can then be found using standard methods for phenomenological plasticity, such as the cutting plane algorithm [124, 125]. The transformation strain-rates are given by

$$\dot{\boldsymbol{\varepsilon}}_{\gamma}^{MT} = \sum_{k=1}^{N} \dot{f}_{\alpha'}^{k} \boldsymbol{\varepsilon}^{MT,k} \tag{2.94}$$

where $\boldsymbol{\varepsilon}^{MT,k}$ and $\dot{f}_{\alpha'}^{k}$ are the deformation transformation and transformation rate of a martensite variant k. The total transformation rate $\dot{f}_{\alpha'}$ is given by the phenomenological Beese and Mohr [123] law

$$\dot{f}_{\alpha'} = \left(f_{\alpha'}^{max} - f_{\alpha'}\right) nD \left(D\bar{\varepsilon}\right)^{n-1} \dot{\bar{\varepsilon}} \tag{2.95}$$

where $f_{\alpha'}^{max}$ is the maximum allowed transformation martensite volume fraction, $f_{\alpha'}$ is the current transformed martensite volume fraction, n and D are material parameters, and $\bar{\varepsilon}$ is the von Mises equivalent plastic strain. The material parameter D is given by

$$D(\eta, \bar{\theta}) = D_0 + D_\eta \eta + D_{\bar{\theta}} \bar{\theta} \tag{2.96}$$

where D_0, D_η and $D_{\bar{\theta}}$ are calibration parameters, η is the stress triaxiality, and $\bar{\theta}$ is the Lode angle. Stress triaxiality and Lode angle are given by

$$\eta = \frac{\mathrm{tr}(\boldsymbol{\sigma})}{3\bar{\sigma}} \tag{2.97}$$

$$\bar{\theta} = 1 - \frac{2}{\pi} \cos^{-1} \left(\frac{27 \det \left(\boldsymbol{\sigma} - \mathrm{tr} \ (\boldsymbol{\sigma}) \right)}{2\bar{\sigma}^3} \right) \tag{2.98}$$

where $\bar{\sigma}$ is the von Mises effective stress. The transformation rates of a martensite variant k are then given by

$$\dot{f}_{\alpha'}^k = \begin{cases} \dot{\xi} \left| \frac{\boldsymbol{\sigma} : \boldsymbol{\varepsilon}^{MT,k}}{\omega_{cr}} \right|^{\frac{1}{p}} & \boldsymbol{\sigma} : \boldsymbol{\varepsilon}^{MT,k} > 0 \\ 0 & \boldsymbol{\sigma} : \boldsymbol{\varepsilon}^{MT,k} \leq 0 \end{cases} \tag{2.99}$$

where p and ω_{cr} are parameters to control the relative activation of different martensite variants and $\dot{\xi}$ is a scaling factor to ensure that the condition $\sum_{k=1}^{N} \dot{f}_{\alpha'}^k = \dot{f}_{\alpha'}$ is met. This ensures that only the martensite variants that minimize the plastic work energy are activated. Finally, the stress update in the material co-rotational frame is given by

$$\boldsymbol{\sigma} = (1 - f_{\alpha'}) \, \boldsymbol{\sigma}_\gamma + \sum_{k=1}^{N} f_{\alpha'}^k \boldsymbol{\sigma}_{\alpha'}^k \tag{2.100}$$

where $\boldsymbol{\sigma}_\gamma$ and $\boldsymbol{\sigma}_{\alpha'}^k$ are the local phase stresses of RA and the martensite variant k. The local phase stresses are then related to the local elastic strain-rates using Hooke's law.

The model was then calibrated using experimental data for QP980 steel and QP1500 steel. Parametric studies were conducted on constituent phase volume fraction, resulting in significant reductions in yield stress, UTS and elongation. The formability of a tailored microstructure was analyzed, suggesting possible methods for formability improvement.

2.4.3.7 Model Comparison

Table 2.2 summarizes the material behaviours captured by each mechanistic transformation model. This shows that all models, except Park et al. [41], can capture temperature dependence of transformation. In contrast, only the Stringfellow et al. and Turteltaub et al. model lineages address the dependence of transformation on strain-rate. Since the kinetics law proposed in the Turteltaub et al. model lineage has a maximum transformation rate, it can only capture this strain-rate dependence at low rates. All models capture the stress-state dependence of transformation; however, this effect is only partially captured in the Stringfellow et al. model lineage because it neglects the Lode angle parameter. Except for the Stringfellow et al. model lineage, all models incorporate multiple martensite variants and, consequently, account for orientation dependence of transformation through the resolved stress on the transformation system. The Stringfellow et al., Cherkaoui et al. and Park et al. model lineages all capture hardening due to differing strength in the austenite and martensite phases using volume averaging of separately modelled austenite and martensite phases. Each of these models also incorporates transformed martensite plasticity, as this allows the model to capture better the local deformation of this phase [15]. The Turteltaub et al. model lineage can partially capture this hardening effect by incorporating the RAVF into the plasticity kinetics law. However, the relatively small value of n ($n = 0.02$ in Yadegari et al. [109]) in the plasticity kinetics results in the RAVF having a little impact when RAVF is significantly greater than zero. This problem is explored in further detail in Section 4.5.4. Furthermore, this method implicitly assumes that the transformed martensite is fully elastic, which is not the case for all steels exhibiting the TRIP effect [15]. Both the Cherkaoui et al. and Ma and Hartmaier model lineages capture local hardening due to the accommodation of transformation strain with plastic slip. The Cherkaoui et al. model lineage incorporates this hardening directly using the homogenization mechanism. The Ma and Hartmaier model only incorporates this hardening indirectly with a lamellar hardening term. The Stringfellow et al., Lee et al., and Turteltaub et al. model lineages each outline a constitutive equation that governs temperature evolution. Yet, the Lee et al. model is only approximate because it does not include the latent heat of transformation. Only the Lee et al., Ma and Hartmaier, and Cherkaoui et al. model lineages incorporate stress-induced and strain-induced transformation mechanics, whereas all other models focus on only one approach. In the Cherkaoui et al. model lineage, strain-induced transformation is only partially accounted for by reducing the critical stress for transformation with increasing strain. Only the Cherkaoui et al., Turteltaub et al., and Ma and Hartmaier model lineages propose a model that is guaranteed to be consistent with the first and second laws of thermodynamics. Finally, only the Turteltaub et al. model lineage includes thermal strains in the model. No model has been proposed that captures

all relevant mechanics to allow robust crystal plasticity simulations of steel exhibiting the TRIP effect.

Table 2.2: Model comparison chart.

		Stringfellow et al. Model Lineage	Cherkaoui et al. Model Lineage	Lee et al. Model Lineage	Turteltaub et al. Model Lineage	Ma and Hartmaier Model Lineage	Park et al. Model Lineage
Incorporated Material Behaviours	Transformation temperature sensitivity						
	Transformation strain-rate sensitivity						
	Transformation stress-state dependence						
	Incorporates martensite variants						
	Transformation orientation dependence						
	Hardening due to stress homogenization						
	Plasticity in transformed martensite						
	Hardening due to local plasticity when accommodating transformation strain						
	Temperature evolution						
	Stress-induced transformation						
	Strain-induced transformation						
	Thermodynamically consistent						
	Includes thermal strain						

Aspect present in model

Aspect partially present in model

Aspect not present in model

2.5 Summary of Deficiencies in Literature

Several authors [9, 10, 83, 84, 86, 95] have shown that modelling TRIP steel in both crash and formability applications require constitutive models that are thermally dependent and applicable over a range of strain-rates and temperatures. For a model to be usable in crystal plasticity, it must correctly account for the orientation dependence of transformation. As presented in Section 2.4.3.7, no model in the literature can simultaneously account for the orientation dependence, thermal dependence and rate-dependence of transformation. Given the importance of thermo-mechanical coupling in modelling TRIP steels, general thermal boundary conditions must be incorporated into RVE modelling techniques. While some works simplify the thermal behaviour, such that no boundary conditions are needed, no method has yet been proposed for incorporating these thermal boundary conditions. Hu et al. [15] showed that it is also essential for a constitutive model to include both martensite plasticity and homogenization of RA and transformed martensite for the lattice strain evolution of each phase to be correctly captured. It is essential to include both the stress and strain-induced martensitic transformation regimes because this will broaden the scope of temperatures at which the model is applicable. Finally, to be physically consistent, it is crucial that the constitutive model satisfies the first and second laws of thermodynamics and includes thermal strains.

3 Research Scope and Objectives

This research aims to develop an advanced constitutive model and the supporting modelling technologies of steels exhibiting the TRIP effect, such as QP steels, over a wide range of temperatures and strain-rates. As such, the research hypothesis is:

> "The development of an advanced constitutive model and supporting modelling technologies will allow accurate simulation of steels exhibiting the TRIP effect over a wide range of temperatures and strain-rates."

The proposed constitutive model must capture elastic, thermal, plastic slip and transformation plasticity deformation modes during stress-induced and strain-induced transformation to achieve this goal. Beyond capturing strain-rate and temperature dependence, the constitutive model must also capture realistic martensite variant formation along with the stress-state and orientation dependence on transformation. The constitutive model must provide a framework that accounts for the local plasticity due to strain accommodation during transformation and martensite plasticity in a consistent thermodynamic framework. By accounting for all these phenomena, designers will fully exploit these materials in future applications of metal forming and crashworthiness applications. The Turteltaub et al. model lineage is used as the basis of this work because it captures the most transformation mechanics while still incorporating rate-dependent plastic slip.

3.1 Research Objectives

The objectives of this research are to:

(1) Develop a baseline model that incorporates stress-induced transformation.

(2) Develop a method to capture general thermal boundary conditions for RVE models.

(3) Extend the baseline model to include homogenization of austenite and transformed martensite, martensite plasticity and rate-dependent strain-induced transformation.

3.2 Summary of Contributions Towards Objectives

The work completed to achieve the research objectives is presented in the next two chapters. Research objectives (1) and (2) are completed in Chapter 4. Research objective (3) is completed in Chapter 5. These chapters are based on the following published or under review manuscripts:

Chapter 4 **D. S. Connolly**, C. P. Kohar, W. Muhammad, L. G. Hector Jr., R. K. Mishra, K. Inal, A Coupled Thermomechanical Crystal Plasticity Model Applied to Quenched and Partitioned Steel, International Journal of Plasticity 103 (2020), 39-66.

Chapter 5 **D. S. Connolly**, C. P. Kohar, K. Inal, A Novel Crystal Plasticity Model Incorporating Transformation Induced Plasticity for a Wide Range of Strain Rates and Temperatures, Under Review at Journal of the Mechanics and Physics of Solids (MPS-D-21-00101) on January 27, 2021.

In addition to these publications, the following publications have been written as a result of this current research. However, these works do not have a direct impact on the overall research objectives of this thesis and are referenced only as supporting work:

- **D.S. Connolly**, C.P. Kohar, R.K. Mishra, K. Inal, A New Coupled Thermomechanical Framework for Modeling Formability in Transformation Induced Plasticity Steels, International Journal of Plasticity, 103 (2018), 39-66.
- **D.S. Connolly**, C.P. Kohar, L.G. Hector Jr., R.K. Mishra, K. Inal, Simulation of TRIP Steel Formability using Thermo-mechanical Crystal Plasticity Finite Element Modeling. International Conference on Plasticity, Damage & Fracture 2019, Panama City, Panama, January 3-9, 2019.
- **D.S. Connolly**, C.P. Kohar, R.K. Mishra, K. Inal, Impact of Thermal Conditions on Predicted Formability of TRIP Steelers, The 12th International Conference and Workshop on Numerical Simulation of 3D Sheet Metal Forming Processes (NUMISHEET 2022), Toronto, Ontario, Canada, July 10, 2022.

3.3 Limitations of Proposed Work

The constitutive models derived in the current study are limited to material that exhibits continuous deformation driven solely through the motion of plastic slip and transformation of RA to plate-like BCT α'-martensite. As such, neither DSA nor propagative instabilities (e.g. PLC bands) are considered. Grain boundaries are assumed to be contiguous with no grain boundary sliding because grain boundary sliding primarily occurs in very high temperatures and creep applications [54, 55]. Transformation to HCP ϵ-martensite is neglected because it is primarily observed in high Mn and austenitic steels, rather than QP steel [126]. The derived constitutive models neglect the effects of strain-gradients on material behaviour and hardening [56]. The model is assumed to have no initial stresses throughout the material due to the difficulty of determining the initial internal stresses and consequent lack of experimental data. Finally, all grains of the same phase are assumed to have the same chemistry and material properties. As such, no distinction is made between film and blocky RA grains.

This research is expected to apply to QP steels under realistic temperatures and strain-rates. While this can include temperatures between $-40\,^{\circ}\mathrm{C}$ and an underhood temperature of $150\,^{\circ}\mathrm{C}$ [127], this work will be restricted to $-10\,^{\circ}\mathrm{C}$ and $85\,^{\circ}\mathrm{C}$ where experimental data exists for QP materials [53]. This work will also be restricted to strain rates between $5 \times 10^{-4}\,\mathrm{s}^{-1}$ and $200\,\mathrm{s}^{-1}$ where QP steel experimental data exists [53]. Finally, the model is calibrated solely to uniaxial tension testing data due to the availability of experimental data [53].

4 A Coupled Thermomechanical Crystal Plasticity Model Applied to Quenched and Partitioned Steel[1]

4.1 Introduction

Various crystal plasticity constitutive models for steels incorporating the TRIP effect have been proposed. Cherkaoui et al. [115, 116] and Petit et al. [42] developed a rate-independent crystal plasticity framework that used a stress-based, thermodynamically consistent transformation criteria and an Eshelby [101] homogenization scheme with an evolving volume fraction to model the TRIP effect. Turteltaub and Suiker [110, 118], Tjahjanto et al. [119, 128], and Yadegari et al. [109] proposed an alternate rate-dependent framework where the TRIP effect is again modelled using a stress-based, thermodynamically consistent transformation criteria. Lee et al. [95] developed a rate-dependent model where the TRIP effect is captured via a probability of transformation at shear band intersection sites where the accumulated slip on slip planes determined the shear band intersection volume fraction. Ma and Hartmaier [120] developed a model where the TRIP effect is assisted by stress and strain using thermodynamic arguments, including additional terms for the TRIP hardening. Park et al. [41] proposed a rate-independent framework wherein the TRIP effect is modelled via an empirical evolution law, which also focused on a single temperature. While these last three frameworks offer exceptional promise, no work has been presented which has demonstrably captured temperature dependence of transformation and provides a constitutive equation for temperature evolution.

The interactions between different grains and phases in the complex microstructure present in TRIP and QP steels can be either approximated using homogenization techniques or directly captured using a representative volume element (RVE) solved with the finite element method (FEM) [40]. While the microstructural morphology is significant for QP steel [43], many works which use FEM simulations neglect the morphology, instead assigning orientations and phases randomly such that bulk microstructural information (e.g., the texture of each phase and phase volume fraction) is well captured [41, 120, 129–131]. While some RVE based models have incorporated aspects of thermal modelling [95, 120], to the author's knowledge, no method for incorporating general thermal boundary conditions

[1]The contents of this chapter have been adapted from:

D. S. Connolly, C. P. Kohar, W. Muhammad, L. G. Hector Jr., R. K. Mishra, K. Inal, A Coupled Thermomechanical Crystal Plasticity Model Applied to Quenched and Partitioned Steel, International Journal of Plasticity 103 (2020), 39-66, available online at https://doi.org/10.1016/j.ijplas.2020.102757

into RVE models have been proposed. This is not trivial because the thickness of the RVE is not necessarily identical to the full specimen.

In this chapter, the stress and martensitic transformation response of a QP1180 steel alloy are characterized using in-situ High Energy X-ray Diffraction (HEXRD) uniaxial tension experiments. The initial microstructure is characterized using Electron Backscatter Diffraction (EBSD) and Scanning Electron Microscope (SEM) data. A novel thermodynamically consistent rate-dependent crystal plasticity formulation simulates the large deformation behaviour of QP steels that exhibit the TRIP effect. The TRIP effect is captured through a martensite variant selection and evolution scheme governed by a driving force that accounts for various effects (e.g. applied stress, orientation temperature, stress state, and martensite surface energy). This proposed model will be one of the first constitutive models, if not the first, suitable for a range of strain-rates and temperatures, which also includes coupling between plastic slip and transformation. A thermodynamically consistent constitutive model is presented for the ferrite and tempered martensite phases to allow for a unified model to capture multi-phase materials, such as QP steel. These constitutive models are implemented into a thermo-mechanical Crystal Plasticity (CP) Finite Element Method (FEM) formulation to study the effect of texture, phase morphology and temperature on the bulk material properties of QP1180 steel. A new method for incorporating thermal boundary conditions in CPFEM models is proposed. Interrupted mechanical conditions are used to emulate the regular pauses in experimental deformation during in-situ uniaxial tension HEXRD experiments. This FEM model is used in conjunction with the experimental data and constraints on thermal behaviour to calibrate the constitutive model. Non-interrupted models are generated using isothermal, adiabatic, and general thermal boundary conditions. These models are used to analyze, for the first time, the effect of thermal boundary conditions on thermo-mechanical behaviour and to compare interrupted and non-interrupted mechanical conditions. Additional non-interrupted cases are simulated for elevated strain-rates and initial temperatures for adiabatic, isothermal, and general thermal conditions to analyze these effects on the predicted stress, RA, and temperature evolution.

4.2 Experimental Characterization

A commercially available QP1180 sheet metal alloy with a nominal thickness of 1.14mm was characterized to generate the experimental data necessary for calibrating the numerical model. Table 4.1 lists the chemical composition of the as-received material.

Table 4.1: Chemical composition (wt. %) of as-received QP1180 sheet metal alloy.

	C	**Mn**	**Si**	**Al**	**Cr**	**Ni**	**Mo**	**P**	**N**	**S**	**Fe**
QP1180	0.19	2.74	1.67	0.05	0.007	0.004	0.002	0.0006	0.0003	0.0001	Bal

The bulk stress and RA evolution response were characterized using an in-situ uniaxial tension test with HEXRD using the 11-ID-C beamline at the Advanced Photon Source (APS) at Argonne National Laboratory. Sub-sized dog-bone shaped tensile specimens with a gauge section of 10 mm × 3.18 mm were tested under uniaxial tension with a constant crosshead speed of 10 µm s^{-1}, which corresponds to a nominal strain rate of 8×10^{-4} s^{-1}. Detailed specimen geometry can be found in [40]. Compliance correction of the load-crosshead displacement was used to calculate the true stress vs. true strain response [15]. The experiment was interrupted at 100 µm increments of crosshead displacement to record Debye rings and load measurements. Following the techniques outlined in Hu et al. [40]), the Debye rings were post-processed to obtain the retained austenite vs. true strain response. Three repeats were performed in the rolling direction (RD) and transverse direction (TD). Fig. 4.1(a) presents the stress-strain response for all experiments. This showed excellent repeatability under uniform elongation with a standard deviation of 7.1 MPa (0.5%) and 7 MPa (0.5%) for RD and TD experiments at 15% strain. Minimal stress anisotropy is observed, with a difference of 23 MPa (1.6%) between average RD and TD responses. Fig. 4.1(b) presents the RA evolution response for all experiments. This showed excellent repeatability under uniform elongation with a standard deviation of 0.21% RA and 0.17% RA for RD and TD experiments at 15% strain. Minimal transformation anisotropy is observed, with a difference of 0.1% RA at 8% strain and 0.8% RA at 15% strain. The RA evolution response measurements began to diverge after uniform elongation (15% true strain) because the photon beam could not always be centred around the localization region.

Next, electron backscatter diffraction (EBSD) measurements using a field emission Nova NanoSEM equipped with a TSL EBSD camera were used to characterize the initial microstructure. An overall scan area of 75 µm × 75 µm with a step size of 100 nm and was used for the EBSD measurements. Fig. 4.2(a) and Fig. 4.2(b) show the EBSD orientations and phase map, respectively. Phases in Fig. 4.2(b) are categorized into face-centred cubic RA and body-centred (BC) groups. However, it is difficult to distinguish between body-centred cubic (BCC) ferrite, body-centred tetragonal (BCT) martensite, and any bainite present in the material. Nevertheless, the initial volume fraction of RA measured via EBSD and HEXRD was approximately 12.9% and 14.3%, respectively. The discrepancy between these two methodologies can be attributed to the difficulty in fully resolving film-type

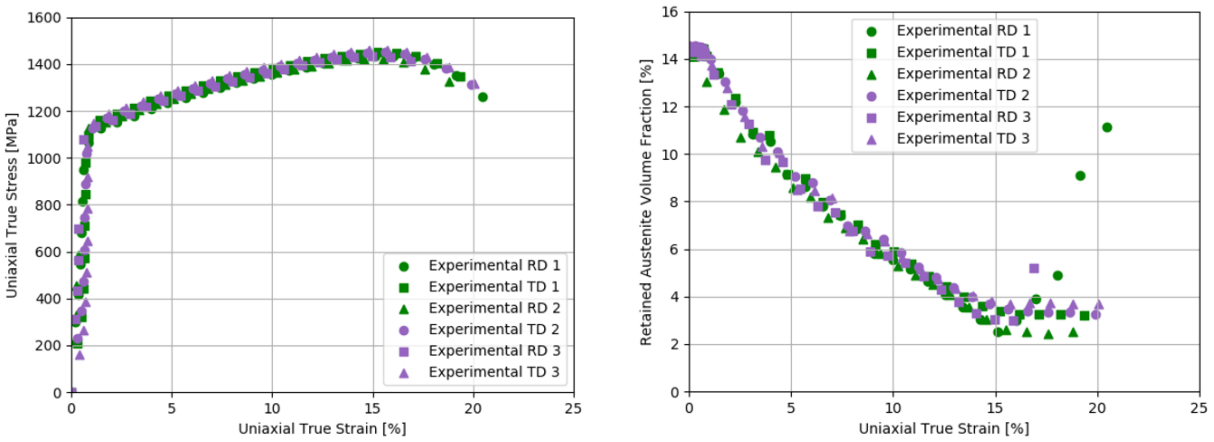

(a) (b)

Fig. 4.1: (a) Stress vs. strain and (b) retained austenite vs strain response for all experiments of QP1180 sheet.

RA from EBSD measurements [53] and the HEXRD method's ability to resolve the RA variation through the thickness [132]. Fig. 4.3(a) and Fig. 4.3(b) present the recalculated RA and BC pole figures, which were generated from the EBSD data using the MTEX analysis software [133]. Both the RA and BC pole figures show low intensities (1.3 and 2.1 max intensity), which indicates that the material should have very little anisotropy; this is consistent with the low stress and transformation anisotropies observed from the in-situ HEXRD experiments shown in Fig. 4.1. Distinguishing the BCC phases' distribution on the EBSD can be determined through scanning electron microscopy (SEM) measurements in conjunction with an EBSD Image Quality (IQ) map. First, the phase volume fraction can be experimentally obtained by performing SEM measurements of the material. Each sample was prepared using standard metallography techniques and etched using a 3% nital solution. Fig. 4.4 presents the SEM image obtained for the material. This figure shows distinct phases of ferrite, blocky RA, and a mixture of film-type RA and martensite. No bainite phase was observed. Through image analysis techniques, a ferrite volume fraction of 20% was obtained for this material, which agrees well with existing literature [132, 134].

Following the methodology presented in Petrov et al. [135] and Santofimia et al. [136], the EBSD IQ map, shown in Fig. 4.5(a), was used to distinguish the BC phases in the EBSD map in Fig. 4.2(b). Fig. 4.5(b) shows the processed EBSD phase map with FCC RA, BCC ferrite, and BCT martensite. After normalizing the IQ, a cut-off value of 0.37 was chosen to ensure that the EBSD phase map yielded the 20% ferrite volume fraction

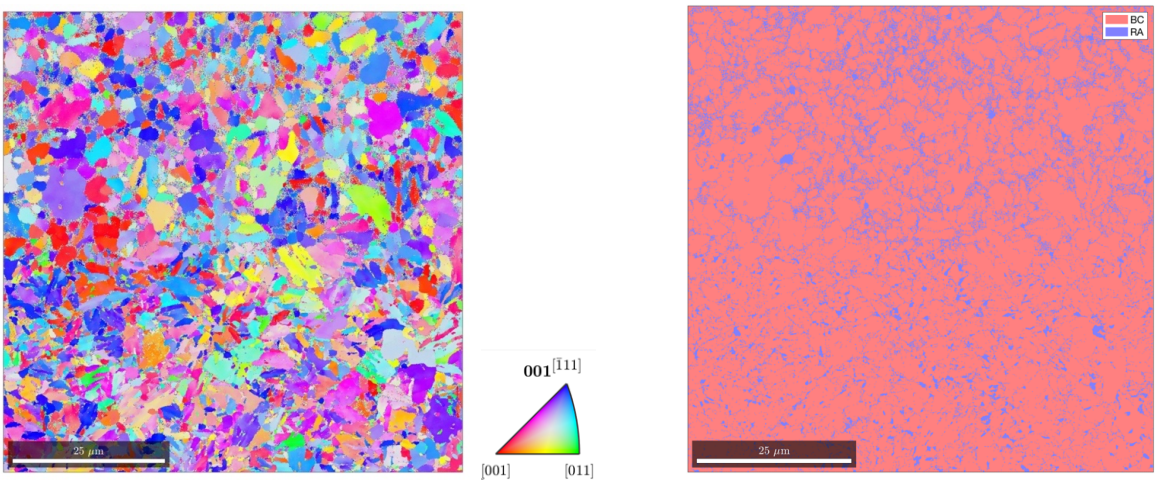

(a) (b)

Fig. 4.2: (a) EBSD orientation and (b) EBSD phase map of QP1180 sheet.

Table 4.2: Experimental SEM phases.

	Ferrite	**Austenite**	**Martensite**
QP1180 Phase Fractions [%]	20.0	12.9	67.9

obtained from the SEM measurement. Table 4.2 summarizes the volume fraction of the individual phases measured in the QP1180 sheet.

4.3 Constitutive Model Formulation

This section details a constitutive model formulation used to simulate the evolution in temperature, stress, and RA fraction for a QP steel. This model will apply to both room temperature and elevated temperatures and at any strain rate. The constitutive model follows a thermodynamically consistent formulation where deformation modes (crystallographic slip and transformation) are conceptualized as thermodynamic fluxes with an associated driving force [108, 109, 137, 138]. These thermodynamic fluxes are then related to the driving forces through constitutive relationships formally called the kinetics functions. RA's crystal lattice structure is a face-centred cubic (FCC) structure, while ferrite has a body-centred cubic (BCC) structure. Although tempered martensite generally follows a body-centred tetragonal (BCT), low carbon concentration in tempered martensite

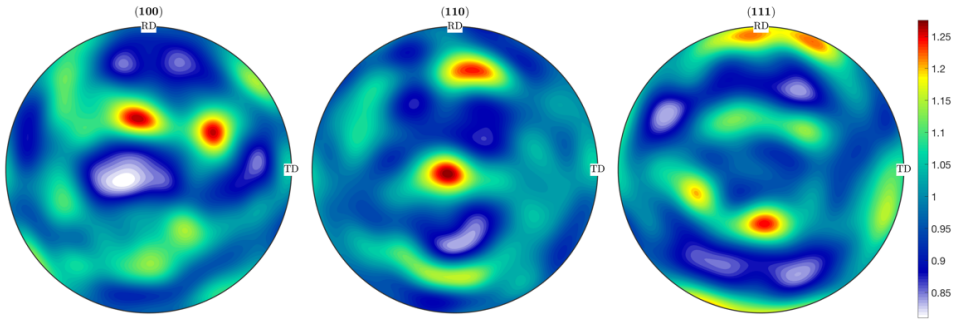

(a)

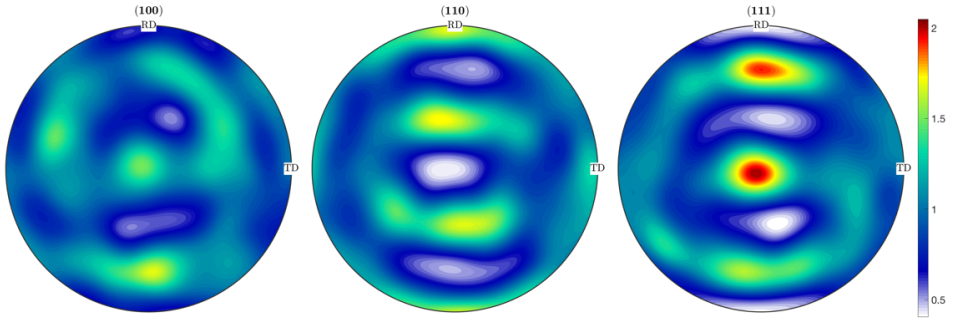

(b)

Fig. 4.3: (a) Retained austenite and (b) body-centred pole figure of QP1180 sheet.

structure caused by diffusion in RA results in tempered martensite having a BCC structure. Nevertheless, transformed martensite from RA has a BCT structure caused by the high carbon concentration in RA. Given the different lattice structures and consequent material behaviours, each phase requires its own distinct calibrated constitutive model. The derivation and incremental formulation of the constitutive model used in this work are presented in five sections. Section 4.3.1 outlines a general framework for the deformation kinematics and governing elastic constitutive equation for a material with the austenite to martensite transformation plasticity mechanism. Deformation is assumed to occur due to thermal, elastic, and inelastic stretching. Inelastic stretching comprises plastic motion of dislocations along slip planes (plastic slip) and transformation along transformation systems. The Asaro and Needleman [107] formulation that describes plastic slip as the shearing along slip systems is employed in this study. Each crystal structure has its own set of active slip systems, α, that are defined by a shear plane normal, $m^{(\alpha)}$ and shear

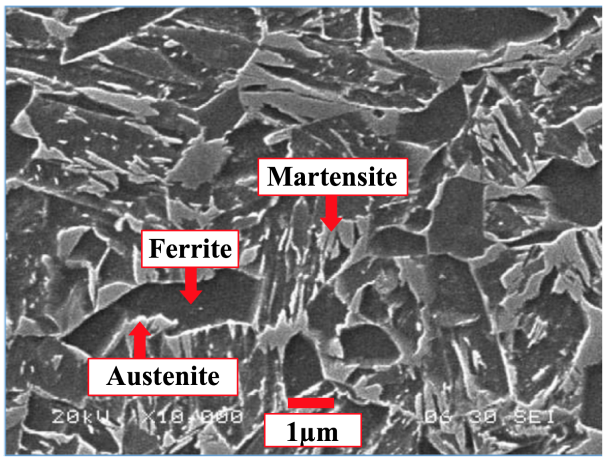

Fig. 4.4: SEM image of QP1180 sheet.

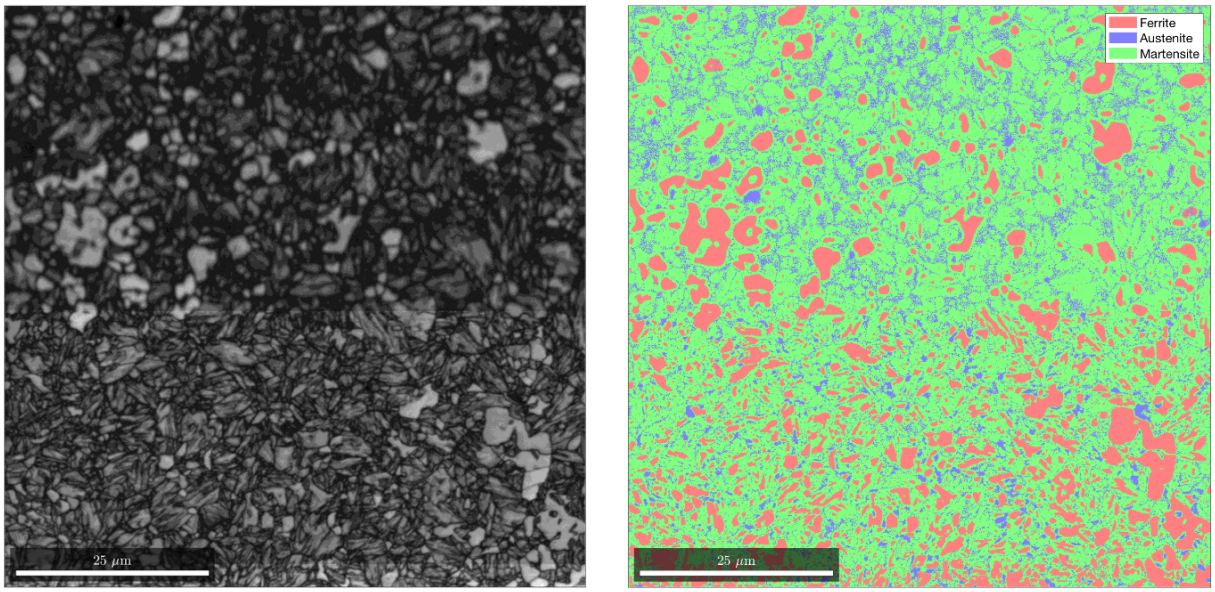

(a) (b)

Fig. 4.5: (a) EBSD Image Quality and (b) processed EBSD phase map.

direction $s^{(\alpha)}$ for each slip system. A list of the shear plane normal and directions are presented in Appendix A. Section 4.3.2 combines the deformation kinematics and elastic constitutive equation with thermodynamic arguments to derive driving forces for plastic

slip and transformation. This formulation follows the thermodynamic framework outlined in Turteltaub and Suiker [110], Tjahjanto et al. [119], and Yadegari et al. [109]. Section 4.3.3 provides specific details about modelling the retained austenite to transformed martensite phase and the choices of transformation and slip systems, kinetics functions, and the elastic constitutive equation. Section 4.3.4 details a BCC constitutive model that is a simplification of the general constitutive framework presented in Sections 4.3.1 and 4.3.2, which is a commonly used model for ferrite and tempered martensite [41, 139, 140]. Fig. 4.6 gives a flowchart summarizing this derivation. Finally, Section 4.3.5 derives an incremental formulation based on the rate-tangent scheme [141], which is appropriate for large time increments.

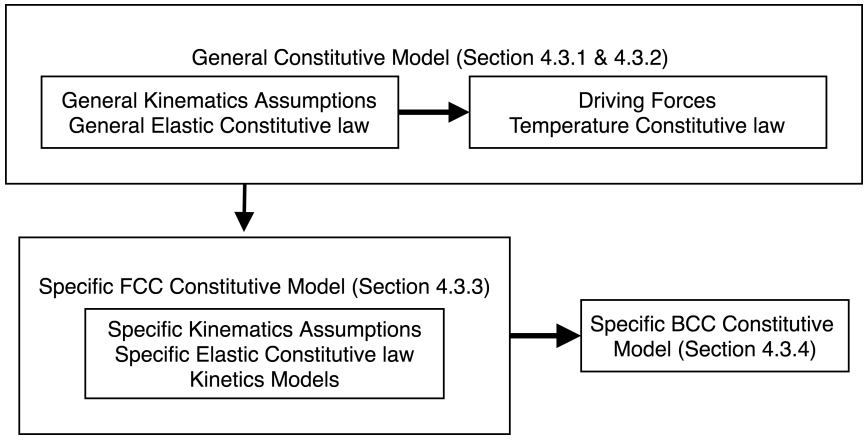

Fig. 4.6: Flowchart of constitutive model derivation.

4.3.1 Deformation Kinematics and Elastic Constitutive Model

Following Clayton [108], a multiplicative decomposition of the deformation gradient, $\mathbf{F}$, is assumed

$$\mathbf{F} = \mathbf{F}_e \mathbf{F}_\theta \mathbf{F}_{in} \tag{4.1}$$

where $\mathbf{F}_e$, $\mathbf{F}_\theta$, and $\mathbf{F}_{in}$ represent the kinematics of elasticity and rigid body motion, thermal deformation, and all inelastic deformation, respectively. Fig. 4.7 illustrates this decomposition where $\mathscr{B}_0$, $\mathscr{B}_{in}$, $\mathscr{B}_\theta$ and $\mathscr{B}$ are the undeformed, inelastically deformed, thermally deformed, and fully deformed configurations, respectively.

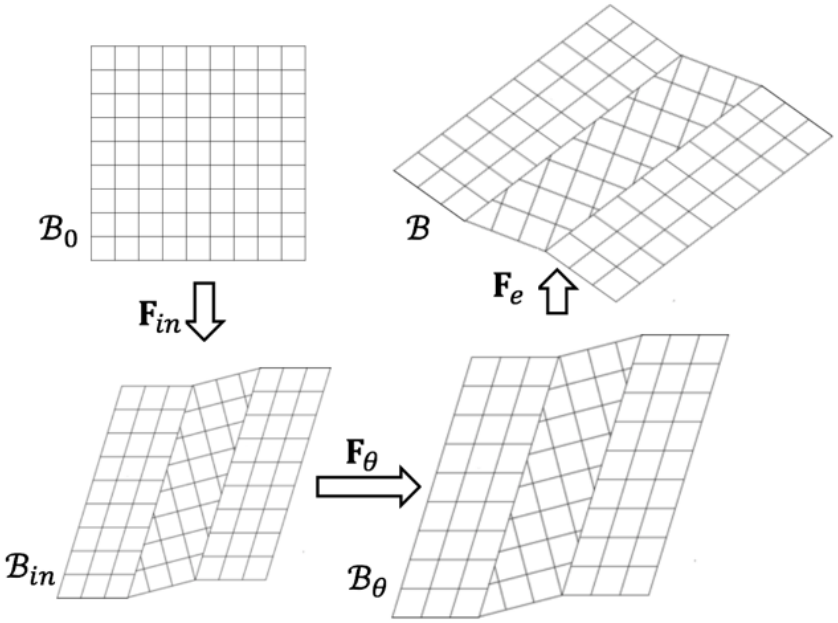

Fig. 4.7: Deformation gradient decomposition.

The velocity gradient, $\mathbf{L}$, is defined by the deformation gradient and can be decomposed into an elastic, $\mathbf{L}_e$, thermal, $\mathbf{L}_\theta$, and inelastic, $\mathbf{L}_{in}$, velocity gradient respectively, such that

$$\mathbf{L} = \dot{\mathbf{F}}\mathbf{F}^{-1} = \mathbf{L}_e + \mathbf{L}_\theta + \mathbf{L}_{in} \tag{4.2}$$

$$\mathbf{L}_e = \dot{\mathbf{F}}_e\mathbf{F}_e^{-1} \tag{4.3}$$

$$\mathbf{L}_\theta = \mathbf{F}_e\dot{\mathbf{F}}_\theta\mathbf{F}_\theta^{-1}\mathbf{F}_e^{-1} \tag{4.4}$$

$$\mathbf{L}_{in} = \mathbf{F}_e\mathbf{F}_\theta\dot{\mathbf{F}}_{in}\mathbf{F}_{in}^{-1}\mathbf{F}_\theta^{-1}\mathbf{F}_e^{-1} \tag{4.5}$$

Kalidindi [142] first proposed that the velocity gradient could be decomposed into individual components representing each constituent inelastic deformation mode. He used this assumption to describe the deformation behaviour of twinning in magnesium for crystal plasticity calculations. Lee et al. [95] proposed a similar approach to represent the deformation of transformation-induced plasticity in steel. These modes are slip plasticity and transformation induced plasticity, represented by $\mathbf{L}_p$ and $\mathbf{L}_{tr}$ respectively, such that

$$\mathbf{L}_{in} = \mathbf{L}_p + \mathbf{L}_{tr} \tag{4.6}$$

This is justified by the underlying assumption that deformation from slip and transformation deformation should be defined in the crystal basis, and therefore contribute to the same velocity gradient component.

The velocity gradient, $\mathbf{L}$, can also be decomposed in symmetric and skew-symmetric components $\mathbf{D}$ and $\boldsymbol{\Omega}$, which in turn can be decomposed into elastic, thermal, dislocation plasticity and transformation plasticity strain rate components

$$\mathbf{D} = \frac{1}{2}\left(\mathbf{L} + \mathbf{L}^T\right) = \mathbf{D}_e + \mathbf{D}_\theta + \mathbf{D}_p + \mathbf{D}_{tr} \tag{4.7}$$

$$\boldsymbol{\Omega} = \frac{1}{2}\left(\mathbf{L} - \mathbf{L}^T\right) = \boldsymbol{\Omega}_e + \boldsymbol{\Omega}_\theta + \boldsymbol{\Omega}_p + \boldsymbol{\Omega}_{tr} \tag{4.8}$$

The thermal strain and spin rates are defined as

$$\mathbf{D}_\theta = A_A(\boldsymbol{\xi})\dot{\theta}\mathbf{I} \tag{4.9}$$

$$\boldsymbol{\Omega}_\theta = \mathbf{0} \tag{4.10}$$

where $\dot{\theta}$ is the rate of change of temperature, $\mathbf{I}$ is the 2nd order identity tensor, and A_A is the thermal expansion coefficient that is a function of the vector of martensite volume fraction, $\boldsymbol{\xi}$. The thermal expansion coefficient is given by

$$A_A(\boldsymbol{\xi}) = \xi^{(0)} A_A^{(0)} + \sum_{\alpha=1}^{N_{tr}} \xi^{(\alpha)} A_A^{(\alpha)} \tag{4.11}$$

where $\xi^{(\alpha)}$ is the volume fraction of a martensite variant α, N_{tr} is the number of martensitic variants, $\xi^{(0)}$ is the RAVF given by $\xi^{(0)} = 1 - \sum_{\alpha=1}^{N_{tr}} \xi^{(\alpha)}$, $A_A^{(0)}$ is the austenite thermal expansion coefficient and $A_A^{(\alpha)}$ is the thermal expansion coefficient for martensite variant α.

As mentioned earlier, slip plasticity is assumed to occur solely due to plastic shearing along slip systems [107]. Each shear plane normal and direction can be distorted, such that

$$\mathbf{s}_e^{(\alpha)} = \mathbf{F}_e \mathbf{F}_\theta \mathbf{s}^{(\alpha)} \tag{4.12}$$

$$\mathbf{m}_e^{(\alpha)} = \mathbf{s}^{(\alpha)} \mathbf{F}_\theta^{-1} \mathbf{F}_e^{-1} \tag{4.13}$$

where $\mathbf{s}_e^{(\alpha)}$ and $\mathbf{m}_e^{(\alpha)}$ are the fully deformed configuration of the shear plane direction and normal, respectively. As in Yadegari et al. [109], plastic slip is assumed not to occur in

newly transformed martensite. The plastic strain and spin rate from dislocation plasticity are given by

$$\mathbf{D}_p = \sum_{\alpha=1}^{N_p} \dot{\gamma}^{(\alpha)} \mathbf{P}_p^{(\alpha)} \qquad (4.14) \qquad\qquad \mathbf{\Omega}_p = \sum_{\alpha=1}^{N_p} \dot{\gamma}^{(\alpha)} \mathbf{W}_p^{(\alpha)} \qquad (4.15)$$

where $\dot{\gamma}^{(\alpha)}$ is the plastic shear rate on slip system α, N_p is the number of slip systems, and $\mathbf{P}_p^{(\alpha)}$ and $\mathbf{W}_p^{(\alpha)}$ are the symmetric and skew-symmetric slip system tensors defined by

$$\mathbf{P}_p^{(\alpha)} = \frac{\mathbf{s}_e^{(\alpha)} \otimes \mathbf{m}_e^{(\alpha)} + \mathbf{m}_e^{(\alpha)} \otimes \mathbf{s}_e^{(\alpha)}}{2} \qquad (4.16) \qquad \mathbf{W}_p^{(\alpha)} = \frac{\mathbf{s}_e^{(\alpha)} \otimes \mathbf{m}_e^{(\alpha)} - \mathbf{m}_e^{(\alpha)} \otimes \mathbf{s}_e^{(\alpha)}}{2} \qquad (4.17)$$

Transformation induced plasticity is assumed to occur solely by plastic deformation along transformation systems that are characterized by a normalized deformation vector, $\mathbf{b}^{(\alpha)}$, and habit plane normal, $\mathbf{d}^{(\alpha)}$, for each transformation system α. Unlike dislocation plasticity, $\mathbf{b}^{(\alpha)}$ and $\mathbf{d}^{(\alpha)}$ are not orthogonal, resulting in significant inelastic volumetric strain. Similar to the plastic slip, the transformation systems are subjected to thermal, elastic and rigid body deformations, such that

$$\mathbf{b}_e^{(\alpha)} = \mathbf{F}_e \mathbf{F}_\theta \mathbf{b}^{(\alpha)} \qquad (4.18) \qquad\qquad \mathbf{d}_e^{(\alpha)} = \mathbf{d}^{(\alpha)} \mathbf{F}_\theta^{-1} \mathbf{F}_e^{-1} \qquad (4.19)$$

where $\mathbf{b}_e^{(\alpha)}$ and $\mathbf{d}_e^{(\alpha)}$ are the fully deformed configurations. The transformation plasticity strain rate, $\mathbf{D}_{tr}$, and spin rate, $\mathbf{\Omega}_{tr}$, tensors are defined as

$$\mathbf{D}_{tr} = \sum_{\alpha=1}^{N_{tr}} \dot{\xi}^{(\alpha)} \mathbf{P}_{tr}^{(\alpha)} \qquad (4.20) \qquad\qquad \mathbf{\Omega}_{tr} = \sum_{\alpha=1}^{N_{tr}} \dot{\xi}^{(\alpha)} \mathbf{W}_{tr}^{(\alpha)} \qquad (4.21)$$

where $\dot{\xi}^{(\alpha)}$ is the transformation rate, N_{tr} is the number of transformation systems, and $\mathbf{P}_{tr}^{(\alpha)}$ and $\mathbf{W}_{tr}^{(\alpha)}$ are the symmetric and skew-symmetric transformation system matrices on the transformation system α defined by

$$\mathbf{P}_{tr}^{(\alpha)} = \hat{\gamma}_{tr} \frac{\mathbf{b}_e^{(\alpha)} \otimes \mathbf{d}_e^{(\alpha)} + \mathbf{d}_e^{(\alpha)} \otimes \mathbf{b}_e^{(\alpha)}}{2} \qquad (4.22) \qquad \mathbf{W}_{tr}^{(\alpha)} = \hat{\gamma}_{tr} \frac{\mathbf{b}_e^{(\alpha)} \otimes \mathbf{d}_e^{(\alpha)} - \mathbf{d}_e^{(\alpha)} \otimes \mathbf{b}_e^{(\alpha)}}{2} \qquad (4.23)$$

where $\hat{\gamma}_{tr}$ is the total deformation magnitude equal for all transformation systems. The kinetic functions for plastic shear rate on a slip system, $\dot{\gamma}^{(\alpha)}$, and the transformation rate, $\dot{\xi}^{(\alpha)}$, are defined as a function of a thermodynamic driving force and critical driving force, such that

$$\dot{\gamma}^{(\alpha)} = \dot{\gamma}^{(\alpha)}\left(f^{(\alpha)}_{p(A)}, g^{(\alpha)}_{p(A)}, \xi^{(0)}\right) \qquad (4.24) \qquad\qquad \dot{\xi}^{(\alpha)} = \dot{\xi}^{(\alpha)}\left(f^{(\alpha)}_{tr}, g^{(\alpha)}_{tr}, \xi^{(0)}\right) \qquad (4.25)$$

where $f^{(\alpha)}_{p(A)}$ and $g^{(\alpha)}_{p(A)}$ are the thermodynamic driving force and critical driving force for plastic slip and $f^{(\alpha)}_{tr}$ and $g^{(\alpha)}_{tr}$ is the thermodynamic driving force and critical driving force for transformation. Coupling between plastic slip and transformation can be incorporated as part of these kinetics functions. Since $\dot{\gamma}^{(\alpha)}$ and represent the total slip and transformation rates in the aggregate, they must be the product of the slip and transformation rates in the RA phase and the current fraction of RA in the aggregate. The thermodynamic driving forces are presented in Section 4.3.2.

The kinematic formulation outlined above is chosen instead of a multiplicative decomposition of the deformation gradient ($\mathbf{F} = \mathbf{F}_e\mathbf{F}_\theta\mathbf{F}_p\mathbf{F}_{tr}$) used in Yadegari et al. [109] and others to ensure the correct evolution of transformation systems with applied strain. In this multiplicative decomposition scheme, the transformation velocity gradient ($\mathbf{L}_{tr} = \mathbf{F}_e\mathbf{F}_\theta\mathbf{F}_p\dot{\mathbf{F}}_{tr}\mathbf{F}^{-1}_{tr}\mathbf{F}^{-1}_p\mathbf{F}^{-1}_\theta\mathbf{F}^{-1}_e$) implies that the transformation systems in the updated configuration ($\mathbf{b}^{(\alpha)}_e = \mathbf{F}_e\mathbf{F}_\theta\mathbf{F}_p\mathbf{b}^{(\alpha)}$ and $\mathbf{d}^{(\alpha)}_e = \mathbf{d}^{(\alpha)}\mathbf{F}^{-1}_p\mathbf{F}^{-1}_\theta\mathbf{F}^{-1}_e$) must convect with plastic slip in addition to elastic and thermal strains. This is unrealistic because the transformation systems are expected to convect with the crystal lattice, and plastic slip strain does not result in changes to the crystal lattice. Next, stress is assumed to follow a hyper-elastic constitutive law

$$\mathbf{S}_e = \mathbb{C}_A\left(\boldsymbol{\xi}\right) : \mathbf{E}_e \qquad (4.26)$$

where $\mathbf{S}_e$ is the second Piola-Kirchhoff stress, $\mathbf{E}_e$ is the elastic Green-Lagrange strain given by $\mathbf{E}_e = (\mathbf{F}^T\mathbf{F}_e - \mathbf{I})/2$, and $\mathbb{C}_A$ is the 4th order elastic moduli tensor. The elastic moduli, $\mathbb{C}_A$, are assumed to be a function of the martensite volume fractions $\boldsymbol{\xi}$ because transformed martensite has different elastic properties than the parent austenite [110]. Eq. (4.26) is expressed at the thermally deformed configuration. The elastic moduli, $\mathbb{C}_A$, are given as a function of the overall thermal and transformation Jacobians J_θ and J_{tr}, such that

$$\mathbb{C}_A\left(\boldsymbol{\xi}\right) = \frac{\mathbb{C}'_A\left(\boldsymbol{\xi}\right)}{J_\theta J_{tr}} \qquad (4.27)$$

where the Jacobians evolve according to $\dot{J}_\theta = J_\theta \mathrm{tr}\left(\mathbf{L}_\theta\right)$ and $\dot{J}_{tr} = J_{tr}\mathrm{tr}\left(\mathbf{L}_{tr}\right)$, and

$$\mathbb{C}'_A\left(\boldsymbol{\xi}\right) = J^{(0)}_\theta\xi^{(0)}\mathbb{C}^{(0)} + (1+\delta_{tr})\sum_{\alpha=1}^{N_{tr}} J^{(\alpha)}_\theta\xi^{(\alpha)}\mathbb{C}^{(\alpha)} \qquad (4.28)$$

where $\xi^{(0)}$ is the RAVF, $\xi^{(\alpha)}$ is the martensite volume fraction, $\mathbb{C}^{(0)}$ is the 4th order elastic moduli of austenite, $\mathbb{C}^{(\alpha)}$ is the elastic moduli for a transformation system α, and δ_{tr} is the volumetric dilation of complete martensite transformation given by $\delta_{tr} = \mathbf{b}^{(\alpha)} \cdot \mathbf{d}^{(\alpha)}$. Next, the total time derivative of Eq. (4.26) is rearranged, giving the elastic Jaumann derivative of the Kirchhoff stress

$$\begin{aligned}\overset{\triangledown}{\boldsymbol{\tau}}_e &= \dot{\boldsymbol{\tau}} + \boldsymbol{\tau}\boldsymbol{\Omega}_e - \boldsymbol{\Omega}_e\boldsymbol{\tau} \\ &= \mathbb{C}_{A(e)}\left(\boldsymbol{\xi}\right) : \mathbf{D}_e + \sum_{\alpha=1}^{N_{tr}} \left(\mathbf{F}_e \left[\left(J_\theta^{(\alpha)}(1+\delta_{tr})\mathbb{C}^{(\alpha)} - J_\theta^{(0)}\mathbb{C}^{(0)}\right) : \mathbf{E}_e\right] \mathbf{F}_e^T\right) \dot{\xi}^{(\alpha)}\end{aligned} \tag{4.29}$$

where $\mathbb{C}_{A(e)}$ is the elastic moduli tensor in the fully deformed configuration defined by

$$\mathbb{C}_{A(e)(abcd)} = \mathbb{C}'_{A(ijkl)} F_{e(ai)} F_{e(bj)} F_{e(ck)} F_{e(dl)} \tag{4.30}$$

It is assumed that $\boldsymbol{\tau} : \mathbf{D}$ and $\mathbf{D} : \boldsymbol{\tau}$ are small relative to $\dot{\boldsymbol{\tau}}$. The total Jaumann rate of the Kirchhoff stress is

$$\overset{\triangledown}{\boldsymbol{\tau}} = \dot{\boldsymbol{\tau}} + \boldsymbol{\tau}\boldsymbol{\Omega} - \boldsymbol{\Omega}\boldsymbol{\tau} = \overset{\triangledown}{\boldsymbol{\tau}}_e - \sum_{\alpha=1}^{N_p} \mathbf{B}_p^{(\alpha)} \dot{\gamma}^{(\alpha)} - \sum_{\alpha=1}^{N_{tr}} \mathbf{B}_{tr}^{(\alpha)} \dot{\xi}^{(\alpha)} \tag{4.31}$$

where

$$\mathbf{B}_p^{(\alpha)} = \mathbf{W}_p^{(\alpha)}\boldsymbol{\tau} + \boldsymbol{\tau}\mathbf{W}_p^{(\alpha)} \tag{4.32}$$

$$\mathbf{B}_{tr}^{(\alpha)} = \mathbf{W}_{tr}^{(\alpha)}\boldsymbol{\tau} + \boldsymbol{\tau}\mathbf{W}_{tr}^{(\alpha)} \tag{4.33}$$

Substituting Eqs. (4.7), (4.9), (4.14), (4.20), and (4.29) into (4.31) yields

$$\begin{aligned}\overset{\triangledown}{\boldsymbol{\tau}} = \mathbb{C}_{A(e)}\left(\boldsymbol{\xi}\right) : \mathbf{D}_e - A_A(\boldsymbol{\xi})\dot{\theta}\left[\mathbb{C}_{A(e)} : \mathbf{I}\right] - \sum_{\alpha=1}^{N_p} \mathbf{R}_{p(A)}^{(\alpha)} \dot{\gamma}^{(\alpha)} \\ - \sum_{\alpha=1}^{N_{tr}} \left(\mathbf{R}_{tr}^{(\alpha)} - \mathbf{F}_e \left[\left(J_\theta^{(\alpha)}(1+\delta_{tr})\mathbb{C}^{(\alpha)} - J_\theta^{(0)}\mathbb{C}^{(0)}\right)\right] \mathbf{F}_e^T\right) \dot{\xi}^{(\alpha)}\end{aligned} \tag{4.34}$$

where $\mathbf{R}_p^{(\alpha)}$ and $\mathbf{R}_{tr}^{(\alpha)}$ are given by

$$\mathbf{R}_p^{(\alpha)} = \mathbb{C}_{A(e)}\left(\boldsymbol{\xi}\right) : \mathbf{P}_p^{(\alpha)} + \mathbf{B}_p^{(\alpha)} \qquad (4.35) \qquad \mathbf{R}_{tr}^{(\alpha)} = \mathbb{C}_{A(e)}\left(\boldsymbol{\xi}\right) : \mathbf{P}_{tr}^{(\alpha)} + \mathbf{B}_{tr}^{(\alpha)} \qquad (4.36)$$

The four terms in Eq. (4.34) represent an elastic trial stress and the thermal, plastic slip, and martensitic transformation correction terms.

4.3.2 Thermodynamic Driving Forces

As presented in the previous section, the rate of plastic slip and transformation is governed by thermodynamic driving forces derived from an energy balance law. The energy balance law in the undeformed configuration is presented as

$$\rho_0 \dot{e} + \boldsymbol{\nabla} \cdot \mathbf{q} - \rho_0 r - \mathbf{S} : \dot{\mathbf{E}} = 0 \qquad (4.37)$$

where ρ_0 is the density of the material in the undeformed configuration, $\dot{e}$ is the internal energy density rate of change, $\boldsymbol{\nabla} \cdot \mathbf{q}$ is the divergence of the heat flux, r is any applied volumetric heating (e.g., electromagnetic), $\mathbf{S}$ is the second Piola-Kirchhoff stress and $\dot{\mathbf{E}}$ is the Green-Lagrange strain rate. These terms represent the change in internal energy of the material, the energy change due to heat flux, the energy change due to volumetric heating, and the energy change due to external work. The second law of thermodynamics is satisfied by enforcing that the energy dissipation rate, $\mathbf{D}$, is everywhere non-negative [110]

$$\mathscr{D} = -\rho_0 \dot{e} + \rho_0 \theta \dot{\eta} + \mathbf{S} : \dot{\mathbf{E}} - \frac{\boldsymbol{\nabla}\theta \cdot \mathbf{q}}{\theta} \geq 0 \qquad (4.38)$$

where $\dot{\eta}$ is the rate of change of entropy density, and θ is the temperature. The dissipation rate can be decomposed into three components

$$\mathscr{D} = -\rho_0 \dot{e} + \rho_0 \theta \dot{\eta} + \mathbf{S} : \dot{\mathbf{E}} - \frac{\boldsymbol{\nabla}\theta \cdot \mathbf{q}}{\theta} = \mathscr{D}_p + \mathscr{D}_{tr} + \mathscr{D}_\theta \geq 0 \qquad (4.39)$$

where $\mathscr{D}_p$, $\mathscr{D}_{tr}$, and $\mathscr{D}_\theta$ are the dissipations associated with dislocation motion, transformation, and heat conduction, respectively. These are given by

$$\mathscr{D}_p = \sum_{\alpha=1}^{N_p} f_p \dot{\gamma}^{(\alpha)} \qquad (4.40) \qquad \mathscr{D}_{tr} = \sum_{\alpha=1}^{N_{tr}} f_{tr} \dot{\xi}^{(\alpha)} \dot{\gamma}^{(\alpha)} \qquad (4.41) \qquad \mathscr{D}_\theta = -\frac{\boldsymbol{\nabla} \cdot \mathbf{q}}{\theta} \qquad (4.42)$$

where $f_p^{(\alpha)}$ and $f_{tr}^{(\alpha)}$ are the driving forces for dislocation plasticity and transformation

plasticity, respectively. These kinetics functions are assumed that the material is strongly dissipative, i.e.

$$\mathscr{D}_p \geq 0 \qquad \mathscr{D}_{tr} \geq 0 \qquad \mathscr{D}_\theta \geq 0 \tag{4.43}$$

The entropy density can be separated into four components

$$\eta = \eta_e + \eta_{tr} + \eta_p + \eta_m \tag{4.44}$$

where η_e is the thermal part of the reversible entropy density, $\eta_t r$ is the transformation entropy density, η_p is the dislocation motion entropy density and η_m is the thermomechanical coupling part of the reversible entropy density. The thermal component of reversible entropy density is defined as [110]

$$\eta_e = h_A\left(\boldsymbol{\xi}\right) \ln\left(\frac{\theta}{\theta_T}\right) + \eta_T \tag{4.45}$$

where h_A is the specific heat capacity of the aggregate material, θ_T is the temperature at which transformation spontaneously occurs in the absence of applied stress or transformation energy barriers, and η_T is the entropy density of the material at the transformation temperature θ_T. The aggregate specific heat capacity is calculated as

$$h_A\left(\boldsymbol{\xi}\right) = h^{(0)}\xi^{(0)} + \sum_{\alpha=1}^{N_{tr}} h^{(\alpha)}\xi^{(\alpha)} \tag{4.46}$$

where $h^{(0)}$ is the specific heat capacity of austenite and $h^{(\alpha)}$ is the specific heat capacity of transformation system α. The rate of the transformation entropy density component is defined as [110]

$$\dot{\eta}_{tr} = \sum_{\alpha=1}^{N_{tr}} \dot{\xi}^{(\alpha)} \frac{\lambda^{(\alpha)}}{\theta_T} \tag{4.47}$$

where $\lambda^{(\alpha)}$ is the latent heat of transformation for transformation system α. Next, the rate of the entropy density dislocation motion component is [119]

$$\dot{\eta}_p = \sum_{\alpha=1}^{N_p} \dot{\gamma}^{(\alpha)} \phi_A^{(\alpha)} \tag{4.48}$$

where $\phi_A^{(\alpha)}$ is the entropy change per unit slip on the slip system α and is assumed to be constant. Now, the mechanical coupling component of the reversible entropy density is a function of the elastic Green-Lagrange strain $\mathbf{E}_e$, the thermal component of the reversible entropy density η_e and the volume fractions of martensite variants ξ, such that $\eta_m = \eta_m(\mathbf{E}_e, \eta_e, \boldsymbol{\xi})$. The specific formulation of the mechanical coupling component of entropy is derived through additional constraints on the dissipation rate. Using the decomposition of entropy and the Legendre transformation between the internal energy and the Helmholtz free energy, defined by $\Psi = e - \theta\eta_e$, the dissipation rate can be rewritten as

$$\mathscr{D} = -\rho_0\dot{\Psi} + \rho_0\dot{\theta}\eta_e + \rho_0\theta\dot{\eta}_m + \rho_0\theta\dot{\eta}_p + \rho_0\theta\dot{\eta}_{tr} + \mathbf{S} : \dot{\mathbf{E}} - \frac{\boldsymbol{\nabla}\theta \cdot \mathbf{q}}{\theta} \tag{4.49}$$

The Helmholtz free energy and total time derivative can be separated into four contributions, such that

$$\Psi = \Psi_m + \Psi_{th} + \Psi_s + \Psi_d + \Psi_\infty \tag{4.50}$$

where Ψ_m is the contribution of bulk elastic strain energy, Ψ_{th} is thermal energy, and Ψ_s is the free energy associated with the creation of interface surfaces between the martensite variants and the RA. In Yadegari et al. [109], Ψ_d is defined as the defect energy that is related to the microstrain, β_A, that is generated from dislocation accumulation in the austenite/martensitic regions in the material, such that $\beta_A = \beta_A(\boldsymbol{\gamma})$. However, an additional defect is produced from the Greenwood-Johnson [72] effect, where an additional plastic strain is generated during transformation in both austenite and the newly formed martensite due to accommodation of the local stress field. As such, this work assumes that the microstrain is a function of both plastic slip and martensite volume fraction, such that $\beta_A = \beta_A(\boldsymbol{\gamma}, \boldsymbol{\sigma})$. Finally, Ψ_∞ is the free energy contribution not categorized as surface or defect-free energy. Substituting the total time derivatives of the Helmholtz free energy Ψ, the microstrain measure β_A and the mechanical coupling component of entropy density, Eqs. (4.45), (4.47), and (4.48) into Eq. (4.49), rewriting $\mathbf{S} : \dot{\mathbf{E}}$ in terms of $\boldsymbol{\tau}$ and $\mathbf{D}$, and using $\dot{\mathbf{E}}_e = \mathbf{F}_e^T\mathbf{D}_e\mathbf{F}_e$ gives Eq. (4.51).

$$
\begin{aligned}
\mathscr{D} = &- \rho_0 \left[\mathbf{F}_e \frac{\partial \Psi}{\partial \mathbf{E}_e} \mathbf{F}_e^T : \mathbf{D}_e + \frac{\partial \Psi}{\partial \theta} \dot{\theta} + \frac{\partial \Psi}{\partial \beta_A} \left(\sum_{\alpha=1}^{N_p} \frac{\partial \beta_A}{\partial \gamma^{(\alpha)}} \dot{\gamma}^{(\alpha)} + \sum_{\alpha=1}^{N_{tr}} \frac{\partial \beta_A}{\partial \xi^{(\alpha)}} \dot{\xi}^{(\alpha)} \right) \right] \\
&+ \rho_0 \theta \left[\mathbf{F}_e \frac{\partial \eta_m}{\partial \mathbf{E}_e} \mathbf{F}_e^T : \mathbf{D}_e + \frac{\partial \eta_m}{\partial \eta_e} \frac{\partial \eta_e}{\partial \theta} \dot{\theta} + \sum_{\alpha=1}^{N_{tr}} \left[\frac{\partial \eta_m}{\partial \xi^{(\alpha)}} + \frac{\partial \eta_m}{\partial \eta_e} \frac{\partial \eta_e}{\partial \xi^{(\alpha)}} \right] \dot{\xi}^{(\alpha)} \right] \\
&+ \rho_0 \theta \left[\sum_{\alpha=1}^{N_{tr}} \dot{\xi}^{(\alpha)} \frac{\lambda^{(\alpha)}}{\theta_T} \right] + \rho_0 \theta \left[\sum_{\alpha=1}^{N_p} \dot{\gamma}^{(\alpha)} \phi_A^{(\alpha)} \right] - \rho_0 \dot{\theta} \left[h_A \left(\boldsymbol{\xi} \right) \ln \left(\frac{\theta}{\theta_T} \right) + \eta_T \right] \\
&+ \boldsymbol{\tau} : \left[\mathbf{D}_e + \mathbf{D}_\theta + \mathbf{D}_p + \mathbf{D}_{tr} \right] - \frac{\boldsymbol{\nabla} \cdot \mathbf{q}}{\theta}
\end{aligned}
\tag{4.51}
$$

where $w_{p(A)}^{(\alpha)} = \frac{\partial \beta_A}{\partial \gamma^{(\alpha)}}$ and $w_{tr}^{(\alpha)} = \frac{\partial \beta_A}{\partial \xi^{(\alpha)}}$. Substituting Eq. (4.9), (4.14) and (4.20) into Eq. (4.51) and isolating for $\mathbf{D}_e$, θ, $\boldsymbol{\gamma}$ and $\boldsymbol{\xi}$ gives

$$
\begin{aligned}
\mathscr{D} = &\left[\boldsymbol{\tau} - \rho_0 \mathbf{F}_e \frac{\partial \Psi}{\partial \mathbf{E}_e} \mathbf{F}_e^T + \rho_0 \theta \mathbf{F}_e \frac{\partial \eta_m}{\partial \mathbf{E}_e} \mathbf{F}_e^T \right] : \mathbf{D}_e \\
&+ \left[A_A \left(\boldsymbol{\xi} \right) \left[\boldsymbol{\tau} : \mathbf{I} \right] - \rho_0 \frac{\partial \Psi}{\partial \theta} + \rho_0 \theta \frac{\partial \eta_m}{\partial \eta_e} \frac{\partial \eta_e}{\partial \theta} - \rho_0 \left[h_A \left(\boldsymbol{\xi} \right) \ln \left(\frac{\theta}{\theta_T} \right) + \eta_T \right] \right] \dot{\theta} \\
&+ \sum_{\alpha=1}^{N_{tr}} \left[\boldsymbol{\tau} : \mathbf{P}_{tr}^{(\alpha)} + \rho_0 \theta \left[\frac{\partial \eta_m}{\partial \xi^{(\alpha)}} + \frac{\partial \eta_m}{\partial \eta_e} \frac{\partial \eta_e}{\partial \xi^{(\alpha)}} \right] + \rho_0 \theta \frac{\lambda^{(\alpha)}}{\theta_T} - \rho_0 \frac{\partial \Psi}{\partial \beta_A} w_{tr}^{(\alpha)} \right] \dot{\xi}^{(\alpha)} \\
&- \sum_{\alpha=1}^{N_{tr}} \left[\rho_0 \frac{\partial \Psi}{\partial \xi^{(\alpha)}} \right] \dot{\xi}^{(\alpha)} + \sum_{\alpha=1}^{N_p} \left[\boldsymbol{\tau} : \mathbf{P}_p^{(\alpha)} + \rho_0 \theta \phi_A^{(\alpha)} - \rho_0 \frac{\partial \Psi}{\partial \beta_A} w_{p(A)}^{(\alpha)} \right] \dot{\gamma}^{(\alpha)} - \frac{\boldsymbol{\nabla} \theta \cdot \mathbf{q}}{\theta}
\end{aligned}
\tag{4.52}
$$

The five terms contained in Eq. (4.52) represent the elastic, thermal rate, transformation, plastic slip, and heat transfer dissipation rates. An exact dissipation rate requires exact forms of the Helmholtz free energy Ψ and the thermomechanical coupling entropy η_m is required to determine the plastic slip and transformation driving forces. Following the Coleman and Noll [113] procedure, the terms multiplied by $\mathbf{D}_e$ and $\dot{\theta}$ must vanish, resulting in the following additional constraints

$$
\rho_0 \frac{\partial \Psi}{\partial \mathbf{E}_e} = J_{tr} J_\theta \mathbf{S}_e + \rho_0 \theta \frac{\partial \eta_m}{\partial \mathbf{E}_e} \tag{4.53}
$$

$$\rho_0 \frac{\partial \Psi}{\partial \theta} = A_A\left(\boldsymbol{\xi}\right)\left[\boldsymbol{\tau} : \mathbf{I}\right] + \rho_0 \theta \frac{\partial \eta_m}{\partial \eta_e}\frac{\partial \eta_e}{\partial \theta} - \rho_0\left[h_A\left(\boldsymbol{\xi}\right)\ln\left(\frac{\theta}{\theta_T}\right) + \eta_T\right] \tag{4.54}$$

Integrating Eq. (4.53) with respect to the elastic Green-Lagrange strain $\mathbf{E}_e$ yields the bulk strain energy contribution

$$\Psi = \frac{\mathbb{C}'_A\left(\boldsymbol{\xi}\right) :: \left(\mathbf{E}_e \otimes \mathbf{E}_e\right)}{2\rho_0} + \theta\eta_m + \Psi_{th} + \Psi_s + \Psi_d + \Psi_\infty \tag{4.55}$$

where the remaining terms are dependent only on temperature θ, martensite volume fractions $\boldsymbol{\xi}$, and microstrain β_A. Substituting Eq. (4.54) into Eq. (4.55) and simplifying gives

$$\eta_m = \frac{A_A\left(\boldsymbol{\xi}\right)}{\rho_0}\left(\boldsymbol{\tau} : \mathbf{I}\right) - \left[\frac{\partial \Psi_{th}}{\partial \theta} + h_A\left(\boldsymbol{\xi}\right)\ln\left(\frac{\theta}{\theta_T}\right) + \eta_T\right] \tag{4.56}$$

Next, the thermomechanical coupling entropy density, eta_m, should disappear when no stress is applied. This constraint implies that

$$\frac{\partial \Psi_{th}}{\partial \theta} + h_A\left(\boldsymbol{\xi}\right)\ln\left(\frac{\theta}{\theta_T}\right) + \eta_T = 0 \quad \Longrightarrow \quad \frac{\partial \Psi_{th}}{\partial \theta} = -h_A\left(\boldsymbol{\xi}\right)\ln\left(\frac{\theta}{\theta_T}\right) - \eta_T = -\eta_e \tag{4.57}$$

Therefore, the thermomechanical coupling part of the entropy density is given by

$$\eta_m = \frac{A_A\left(\boldsymbol{\xi}\right)}{\rho_0}\left(\boldsymbol{\tau} : \mathbf{I}\right) \tag{4.58}$$

Now, integrating Eq. (4.57) for temperature, θ, leads to

$$\Psi_{th} = -h_A\left(\boldsymbol{\xi}\right)\theta\left(\ln\left(\frac{\theta}{\theta_T}\right) - 1\right) - \eta_T\theta = -\eta_e\theta + h_A\left(\boldsymbol{\xi}\right)\theta \tag{4.59}$$

where Φ_s,Φ_d and Φ_∞ are the Helmholtz free energy components dependent only on martensite volume fractions $\boldsymbol{\xi}$ and microstrain β_A. Tjahjanto et al. [119] showed that under certain assumptions that Ψ_d is given by

$$\Psi_d = \frac{\omega_A \mu'_A\left(\boldsymbol{\xi}\right)}{2\rho_0}\beta_A^2 \tag{4.60}$$

where ω_A is a scalar relating changes in microstrain to changes in internal energy and

$\mu'_A(\boldsymbol{\xi})$ is the overall elastic shear modulus of the crystal given by

$$\mu'_A(\boldsymbol{\xi}) = J_\theta^{(0)}\xi^{(0)}\mu_A^{(0)} + (1+\delta_T)\sum_{\alpha=1}^{N_{tr}} J_\theta^{(\alpha)}\xi^{(\alpha)}\mu_A^{(\alpha)} \tag{4.61}$$

where $\mu_A^{(0)}$ and $\mu_A^{(\alpha)}$ are the elastic shear moduli of the austenite phase and the martensite variant α, respectively. Next, the surface energy, Φ_s, is represented as

$$\Psi_s = \sum_{\alpha=1}^{N_{tr}} \frac{\chi}{\ell_0\rho_0}\left(1-\xi^{(\alpha)}\right)\xi^{(\alpha)} \tag{4.62}$$

where χ is the interfacial energy per unit area and ℓ_0 is the ratio between the mean initial volume and surface area of the martensite variants. Finally, the remaining free energy contribution, Ψ_∞, represents the energy barrier for transformation at the transformation temperature θ_T with no applied stress, microstrain or pre-existing martensite, such that

$$\Psi_\infty = \sum_{\alpha=1}^{N_{tr}} \lambda^{(\alpha)}\xi^{(\alpha)} - h_A(\boldsymbol{\xi})\,\theta_T \tag{4.63}$$

Therefore, the total free energy is defined as

$$\begin{aligned}\Psi =& \frac{\mathbb{C}'_A(\boldsymbol{\xi}) :: (\mathbf{E}_e \otimes \mathbf{E}_e)}{2\rho_0} + \frac{A_A(\boldsymbol{\xi})}{\rho_0}\theta(\boldsymbol{\tau}:\mathbf{I}) + \frac{\omega_A\mu'_A(\boldsymbol{\xi})}{2\rho_0}\beta_A^2 \\ &+ \sum_{\alpha=1}^{N_{tr}}\left[\frac{\chi}{\ell_0\rho_0}\left(1-\xi^{(\alpha)}\right) + \lambda^{(\alpha)}\right]\xi^{(\alpha)} - \eta_e\theta + h_A(\boldsymbol{\xi})(\theta-\theta_T)\end{aligned} \tag{4.64}$$

Thus, the driving force for plastic slip is defined as

$$f_{p(A)}^{(\alpha)} = \boldsymbol{\tau} : \mathbf{P}_p^{(\alpha)} - \omega_A w_{p(A)}^{(\alpha)}\mu'_A(\boldsymbol{\xi})\,\beta_A + \rho_0\theta\phi_A^{(\alpha)} \tag{4.65}$$

The driving force for transformation is defined as

$$
\begin{aligned}
f_{tr}^{(\alpha)} =& \boldsymbol{\tau} : \mathbf{P}_{tr}^{(\alpha)} + \theta A_A\left(\xi\right)\left(\mathbf{F}_e\left[\left(J_\theta^{(0)}\mathbb{C}^{(0)} - (1+\delta_T)J_\theta^{(\alpha)}\mathbb{C}^{(\alpha)}\right) : \mathbf{E}_e\right]\mathbf{F}_e^T\right) : \mathbf{I} \\
&+ \frac{\chi}{\ell_0}\left[2\xi^{(\alpha)} - 1\right] + \theta\left[A^{(0)} - A^{(\alpha)}\right](\boldsymbol{\tau} : \mathbf{I}) + \rho_0\frac{\lambda_T^{(\alpha)}}{\theta_T}\left[\theta - \theta_T\right] \\
&+ \rho_0\left[h^{(0)} - h^{(\alpha)}\right]\left[\theta - \theta_T - \ln\left(\frac{\theta}{\theta_T}\right)\theta\right] + \frac{\omega_A}{2}\left[J_\theta^{(0)}\mu^{(0)} - J_\theta^{(\alpha)}\mu^{(\alpha)}\right]\beta_A^2 \\
&- \omega_A w_{tr}^{(\alpha)}\mu_A'\left(\boldsymbol{\xi}\right)\beta_A
\end{aligned}
\tag{4.66}
$$

Finally, the temperature evolution is obtained by substituting Eq. (4.64) into Eq. (4.37), using the Legendre transformation and rearranging to produce

$$
\rho_0 h_A\left(\boldsymbol{\xi}\right)\dot{\theta} = \rho_0 r - \boldsymbol{\nabla}\cdot\mathbf{q} - \mathbf{M}_{e(A)} : \mathbf{D}_e + \sum_{\alpha=1}^{N_p} M_{p(A)}^{(\alpha)}\dot{\gamma}^{(\alpha)} + \sum_{\alpha=1}^{N_p} M_{tr}^{(\alpha)}\dot{\xi}^{(\alpha)} \tag{4.67}
$$

where

$$
\mathbf{M}_{e(A)} = 4\theta A_A\left(\boldsymbol{\xi}\right)\boldsymbol{\tau} + \theta A_A\left(\boldsymbol{\xi}\right)\mathbf{F}_e\left[\mathbf{I} : \mathbb{C}_A'\left(\boldsymbol{\xi}\right)\right]\mathbf{F}_e^T \tag{4.68}
$$

$$
M_{p(A)}^{(\alpha)} = \boldsymbol{\tau} : \mathbf{P}_p^{(\alpha)} - \omega_A w_{p(A)}^{(\alpha)}\mu_A'\left(\boldsymbol{\xi}\right)\beta_A \tag{4.69}
$$

$$
\begin{aligned}
M_{tr(A)}^{(\alpha)} =& \boldsymbol{\tau} : \mathbf{P}_{tr}^{(\alpha)} + \theta A_A\left(\boldsymbol{\xi}\right)\left(\mathbf{F}_e\left[\left(J_\theta^{(0)}\mathbb{C}^{(0)} - (1+\delta_T)J_\theta^{(\alpha)}\mathbb{C}^{(\alpha)}\right) : \mathbf{E}_e\right]\mathbf{F}_e^T\right) : \mathbf{I} \\
&+ \frac{1}{2}\left[J_\theta^{(0)}\mathbb{C}^{(0)} - (1+\delta_T)J_\theta^{(\alpha)}\mathbb{C}^{(\alpha)}\right] :: \left[\mathbf{E}_e \otimes \mathbf{E}_e\right] + \frac{\chi}{\ell_0}\left[2\xi^{(\alpha)} - 1\right] \\
&+ \frac{\omega_A}{2}\left[J_\theta^{(0)}\mu^{(0)} - J_\theta^{(\alpha)}\mu^{(\alpha)}\right]\beta_A^2 + \theta\left[A_A^{(0)} - A_A^{(\alpha)}\right](\boldsymbol{\tau} : \mathbf{I}) \\
&- \omega_A w_{tr}^{(\alpha)}\mu_A'\left(\boldsymbol{\xi}\right)\beta_A - \rho_0\lambda_T^{(\alpha)} + \rho_0\left[h^{(0)} - h^{(\alpha)}\right]\left[\theta - \theta_T\right]
\end{aligned}
\tag{4.70}
$$

4.3.3 RA to Martensite Specific Constitutive Functions

4.3.3.1 Martensite Variant Selection

The RA transformation systems are modelled using the theory of martensitic transformation [143, 144], initially proposed for use in crystal plasticity by Turteltaub and Suiker

[110, 118]. This theory assumes that three possible BCT martensite sub-variants combine to form 24 possible twinned martensite variants. It is well suited for modelling QP steels because twinned martensite is the primary martensite morphology formed during transformation in QP steel [40, 43, 65]. Each twin is made of two sub-variants where the volume fractions and orientations of each twin sub-variant are determined by satisfying compatibility conditions between the sub-variants. Compatibility between the sub-variants is

$$\mathbf{R}^{(\alpha)}\mathbf{U}^{(\beta_1)} - \mathbf{U}^{(\beta_2)} = \mathbf{a}^{(\alpha)} \otimes \mathbf{n}^{(\alpha)} \tag{4.71}$$

where $\mathbf{U}^{(\beta_1)}$ and $\mathbf{U}^{(\beta_2)}$ are the stretch tensors of sub-variants β_1 and β_2 relative to the RA phase, $\mathbf{R}^{(\alpha)}$ is the relative orientation between sub-variants β_1 and β_2 for transformation system α, and $\mathbf{a}^{(\alpha)}$ and $\mathbf{n}^{(\alpha)}$ are the twin shear vector and twin plane normal for transformation system α. Note that the stretch tensors $\mathbf{U}^{(\beta_1)}$ and $\mathbf{U}^{(\beta_2)}$ are defined in an intermediate martensitic basis related to the austenite basis by a Bain rotation. Next, compatibility between the twinned structure and the RA phase is governed by

$$\overline{\mathbf{R}}^{(\alpha)} \left(\lambda^{(\alpha,\beta_1)} \mathbf{R}^{(\alpha)} \mathbf{U}^{(\beta_1)} - \lambda^{(\alpha,\beta_2)} \mathbf{U}^{(\beta_2)} \right) = \overline{\mathbf{b}}^{(\alpha)} \otimes \mathbf{d}^{(\alpha)} \tag{4.72}$$

where $\overline{\mathbf{R}}^{(\alpha)}$ is the orientation between the twinned structure and the austenite phase, $\lambda^{(\alpha,\beta_1)}$ and $\lambda^{(\alpha,\beta_2)}$ are the volume fraction of sub-variants β_1 and β_2 for transformation system α, and $\overline{\mathbf{b}}^{(\alpha)}$ and $\mathbf{d}^{(\alpha)}$ are the deformation vector and habit plane normal of transformation system α. The volume fractions $\lambda^{(\alpha,\beta_1)}$ and $\lambda^{(\alpha,\beta_2)}$ are related to each other using volume conservation given by $\lambda^{(\alpha,\beta_1)} + \lambda^{(\alpha,\beta_2)} = 1$. The magnitude of the deformation vector is $\hat{\gamma}_{tr} = \|\overline{\mathbf{b}}^{(\alpha)}\|$ and the normalized deformation direction $\mathbf{b}^{(\alpha)}/\hat{\gamma}_{tr}$. To solve these compatibility equations, it is necessary to specify the stretch tensors of each sub-variant relative to the parent RA phase. The stretch tensors of each sub-variant relative to the parent RA phase is defined by

$$\mathbf{U}^{\beta} = \left(\sqrt{2}\frac{a^M}{a^A} \right) \mathbf{I} + \left(\frac{c^M}{a^M} - \sqrt{2}\frac{a^M}{a^A} \right) \mathbf{e}_A^{(\beta)} \otimes \mathbf{e}_A^{(\beta)} \tag{4.73}$$

where a^M and c^M are the lattice parameters of the BCT martensite sub-variant, a^A is the lattice parameter of the parent RA, and $\left\{ \mathbf{e}_A^{(\beta)} \right\}_{\beta=1}^{3}$ is an orthonormal basis aligned with the cubic axes of the RA phase. It should be noted that the lattice parameters, a^M, c^M and a^A are dependent on the carbon content of the RA phase in the alloy, and thus are alloy dependent.

4.3.3.2 Elastic Constitutive Model for Transformed Systems

The coefficients of the elasticity tensors associated with each transformation variant α, as expressed in the austenitic basis, can be found from the elasticity tensors of the constituent martensite sub-variants using

$$\begin{aligned}\mathbb{C}^{(\alpha)}_{A(abcd)} =& \lambda^{(\alpha,\beta_1)}\mathbb{E}^{(\beta_1)}_{ijkl}\widehat{Q}^{(\alpha,\beta_1)}_{ai}\widehat{Q}^{(\alpha,\beta_1)}_{bj}\widehat{Q}^{(\alpha,\beta_1)}_{ck}\widehat{Q}^{(\alpha,\beta_1)}_{dl} \\ & \lambda^{(\alpha,\beta_2)}\mathbb{E}^{(\beta_2)}_{ijkl}\widehat{Q}^{(\alpha,\beta_2)}_{ai}\widehat{Q}^{(\alpha,\beta_2)}_{bj}\widehat{Q}^{(\alpha,\beta_2)}_{ck}\widehat{Q}^{(\alpha,\beta_2)}_{dl}\end{aligned} \tag{4.74}$$

where $\mathbb{E}^{(\beta_1)}_{ijkl}$ and $\mathbb{E}^{(\beta_2)}_{ijkl}$ are the coefficients of the elasticity tensors for sub-variants of a transformation system β_1 and β_2, and $\widehat{\mathbf{Q}}^{(\alpha,\beta_2)}$ and $\widehat{\mathbf{Q}}^{(\alpha,\beta_1)}$ are the rotations between the austenitic basis and the bases of sub-variants β_1 and β_2, as calculated for transformation system α. The sub-variants rotation tensors in the austenitic basis are defined as

$$\widehat{\mathbf{Q}}^{(\alpha,\beta_1)} = \overline{\mathbf{R}}^{(\alpha)}\mathbf{R}^{(\alpha)}\mathbf{R}^{(\beta_1)}_{\star} \tag{4.75}$$

$$\widehat{\mathbf{Q}}^{(\alpha,\beta_2)} = \overline{\mathbf{R}}^{(\alpha)}\mathbf{R}^{(\beta_2)}_{\star} \tag{4.76}$$

where $\mathbf{R}^{(\beta)}_{\star}$ represents the rotation between the austenite basis and an intermediate basis defined by the Bain rotation β. The rotation tensors $\widehat{\mathbf{Q}}^{(\alpha,\beta_1)}$ and $\widehat{\mathbf{Q}}^{(\alpha,\beta_2)}$ differ by the rotation tensor $\mathbf{R}^{(\alpha)}$, which is the rotation between the martensite sub-variants. These Bain rotations [66] are given by

$$\mathbf{R}^{(1)}_{\star} = \begin{bmatrix} 1 & 0 & 0 \\ 0 & \frac{\sqrt{2}}{2} & -\frac{\sqrt{2}}{2} \\ 0 & \frac{\sqrt{2}}{2} & \frac{\sqrt{2}}{2} \end{bmatrix} \tag{4.77}$$

$$\mathbf{R}^{(2)}_{\star} = \begin{bmatrix} \frac{\sqrt{2}}{2} & 0 & \frac{\sqrt{2}}{2} \\ 0 & 1 & 0 \\ -\frac{\sqrt{2}}{2} & 0 & \frac{\sqrt{2}}{2} \end{bmatrix} \tag{4.78}$$

$$\mathbf{R}^{(3)}_{\star} = \begin{bmatrix} \frac{\sqrt{2}}{2} & -\frac{\sqrt{2}}{2} & 0 \\ \frac{\sqrt{2}}{2} & \frac{\sqrt{2}}{2} & 0 \\ 0 & 0 & 1 \end{bmatrix} \tag{4.79}$$

Now, the elasticity tensor of an FCC RA crystal, $\mathbb{C}^{(0)}$, and the BCT sub-variants, $\mathbb{E}^{(i)}$, are presented in Voigt notation

$$\mathbb{E}^{(1)} = \begin{pmatrix} \kappa_4^S & \kappa_3^S & \kappa_3^S & 0 & 0 & 0 \\ \kappa_3^S & \kappa_1^S & \kappa_3^S & 0 & 0 & 0 \\ \kappa_3^S & \kappa_2^S & \kappa_1^S & 0 & 0 & 0 \\ 0 & 0 & 0 & \kappa_6^S & 0 & 0 \\ 0 & 0 & 0 & 0 & \kappa_5^S & 0 \\ 0 & 0 & 0 & 0 & 0 & \kappa_5^S \end{pmatrix} \tag{4.80}$$

$$\mathbb{E}^{(1)} = \begin{pmatrix} \kappa_1^S & \kappa_2^S & \kappa_3^S & 0 & 0 & 0 \\ \kappa_2^S & \kappa_1^S & \kappa_3^S & 0 & 0 & 0 \\ \kappa_3^S & \kappa_3^S & \kappa_4^S & 0 & 0 & 0 \\ 0 & 0 & 0 & \kappa_5^S & 0 & 0 \\ 0 & 0 & 0 & 0 & \kappa_5^S & 0 \\ 0 & 0 & 0 & 0 & 0 & \kappa_6^S \end{pmatrix} \tag{4.82}$$

$$\mathbb{E}^{(2)} = \begin{pmatrix} \kappa_1^S & \kappa_3^S & \kappa_2^S & 0 & 0 & 0 \\ \kappa_3^S & \kappa_4^S & \kappa_3^S & 0 & 0 & 0 \\ \kappa_2^S & \kappa_3^S & \kappa_1^S & 0 & 0 & 0 \\ 0 & 0 & 0 & \kappa_5^S & 0 & 0 \\ 0 & 0 & 0 & 0 & \kappa_6^S & 0 \\ 0 & 0 & 0 & 0 & 0 & \kappa_5^S \end{pmatrix} \tag{4.81}$$

$$\mathbb{C}^{(0)} = \begin{pmatrix} \kappa_1^A & \kappa_2^A & \kappa_2^A & 0 & 0 & 0 \\ \kappa_2^A & \kappa_1^A & \kappa_2^A & 0 & 0 & 0 \\ \kappa_2^A & \kappa_2^A & \kappa_1^A & 0 & 0 & 0 \\ 0 & 0 & 0 & \kappa_3^A & 0 & 0 \\ 0 & 0 & 0 & 0 & \kappa_3^A & 0 \\ 0 & 0 & 0 & 0 & 0 & \kappa_3^A \end{pmatrix} \tag{4.83}$$

where κ_1^S–κ_6^S are the elastic coefficients of the sub-variants and κ_1^A–κ_3^A are the elastic coefficients for austenite.

4.3.3.3 Kinetics Functions for Dislocation Plasticity and Transformation

The dislocation plasticity kinetics function follows the power-law formulation [145]

$$\dot{\gamma}^{(\alpha)} = \dot{a}_{p(A)} \xi^{(0)} \text{sign}\left(f_{p(A)}\right) \left| \frac{f_{p(A)}^{(\alpha)}}{g_{p(A)}^{(\alpha)}} \right|^{\frac{1}{m_{p(A)}}} \tag{4.84}$$

where $\dot{a}_{p(A)}$ is the reference dislocation plasticity shear rate, $g_{p(A)}^{(\alpha)}$ is the critical driving force for dislocation plasticity on slip system α, and $m_{p(A)}$ is the dislocation plasticity strain rate exponent. Yadegari et al. [109] proposed the following kinetic law

$$\dot{\xi}^{(\alpha)} = \dot{a}_{tr} \tanh\left(\frac{\langle f_{tr}^{(\alpha)} - g_{tr}^{(\alpha)} \rangle}{v_{tr} g_{tr}^{(\alpha)}} \right) \tag{4.85}$$

where $\dot{a}_{tr}$ is the reference transformation rate, $g_{tr}^{(\alpha)}$ is the critical driving force for transformation, v_{tr} is a viscosity-like parameter, and Macaulay brackets are used to prevent reverse transformation. The primary disadvantage of this model is that the hyperbolic tangent function saturates, ensuring that the maximum transformation rate under any loading condition is $\dot{a}_{tr}$. This is in direct conflict with the experimental observations from QP steels, wherein transformation rate scales with the applied strain-rate [53]. To address this, a transformation kinetics function is proposed, in analogy to the work of Kalidindi [142] and Lévesque et al. [99] (for modelling twinning in magnesium and titanium). This law exhibits power-law type rate-sensitive behaviour and is given by:

$$\dot{\xi}^{(\alpha)} = \dot{a}_{tr}\xi^{(0)} \left\langle \frac{f_{tr}^{(\alpha)}}{g_{tr}^{(\alpha)}} \right\rangle^{\frac{1}{m_{tr}}} \tag{4.86}$$

where $\dot{a}_{tr}$, $g_{tr}^{(\alpha)}$ are defined as in eq. (4.85) and $m_t r$ is the transformation rate exponent. Since reversible transformation is not considered in this work, Macaulay brackets are used to prevent transformation when $f_{tr}^{(\alpha)}$ is less than zero.

The dislocation plasticity critical driving force is defined using an initial value $g_{p(A)}^{0}$ for all slip systems and governed by a rate of change law defined by

$$\dot{g}_{p(A)}^{(\alpha)} = \sum_{\beta=1}^{N_p} q_{p(A)}^{(\alpha\beta)} h_{p(A)} \left|\dot{\gamma}^{(\beta)}\right| + \sum_{\beta=1}^{N_{tr}} q_{c}^{(\alpha\beta)} h_c \dot{\xi}^{(\beta)} \tag{4.87}$$

where $q_{p(A)}^{(\alpha\beta)}$ and $q_{c}^{(\alpha\beta)}$ are the dislocation plasticity and transformation latent hardening matrices, and $h_{p(A)}$ and h_c capture the dependency of the critical driving force on plastic slip and transformation, respectively. Similar to the work presented in Ma and Hartmaier [120], the transformation dependency term h_c is introduced to capture the hardening of the RA phase due to transformation induced RA plasticity caused by the Greenwood-Johnson effect [72] and increased dislocation obstacles. The slip dependency function, $h_{p(A)}$, follows a Chang-Asaro type hardening law [112]

$$h_{p(A)} = h_{p(A)}^{s} + \left(h_{p(A)}^{0} - h_{p(A)}^{s}\right) \operatorname{sech}^2 \left(\frac{h_{p(A)}^{0} - h_{p(A)}^{s}}{g_{p(A)}^{s} - g_{p(A)}^{0}} \gamma_a \right) \tag{4.88}$$

$$\gamma_a = \sum_{\alpha=1}^{N_p} \int_0^t \left|\dot{\gamma}^{(\alpha)}\right| \, \mathrm{d}t \tag{4.89}$$

where $h^0_{p(A)}$ and $h^s_{p(A)}$ are the initial and saturation hardening rate, $g^s_{p(A)}$ is the saturation critical driving force, and γ_a is the accumulated absolute slip. The coupling of transformation to slip hardening functions, h_c, is also assumed to follow a Chang-Asaro type hardening law

$$h_c = h^s_c + \left(h^0_c - h^s_c\right) \operatorname{sech}^2\left(\frac{h^0_c - h^s_c}{g^s_c - g^0_c}\xi_a\right) \tag{4.90}$$

$$\xi_a = \sum_{\alpha=1}^{N_{tr}} \int_0^t \left|\dot{\xi}^{(\alpha)}\right| \, \mathrm{d}t = 1 - \xi^{(0)} \tag{4.91}$$

where h^0_c and h^s_c are the initial and saturation hardening rate, g^0_c and g^s_c are the initial and saturation critical driving forces, and ξ_a is the amount of RA that has transformed. The dislocation plasticity latent hardening matrix, $q^{(\alpha\beta)}_{p(A)}$, assumes that the slip systems are arranged with coplanar slip system sets $\{1,2,3\}$, $\{4,5,6\}$, $\{7,8,9\}$, $\{10,11,12\}$, such that

$$q^{(\alpha\beta)}_{p(A)} = \begin{bmatrix} \mathbf{A} & q_{p(A)}\mathbf{A} & q_{p(A)}\mathbf{A} & q_{p(A)}\mathbf{A} \\ q_{p(A)}\mathbf{A} & \mathbf{A} & q_{p(A)}\mathbf{A} & q_{p(A)}\mathbf{A} \\ q_{p(A)}\mathbf{A} & q_{p(A)}\mathbf{A} & \mathbf{A} & q_{p(A)}\mathbf{A} \\ q_{p(A)}\mathbf{A} & q_{p(A)}\mathbf{A} & q_{p(A)}\mathbf{A} & \mathbf{A} \end{bmatrix} \tag{4.92}$$

where and $\mathbf{A}$ is a 3×3 matrix of ones and $q_{p(A)}$ is the dislocation plasticity latent hardening parameter. Next, it is assumed that $q^{(\alpha\beta)}_c$ is an $N_p \times N_{tr}$ matrix of ones. In a similar manner, the critical transformation driving force uses an initial value g^0_{tr} for all transformation systems and a rate of change law

$$\dot{g}^{(\alpha)}_{tr} = \sum_{\beta=1}^{N_{tr}} q^{(\alpha\beta)}_{tr} h_{tr} \dot{\xi}^{(\beta)} \tag{4.93}$$

where $q^{(\alpha\beta)}_{tr}$ is the transformation latent hardening matrix, h_{tr} is the transformation critical force hardening rate and $q^{(\alpha\beta)}_{tr}$ is an $N_{tr} \times N_{tr}$ matrix of ones. The hardening rate h_{tr} is governed by

$$h_{tr} = h^s_{tr} + \left(h^0_{tr} - h^s_{tr}\right) \operatorname{sech}^2\left(\frac{h^0_{tr} - h^s_{tr}}{g^s_{tr} - g^0_{tr}}\gamma_a\right) \tag{4.94}$$

where h^0_{tr}, h^s_{tr}, and g^s_{tr} are the transformation initial hardening rate, saturation hardening

rate, and saturation critical driving force, respectively.

Finally, a specific definition of the microstrain, β_A, is given by [108, 119]

$$c_A \mu'_A(\boldsymbol{\xi})\,\beta_A = \frac{1}{N_p}\sum_{\alpha=1}^{N_p} g^{(\alpha)}_{p(A)} \tag{4.95}$$

where c_A represents the interaction effect between dislocations. It should be mentioned that this formulation differs from Yadegari et al. [109] by incorporating the dependence of the critical driving force $g^{(\alpha)}_{p(A)}$ on the martensite volume fractions $\boldsymbol{\xi}$. Thus, the specific definitions of the derivatives of the microstrain function $w^{(\alpha)}_p = \frac{\partial \beta_A}{\partial \gamma^{(\alpha)}}$ and $w^{(\alpha)}_{tr} = \frac{\partial \beta_A}{\partial \xi^{(\alpha)}}$ are given by

$$w^{(\alpha)}_p = \frac{1}{c_A \mu'_A(\boldsymbol{\xi})\,N_p}\sum_{\beta=1}^{N_p} q^{(\alpha\beta)}_p h_{p(A)} \text{sign}\left(\dot{\gamma}^{(\beta)}\right) \tag{4.96}$$

$$w^{(\alpha)}_{tr} = \frac{1}{c_A \mu'_A(\boldsymbol{\xi})\,N_p}\sum_{\beta=1}^{N_p} q^{(\alpha\beta)}_c h_c \tag{4.97}$$

4.3.4 BCC Specific Constitutive Functions

The BCC crystal plasticity framework can be conceptualized as a simplification of the RA crystal plasticity model where $\boldsymbol{\xi} = \dot{\boldsymbol{\xi}} = \mathbf{0}$ and $\xi^{(0)} = 1$. The kinematics simplify such that $\mathbf{L}_i n = \mathbf{L}_p$ and the thermal expansion coefficient becomes constant, A_B. The total Jaumann rate of the Kirchhoff stress becomes

$$\overset{\triangledown}{\boldsymbol{\tau}} = \mathbb{C}_{B(e)} : \mathbf{D} - A_B \dot{\theta}\left[\mathbb{C}_{B(e)} : \mathbf{I}\right] - \sum_{\alpha=1}^{N_p} \mathbf{R}^{(\alpha)}_{p(B)} \dot{\gamma}^{(\alpha)} \tag{4.98}$$

where $\mathbb{C}_{B(e)(abcd)} = \mathbb{C}_{B(ijkl)} F_{e(ai)} F_{e(bj)} F_{e(ck)} F_{e(dl)}$, the elasticity matrix $\mathbb{C}_B$ in Voigt notation is related to κ^B_1, κ^B_2 and κ^B_3 as in Eq. (4.83), and $\mathbf{R}^{(\alpha)}_{p(B)}$ is a simplification of Eq. (4.35). Repeating the thermodynamic procedure in Section 4.3.2, the driving force for dislocation slip is given by

$$f^{(\alpha)}_{p(B)} = \boldsymbol{\tau} : \mathbf{P}^{(\alpha)}_p - \omega_B w^{(\alpha)}_{p(B)} \mu'_B \beta_B + \rho_0 \theta \phi^{(\alpha)}_B \tag{4.99}$$

where μ'_B is a constant input. The thermal change is given by

$$\rho_0 h_B \dot{\theta} = \rho_0 r - \boldsymbol{\nabla} \cdot \mathbf{q} - \mathbf{M}_{e(B)} : \mathbf{D}_e + \sum_{\alpha=1}^{N_p} M_{p(B)}^{(\alpha)} \dot{\gamma}^{(\alpha)} \tag{4.100}$$

where $\mathbf{M}_{e(B)}$ and $M_{p(B)}^{(\alpha)}$ are related to the BCC variables such that

$$\mathbf{M}_{e(B)} = 4\theta A_B \boldsymbol{\tau} + \theta A_B \mathbf{F}_e \left[\mathbf{I} : \mathbb{C}_B\right] \mathbf{F}_e^T \tag{4.101}$$

$$M_{p(B)}^{(\alpha)} = \boldsymbol{\tau} : \mathbf{P}_p^{(\alpha)} - \omega_B w_{p(B)}^{(\alpha)} \mu'_B \beta_B \tag{4.102}$$

The kinetics function and the rate of change in the critical driving force $\dot{g}_{p(B)}^{(\alpha)}$, which is initially given by $g_{p(B)}^0$, is given by

$$\dot{\gamma}^{(\alpha)} = \dot{a}_{p(B)} \text{sign}\left(f_{p(B)}\right) \left| \frac{f_{p(B)}^{(\alpha)}}{g_{p(B)}^{(\alpha)}} \right|^{\frac{1}{m_{p(B)}}} \tag{4.103}$$

$$\dot{g}_{p(B)}^{(\alpha)} = \sum_{\beta=1}^{N_p} q_{p(B)}^{(\alpha\beta)} h_{p(B)} \left|\dot{\gamma}^{(\beta)}\right| \tag{4.104}$$

where the latent hardening matrix $q_{p(B)}^{(\alpha\beta)}$ is given by [146]

$$q_{p(B)}^{(\alpha\beta)} = q_{p(B)} + \left(1 - q_{p(B)}\right) \delta_{\alpha\beta} \tag{4.105}$$

where $q_{p(B)}$ is the latent hardening coefficient for the BCC material. Finally, the hardening rate $h_{p(B)}$, microstrain β_B and partial derivative $w_{p(B)}^{(\alpha)}$ can be related to the BCC variables as in Eqs. (4.88), (4.95) and (4.96), respectively.

4.3.5 Incremental Formulation Derivation

This section provides a derivation of the incremental numerical formulation of the RA constitutive model implementation. The BCC constitutive model is derived from this implementation by removing superfluous sections when $\boldsymbol{\xi} = 0$. The constitutive model is implemented using an extension of the rate tangent algorithm [141] initially used for crystal plasticity Peirce et al. [147]. This algorithm provides a higher-order estimate of the

plastic slip vector increment $\Delta\boldsymbol{\gamma}$ and the volume fraction vector increment $\Delta\boldsymbol{\xi}$ to facilitate the use of larger time steps in the LS-Dyna Implicit solver and is derived as follows. These parameters are estimated using

$$\Delta\boldsymbol{\gamma} = \Delta\gamma^{(\alpha)} = \left[(1-\Lambda)\,\dot{\gamma}^{(\alpha)}(t) + \Lambda\dot{\gamma}^{(\alpha)}(t+\Delta t)\right]\Delta t \tag{4.106}$$

$$\Delta\boldsymbol{\xi} = \Delta\xi^{(\alpha)} = \left[(1-\Lambda)\,\dot{\xi}^{(\alpha)}(t) + \Lambda\dot{\xi}^{(\alpha)}(t+\Delta t)\right]\Delta t \tag{4.107}$$

where Λ is an integration scheme parameter. When $\Lambda = 0$, this algorithm reduces to a first-order forward Euler method. In this work, $\Lambda = 0.5$, which has been found to give good results in most cases. The rate terms at time $t + \Delta t$ are estimated using a Taylor expansion

$$\dot{\gamma}^{(\alpha)}(t+\Delta t) = \dot{\gamma}^{(\alpha)}(t) + \frac{\partial\dot{\gamma}^{(\alpha)}(t)}{\partial\xi^{(0)}}\Delta\xi^{(0)} + \frac{\partial\dot{\gamma}^{(\alpha)}(t)}{\partial g_p^{(\alpha)}}\Delta g_p^{(\alpha)} + \frac{\partial\dot{\gamma}^{(\alpha)}(t)}{\partial f_p^{(\alpha)}}\Delta f_p^{(\alpha)} \tag{4.108}$$

$$\dot{\xi}^{(\alpha)}(t+\Delta t) = \dot{\xi}^{(\alpha)}(t) + \frac{\partial\dot{\xi}^{(\alpha)}(t)}{\partial\xi^{(0)}}\Delta\xi^{(0)} + \frac{\partial\dot{\xi}^{(\alpha)}(t)}{\partial g_{tr}^{(\alpha)}}\Delta g_{tr}^{(\alpha)} + \frac{\partial\dot{\xi}^{(\alpha)}(t)}{\partial f_{tr}^{(\alpha)}}\Delta f_{tr}^{(\alpha)} \tag{4.109}$$

where the derivatives $\frac{\partial\dot{\gamma}^{(\alpha)}(t)}{\partial\xi^{(0)}}$ and $\frac{\partial\dot{\xi}^{(\alpha)}(t)}{\partial\xi^{(0)}}$ and the increment $\Delta\xi^{(0)}$ are given by Eqs. (4.110), (4.111) and (4.112).

$$\frac{\partial\dot{\gamma}^{(\alpha)}(t)}{\partial\xi^{(0)}} = \frac{\dot{\gamma}^{(\alpha)}(t)}{\xi^{(0)}} \tag{4.110}$$

$$\frac{\partial\dot{\xi}^{(\alpha)}(t)}{\partial\xi^{(0)}} = \frac{\dot{\xi}^{(\alpha)}(t)}{\xi^{(0)}} \tag{4.111}$$

$$\Delta\xi^{(0)} = -\sum_{\alpha=1}^{N_{tr}}\Delta\xi^{(\alpha)} \tag{4.112}$$

Partial derivatives with respect to the driving force and critical driving force are given by Eqs. (4.113) to (4.116).

$$\frac{\partial\dot{\gamma}^{(\alpha)}(t)}{\partial g_p^{(\alpha)}} = -\frac{\dot{\gamma}^{(\alpha)}(t)}{g_p^{(\alpha)}(t)\,m_p} \tag{4.113}$$

$$\frac{\partial\dot{\gamma}^{(\alpha)}(t)}{\partial g_{tr}^{(\alpha)}} = -\frac{\dot{\gamma}^{(\alpha)}(t)}{g_{tr}^{(\alpha)}(t)\,m_{tr}} \tag{4.114}$$

$$\frac{\partial\dot{\gamma}^{(\alpha)}(t)}{\partial f_p^{(\alpha)}} = -\frac{\dot{\gamma}^{(\alpha)}(t)}{f_p^{(\alpha)}(t)\,m_p} \tag{4.115}$$

$$\frac{\partial\dot{\gamma}^{(\alpha)}(t)}{\partial f_{tr}^{(\alpha)}} = -\frac{\dot{\gamma}^{(\alpha)}(t)}{f_{tr}^{(\alpha)}(t)\,m_{tr}} \tag{4.116}$$

The critical driving force increments, shown in Eq. (4.119) and (4.120), are derived using approximations (4.117) and (4.118).

$$\Delta\gamma^{(\alpha)} \approx \dot{\gamma}^{(\alpha)}\Delta t, \qquad \Delta\xi^{(\alpha)} \approx \dot{\xi}^{(\alpha)}\Delta t \tag{4.117}$$

$$\Delta g_p^{(\alpha)} \approx \dot{g}_p^{(\alpha)}\Delta t, \qquad \Delta g_{tr}^{(\alpha)} \approx \dot{g}_{tr}^{(\alpha)}\Delta t \tag{4.118}$$

$$\Delta g_p^{(\alpha)} = \sum_{\beta=1}^{N_p} q_{p(A)}^{(\alpha\beta)} h_{p(A)} \text{sign}\left(\dot{\gamma}^{(\beta)}\right) \Delta\gamma^{(\beta)} + \sum_{\beta=1}^{N_{tr}} q_c^{(\alpha\beta)} h_c \Delta\xi^{(\beta)} \tag{4.119}$$

$$\Delta g_{tr}^{(\alpha)} = \sum_{\beta=1}^{N_{tr}} q_{tr}^{(\alpha\beta)} h_{tr} \text{sign}\Delta\xi^{(\beta)} \tag{4.120}$$

The driving force increments, shown in Eqs. (4.122) and (4.123), are derived using the approximations (4.117) and (4.121). To simplify the presentation of the equation, the intermediate variables $H_{c1}^{(\alpha)}$, $H_{p1}^{(\alpha\beta)}$, $H_{t1}^{(\alpha\beta)}$, $\mathbf{R}_{tr}^{'(\alpha)}$, $H_{c2}^{(\alpha)}$, $H_{p2}^{(\alpha)}$, and $H_{t2}^{(\alpha)}$ are introduced.

$$\Delta f_p^{(\alpha)} \approx \dot{f}_p^{(\alpha)}\Delta t, \qquad \Delta f_{tr}^{(\alpha)} \approx \dot{f}_{tr}^{(\alpha)}\Delta t \tag{4.121}$$

$$\Delta f_p^{(\alpha)} = \mathbf{R}_p^{(\alpha)} : \mathbf{D}\Delta t + H_{c1}^{(\alpha)}\Delta t - \sum_{\beta=1}^{N_p} H_{p1}^{(\alpha\beta}\Delta\gamma^{(\beta)} + \sum_{\beta=1}^{N_{tr}} H_{t1}^{(\alpha\beta)}\Delta\xi^{(\beta)} \tag{4.122}$$

$$\Delta f_{tr}^{(\alpha)} = \mathbf{R}_{tr}^{'(\alpha)} : \mathbf{D}\Delta t + H_{c2}^{(\alpha)}\Delta t - \sum_{\beta=1}^{N_p} H_{p2}^{(\alpha\beta}\Delta\gamma^{(\beta)} + \sum_{\beta=1}^{N_{tr}} H_{t2}^{(\alpha\beta)}\Delta\xi^{(\beta)} \tag{4.123}$$

The intermediate variables used in the dislocation plasticity driving force increment are given by Eqs. (4.124) to (4.126)

$$H_{c1}^{(\alpha)} = \left[\rho_0\phi^{(\alpha)} - A_T\left(\boldsymbol{\xi}\right)\mathbf{R}_p^{(\alpha)} : \mathbf{I}\right]\dot{\theta} \tag{4.124}$$

$$H_{p1}^{(\alpha\beta)} = \mathbf{R}_p^{(\alpha)} : \mathbf{P}_p^{(\beta)} + \omega_A w_p^{(\alpha)} w_p^{(\beta)} \mu'\left(\boldsymbol{\xi}\right) \tag{4.125}$$

$$H_{t1}^{(\alpha\beta)} = \mathbf{R}_p^{(\alpha)} : \mathbf{P}_{tr}^{(\beta)} + \omega_A w_p^{(\alpha)}\left[(1+\delta_T) J_\theta^{(\alpha)}\mu^{(\alpha)} - J_\theta^{(0)}\mu^{(0)}\right]\beta_A + \omega_A w_p^{(\alpha)} w_{tr}^{(\alpha)}\mu'\left(\boldsymbol{\xi}\right) \tag{4.126}$$

The intermediate variables used in the transformation driving force increment are given by Eqs. (4.127) to (4.130)

$$\begin{aligned}\mathbf{R}_{tr}^{'(\alpha)} =&\mathbf{R}_{tr}^{(\alpha)} - \theta A_A\left(\boldsymbol{\xi}\right)\left[4\mathbf{E}_e + \mathbf{I}\right] : \left[\mathbf{F}_e\left(\left(1+\delta_T\right)J_\theta^{(\alpha)}\mathbb{C}^{(\alpha)} - J_\theta^{(0)}\mathbb{C}^{(0)}\right)\mathbf{F}_e^T\right] \\ &- \theta\left[A_A^{(\alpha)} - A_A^{(0)}\right]\end{aligned} \tag{4.127}$$

$$\begin{aligned}H_{p2}^{(\alpha\beta)} =&\mathbf{P}_{tr}^{(\alpha)} : \mathbb{C}_e : \mathbf{P}_p^{(\beta)} - \left[\mathbf{P}_{tr}^{(\alpha)}\boldsymbol{\tau} - \boldsymbol{\tau}\mathbf{P}_{tr}^{(\alpha)}\right] : \mathbf{W}_p^{(\beta)} + \omega_A w_p^{(\beta)} w_{tr}^{(\alpha)}\mu'\left(\boldsymbol{\xi}\right) \\ &- \theta A_A\left(\boldsymbol{\xi}\right)\left[4\mathbf{E}_e + \mathbf{I}\right] : \left[\mathbf{F}_e\left(\left(1+\delta_T\right)J_\theta^{(\alpha)}\mathbb{C}^{(\alpha)} - J_\theta^{(0)}\mathbb{C}^{(0)}\right)\mathbf{F}_e^T\right] : \mathbf{P}_p^{(\beta)} \\ &- \theta\left[A_A^{(\alpha)} - A_A^{(0)}\right]\left[4\boldsymbol{\tau} + \mathbf{F}_e\left[\mathbf{I} : \mathbb{C}'\left(\boldsymbol{\xi}\right)\right]\mathbf{F}_e^T\right] : \mathbf{P}_p^{(\beta)} \\ &+ \omega_A w_p^{(\beta)}\left[\left(1+\delta_T\right)J_\theta^{(\alpha)}\mu^{(\alpha)} - J_\theta^{(0)}\mu^{(0)}\right]\beta_A\end{aligned} \tag{4.128}$$

$$\begin{aligned}H_{t2}^{(\alpha\beta)} =&\mathbf{P}_{tr}^{(\alpha)} : \mathbb{C}_e : \mathbf{P}_{tr}^{(\beta)} + \omega_A w_{tr}^{(\beta)}\left[\left(1+\delta_T\right)J_\theta^{(\alpha)}\mu^{(\alpha)} - J_\theta^{(0)}\mu^{(0)}\right]\beta_A \\ &- \theta A_A\left(\boldsymbol{\xi}\right)\left[4\mathbf{E}_e + \mathbf{I}\right] : \left[\mathbf{F}_e\left(\left(1+\delta_T\right)J_\theta^{(\alpha)}\mathbb{C}^{(\alpha)} - J_\theta^{(0)}\mathbb{C}^{(0)}\right)\mathbf{F}_e^T\right] : \mathbf{P}_{tr}^{(\beta)} \\ &+ \theta\left[A_A^{(\alpha)} - A_A^{(0)}\right]\left[\left(1+\delta_T\right)J_\theta^{(\alpha)}\mu^{(\alpha)} - J_\theta^{(0)}\mu^{(0)}\right] : \left[\mathbf{E}_e\otimes\mathbf{E}_e + \mathbf{E}_e\otimes\mathbf{I}\right] \\ &+ \theta\left[A_A^{(\beta)} - A_A^{(0)}\right]\left(\mathbf{F}_e\left[\left(\left(1+\delta_T\right)J_\theta^{(\alpha)}\mathbb{C}^{(\alpha)} - J_\theta^{(0)}\mathbb{C}^{(0)}\right) : \mathbf{E}_e\right]\mathbf{F}_e^T : \mathbf{I}\right) \\ &+ \left[\mathbf{W}_{tr}^{(\alpha)}\boldsymbol{\tau} - \boldsymbol{\tau}\mathbf{W}_{tr}^{(\alpha)}\right] : \mathbf{P}_{tr}^{(\beta)} - \frac{2\chi}{\ell_0}\delta_{\alpha\beta} + \omega_A w_{tr}^{(\beta)} w_{tr}^{(\alpha)}\mu'\left(\boldsymbol{\xi}\right) \\ &- \theta\left[A_A^{(\alpha)} - A_A^{(0)}\right]\left[4\boldsymbol{\tau} + \mathbf{F}_e\left[\mathbf{I} : \mathbb{C}'\left(\boldsymbol{\xi}\right)\right]\mathbf{F}_e^T\right] : \mathbf{P}_{tr}^{(\beta)}\end{aligned} \tag{4.129}$$

$$\begin{aligned}H_{c2}^{(\alpha)} =&\rho_0\frac{\lambda_T^{(\alpha)}}{\theta_T}\dot{\theta} - A_A\left(\boldsymbol{\xi}\right)\left(\mathbf{F}_e\left[\left(\left(1+\delta_T\right)J_\theta^{(\alpha)}\mathbb{C}^{(\alpha)} - J_\theta^{(0)}\mathbb{C}^{(0)}\right) : \mathbf{E}_e\right]\mathbf{F}_e^T : \mathbf{I}\right)\dot{\theta} \\ &+ \rho_0\left[h^{(\alpha)} - h^{(0)}\right]\ln\left(\frac{\theta}{\theta_T}\right)\dot{\theta} - \left[A_A^{(\alpha)} - A_A^{(0)}\right]\left(\boldsymbol{\tau} : \mathbf{I}\right)\dot{\theta} - \dot{\theta}A_T\left(\boldsymbol{\xi}\right)\left[\mathbf{P}_{tr}^{(\alpha)} : \mathbb{C}_e\right] : \mathbf{I} \\ &+ \theta A_A\left(\boldsymbol{\xi}\right)\left[4\mathbf{E}_e + \mathbf{I}\right] : \left[\mathbf{F}_e\left(\left(1+\delta_T\right)J_\theta^{(\alpha)}\mathbb{C}^{(\alpha)} - J_\theta^{(0)}\mathbb{C}^{(0)}\right)\mathbf{F}_e^T\right] : \left[A_A\left(\boldsymbol{\xi}\right)\mathbf{I}\right]\dot{\theta} \\ &\theta\left[A_A^{(\alpha)} - A_A^{(0)}\right]\left[4\boldsymbol{\tau} + \mathbf{F}_e\left[\mathbf{I} : \mathbb{C}'\left(\boldsymbol{\xi}\right)\right]\mathbf{F}_e^T\right] : \left[A_T\left(\boldsymbol{\xi}\right)\mathbf{I}\right]\dot{\theta}\end{aligned} \tag{4.130}$$

Eqs. (4.106) to (4.130) are combined and simplified, resulting in a set of implicit equations for $\Delta\boldsymbol{\gamma}$ and $\Delta\boldsymbol{\xi}$ as shown in Eqs. (4.131) and (4.132). As before, several intermediate variables have been introduced to simplify the presentation.

$$\sum_{\beta=1}^{N_p} G_{p1}^{(\alpha\beta)}\Delta\gamma^{(\beta)} + \sum_{\beta=1}^{N_{tr}} G_{t1}^{(\alpha\beta)}\Delta\xi^{(\beta)} = \left(G_{c1}^{(\alpha)} + \mathbf{Q}_p^{(\alpha)} : \mathbf{D}\right)\Delta t \tag{4.131}$$

$$\sum_{\beta=1}^{N_p} G_{p2}^{(\alpha\beta)} \Delta\gamma^{(\beta)} + \sum_{\beta=1}^{N_{tr}} G_{t2}^{(\alpha\beta)} \Delta\xi^{(\beta)} = \left(G_{c2}^{(\alpha)} + \mathbf{Q}_{tr}^{(\alpha)} : \mathbf{D} \right) \Delta t \tag{4.132}$$

The intermediate variables used in Eq. (4.131) are given by Eq. (4.133) to (4.136).

$$G_{p1}^{(\alpha\beta)} = \delta_{\alpha\beta} + \frac{\dot{\gamma}^{(\alpha)}(t)\,\Lambda\Delta t}{g_p^{(\alpha)} m_p} q_{p(A)}^{(\alpha\beta)} h_{p(A)} \operatorname{sign}\left(\dot{\gamma}^{(\beta)}\right) + \frac{\dot{\gamma}^{(\alpha)}(t)\,\Lambda\Delta t}{f_p^{(\alpha)} m_p} H_{p1}^{(\alpha\beta)} \tag{4.133}$$

$$G_{t1}^{(\alpha\beta)} = \frac{\dot{\gamma}^{(\alpha)}(t)\,\Lambda\Delta t}{\xi^{(0)}} + \frac{\dot{\gamma}^{(\alpha)}(t)\,\Lambda\Delta t}{g_p^{(\alpha)} m_p} q_c^{(\alpha\beta)} h_c + \frac{\dot{\gamma}^{(\alpha)}(t)\,\Lambda\Delta t}{f_p^{(\alpha)} m_p} H_{t1}^{(\alpha\beta)} \tag{4.134}$$

$$G_{c1}^{(\alpha)} = \dot{\gamma}^{(\alpha)}(t) + \frac{\dot{\gamma}^{(\alpha)}(t)\,\Lambda\Delta t}{f_p^{(\alpha)} m_p} H_{c1}^{(\alpha)} \tag{4.135}$$

$$\mathbf{Q}_p^{(\alpha)} = \frac{\dot{\gamma}^{(\alpha)}(t)\,\Lambda\Delta t}{f_p^{(\alpha)} m_p} \mathbf{R}_p^{(\alpha)} \tag{4.136}$$

The intermediate variables used in Eq. (4.132) are given by Eq. (4.137) to (4.140).

$$G_{p2}^{(\alpha\beta)} = \frac{\dot{\xi}^{(\alpha)}(t)\,\Lambda\Delta t}{g_{tr}^{(\alpha)} m_{tr}} H_{p2}^{(\alpha\beta)} \tag{4.137}$$

$$G_{t1}^{(\alpha\beta)} = \delta_{\alpha\beta} + \frac{\dot{\xi}^{(\alpha)}(t)\,\Lambda\Delta t}{\xi^{(0)}} + \frac{\dot{\xi}^{(\alpha)}(t)\,\Lambda\Delta t}{g_{tr}^{(\alpha)} m_{tr}} q_{tr}^{(\alpha\beta)} h_{tr} + \frac{\dot{\xi}^{(\alpha)}(t)\,\Lambda\Delta t}{f_{tr}^{(\alpha)} m_{tr}} H_{t2}^{(\alpha\beta)} \tag{4.138}$$

$$G_{c2}^{(\alpha)} = \dot{\xi}^{(\alpha)}(t) + \frac{\dot{\xi}^{(\alpha)}(t)\,\Lambda\Delta t}{f_{tr}^{(\alpha)} m_{tr}} H_{c2}^{(\alpha)} \tag{4.139}$$

$$\mathbf{Q}_{tr}^{(\alpha)} = \frac{\dot{\xi}^{(\alpha)}(t)\,\Lambda\Delta t}{f_{tr}^{(\alpha)} m_{tr}} \mathbf{R}_{tr}^{\prime(\alpha)} \tag{4.140}$$

Eq. (4.141) shows a single set of linear equations for $\frac{\Delta\boldsymbol{\gamma}}{\Delta t}$ and $\frac{\Delta\boldsymbol{\xi}}{\Delta t}$ found by combining Eqs. (4.131) and (4.132). This equation can be solved using standard techniques, resulting in Eq. (4.142).

$$\begin{bmatrix} \mathbf{G}_{p1} & \mathbf{G}_{t1} \\ \mathbf{G}_{p2} & \mathbf{G}_{t2} \end{bmatrix} \begin{bmatrix} \Delta\boldsymbol{\gamma}/\Delta t \\ \Delta\boldsymbol{\xi}/\Delta t \end{bmatrix} = \begin{bmatrix} \mathbf{G}_{c1} + \mathbf{Q}_p : \mathbf{D} \\ \mathbf{G}_{c2} + \mathbf{Q}_{tr} : \mathbf{D} \end{bmatrix} \tag{4.141}$$

$$\begin{bmatrix} \Delta\boldsymbol{\gamma}/\Delta t \\ \Delta\boldsymbol{\xi}/\Delta t \end{bmatrix} = \begin{bmatrix} \mathbf{y}_{c1} + \mathbf{Y}_p : \mathbf{D} \\ \mathbf{y}_{c2} + \mathbf{Y}_{tr} : \mathbf{D} \end{bmatrix} \tag{4.142}$$

Substituting the rates $\frac{\Delta\boldsymbol{\gamma}}{\Delta t}$ and $\frac{\Delta\boldsymbol{\xi}}{\Delta t}$ into Eq. (4.34) in place of $\dot{\boldsymbol{\gamma}}(t)$ and $\dot{\boldsymbol{\xi}}(t)$ yields Eq. (4.143) to (4.145), which better approximates stress evolution over a single timestep allowing the use of larger timesteps.

$$\overset{\triangledown}{\boldsymbol{\tau}} = \overline{\mathbb{C}} : \mathbf{D} - \dot{\overline{\boldsymbol{\sigma}}} \tag{4.143}$$

$$\begin{aligned}\overline{\mathbb{C}} =& \mathbb{C}_{A(e)}\left(\boldsymbol{\xi}\right) - \sum_{\alpha=1}^{N_p} \mathbf{R}_p^{(\alpha)} \otimes \mathbf{Y}_p^{(\alpha)} \\ & - \sum_{\alpha=1}^{N_{tr}} \left[\mathbf{R}_{tr}^{(\alpha)} - \mathbf{F}_e \left[\left(J_\theta^{(\alpha)}(1+\delta_{tr})\mathbb{C}^{(\alpha)} - J_\theta^{(0)}\mathbb{C}^{(0)}\right)\right]\mathbf{F}_e^T\right] \otimes \mathbf{Y}_{tr}^{(\alpha)}\end{aligned} \tag{4.144}$$

$$\begin{aligned}\dot{\overline{\boldsymbol{\sigma}}} =& \sum_{\alpha=1}^{N_p} \mathbf{R}_p^{(\alpha)} y_p^{(\alpha)} + A_A(\boldsymbol{\xi})\dot{\theta}\left[\mathbb{C}_e : \mathbf{I}\right] \\ & + \sum_{\alpha=1}^{N_{tr}} \left(\mathbf{R}_{tr}^{(\alpha)} - \mathbf{F}_e \left[\left(J_\theta^{(\alpha)}(1+\delta_{tr})\mathbb{C}^{(\alpha)} - J_\theta^{(0)}\mathbb{C}^{(0)}\right)\right]\mathbf{F}_e^T\right) y_{tr}^{(\alpha)}\end{aligned} \tag{4.145}$$

To utilize the LS-Dyna implicit formulation, the tangent modulus $\mathscr{L} = \frac{\partial \overset{\triangledown}{\boldsymbol{\tau}}}{\partial \mathbf{D}}$ must be provided to the solver. For this integration scheme, the tangent modulus is given by Eq. (4.146)

$$\mathscr{L} = \frac{\partial \overset{\triangledown}{\boldsymbol{\tau}}}{\partial \mathbf{D}} = \overline{C} \tag{4.146}$$

4.4 Finite Element Modelling

Finite element (FE) simulations are constructed to simulate the bulk material response of the QP1180 sheet metal alloy under the conditions applied during the in-situ uniaxial tension HEXRD experiment. The constitutive modelling framework outlined in Section 4.3 is implemented as a user-defined material subroutine (UMAT) into a non-linear coupled thermo-mechanical implicit formulation of the commercial finite element software, LS-Dyna [148]. The implementation details are provided in Section 4.4.1. Fig. 4.8(a) presents the schematic of the FE model boundary conditions. Fig. 4.8(c) and Fig. 4.8(c) present the assigned phases and material orientation for the mesh. The FE model utilized eight-node hexahedral elements (*ELFORM=2) with an element size of $0.375\,\mu m \times 0.375\,\mu m \times 0.25\,\mu m$ to generate a $200 \times 200 \times 1$ element mesh. The initial length, L_0, and thickness, t_0, of the FE model is $75\,\mu m$ and $0.25\,\mu m$, respectively. Each element was assigned the material properties of the EBSD point closest to the element centroid. The X_1, X_2 and X_3 axes are assumed to coincide with the sheet's rolling, transverse, and normal directions, respectively.

All surfaces of the FE model are constrained to remain planar. The thermal and mechanical boundary conditions on the FE model are as follows

$$\begin{aligned}
&u_1 = u_2 = u_3 \text{ on } X_1 = X_2 = X_3 = 0 \\
&\overline{q} = u_1 = 0 \text{ on plane } X_1 = 0 \\
&\overline{q} = u_2 = 0 \text{ on plane } X_2 = 0 \\
&\overline{q} = \overline{q}\,(T)\,,\ \dot{u}_3 = 0 \text{ on plane } X_3 = 0 \\
&\overline{q} = 0,\ \dot{u}_1 = \overline{u}\,(t) \text{ on plane } X_1 = L_0 \\
&\overline{q} = 0,\ \dot{u}_2 = \text{given by planar constrain on plane } X_2 = L_0 \\
&\overline{q} = \overline{q}\,(T)\,,\ \dot{u}_3\text{given by planar constrain on plane } X_3 = t_0
\end{aligned} \tag{4.147}$$

where the planar constraint is calculated such that surfaces $X_2 = L_0$ and $X_3 = t_0$ remain planar, without any net force applied to the plane.

Fig. 4.8(d) shows the applied velocity boundary condition $\overline{u}\,(t)$. This condition is an interrupted velocity profile with a maximum velocity of $60\,\mathrm{nm\,s^{-1}}$, resulting in a maximum nominal strain-rate of $8 \times 10^{-4}\,\mathrm{s^{-1}}$. Velocity pulses are composed of a 2.5 s ramp function, 8.5 s at a constant velocity, and a 2.5 s ramp down, which are separated by 10 s pauses to simulate the experimental conditions during the HEXRD test. These pauses must be included due to their potential implications on temperature evolution and the resultant mechanical response. Overall, each pulse results in 0.88% strain, which matches the average strain per pulse found experimentally after compliance correction. The FE model is deformed until a final bulk true strain of approximately 15% is achieved in the model; the simulation time is 460 s to achieve the final bulk true strain.

The initial temperature was assumed to be 293 K and the heat flux $\overline{q}\,(T)$ was derived to obtain the same average internal energy density evolution in the RVE as in a hypothetical full specimen. The average internal energy density evolution for the bulk sample and RVE is given by

$$\frac{1}{V_{samp}} \int_{V_{samp}} \rho_0 \dot{e}\ \mathrm{d}V = \frac{1}{V_{samp}} \int_{V_{samp}} \rho_0 r + \mathbf{S} : \dot{\mathbf{E}}\ \mathrm{d}V - \frac{1}{V_{samp}} \oint_{S_{samp}} \mathbf{q} \cdot \mathbf{n}\ \mathrm{d}A \tag{4.148}$$

$$\frac{1}{V_{RVE}} \int_{V_{RVE}} \rho_0 \dot{e}\ \mathrm{d}V = \frac{1}{V_{RVE}} \int_{V_{RVE}} \rho_0 r + \mathbf{S} : \dot{\mathbf{E}}\ \mathrm{d}V - \frac{1}{V_{samp}} \oint_{S_{RVE}} \mathbf{q} \cdot \mathbf{n}\ \mathrm{d}A \tag{4.149}$$

Given that the RVE should be representative of the bulk behaviour, this implies that the

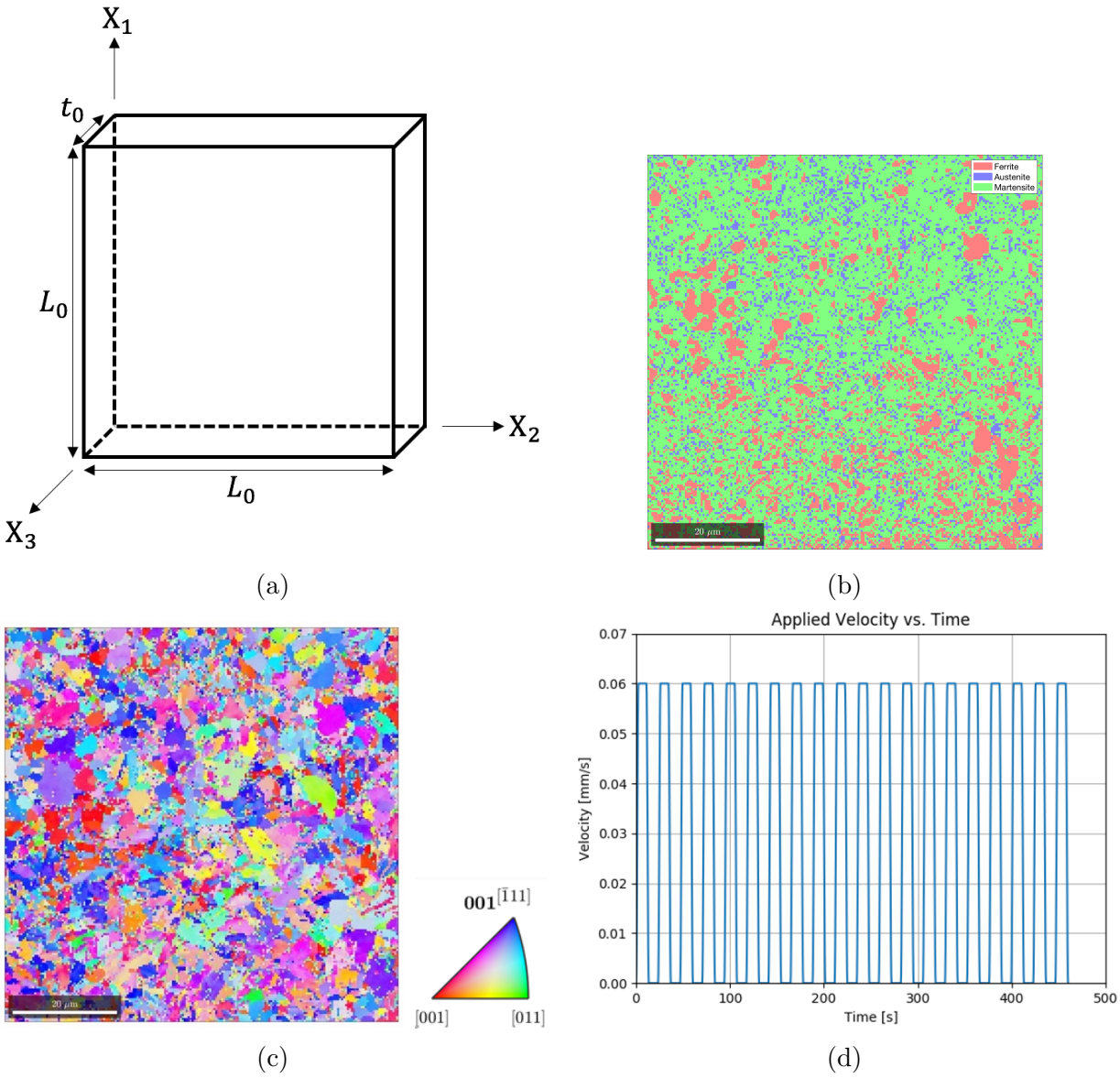

Fig. 4.8: (a) Schematic of FE boundary conditions, (b) assigned FE phase, (c) assigned FE orientation and (d) applied velocity profile.

internal energy of the bulk sample and the RVE are equal, such that

$$\frac{1}{V_{samp}} \int_{V_{samp}} \rho_0 \dot{e} \, \mathrm{d}V = \frac{1}{V_{RVE}} \int_{V_{RVE}} \rho_0 \dot{e} \, \mathrm{d}V \tag{4.150}$$

$$\frac{1}{V_{samp}} \int_{V_{samp}} \rho_0 r + \mathbf{S} : \dot{\mathbf{E}} \, \mathrm{d}V = \frac{1}{V_{RVE}} \int_{V_{RVE}} \rho_0 r + \mathbf{S} : \dot{\mathbf{E}} \, \mathrm{d}V \tag{4.151}$$

These together with (4.148) and (4.149) implies that

$$\frac{1}{V_{samp}} \oint_{S_{samp}} \mathbf{q} \cdot \mathbf{n} \, \mathrm{d}A = \frac{1}{V_{RVE}} \oint_{S_{RVE}} \mathbf{q} \cdot \mathbf{n} \, \mathrm{d}A \tag{4.152}$$

Assuming a wide prismatic sample and an RVE with areas of A_{samp} and A_{RVE}, and thicknesses of t_{samp} and t_{RVE}, the heat flux into the volume is given by

$$\oint_{S_{samp}} \mathbf{q} \cdot \mathbf{n} \, \mathrm{d}A = 2 \int_{A_{samp}} \widehat{q}\,(T) \; \mathrm{d}A \tag{4.153}$$

$$\oint_{S_{RVE}} \mathbf{q} \cdot \mathbf{n} \, \mathrm{d}A = 2 \int_{A_{RVE}} \overline{q}\,(T) \; \mathrm{d}A \tag{4.154}$$

where $\widehat{q}\,(T)$ and $\overline{q}\,(T)$ are the average specific heat fluxes on the sample and RVE normal surfaces, respectively. Substituting Eqs. (4.153) and (4.154) into (4.152) gives

$$\frac{1}{A_{samp} t_{samp}} \int_{A_{samp}} \widehat{q}\,(T) \; \mathrm{d}A = \frac{1}{A_{RVE} t_{RVE}} \int_{A_{RVE}} \overline{q}\,(T) \; \mathrm{d}A \tag{4.155}$$

For this to be true for any sample and RVE dimensions, the following relationship must hold:

$$\frac{\widehat{q}\,(T)}{t_{samp}} = \frac{\overline{q}\,(T)}{t_{RVE}} \tag{4.156}$$

Following Connolly et al. [10], the sample heat flux should include convection with a coefficient of $15\,\mathrm{W\,m^{-2}\,K^{-1}}$ and radiation with an emissivity coefficient of 0.8. Therefore, given the full thickness of 1.14 mm and the RVE thickness of 0.25 µm, the heat flux convection coefficient and emissivity coefficient used in the RVE model is $3.28\,\mathrm{mW\,m^{-2}\,K^{-1}}$ and 1.7516×10^{-4} respectively.

4.4.1 LS-Dyna Implementation Overview

This section provides an overview of the incremental numerical formulation into LS-Dyna Implicit. The LS-Dyna Implicit coupled thermo-mechanical FEM solver used in this work uses sequentially coupled implicit linear thermal and implicit non-linear mechanical solvers. Fig. 4.9 shows a flowchart outlining this algorithm. To implement the numerical model, both thermal and mechanical subroutines must be provided. The thermal user-defined material in LS-Dyna must define the:

(1) Heat generation rate

(2) Specific heat capacity

The heat generation rate Q is derived from Eq. (4.67) using

$$Q = \rho_0 r - \mathbf{M}_{e(A)} : \mathbf{D}_e + \sum_{\alpha=1}^{N_p} M_{p(A)}^{(\alpha)} \dot{\gamma}^{(\alpha)} + \sum_{\alpha=1}^{N_{tr}} M_{tr}^{(\alpha)} \dot{\xi}^{(\alpha)} \tag{4.157}$$

To calculate the increment in material properties, the kinematic and stress equation must be presented in incremental form. The incremental kinematic equation are given by

$$\mathbf{L}_{(n+1)} = \frac{\Delta \mathbf{F}}{\Delta t} \mathbf{F}_{(n)}^{-1} \tag{4.158}$$

$$\mathbf{D}_{(n+1)} = \frac{\mathbf{L}_{(n+1)} + \mathbf{L}_{(n+1)}^T}{2} \tag{4.159}$$

$$\mathbf{\Omega}_{(n+1)} = \frac{\mathbf{L}_{(n+1)} - \mathbf{L}_{(n+1)}^T}{2} \tag{4.160}$$

where subscript (n) and $(n+1)$ indicate variables in timestep n and $n+1$, respectively. The incremental form of the stress update is given by

$$\widetilde{\boldsymbol{\tau}}_{(n+1)} = \boldsymbol{\tau}_{(n)} + \boldsymbol{\tau}_{(n)} \mathbf{\Omega}_{(n+1)} \Delta t - \mathbf{\Omega}_{(n+1)} \boldsymbol{\tau}_{(n)} \Delta t \tag{4.161}$$

$$\boldsymbol{\tau}_{(n+1)} = \widetilde{\boldsymbol{\tau}}_{(n+1)} + \overline{\mathbb{C}}_{(n)} : \mathbf{D}_{(n+1)} \Delta t - \dot{\overline{\boldsymbol{\sigma}}}_{(n)} \Delta t \tag{4.162}$$

The increments in plastic slip and transformation are calculated using Eq. (4.142). These are then used to update the total slip and absolute slip on each slip system and the transformed volume fractions using

$$\gamma^{(\alpha)}_{(n+1)} = \gamma^{(\alpha)}_{(n+1)} + \Delta\gamma^{(\alpha)} \tag{4.163}$$

$$\xi^{(\alpha)}_{(n+1)} = \xi^{(\alpha)}_{(n+1)} + \Delta\xi^{(\alpha)} \tag{4.164}$$

$$\gamma_{a(n+1)} = \gamma_{a(n)} + \sum_{\alpha=1}^{N_p} \left|\Delta\xi^{(\alpha)}\right| \tag{4.165}$$

$$\xi^{(0)}_{(n+1)} = \xi^{(0)}_{(n+1)} - \sum_{\alpha=1}^{N_{tr}} \Delta\xi^{(\alpha)} \tag{4.166}$$

The incremental update of the critical plastic slip and TRIP driving forces is given by

$$g^{(\alpha)}_{p(n+1)} = g^{(\alpha)}_{p(n)} + \sum_{\beta=1}^{N_p} q^{(\alpha\beta)}_{p} h_p \Delta\gamma^{(\beta)} \tag{4.167}$$

$$g^{(\alpha)}_{tr(n+1)} = g^{(\alpha)}_{tr(n)} + \sum_{\beta=1}^{N_{tr}} q^{(\alpha\beta)}_{tr} h_{tr(n)} \Delta\xi^{(\beta)} \tag{4.168}$$

The incremental update of the plastic slip systems and the TRIP systems are given by

$$\begin{aligned}
\mathbf{s}^{(\alpha)}_{e(n+1)} &= \left[\mathbf{I} + \Delta\mathbf{F}\mathbf{F}^{-1}_{(n)} - \sum_{\alpha=1}^{N_p} \mathbf{P}^{(\alpha)}_{p} \Delta\gamma^{(\alpha)} - \sum_{\alpha=1}^{N_{tr}} \mathbf{P}^{(\alpha)}_{tr} \Delta\xi^{(\alpha)}\right] \mathbf{s}^{(\alpha)}_{e(n)} \\
\mathbf{m}^{(\alpha)}_{e(n+1)} &= \mathbf{m}^{(\alpha)}_{e(n)} \left[\mathbf{I} + \Delta\mathbf{F}\mathbf{F}^{-1}_{(n)} - \sum_{\alpha=1}^{N_p} \mathbf{P}^{(\alpha)}_{p} \Delta\gamma^{(\alpha)} - \sum_{\alpha=1}^{N_{tr}} \mathbf{P}^{(\alpha)}_{tr} \Delta\xi^{(\alpha)}\right]^{-1}
\end{aligned} \tag{4.169}$$

$$\begin{aligned}
\mathbf{b}^{(\alpha)}_{e(n+1)} &= \left[\mathbf{I} + \Delta\mathbf{F}\mathbf{F}^{-1}_{(n)} - \sum_{\alpha=1}^{N_p} \mathbf{P}^{(\alpha)}_{p} \Delta\gamma^{(\alpha)} - \sum_{\alpha=1}^{N_{tr}} \mathbf{P}^{(\alpha)}_{tr} \Delta\xi^{(\alpha)}\right] \mathbf{b}^{(\alpha)}_{e(n)} \\
\mathbf{d}^{(\alpha)}_{e(n+1)} &= \mathbf{d}^{(\alpha)}_{e(n)} \left[\mathbf{I} + \Delta\mathbf{F}\mathbf{F}^{-1}_{(n)} - \sum_{\alpha=1}^{N_p} \mathbf{P}^{(\alpha)}_{p} \Delta\gamma^{(\alpha)} - \sum_{\alpha=1}^{N_{tr}} \mathbf{P}^{(\alpha)}_{tr} \Delta\xi^{(\alpha)}\right]^{-1}
\end{aligned} \tag{4.170}$$

Pseudocode for this algorithm, including the implementation of the thermal and mechanical subroutines, is presented in Alg. 1

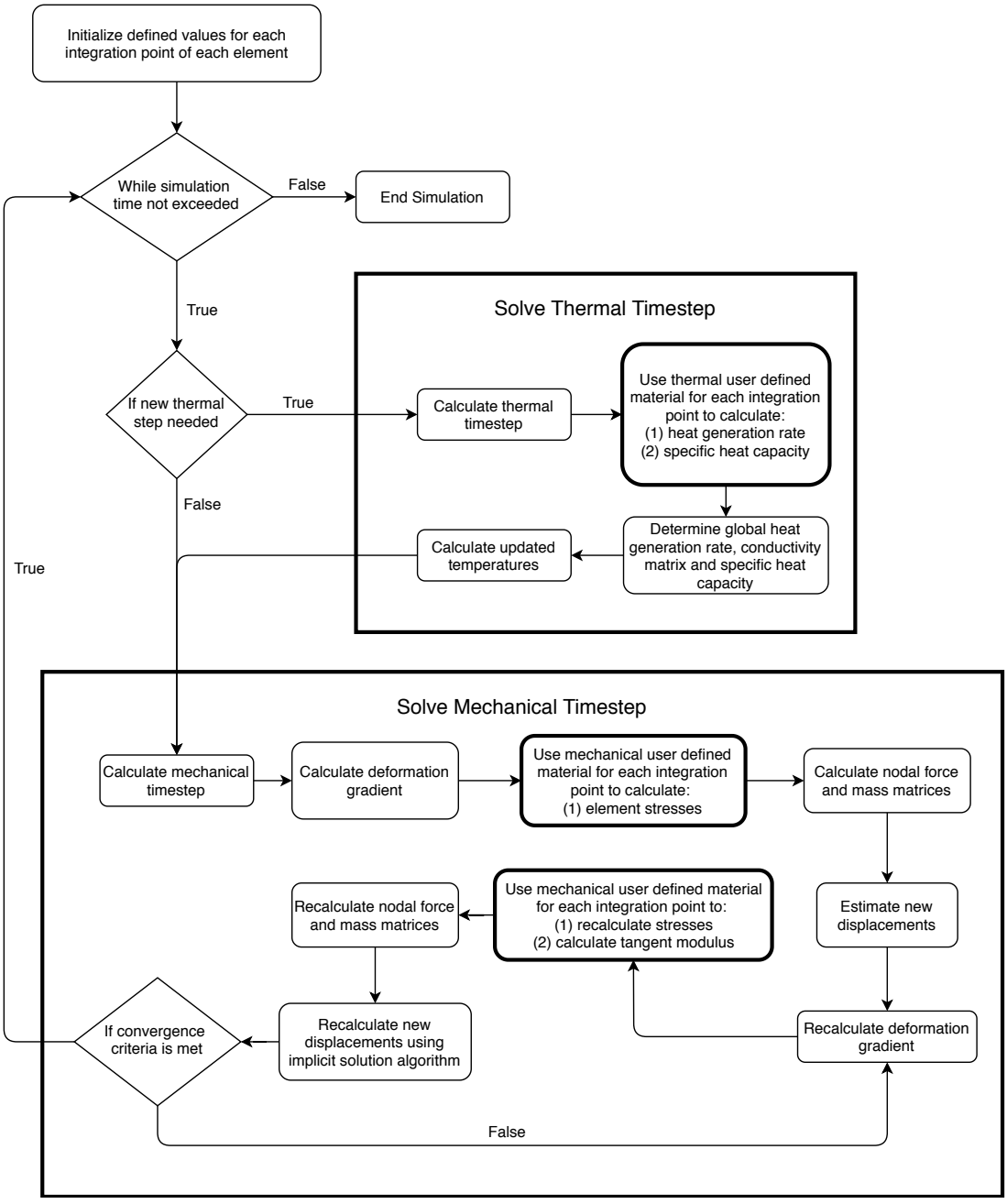

Fig. 4.9: LS-Dyna solver flowchart.

Algorithm 1 Constitutive model integration.

procedure THERMAL SUBROUTINE ▷ Calculate heat generation and heat capacity
  $Q \leftarrow$ CALCULATE HEAT GENERATION() ▷ Use Eq. (4.157)
  $h_A(\boldsymbol{\xi}) \leftarrow$ CALCULATE HEAT CAPACITY() ▷ Use Eq. (4.46)
  return $Q,\ h_A(\boldsymbol{\xi})$
end procedure
procedure MECHANICAL SUBROUTINE
  $\mathbf{L}_{(n+1)},\ \mathbf{D}_{(n+1)},\ \boldsymbol{\Omega}_{(n+1)} \leftarrow$ KINEMATICS() ▷ Use Eqs. (4.158) to (4.160)
  $\widetilde{\boldsymbol{\tau}}_{(n+1)} \leftarrow$ JAUMANN() ▷ Use Eq. (4.161)
  $\mathbf{f}_{p(n)},\ \mathbf{f}_{tr(n)} \leftarrow$ DRIVING FORCES() ▷ Use Eqs. (4.65) and (4.66)
  $\dot{\boldsymbol{\gamma}}_{(n)},\ \dot{\boldsymbol{\xi}}_{(n)} \leftarrow$ RATES() ▷ Use Eqs. (4.84) and (4.86)
  $y_{c1},\ y_{c2},\ \mathbf{Y}_p,\ \mathbf{Y}_{tr} \leftarrow$ RATE TANGENT() ▷ Use Eqs. (4.124) to (4.142)
  $\Delta\boldsymbol{\gamma},\ \Delta\boldsymbol{\xi} \leftarrow$ INCREMENTS() ▷ Use Eq. (4.142)
  $\boldsymbol{\tau}_{(n+1)},\ \overline{\mathbb{C}} \leftarrow$ STRESS() ▷ Use Eqs. (4.143) to (4.145)
  $\boldsymbol{\gamma}_{(n+1)},\ \gamma_{a(n+1)},\ \boldsymbol{\xi}_{(n+1)} \leftarrow$ UPDATE KINETICS() ▷ Use Eqs. (4.163) to (4.166)
  $\mathbf{g}_{p(n+1)},\ \mathbf{g}_{tr(n+1)} \leftarrow$ UPDATE CRITICAL FORCE() ▷ Use Eqs. (4.166) and (4.168)
  $\mathbf{s}_{e(n+1)},\ \mathbf{m}_{e(n+1)} \leftarrow$ UPDATE SLIP SYSTEMS() ▷ Use Eq. (4.169)
  $\mathbf{b}_{e(n+1)},\ \mathbf{d}_{e(n+1)} \leftarrow$ UPDATE TRIP SYSTEMS() ▷ Use Eq. (4.170)
  return $\boldsymbol{\tau}_{(n+1)},\ \overline{\mathbb{C}},\ \boldsymbol{\gamma}_{(n+1)},\ \gamma_{a(n+1)},\ \boldsymbol{\xi}_{(n+1)},\ \mathbf{g}_{p(n+1)}$
  return $\mathbf{g}_{tr(n+1)},\ \mathbf{s}_{e(n+1)},\ \mathbf{m}_{e(n+1)},\ \mathbf{b}_{e(n+1)},\ \mathbf{d}_{e(n+1)}$
end procedure

4.5 Results and Discussion

In this section, the experimental RA and stress evolution data are used in conjunction with physically derived parameter constraints and the described FEM model to calibrate the constitutive parameters. The local deformation behaviour of the calibrated model and the orientation dependence of transformation are analyzed. Elevated temperature studies are conducted to explore the effect of temperature on bulk stress and transformation responses and the local deformation response.

4.5.1 Model Calibration and Analysis

The material coefficients used for the crystal plasticity model of QP1180 were obtained by the method of inverse analysis where the FE model was simultaneously calibrated to the

experimental stress-strain and austenite evolution responses (Fig. 4.1). It is assumed that the calibrated model should have the same ratio of transformed martensite to initial RA content as the experimental data. The model is calibrated to the normalized RA fraction to ensure this criterion is satisfied as defined by

$$\text{Normalized RA Fraction} = \frac{RA\,(t)}{RA\,(0)} = \frac{\xi_i^{(0)Exp}}{\xi_1^{(0)Exp}} \tag{4.171}$$

Several model parameters were obtained from the literature to reduce the burden of the calibration process. In this section, retained austenite, ferrite, tempered martensite, and transformed martensite are denoted by the subscripts A, F, M, and S, respectively.

4.5.1.1 Parameters Obtained from Literature

Table 4.3 presents the coefficients taken from literature, which are used to model the QP1180 sheet metal alloy. The elasticity, specific heat capacity, thermal expansion, surface energy, and latent heat of transformation coefficients are collected from Yadegari et al. [109]. The lattice parameters of the transformed martensite sub-variants, a^M, c^M, and the parent RA phase, a^A, in Eq. (4.73) are dependent on the carbon concentration, p_c, of the RA phase. Similar QP steels in the literature have observed a carbon content of approximately 1.4wt% in the blocky RA [65, 149]. Accordingly, this model assumes that the QP1180 sheet alloy study has a carbon content of $p_c = 1.4$wt%. These lattice parameters, in Å, are empirically related to the RA carbon concentration, in wt%, through Turteltaub and Suiker [118]

$$c^M = 2.861 + 0.116(p_c) \tag{4.172}$$

$$c^M = 2.861 - 0.012(p_c) \tag{4.173}$$

$$c^M = 2.861 + 0.044(p_c) \tag{4.174}$$

4.5.1.2 Parameters Calibrated from Experiments

The remaining model parameters are obtained by minimizing an error function comprised of the stress-strain and austenite evolution response from the FEM model and the experimental measurements. The mean squared error, MSE, function that is used as the error function is defined as

Table 4.3: Model parameters obtained from literature.

Elastic Moduli [GPa]	$\kappa_1^A = 286.8,\ \kappa_2^A = 166.4,\ \kappa_3^A = 145$ $\kappa_1^S = 372.4,\ \kappa_2^S = 345,\ \kappa_3^S = 191,\ \kappa_4^S = 508.5,\ \kappa_5^S = 201.9,\ \kappa_6^S = 229.5$ $\kappa_1^F = 233.5,\ \kappa_2^F = 135.5,\ \kappa_3^F = 118$ $\kappa_1^M = 233.5,\ \kappa_2^M = 135.5,\ \kappa_3^M = 118$
Defect Energy Parameters	$\mu_A^{(0)} = 67.5\,\text{GPa},\ \mu_A^{(\alpha)} = 98.4\,\text{GPa},\ c_A = 0.5$ $\mu_F^{(0)} = 55\,\text{GPa},\ c_A = 0.5$ $\mu_M^{(0)} = 98.4\,\text{GPa},\ c_A = 0.5$
Thermal Parameters	$h^{(0)} = 519\,\text{mJ}\,\text{g}^{-1}\,\text{K}^{-1},\ h^{(\alpha)} = h^M = h^F = 450\,\text{mJ}\,\text{g}^{-1}\,\text{K}^{-1}$ $A_A^{(0)} = A_F = 2.1 \times 10^{-5}\,\text{K}^{-1},\ A_A^{(\alpha)} = A_M = 1.7 \times 10^{-5}\,\text{K}^{-1}$ $\rho = 7.8 \times 10^{-3}\,\text{g}\,\text{mm}^{-3}$
Transformation Parameters	$\chi = 2 \times 10^{-4}\,\text{mJ}\,\text{mm}^{-2},\ \ell_0 = 5 \times 10^{-5}\,\text{mm},\ \lambda^{(\alpha)} = -50\,500\,\text{mJ}\,\text{g}^{-1}$
Lattice Parameters	$c^M = 3.0234\,\text{Å},\ c^M = 2.8442\,\text{Å},\ c^M = 2.9226\,\text{Å}$

$$\text{MSE} = \sum_{i=1}^{n} \left(\frac{\frac{1}{E}\sum_{e=1}^{E} \sigma_{i,e}^{FEM} - \sigma_i^{Exp}}{\sigma_i^{Exp}} \right)^2 + \left(\frac{\frac{1}{E}\sum_{e=1}^{E} \xi i, e^{(0)FEM}}{\frac{1}{E}\sum_{e=1}^{E} \xi 1, e^{(0)FEM}} - \frac{\xi_i^{(0)Exp}}{\xi_1^{(0)Exp}} \right)^2 \tag{4.175}$$

where n is the number of experimental measurements, and E is the number of elements in the FE model. The remaining model parameters were manually varied until the error function reached an acceptable tolerance. Table 4.4 presents the calibrated coefficients for the QP1180 sheet metal alloy. During calibration, it was determined that a constant plastic slip to transformation coupling coefficient (h_c) was sufficient, and thus, h_c^0 and h_c^s are identical. The following approach was adopted for the calibration process; Two constraints were imposed during the calibration process to yield physically relevant parameters: A thermal constraint was imposed to ensure that thermally driven transformation does not occur above the martensite start temperature, M_s. The martensite start temperature is empirically related to the carbon concentration, p_c, in the alloy through [118, 150]

$$M_s = 768 - 355(p_c) = 271\,\text{K at } p_c = 1.4\% \tag{4.176}$$

For transformation to activate at the $\theta = M_s$, the driving force and critical activation force must be approximately equal, $g_{tr}^0 \approx f_{tr}^{(\alpha)}$, when $\boldsymbol{\tau} = \boldsymbol{\gamma} = \boldsymbol{\xi} = \mathbf{0}$ (note that in this condition, $f_{tr}^{(\alpha)}$ is equal for all martensite variants α). From Eq. (4.66), this criterion yields

$$\begin{aligned} g_{tr}^0 \approx f_{tr}^{(\alpha)} = &- \frac{\chi}{\ell_0} + \rho_0 \frac{\lambda_T^{(\alpha)}}{\theta_T} \left[M_s - \theta_T\right] - \omega_A \frac{\sum_{\beta=1}^{N_p} q_c^{(\alpha\beta)} h_c}{c_A \mu_A' \left(\boldsymbol{\xi}\right) N_p} \mu_A' \left(\boldsymbol{\xi}\right) \beta_A \\ &+ \rho_0 \left[h^{(0)} - h^{(\alpha)}\right] \left[M_s - \theta_T - \ln\left(\frac{M_s}{\theta_T}\right) M_s\right] \\ &+ \frac{\omega_A}{2} \left[J_\theta^{(0)} \mu^{(0)} - J_\theta^{(\alpha)} \mu^{(\alpha)}\right] \beta_A^2 \end{aligned} \tag{4.177}$$

Next, an additional constraint was imposed to ensure that the Taylor-Quinney coefficient (ζ) varies between approximately 0.80 and 1.00 without the presence of transformation [79]. In the absence of martensitic transformation, the Taylor-Quinney coefficient is defined by

$$\zeta = \frac{\int_V \frac{\dot{Q}_p}{\dot{W}_p} \, \mathrm{d}V}{V} = \frac{\int_V \frac{\sum_{\alpha=1}^{N_p} M_{p(A)}^{(\alpha)} \dot{\gamma}^{(\alpha)}}{\sum_{\alpha=1}^{N_p} \boldsymbol{\tau} : \mathbf{P}_p^{(\alpha)} \dot{\gamma}^{(\alpha)}} \, \mathrm{d}V}{V} \tag{4.178}$$

where V is the volume of the FE model. This constraint is achieved by performing a simulation where transformation was deactivated. This constraint places limits on the dislocation energy coefficients ω_A, ω_F and ω_M and is enforced separately for each phase to ensure that the behaviour of each phase is physical.

Table 4.4: Calibrated coefficients for QP1180 sheet metal alloy.

Hardening [MPa]	$g_{p(A)}^0 = 265$, $g_{p(A)}^s = 350$, $h_{p(A)}^0 = 3720$, $h_{p(A)}^s = 357$ $g_{p(F)}^0 = 216$, $g_{p(F)}^s = 254$, $h_{p(F)}^0 = 52$, $h_{p(F)}^s = 10.5$ $g_{p(M)}^0 = 523$, $g_{p(M)}^s = 550.5$, $h_{p(M)}^0 = 118$, $h_{p(M)}^s = 15$ $g_{tr}^0 = 90$, $g_{tr}^s = 91$, $h_{tr}^0 = 930$, $h_{tr}^s = 3.5$, $h_c^0 = h_c^s = 1163$
Defect Energy	$\omega_A = 0.5$, $\omega_F = 18$, $\omega_M = 16$
Kinetics Law	$\dot{a}_{p(A)} = \dot{a}_{p(F)} = \dot{a}_{p(M)} = \dot{a}_{tr} = 1 \times 10^{-3}\,\mathrm{s}^{-1}$ $m_{p(A)} = m_{p(F)} = m_{p(M)} = 0.02$, $m_{tr} = 0.05$, $\theta_T = 370\,\mathrm{K}$

4.5.1.3 Comparison Between Simulations and Experiments

Fig. 4.10(a) and Fig. 4.10(b) present the calibrated and experimental stress and normalized RA fraction vs. strain responses, while Fig. 4.10(c) presents the average temperature evolution for the bulk material. These comparisons are conducted as far as the experimental ultimate tensile stress because the RVE model assumes planar surfaces for all faces and is therefore unable to capture the substantial localized deformation beyond that point. The simulated response shows good agreement between experimental and calibrated stress-strain and normalized RAVF responses. The temperature evolution is non-monotonic, with heating and cooling occur during loading and when loading is interrupted, respectively. This forms a quasi-equilibrium wherein the amount of heating during loading is equal to the cooling during the paused phase. The impact of the thermal boundary conditions on thermal and mechanical response is analyzed in further detail in Section 4.5.2.

4.5.1.4 Analysis of Deformation Behaviour Under Uniaxial Tension

Fig. 4.11(a) and Fig. 4.11(b) show the local distribution of the equivalent (von Mises) stress and strain, respectively, in the final deformed configuration. In Fig. 4.11(a), the low strength ferrite is presented in blue, the medium strength tempered martensite is presented in green, and the RA elements containing high strength transformed martensite are presented red. This figure shows that the high carbon RA that transforms into martensite acts as embedded particles that strengthen the material during deformation. The morphology of the low-strength ferrite creates islands of low stress throughout the model. These high-strength RA particles combined with the soft ferritic islands result in significant shear banding in the ferrite phase. Fig. 4.12 summarizes the statistical distribution of the variability in martensite transformation using a box and whisker plot as a function of strain. The central line and dot of the box and whisker plots represent the median and mean normalized RA fraction. The limits of each box represent the 25^{th} and 75^{th} percentile data, and the endpoints of the whiskers represent the overall data range. The transformation rate varies significantly throughout the mesh of the specimen. Some elements transformed entirely within the first 4% bulk strain, while other elements transform less than 3% in 15% bulk strain. As measured by the interquartile range, the variance in the normalized RA fraction significantly increases as a function of strain, indicating a sustained variance in the transformation rate.

Fig. 4.13 shows the dependence of the RA fraction on crystal orientation at 5% strain increments during the simulation. A value of 1.0 indicates an element that is fully austenitic,

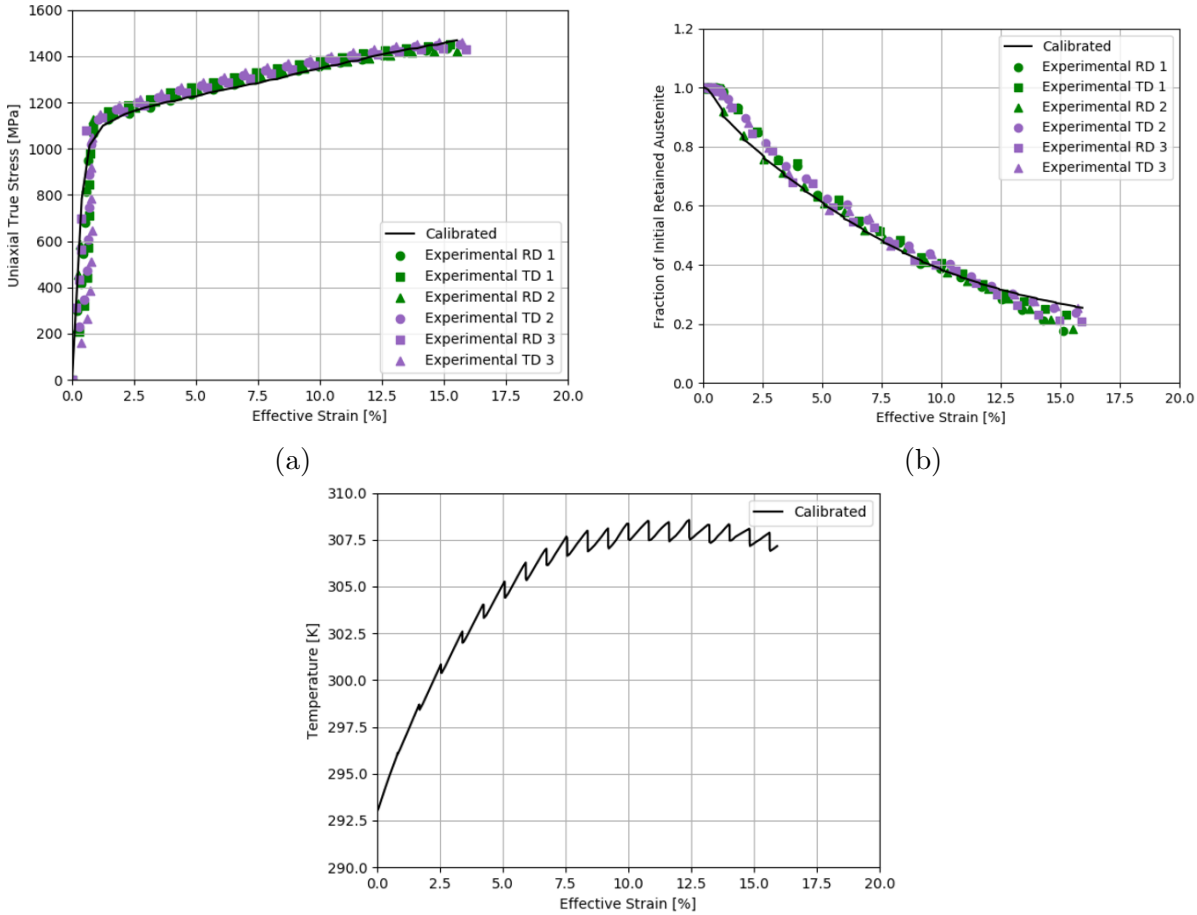

Fig. 4.10: (a) Stress vs. strain, (b) normalized RA fraction vs. strain and (c) temperature vs. effective strain.

while a value of 0.0 corresponds to a fully transformed martensite element. The (100) pole figure shows three high transformation bands, with transformation occurring readily when the (100) direction is aligned near the rolling direction or near the TD-ND plane. The (111) pole figure shows two high transformation bands when the (111) direction is aligned approximately halfway between the RD and the TD-ND plane. The (110) shows a less defined pattern, wherein there is slightly less transformation when the (110) direction is aligned with the RD or along the ND plane. The orientation effect appears to thoroughly explain

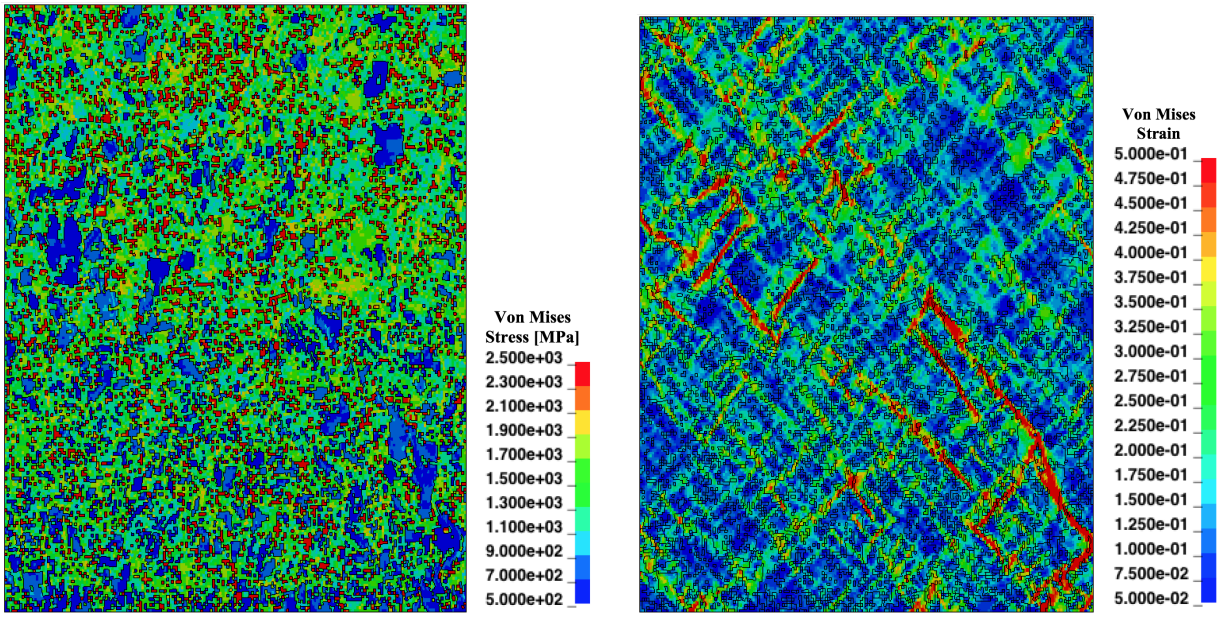

(a) (b)

Fig. 4.11: (a) Equivalent stress and (b) equivalent strain distribution in the final deformed configuration of QP1180 sheet metal alloy.

the transformation's variability, with clear band patterns forming in both the (100) and (111) pole figures. These results indicate preferential transformation near the ⟨100⟩ crystal direction, which is consistent with experimental observations of orientation dependence for several TRIP alloys [22, 151].

This orientation dependence is primarily a result of the favourability of the transformation of different orientations at constant equivalent stress, as measured by the maximum generalized TRIP Schmid factor

$$s_{tr} = \max\left(\frac{\boldsymbol{\tau} : \mathbf{P}_{tr}^{(\alpha)}}{\sigma_{vm}}\right) \tag{4.179}$$

where the Schmid factor is normalized by the von Mises equivalent stress, σ_{vm}. Fig. 4.14 shows the orientation dependence of the maximum generalized TRIP Schmid factor. This correlates directly with the orientation dependence of transformation, showing that orientation dependence of transformation is primarily driven by the transformation systems and is unrelated to the orientation dependence of the stress magnitude.

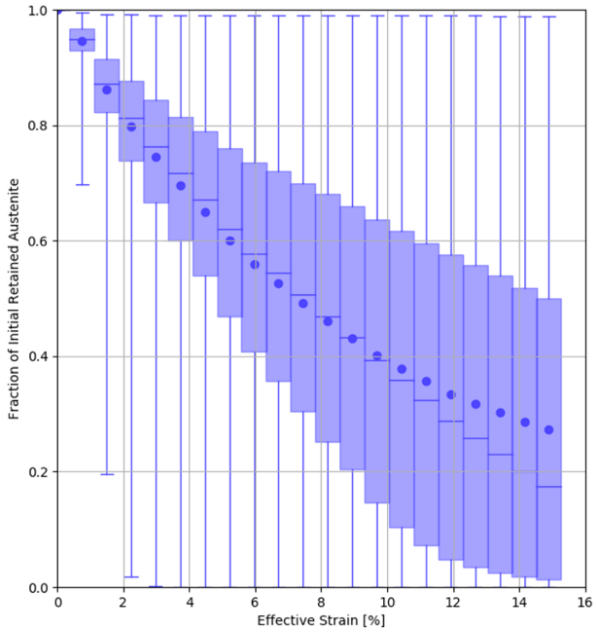

Fig. 4.12: Box and whisker plots of normalized RA fraction vs. strain.

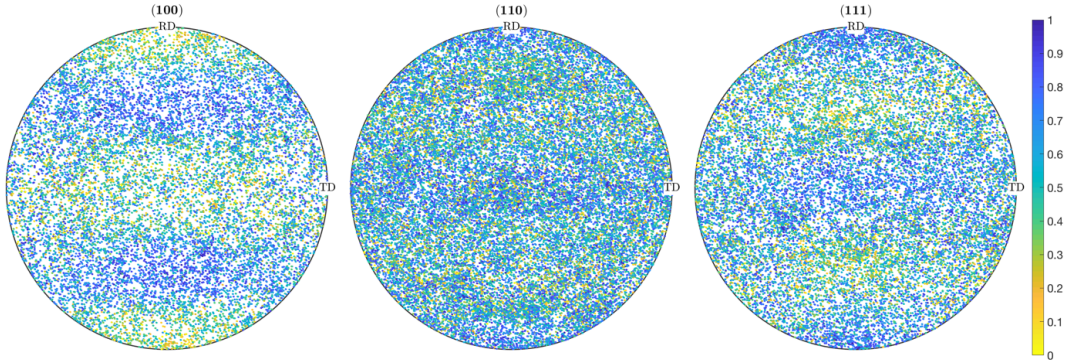

(a)

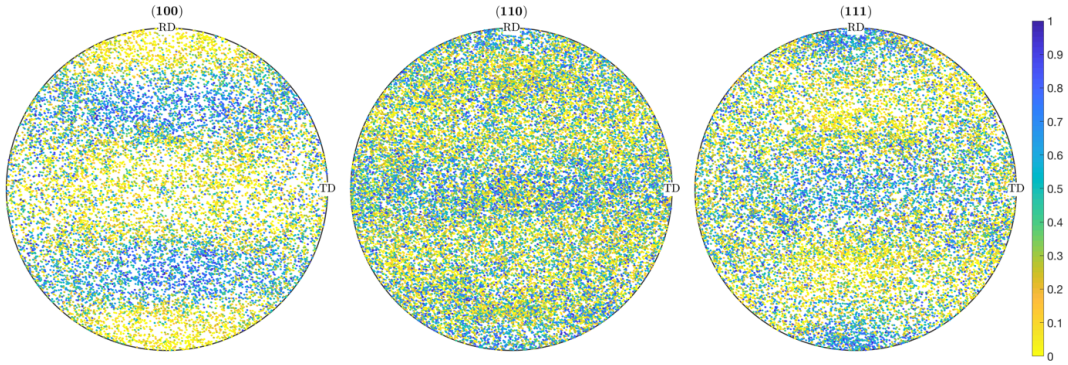

(b)

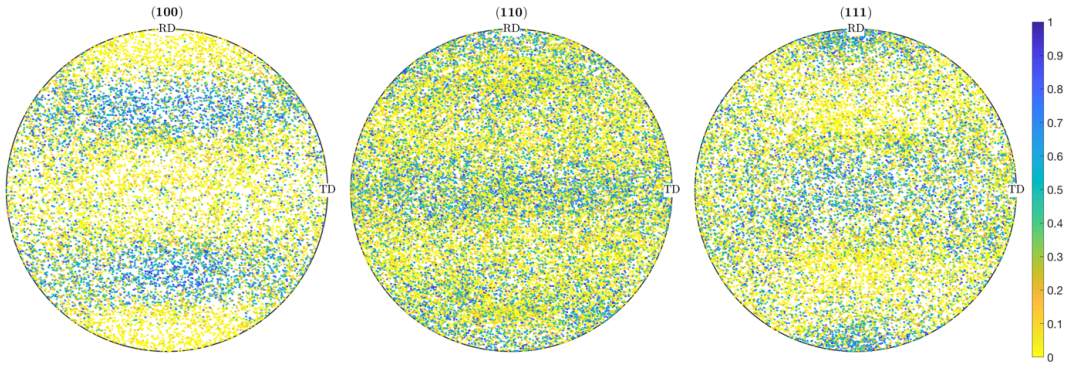

(c)

Fig. 4.13: Orientation dependence of RA fraction at (a) 5%, (b) 10% and (c) 15% strain.

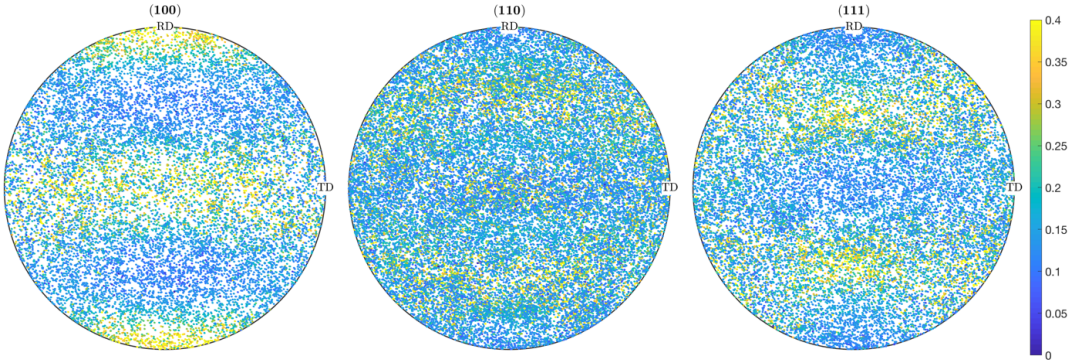

(a)

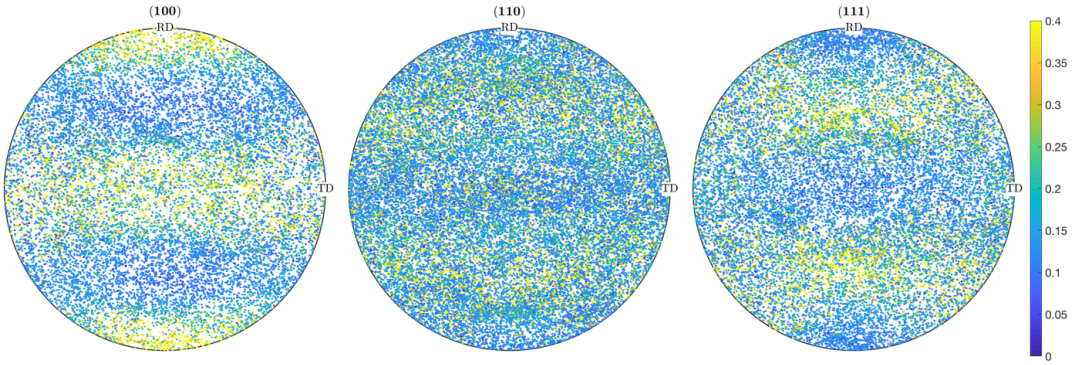

(b)

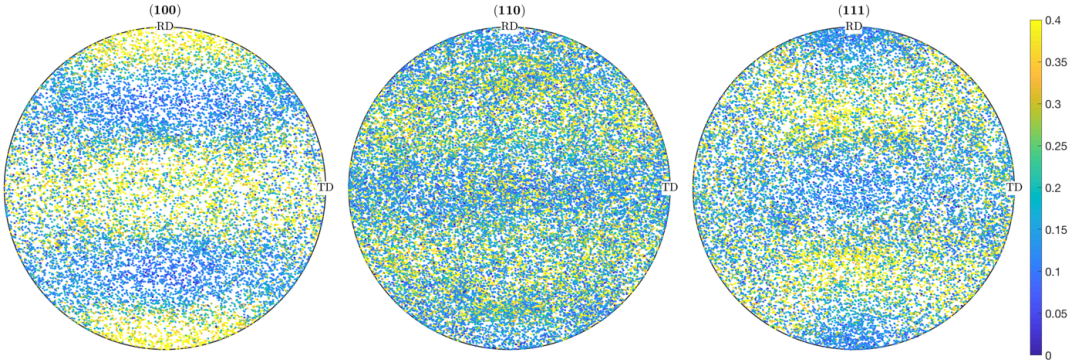

(c)

Fig. 4.14: Orientation dependence of the max generalized TRIP Schmid factor at (a) 5%, (b) 10% and (c) 15% strain.

4.5.2 Analysis of Thermal Boundary Conditions

Since martensitic transformation is known to be temperature-dependent [18, 53, 82], this study aims to determine the impact of thermal boundary conditions on thermo-mechanical behaviour predicted by the outlined RVE model. This section will also compare the influence of interrupted and non-interrupted conditions on the mechanical response. This is accomplished by simulating the calibrated model with a constant strain-rate and isothermal, adiabatic, and general thermal boundary conditions. The constant strain-rate condition is imposed by modifying the applied velocity from the interrupted condition to $\dot{u}_1 = L_0\dot{\varepsilon}\exp(\dot{\varepsilon}t)$ where $L_0 = 75\,\mu\text{m}$ is the sample length, $\dot{\varepsilon} = 8 \times 10^{-4}\,\text{s}^{-1}$ is the applied strain-rate, and t is time. Fig. 4.15 compares the bulk stress, RA, and temperature evolution for the adiabatic, general, and isothermal conditions compared to the calibrated model and experimental results. Fig. 4.16 shows the equivalent stress and strain distributions for the re-simulated isothermal, general, and adiabatic conditions at the end of the simulation. Major differences are observed between the temperature evolution profiles of the non-interrupted and interrupted (calibrated) general conditions, where the final temperature rise and retained RA predictions were 72% and 16.7% higher. This result is attributed to the pauses that allow for significant cooling, resulting in a much lower asymptotic temperature than in the general condition. Additionally, the predicted final RA value of the adiabatic and isothermal conditions varied by 14% and -43% from the non-interrupted general condition. This result means that neither isothermal nor adiabatic conditions accurately approximate the non-interrupted general condition. The final RA value of these conditions also differed by 33% and -33% from the interrupted general condition, meaning neither condition could accurately approximate the interrupted general condition, either. The differences between adiabatic, isothermal, and general conditions result from the noticeable differences in the predicted temperature evolution. The final temperatures of the adiabatic and isothermal conditions were 338 K and 293 K, compared to the interrupted and non-interrupted general final temperatures of 308 K and 319 K. Despite the significant variance in predicted temperature and RA evolution, the predicted stress evolution variance was relatively low. As such, the localization variation is minimal because the difference in either the stress and RA distribution in the microstructure is minimal. Yet, this study suggests two considerations for experimental design: first, the behaviour observed during interrupted testing, such as in-situ HEXRD tests, may not represent non-interrupted material behaviour. Next, the stress vs. strain response may be insufficient to verify that all mechanical behaviour is identical between the tests. To control this behaviour, it is recommended that possible discrepancies between interrupted and non-interrupted mechanical tests be investigated in greater detail.

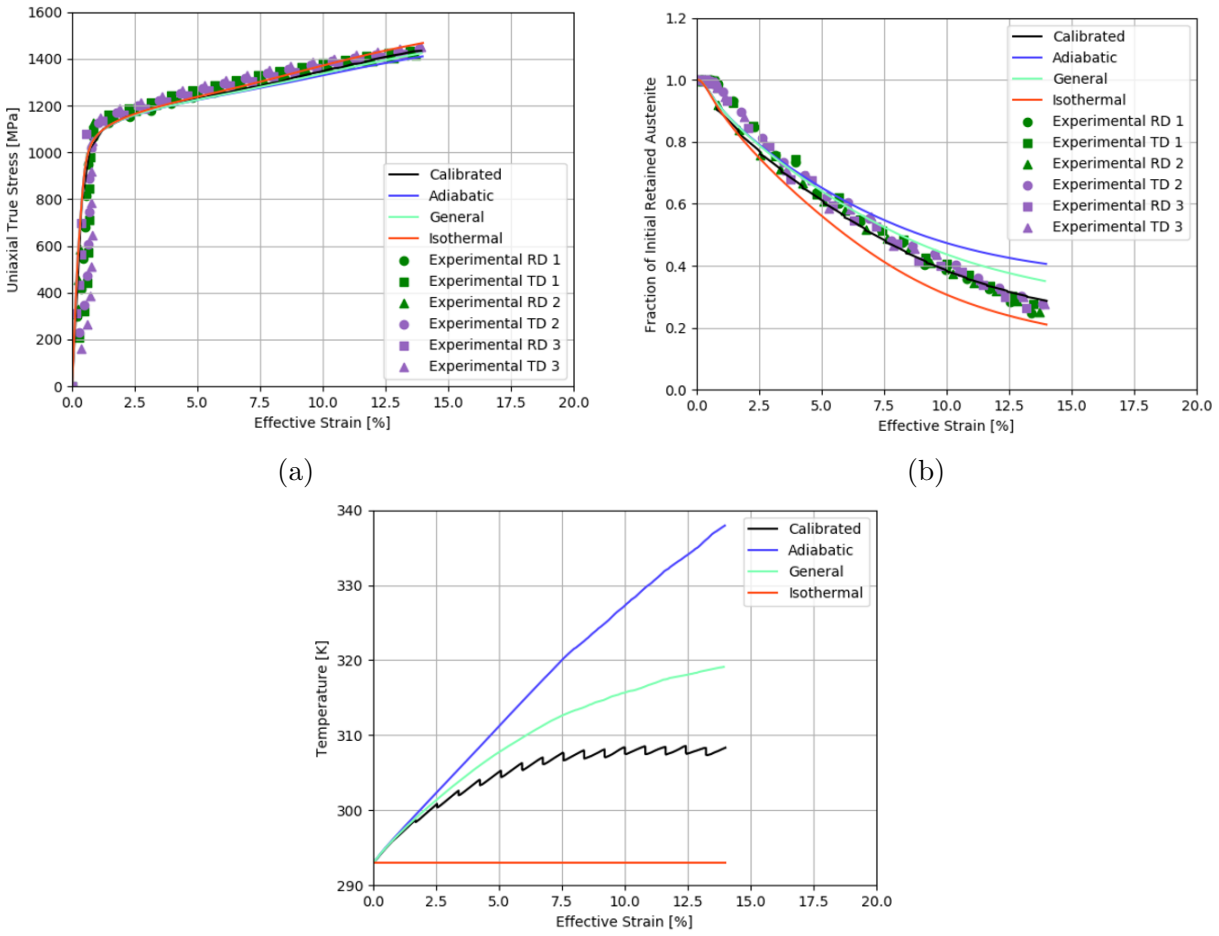

Fig. 4.15: (a) Calibrated stress vs. strain, (b) calibrated normalized RA fraction vs. strain and (c) temperature vs. effective strain.

4.5.3 Effect of Temperature on Deformation

Since martensitic transformation is known to have coupled temperature and strain-rate dependence [18, 21, 53, 82], the aim of this section is to analyze the effect of initial temperature, strain-rate and thermal boundary condition on predicted stress, RA and temperature evolution. The non-interrupted model that was presented in Section 4.5.2 is repeated for initial temperatures of 293 K, 330 K, 360 K and 390 K and strain-rates of $8 \times 10^{-4}\,\mathrm{s}^{-1}$, $8 \times 10^{-3}\,\mathrm{s}^{-1}$ and $8 \times 10^{-2}\,\mathrm{s}^{-1}$, each under adiabatic, isothermal, and general

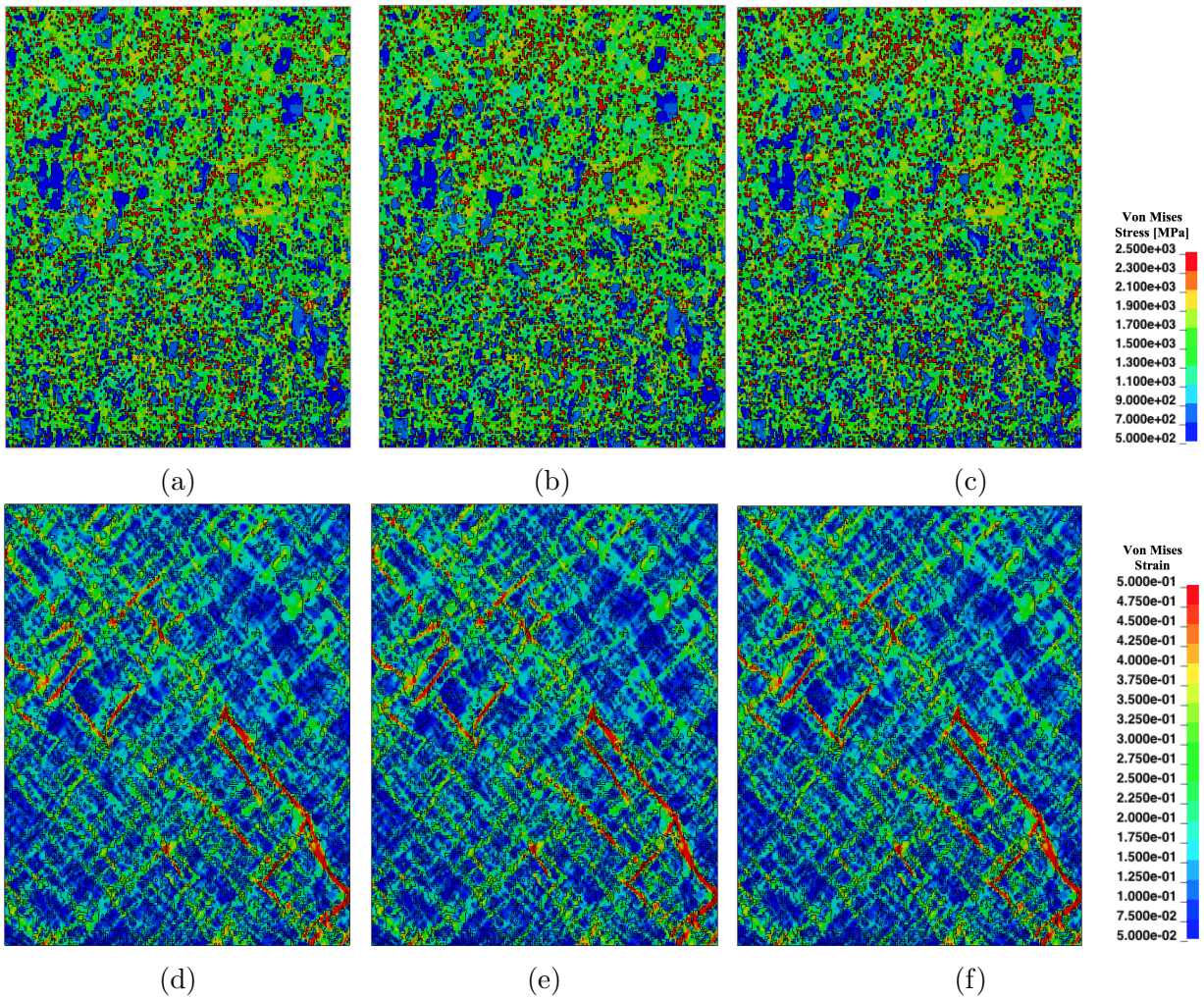

Fig. 4.16: (a) Adiabatic, (b) and (c) equivalent stress and (d) adiabatic, (e) general, and (f) isothermal equivalent strain distribution in the final deformed configuration of QP1180 sheet metal alloy.

thermal boundary conditions. Fig. 4.17 shows contour plots of the final RA fraction, stress and temperature rise vs. the initial temperature, and applied strain-rate. This shows that RA fraction increases with initial temperature and strain-rate. In the isothermal case, the RA fraction increased from 0.2 to 0.36 at room temperature as strain-rate increased from $8 \times 10^{-4}\,\mathrm{s}^{-1}$ to $8 \times 10^{-2}\,\mathrm{s}^{-1}$. For the non-interrupted general and adiabatic cases at room temperature, increasing strain-rate also leads to an increasing temperature rise, thereby

increasing the rate of suppression of transformation. This matches experimental observations for many steel alloys [9, 18]; however, recent experiment analysis demonstrates that some steels exhibit more complex strain-rate dependence of transformation [152]. For the non-interrupted general case, the RA fraction increases from 0.35 to 0.52 as strain-rate increased from $8 \times 10^{-4}\,\mathrm{s}^{-1}$ to $8 \times 10^{-2}\,\mathrm{s}^{-1}$. For the isothermal case, it increased from 0.4 to 0.6 under the same conditions. Finally, at a temperature of 410 K, the transformation was entirely suppressed in all cases. Since the increase in RA fraction with strain-rate occurs even in the isothermal case, this effect cannot solely be due to increases in temperature at elevated strain-rate. For all cases, stress increases with strain-rate and decreases with initial temperature. As the initial temperature increases, the final stress is reduced due to a reduction in hardening as transformation is suppressed. At the lowest strain-rate, this results in a decrease of 25%, 18%, and 16% in stress for the isothermal, non-interrupted general and adiabatic conditions. The reductions for the non-interrupted general and adiabatic conditions are less than the reduction for isothermal conditions because there is less transformation in those conditions, and therefore less transformation hardening to remove. Reduced hardening due to reduced transformation from increased temperature matches the majority of observed trends for TRIP steels [53, 79]. The exception is the QP3Mn studied by Poling [53], which did not exhibit significant bulk stress temperature dependence despite RA transformation depending significantly on temperature. This may indicate that, unlike other TRIP steels, the martensitic transformation may not significantly contribute to bulk hardening in QP3Mn steel. At room temperature, the stress increases by 6%, 6.3%, and 8% as strain-rate increases. This occurs due to the inherent rate dependence of the chosen crystal plasticity formulation. The increase of stress with strain-rate matches existing results for TRIP steels, but not for all QP steels [53, 78].

Significant temperature rise is observed in both non-isothermal conditions. A minimum temperature rise of 30 K was observed at a rate and temperature of $8 \times 10^{-4}\,\mathrm{s}^{-1}$ and 293 K for the non-interrupted general condition. A maximum temperature rise of 55 K was observed at a rate and temperature of $8 \times 10^{-2}\,\mathrm{s}^{-1}$ and 293 K. As the rate increases, the difference between the adiabatic and non-interrupted general conditions becomes substantially smaller. To understand when the difference is negligible, Fig. 4.18 shows the ratio of temperature rise in the non-interrupted general and adiabatic thermal boundary conditions. This shows that the adiabatic condition is a good approximation at or above $\dot{\varepsilon} = 8 \times 10^{-2}\,\mathrm{s}^{-1}$, but a poor approximation otherwise. This matches the results of Poling [53] that found that an adiabatic approximation was accurate at $\dot{\varepsilon} = 1 \times 10^{-1}\,\mathrm{s}^{-1}$.

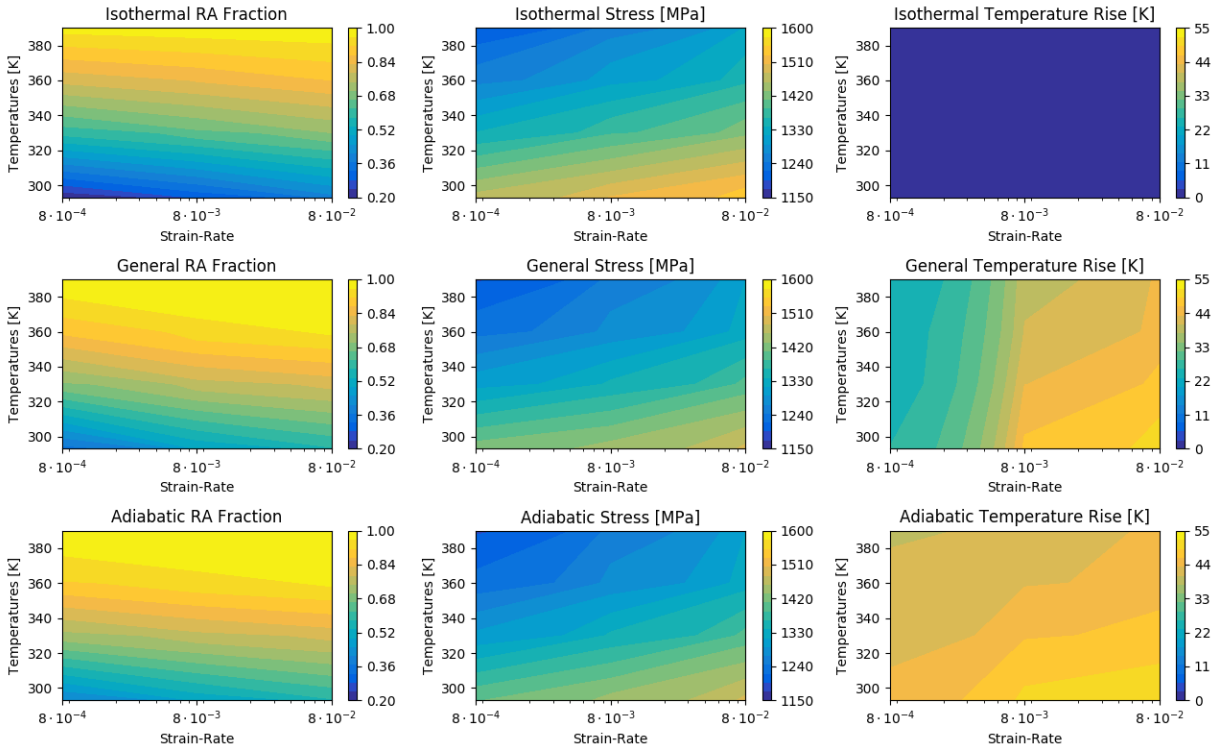

Fig. 4.17: Simulated final RA, von Mises effective stress and temperature rise as a function of strain-rate and initial temperature for isothermal, non-interrupted general and adiabatic conditions.

4.5.4 Model Comparison and Limitations

Table 4.5 shows a comparison between the previously existing works and the constitutive model derived in this chapter(referred to as Connolly Model #1). This shows that Connolly Model #1 is the first model to capture temperature and strain-rate sensitivity of transformation while also incorporating martensite variants and the orientation dependence of transformation. Furthermore, hardening due to local plasticity during accommodation of transformation strain has been implicitly accounted for using the transformation dependency term h_c of the critical plastic slip driving force evolution.

There are two main limitations to the constitutive model presented in Section 4.3. The first is the implicit assumption that transformed martensite is fully elastic. This is highlighted in Fig. 4.19, which presents the statistical distribution of the variability of σ_{11} using a box and whisker plot as a function of strain. The bounds are defined as in

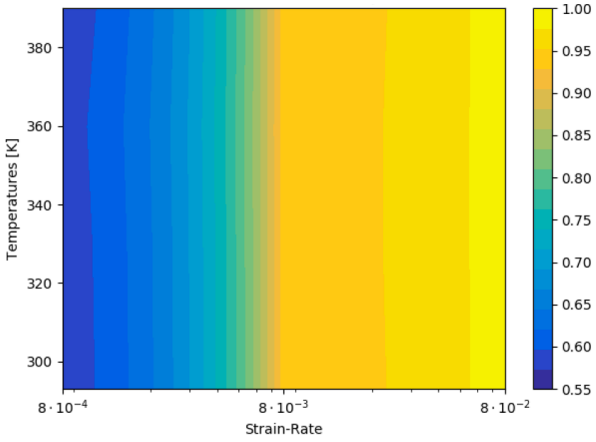

Fig. 4.18: Simulated ratio of non-interrupted general to adiabatic temperature rise as a function of temperature and strain-rate.

Fig. 4.12 with the limits of each box representing the 25$^{\text{th}}$ and 75$^{\text{th}}$ percentile data, and the endpoints of the whiskers representing the complete data range. The high maximum stress results from the transformed martensite's elastic deformation behaviour and results in stresses that are much higher than observed experimentally [15]. While the proposed constitutive model can accurately capture the bulk deformation properties, it is unlikely to accurately capture local deformation mechanics. Furthermore, the relatively small value of $m_{p(A)}$ in the plasticity kinetics results (Eq. (4.84)) in the RAVF having little impact when RAVF is significantly greater than zero. This can be explored conceptually using a hypothetical case where plastic slip rates are constant as the RAVF changes, which is approximately correct as long as the plastic stiffness is much lower than the elastic stiffness. In this hypothetical case, the stress ratio between two models that are identical except for different RAVF can be derived using

$$\frac{\sigma_t}{\sigma_u} \approx \frac{f^{(\alpha)}_{p(A)(t)}}{f^{(\alpha)}_{p(A)(u)}} = \frac{\left|\frac{\dot{\gamma}^{(\alpha)}}{a_0 \xi^{(0)}_t}\right|^{m_{p(A)}} g_{p(A)}}{\left|\frac{\dot{\gamma}^{(\alpha)}}{a_0 \xi^{(0)}_u}\right|^{m_{p(A)}} g_{p(A)}} = \left|\frac{\xi^{(0)}_u}{\xi^{(0)}_t}\right|^{m_{p(A)}} \tag{4.180}$$

where σ_t and $\xi^{(0)}_t$ represent the stress level and RAVF in a partially transformed case and σ_u and $\xi^{(0)}_u = 1$ represent the stress level and RAVF in the untransformed case, and where $f_{p(A)}$ is determined by rearranging Eq. (4.84). This equation shows that 50% transformation results in a 1.4% increase in stress and 90% transformation results in a 4.7% increase in

Table 4.5: Model comparison chart.

		Stringfellow et al. Model Lineage	Cherkaoui et al. Model Lineage	Lee et al. Model Lineage	Turteltaub et al. Model Lineage	Ma and Hartmaier Model Lineage	Park et al. Model Lineage	Connolly Model #1
Incorporated Material Behaviours	Transformation temperature sensitivity							
	Transformation strain-rate sensitivity							
	Transformation stress-state dependence							
	Incorporates martensite variants							
	Transformation orientation dependence							
	Hardening due to stress homogenization							
	Plasticity in transformed martensite							
	Hardening due to local plasticity when accommodating transformation strain							
	Temperature evolution							
	Stress-induced transformation							
	Strain-induced transformation							
	Thermodynamically consistent							
	Includes thermal strain							

Aspect present in model

Aspect partially present in model

Aspect not present in model

stress. This stress increase is much lower than expected in practice. For example, Lai et al. [153] performed experiments to study the effect of martensite volume fraction on quenched and tempered (QT) DP steel a 15% stress increase for 11% martensite and a 95% increase for 35% martensite for QT-740. Rectifying this limitation requires implementation of a general homogenization scheme and plasticity in the transformed martensite, as discussed in Chapter 3.

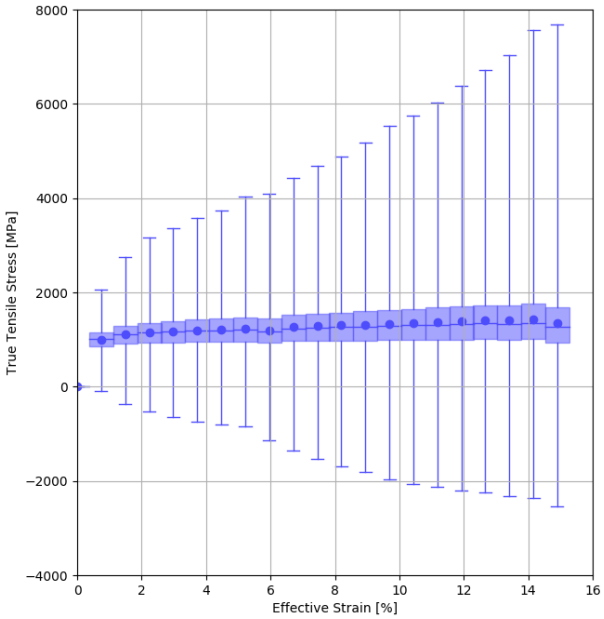

Fig. 4.19: Box and whisker plots of true X stress vs. strain.

The second limitation of the proposed constitutive model arises from the kinetics law's specific choice (Eq. (4.86)). While this type of kinetics law has been used for similar deformation modes, it does not capture the TRIP effect's strain-induced transformation mode. Furthermore, the method for introducing rate sensitivity into the kinetics equation is fundamentally justified only for deformation modes with a thermal activation mode (e.g. plastic slip) and conflicts with the athermal mechanics of martensitic transformation. This is illustrated by resimulating the interrupted simulation with a strain-rate of zero (i.e. no applied deformation). To test the predicted effects on long-term storage, the simulation time is also extended to 7 days. This is equivalent to allowing the material to sit at room temperature for 460 s and 7 d, respectively. The RAVF vs. time response for these simulations are reported in Fig. 4.20. This shows that throughout the interrupted simulation 1.7% of the total RA transforms solely due to the thermal driving force at room temperature and that over one week approximately 16% of the total RA would transform. This is significant because the athermal nature of martensitic transformation requires no transformation under these conditions in practice. This limitation may be corrected by using a kinetics law that correctly captures strain-induced transformation and the athermal nature of martensitic transformation.

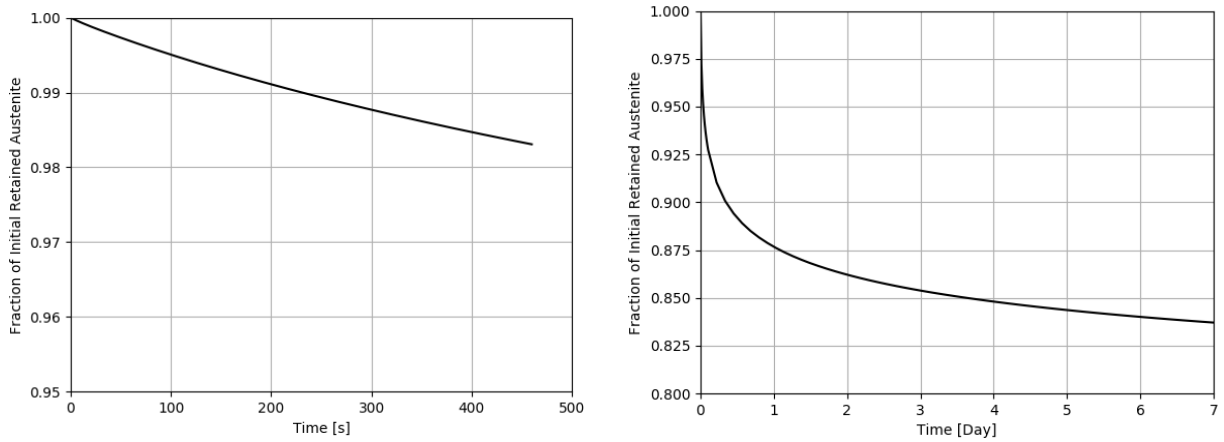

(a) 460 s simulation (b) 7 d simulation

Fig. 4.20: Normalized RA fraction vs. strain at constant temperature without applied deformation

4.6 Chapter Conclusion

This chapter presented a novel thermodynamically consistent constitutive model based on rate-dependent crystal plasticity. The model accounts for temperature, strain-rate, and orientation-dependent transformation and includes new terms to capture the hardening in the RA phase due to the accommodation of plastic strain from transformation. This constitutive model was implemented into an implicit UMAT version of the commercial FE software, LS-Dyna, to simulate the local deformation of QP steels with the TRIP effect. A novel method was proposed for incorporating thermal boundary conditions into RVE models. The constitutive model and thermal boundary condition method presented here enable for the first time rigorous coupled thermo-mechanical crystal plasticity simulations of steel exhibiting the TRIP effect. SEM, EBSD, and in-situ uniaxial tension HEXRD experiments were conducted to characterize the initial microstructure and bulk deformation behaviour of a commercially available QP1180 steel alloy to demonstrate the capabilities of this model. FE models were constructed from the initial microstructure data and used in conjunction with the experimental bulk response to calibrate the constitutive model. Several analyses were carried out, with specific conclusions as follows:

- A significant variance in RA transformation was observed, with the final RA content of the elements varying between 0% and 98.9%. This was primarily explained by

the dependence of the transformation rate on crystal orientation and was consistent with experimental observations of preferential transformation along the $\langle 100 \rangle$ crystal direction.

- Simulation of non-interrupted vs. interrupted conditions predicted that the final temperature was 11 K higher, resulting in 16.7% less martensitic transformation. These differences were not detectable solely using the stress vs. strain curve. This suggests that in-situ uniaxial tension HEXRD experiments may not have the same transformation rate as standard uniaxial tension tests, despite similar stress vs. strain curves.

- Neither isothermal nor adiabatic conditions accurately captured room-temperature quasi-static behaviour, as predicted using the interrupted general thermal conditions. Isothermal conditions predicted 33% more RA, while adiabatic conditions predicted 33% less RA than non-isothermal interrupted conditions.

- Increased initial temperature decreased both the amount of transformation and the bulk stress, which matches the majority of existing literature for steels exhibiting the TRIP effect. At 390 K, martensite transformation was entirely suppressed, and final stress decreased by approximately 25%. Final RA fraction and equivalent stress increased by 80% and 6% as strain-rate increased from $8 \times 10^{-4}\,\mathrm{s}^{-1}$ to $8 \times 10^{-2}\,\mathrm{s}^{-1}$ at room temperature. This matches results for TRIP steels, but not all QP steels.

- Predicted temperature evolution for non-interrupted general and adiabatic cases are nearly identical for a strain-rate of $8 \times 10^{-2}\,\mathrm{s}^{-1}$.

Two primary limitations of the proposed model were presented. These are:

- The assumption of elasticity in the transformed martensite phase introduces difficulty in capturing the deformation behaviour of individual phases.

- The kinetics law does not capture strain-induced transformation or the athermal nature of martensitic transformation.

5 A Novel Crystal Plasticity Model Incorporating Transformation Induced Plasticity for a Wide Range of Strain Rates and Temperatures[1]

5.1 Introduction

As highlighted in Chapter 4, Connolly et al. [154] recently proposed a stress-assisted transformation model with rate-dependent plastic slip that built upon the work of Yadegari et al. [109]. Transformation driving forces were derived from thermodynamic arguments, and novel kinetics laws were proposed to capture the rate dependence of transformation better. While each of the model lineages outlined in this thesis, including Connolly Model #1 as proposed in Chapter 4, offer distinct advantages and have shown great utility, to the author's knowledge, no crystal plasticity model has been proposed that incorporates strain-induced transformation that is dependent on strain-rate and temperature. A few models incorporate transformed martensite plasticity or a direct homogenization model needed to most accurately account for transformation hardening. Furthermore, to the author's knowledge, no model presents rigorous homogenization of the thermodynamic equations. Correctly incorporating thermodynamic homogenization better captures the underlying physics and results in a higher fidelity transformation driving force. In particular, the baseline Connolly Model #1 does not incorporate homogenization, plasticity in the transformed martensite, or strain-induced transformation. Furthermore, the hardening due to local plasticity is not fully captured. To achieve the objects outlined in Chapter 3, these limitations must be addressed.

This chapter presents a novel thermo-mechanically coupled constitutive model incorporating rate and temperature-dependent strain-induced transformation. RA and transformed martensite mechanical thermo-elasto-viscoplastic behaviour is explicitly modelled, and a modified Taylor homogenization law is proposed to determine strain partitioning while accounting for transformation. This homogenization approach is generalized to the thermodynamic behaviour, which is then used to derive driving forces that account for various physical mechanisms (e.g. applied stress, temperature, crystal orientation, stored

[1]The contents of this chapter are adapted from:

D. S. Connolly, C. P. Kohar, K. Inal, A Novel Crystal Plasticity Model Incorporating Transformation Induced Plasticity for a Wide Range of Strain Rates and Temperatures, Under Review at The Journal of the Mechanics and Physics of Solids (MPS-D-21-00101). Submitted on January 27, 2021.

dislocation energy). The thermodynamic behaviour is further used to derive a constitutive law governing temperature evolution. The model is then calibrated and validated for a QP3Mn alloy over a large range of temperatures ($-10\,^{\circ}\mathrm{C}$ – $70\,^{\circ}\mathrm{C}$) and strain-rates ($5 \times 10^{-4}\,\mathrm{s}^{-1}$ – $200\,\mathrm{s}^{-1}$) using experimental observations for a QP3Mn alloy that were presented in Poling [53]. The evolution of the Taylor-Quinney coefficient and the orientation dependence of transformation are then analyzed. The model is recalibrated without strain-rate dependent transformation compared to the validated model to determine the necessity of the strain-rate dependence incorporated in this work. Finally, plane strain and equibiaxial tension simulations are conducted to analyze the strain-path dependence of the validated model's mechanical behaviour.

5.2 Constitutive Model

The constitutive model presented here is developed to capture the aggregate behaviour of a steel polycrystalline aggregate with an initial microstructure consisting of a combination of austenite, ferrite and martensite grains. Since austenite can transform into martensite under applied thermo-mechanical loading, this model must incorporate the constitutive behaviours of the initial austenite phase, the transformed martensite phase, and the transformation process. The derivation of this constitutive model is collected into several sections. In brief, these sections:

- Present a micromechanical representation of transformation;
- Derive the deformation kinematics for the polycrystalline aggregate;
- Present stress evolution law for the polycrystalline aggregate;
- Derive plastic slip and transformation thermodynamic driving forces and a temperature evolution law;
- Present the kinematics for plastic slip and transformation.

The proposed model's primary novel aspects are the modified Taylor homogenization law for capturing TRIP strain and transformation hardening, rigorous homogenization of the governing thermodynamic equations, and the proposed transformation kinetics law.

5.2.1 Micromechanics

This work focuses on thin-plate twinned martensite because it is the primary type that forms in high carbon RA, such as in QP alloys [40, 43, 65]. This is modelled using the phenomenological theory of martensite transformation [143, 144] and was first proposed for use in crystal plasticity by Turteltaub and Suiker [110, 118]. Fig. 5.1 presents the twinned microstructure of thin-plate martensite at several relevant length scales (modified from Turteltaub and Suiker [110]). In order of highest level to lowest, these lengths scales are the mesoscale, upper microscale, lower microscale, and lattice scale. At the mesoscale, only the homogenized behaviour of the austenitic aggregate can be observed. At the upper microscale, the individual austenite and transformed martensite phases can be observed. At the lower microscale, an alternating twinned structure can be seen within each martensite plate. Finally, at the lattice scale, the individual orientations of the martensite variants can be seen within each of the martensite twins.

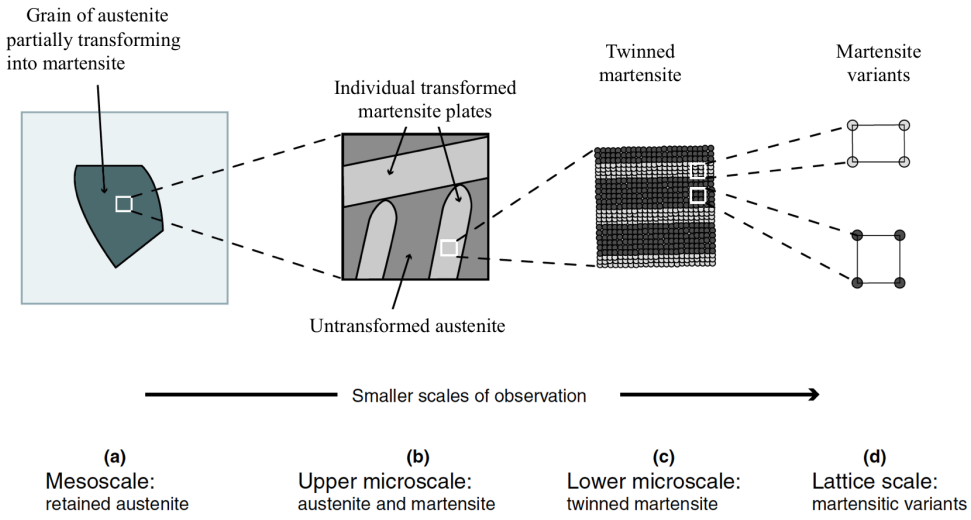

Fig. 5.1: Austenite and martensite microstructure at several length scales. Modified from Turteltaub and Suiker [110].

These martensite variants have a body-centred tetragonal (BCT) structure at the lattice scale, which may be one of three possible variants that correspond to three axes along which the lattice may stretch. Each martensite variant ζ of the austenite grain α' is related to the austenite lattice through the stretch tensor $\mathbf{U}^{(\alpha',\zeta)}$, given by

$$\mathbf{U}^{(\alpha',\zeta)} = \left(\sqrt{2}\,\frac{a^M}{a^A}\right)\mathbf{I} + \left(\frac{c^M}{a^A} - \sqrt{2}\,\frac{a^M}{a^A}\right)\mathbf{e}_\zeta^{(\alpha',\zeta)} \otimes \mathbf{e}_\zeta^{(\alpha',\zeta)} \tag{5.1}$$

where a^M and c^M are the lattice parameters of the BCT martensite, a^A is the lattice parameter of the austenite and $\left\{\mathbf{e}_i^{(\alpha',\zeta)}\right\}_{i=1}^{3}$ is an orthonormal basis aligned with the tetragonal axes of the martensite variant ζ of the austenite grain α'. These basis vectors of the martensite variant β are related to the austenite lattice through

$$\mathbf{e}_i^{(\alpha',\zeta)} = \mathbf{R}_\star^{(\zeta)}\mathbf{e}_i^{(\alpha')} \tag{5.2}$$

where $\mathbf{R}_\star^{(\alpha',\zeta)}$ is a rotation tensor relating the lattice vectors and $\left\{\mathbf{e}_i^{(\alpha')}\right\}_{i=1}^{3}$ is an orthonormal basis aligned with the cubic axes of the austenite phase. The rotation tensors $\mathbf{R}_\star^{(\zeta)}$ are defined in the austenite basis by

$$\mathbf{R}_\star^{(1)} = \begin{bmatrix} 1 & 0 & 0 \\ 0 & \frac{\sqrt{2}}{2} & -\frac{\sqrt{2}}{2} \\ 0 & \frac{\sqrt{2}}{2} & \frac{\sqrt{2}}{2} \end{bmatrix}, \qquad \mathbf{R}_\star^{(2)} = \begin{bmatrix} \frac{\sqrt{2}}{2} & 0 & \frac{\sqrt{2}}{2} \\ 0 & 1 & 0 \\ -\frac{\sqrt{2}}{2} & 0 & \frac{\sqrt{2}}{2} \end{bmatrix}, \qquad \mathbf{R}_\star^{(3)} = \begin{bmatrix} \frac{\sqrt{2}}{2} & -\frac{\sqrt{2}}{2} & 0 \\ \frac{\sqrt{2}}{2} & \frac{\sqrt{2}}{2} & 0 \\ 0 & 0 & 1 \end{bmatrix} \tag{5.3}$$

When forming the twinned structure, the martensite variants undergo additional rotations to maintain material compatibility. First, compatibility between the martensite variants in a twinned relationship is enforced using

$$\overline{\mathbf{R}}^{(\beta)}\mathbf{U}^{\left(\alpha',\zeta_1^\beta\right)} - \mathbf{U}^{\left(\alpha',\zeta_2^\beta\right)} = \mathbf{a}^{(\alpha',\beta)} \otimes \mathbf{n}^{(\alpha',\beta)} \tag{5.4}$$

where $\overline{\mathbf{R}}^{(\beta)}$ represents the relative rotations between the twinned martensite variants ζ_1^β and ζ_2^β of the martensite plate orientation β, and $\mathbf{a}^{(\alpha',\beta)}$ and $\mathbf{n}^{(\alpha',\beta)}$ are the twin shear vector and the twin shear plane normal for the martensite plate orientation β of the austenite grain α'. The compatibility between the austenite phase and martensite variants is enforced using

$$[\![\mathbf{F}]\!]^{(\alpha',\beta)} = \widehat{\mathbf{R}}^{(\beta)}\left(\lambda^{\left(\zeta_1^\beta\right)}\overline{\mathbf{R}}^{(\beta)}\mathbf{U}^{\left(\alpha',\zeta_1^\beta\right)} + \lambda^{\left(\zeta_2^\beta\right)}\mathbf{U}^{\left(\alpha'\zeta_2^\beta\right)}\right) - \mathbf{I} = \widehat{\gamma}_{tr}\mathbf{b}^{(\alpha',\beta)} \otimes \mathbf{d}^{(\alpha',\beta)} \tag{5.5}$$

where $[\![\mathbf{F}]\!]^{(\alpha',\beta)}$ represents the jump in deformation gradient between the austenite and martensite plate orientation β of the austenite grain α', $\widehat{\mathbf{R}}^{(\beta)}$ is the rotation of the twinned martensite structure and the austenite phase, $\lambda^{(\zeta_1^\beta)}$ and $\lambda^{(\zeta_2^\beta)}$ are the volume fractions of the twinned martensite variants ζ_1^β and ζ_2^β within the martensite plate orientation β, $\widehat{\gamma}_{tr}$ is the total shear during transformation, and $\mathbf{b}^{(\alpha',\beta)}$ and $\mathbf{d}^{(\alpha',\beta)}$ are the transformation shear direction and habit plane normal for martensite plate orientation β of the austenite grain α'. Since there are two twinned martensite variants, the volume fractions obey the identity $\lambda^{(\zeta_1^\beta)} + \lambda^{(\zeta_2^\beta)} = 1$. Overall, there are 24 unique solutions to Eqs. (5.4) and (5.5). This results in 24 unique martensite plate orientations and 48 unique martensite variants (i.e. two unique variant orientations per plate orientation) per austenite grain. The transformation shear direction $\mathbf{b}^{(\alpha',\beta)}$ and habit plane normal $\mathbf{d}^{(\alpha',\beta)}$ for a martensite orientation β transformed from austenite grain α' are defined in terms of the austenite grain α' basis by

$$\mathbf{b}^{(\alpha',\beta)} = b_i^{(\beta)}\mathbf{e}_i^{(\alpha')} \tag{5.6}$$

$$\mathbf{d}^{(\alpha',\beta)} = d_i^{(\beta)}\mathbf{e}_i^{(\alpha')} \tag{5.7}$$

where $b_j^{(\beta)}$ and $d_j^{(\beta)}$ are components that are independent of the specific austenite grain orientation. Combining Eqs. (5.4) and (5.5) gives the following orientation relationship between the austenite basis and martensite variant bases of martensite plate orientation β of austenite grain α'

$$\mathbf{e}_i^{\left(\alpha',\zeta_1^\beta\right)} = \widehat{\mathbf{Q}}^{\left(\zeta_1^\beta\right)}\mathbf{e}_i^{(\alpha')}, \qquad \mathbf{e}_i^{\left(\alpha',\zeta_2^\beta\right)} = \widehat{\mathbf{Q}}^{\left(\zeta_2^\beta\right)}\mathbf{e}_i^{(\alpha')} \tag{5.8}$$

where $\widehat{\mathbf{Q}}^{\left(\zeta_1^\beta\right)}$ and $\widehat{\mathbf{Q}}^{\left(\zeta_2^\beta\right)}$ are rotation tensors between austenite and martensite variants ζ_1^β and ζ_2^β of martensite plate orientation β of austenite grain α'. These are given by

$$\widehat{\mathbf{Q}}^{\left(\zeta_1^\beta\right)} = \widehat{\mathbf{R}}^{(\beta)}\overline{\mathbf{R}}^{(\beta)}\mathbf{R}_\star^{\left(\zeta_1^\beta\right)}, \qquad \widehat{\mathbf{Q}}^{\left(\zeta_2^\beta\right)} = \widehat{\mathbf{R}}^{(\beta)}\mathbf{R}_\star^{\left(\zeta_2^\beta\right)} \tag{5.9}$$

Specific values of the austenite and martensite lattice parameters, rotation matrices, and transformation systems are given in Appendix B.

Throughout the rest of this work, it is convenient to refer to martensite variants using a single variable α when referring to single crystal behaviour and using the tuple (α', ζ_i^β) when referring to transformation behaviour. Since (α', ζ_i^β) refers to a unique transformed martensite variant, there is a one to one mapping between α and (α', ζ_i^β) and the terms will be used interchangably.

5.2.2 Deformation Kinematics

The velocity gradient $\langle \mathbf{L} \rangle$ is given by a volumetric average of the local velocity gradients ($\mathbf{L}$) throughout the aggregate material, as shown by

$$\langle \mathbf{L} \rangle = \sum_{\alpha=1}^{N_g} \xi^{(\alpha)} \mathbf{L}^{(\alpha)} + \mathbf{L}_{tr} \tag{5.10}$$

where $\xi^{(\alpha)}$ and $\mathbf{L}^{(\alpha)}$ are the grain volume fraction and local velocity gradient of the grain α, N_g is the number of grains present in the aggregate, $\mathbf{L}_{tr}$ is the velocity gradient from martensitic transformation at the boundaries between austenite and transformed martensite plates, and the notation $\langle \star \rangle = \frac{1}{V} \int_V (\star)\ \mathrm{d}V$ indicates a volume average. Since the volume fractions of the variants i within a martensite orientation β are not independent, an additional variable $\overline{\xi}^{(\alpha',\beta)}$ representing the volume fraction of the martensite orientation β transforming from the austenite grain α' is defined as

$$\xi^{\left(\alpha',\zeta_i^\beta\right)} = \lambda^{\left(\zeta_i^\beta\right)} \overline{\xi}^{(\alpha',\beta)} \tag{5.11}$$

The volume fraction $\xi^{(\alpha')}$ of an austenite grain α' is related to the volume fractions $\xi^{\left(\alpha',\zeta_i^\beta\right)}$ of the variant ζ_i^β of martensite plate β transformed from austenite grain α' and to the volume fraction $\overline{\xi}^{(\alpha',\beta)}$ of the martensite orientation β transformed from austenite grain α' through

$$\xi^{(\alpha')} = \xi_0^{(\alpha')} - \sum_{\beta=1}^{24} \sum_{i=1}^{2} \xi^{\left(\alpha',\zeta_i^\beta\right)} = \xi_0^{(\alpha')} - \sum_{\beta=1}^{24} \overline{\xi}^{(\alpha',\beta)} \tag{5.12}$$

where $\xi_0^{(\alpha')}$ is the initial volume fractions of the austenite grain α'. The local velocity gradients are then determined using a modified Taylor [96] assumption, wherein the local velocity gradient in each grain is identical

$$\langle \mathbf{L} \rangle - \mathbf{L}_{tr} = \mathbf{L}^{(\alpha)} \quad \forall \alpha \tag{5.13}$$

The use of the Taylor assumption is common in crystal plasticity-based models incorporating the TRIP effect [118], including In this work, austenite is modelled as a face-centred cubic (FCC) phase, ferrite is modelled as a body-centred cubic (BCC) phase, and the BCT martensite phases are approximated as body-centred cubic (BCC) for elastic, thermal and

plastic slip deformations. This assumption is common in crystal plasticity modelling of martensite [41, 140, 154].

Following Clayton [108], the local deformation for each grain α is given by a multiplicative decomposition of the deformation gradient

$$\mathbf{F}^{(\alpha)} = \mathbf{F}_e^{(\alpha)}\mathbf{F}_\theta^{(\alpha)}\mathbf{F}_p^{(\alpha)} \tag{5.14}$$

where $\mathbf{F}^{(\alpha)}$, $\mathbf{F}_e^{(\alpha)}$, $\mathbf{F}_\theta^{(\alpha)}$ and $\mathbf{F}_p^{(\alpha)}$ are the total, elastic, thermal and plastic slip deformation gradients for grain α. Fig. 5.2 illustrates this decomposition, where $\mathscr{B}_0$, $\mathscr{B}_p$, $\mathscr{B}_\theta$ and $\mathscr{B}$ are the undeformed, plastically deformed, thermally deformed and fully deformed configurations respectively.

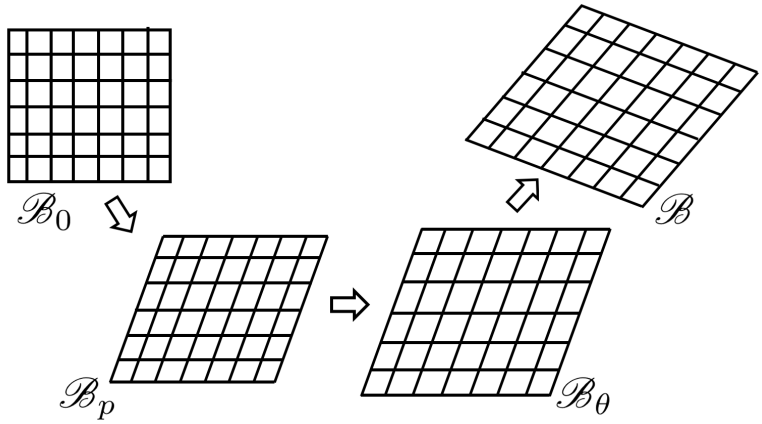

Fig. 5.2: Deformation gradient decomposition.

The velocity gradient can then be calculated as

$$\mathbf{L}^{(\alpha)} = \dot{\mathbf{F}}^{(\alpha)}\left[\mathbf{F}^{(\alpha)}\right]^{-1} = \mathbf{L}_e^{(\alpha)} + \mathbf{L}_\theta^{(\alpha)} + \mathbf{L}_p^{(\alpha)} \tag{5.15}$$

where $\mathbf{L}_e^{(\alpha)}$, $\mathbf{L}_\theta^{(\alpha)}$ and $\mathbf{L}_p^{(\alpha)}$ are the elastic, thermal and plastic slip velocity gradients given by

$$\mathbf{L}_e^{(\alpha)} = \dot{\mathbf{F}}_e^{(\alpha)}\left[\mathbf{F}_e^{(\alpha)}\right]^{-1} \tag{5.16a}$$

$$\mathbf{L}_\theta^{(\alpha)} = \mathbf{F}_e^{(\alpha)}\left[\dot{\mathbf{F}}_\theta^{(\alpha)}\left[\mathbf{F}_\theta^{(\alpha)}\right]^{-1}\right]\left[\mathbf{F}_e^{(\alpha)}\right]^{-1} \tag{5.16b}$$

$$\mathbf{L}_p^{(\alpha)} = \mathbf{F}_e^{(\alpha)}\mathbf{F}_\theta^{(\alpha)}\left[\dot{\mathbf{F}}_p^{(\alpha)}\left[\mathbf{F}_p^{(\alpha)}\right]^{-1}\right]\left[\mathbf{F}_\theta^{(\alpha)}\right]^{-1}\left[\mathbf{F}_e^{(\alpha)}\right]^{-1} \tag{5.16c}$$

The thermal velocity gradients are given by

$$\mathbf{L}_\theta^{(\alpha)} = A^{(\alpha)}\mathbf{I}\dot{\theta} \tag{5.17}$$

where $A^{(\alpha)}$ is the linear thermal expansion coefficient for grain α, $\mathbf{I}$ is the second order identity tensor and $\dot{\theta}$ is the rate of change of temperature. In this work, all grains α are assumed to have the same temperature. The plastic slip velocity gradients are given by

$$\mathbf{L}_p^{(\alpha)} = \sum_{i=1}^{N_p^{(\alpha)}} \dot{\gamma}^{(\alpha,i)}\left[\mathbf{s}_e^{(\alpha,i)} \otimes \mathbf{m}_e^{(\alpha,i)}\right] \tag{5.18}$$

where $N_p^{(\alpha)}$ is the number of slip systems for grain α, $\dot{\gamma}^{(\alpha,i)}$ is the slip rate for slip system i of grain α, and $\mathbf{s}_e^{(\alpha,i)}$ and $\mathbf{m}_e^{(\alpha,i)}$ are the slip system direction and normal plane of the slip system i for grain α in the fully deformed configuration. The slip system direction and normal vectors for austenite, ferrite, and pre-existing martensite in the fully deformed configuration are related to the undeformed configuration by

$$\mathbf{s}_e^{(\alpha,i)} = \mathbf{F}_e^{(\alpha)}\mathbf{F}_\theta^{(\alpha)}\mathbf{s}^{(\alpha,i)} \tag{5.19}$$

$$\mathbf{m}_e^{(\alpha,i)} = \mathbf{m}^{(\alpha,i)}\left[\mathbf{F}_\theta^{(\alpha)}\right]^{-1}\left[\mathbf{F}_e^{(\alpha)}\right]^{-1} \tag{5.20}$$

where $\mathbf{s}^{(\alpha,i)}$ and $\mathbf{m}^{(\alpha,\beta)}$ are the slip system direction and normal plane of the slip system β for grain α in the undeformed configuration. These are expressed in terms of the cubic basis of the grain α by

$$\mathbf{s}^{(\alpha,i)} = s_j^{(i)}\mathbf{e}_j^{(\alpha)} \tag{5.21}$$

$$\mathbf{m}^{(\alpha,i)} = m_j^{(i)}\mathbf{e}_j^{(\alpha)} \tag{5.22}$$

where $s_j^{(i)}$ and $m_j^{(i)}$ are components that are independent of the specific grain orientation and where $\left\{\mathbf{e}_j^{(\alpha)}\right\}_{j=1}^{3}$ is the cubic basis of grain α. The specific values of the slip directions and normals in the undeformed configuration are given in Appendix A.

However, the slip system orientations in a newly transformed region of transforming martensite grains may not be the same as in the existing transformed material. This is because the orientation in a newly transformed region is dependent on the parent austenite orientation, whereas the orientations in the existing transformed material may have evolved independently. In this case, the change in slip system orientations is determined as a

function of the newly transformed slip system orientations and the change in orientation in the existing transformed grain. This gives

$$\begin{aligned}\Delta\left(\xi^{(\alpha)}\mathbf{s}_e^{(\alpha,i)}\right) &= \Delta\xi^{(\alpha)}\mathbf{s}_e^{(\alpha,i)} + \xi^{(\alpha)}\Delta\mathbf{s}_e^{(\alpha,i)} = \Delta\xi^{(\alpha)}\hat{\mathbf{s}}_e^{(\alpha,i)} + \xi^{(\alpha)}\left[\mathbf{L}_e^{(\alpha)} + \mathbf{L}_\theta^{(\alpha)}\right]\mathbf{s}_e^{(\alpha,i)}\Delta t \\ \Delta\left(\xi^{(\alpha)}\mathbf{m}_e^{(\alpha,i)}\right) &= \Delta\xi^{(\alpha)}\mathbf{m}_e^{(\alpha,i)} + \xi^{(\alpha)}\Delta\mathbf{m}_e^{(\alpha,i)} = \Delta\xi^{(\alpha)}\hat{\mathbf{m}}_e^{(\alpha,i)} - \xi^{(\alpha)}\mathbf{m}_e^{(\alpha,i)}\left[\mathbf{L}_e^{(\alpha)} + \mathbf{L}_\theta^{(\alpha)}\right]\Delta t\end{aligned} \tag{5.23}$$

where $\hat{\mathbf{s}}_e^{(\alpha,i)`}$ and $\hat{\mathbf{m}}_e^{(\alpha,i)}$ are the slip system directions and normals in the newly transformed material. These are defined by

$$\begin{aligned}\hat{\mathbf{s}}^{(\alpha,i)} &= \hat{\mathbf{s}}^{\left(\left(\alpha',\zeta_l^\beta\right),i\right)} = s_j^{(i)}\hat{\mathbf{e}}_j^{\left(\alpha',\zeta_k^\beta\right)} = s_j^{(i)}\widehat{Q}_{jk}^{\left(\zeta_l^\beta\right)}\mathbf{e}_k^{(\alpha')} \\ \hat{\mathbf{m}}^{(\alpha,i)} &= \hat{\mathbf{m}}^{\left(\left(\alpha',\zeta_l^\beta\right),i\right)} = m_j^{(i)}\hat{\mathbf{e}}_j^{\left(\alpha',\zeta_l^\beta\right)} = m_j^{(i)}\widehat{Q}_{jk}^{\left(\zeta_l^\beta\right)}\mathbf{e}_k^{(\alpha')}\end{aligned} \tag{5.24}$$

Taking the limit and rearranging for the slip directions and normals gives

$$\begin{aligned}\dot{\mathbf{s}}_e^{(\alpha,i)} &= \dot{\mathbf{s}}_e^{(\alpha,i)}\frac{\dot{\xi}^{(\alpha)}}{\xi^{(\alpha)}}\left[\hat{\mathbf{s}}^{(\alpha,i)} - \mathbf{s}_e^{(\alpha,i)}\right] + \left[\mathbf{L}_e^{(\alpha)} + \mathbf{L}_\theta^{(\alpha)}\right]\mathbf{s}_e^{(\alpha,i)} \\ \dot{\mathbf{m}}_e^{(\alpha,i)} &= \frac{\dot{\xi}^{(\alpha)}}{\xi^{(\alpha)}}\left[\hat{\mathbf{m}}^{(\alpha,i)} - \mathbf{m}_e^{(\alpha,i)}\right] - \mathbf{m}_e^{(\alpha,i)}\left[\mathbf{L}_e^{(\alpha)} + \mathbf{L}_\theta^{(\alpha)}\right]\end{aligned} \tag{5.25}$$

While similar relationships also hold for other internal variables (e.g. dislocation density, elastic strain, and plastic strain), this work assumes that the newly transformed internal variables have the same value as in the existing transformed material. As such, this effect is not explicitly included for other internal variables.

The presence of plastic slip in a grain α results in the accumulation of the dislocations, as measured by the dislocation density $\rho_d^{(\alpha)}$. The initial dislocation density is given by $\rho_{d,0}^{(\alpha)}$ and the rate of change $\dot{\rho}_d^{(\alpha)}$ is given by

$$\dot{\rho}_d^{(\alpha)} = \sum_{i=1}^{N_p^{(\alpha)}}\left[\frac{1}{b^{(\alpha)}k_1^{(\alpha)}}\sqrt{\rho_d^{(\alpha)}} - k_2^{(\alpha)}\rho_d^{(\alpha)}\right]\left|\dot{\gamma}^{(\alpha,i)}\right| \tag{5.26}$$

where $b^{(\alpha)}$ is the Burger's vector of grain α and $k_1^{(\alpha)}$ and $k_2^{(\alpha)}$ are calibration coefficients for grain α. In this equation, the first term represents the dislocation generation and the

second term represents dynamic recovery of dislocations. Unlike in Connolly et al. [154], it is assumed that the dislocation density is independent of the grain volume fractions as the impact of transformation strain is instead captured through homogenization (as in Eq. (5.10)).

Following the work of Cherkaoui et al. [115], the transformation velocity gradients are given by

$$\mathbf{L}_{tr} = \frac{1}{V} \sum_{\alpha'=1}^{N_a} \sum_{\beta=1}^{24} \int_{S^{(\alpha',\beta)}} \left[\!\left[\frac{\partial \mathbf{u}}{\partial \mathbf{x}} \right]\!\right] \mathbf{w} \cdot \mathbf{n} \, \mathrm{d}S^{(\alpha',\beta)} \tag{5.27}$$

where V is the volume of the polycrystal aggregate, N_a is the number of austenite grains, $S^{(\alpha',\beta)}$ represents the transformation surface from austenite to martensite plate orientation β of austenite grain α', $[\![\star]\!]$ represents the jump across the surface $S^{(\alpha',\beta)}$ at a point along the surface, and where $\frac{\partial \mathbf{u}}{\partial \mathbf{x}}$, $\mathbf{n}$ and $\mathbf{w}$ are the jump in displacement gradient associated with complete transformation from austenite to a martensite variant, the surface normal vector and the velocity of the transforming boundary at a point on the surface $S^{(\alpha',\beta)}$. This equation is independent of the specific shape or size of the transformed martensite grains. The jump in the deformation gradient across the transforming boundary is given by

$$\left[\!\left[\frac{\partial \mathbf{u}}{\partial \mathbf{x}} \right]\!\right] \Bigg|_{S^{(\alpha',\beta)}} \approx [\![\mathbf{F}]\!]^{(\alpha',\beta)} = \hat{\gamma}_{tr} \mathbf{b}_e^{(\alpha',\beta)} \otimes \mathbf{d}_e^{(\alpha',\beta)} \tag{5.28}$$

where $\mathbf{b}_e^{(\alpha',\beta)}$ and $\mathbf{d}_e^{(\alpha',\beta)}$ are the transformation direction and the transformation habit plane in the fully deformed configuration. Next, the surface integral of the normal velocity over the surface $S^{(\alpha',\beta)}$ is directly related to the transformation rate of martensite plate orientation β of austenite grain α' through

$$\frac{1}{V} \int_{S^{(\alpha',\beta)}} \mathbf{w} \cdot \mathbf{n} \, \mathrm{d}S^{(\alpha',\beta)} = \dot{\xi}^{(\alpha',\beta)} \tag{5.29}$$

Combining Eqs. (5.27), (5.28), and (5.29) gives

$$\mathbf{L}_{tr} = \sum_{\alpha'=1}^{N_a} \sum_{\beta=1}^{24} \dot{\xi}^{(\alpha',\beta)} \left[\hat{\gamma}_{tr} \mathbf{b}_e^{(\alpha',\beta)} \otimes \mathbf{d}_e^{(\alpha',\beta)} \right] \tag{5.30}$$

matching the derivations in Connolly et al. [154]. Since the jump in deformation gradient due to transformation ($[\![\mathbf{F}]\!]^{(\alpha',\beta)}$) is defined in terms of the austenite lattice at the time of

transformation, the transformation systems must convect with the austenite lattice such that

$$\mathbf{b}_e^{(\alpha',\beta)} = \mathbf{F}_e^{(\alpha')}\mathbf{F}_\theta^{(\alpha')}\mathbf{b}^{(\alpha',\beta)} \qquad (5.31) \qquad \mathbf{d}_e^{(\alpha',\beta)} = \mathbf{d}^{(\alpha',\beta)}\left[\mathbf{F}_\theta^{(\alpha')}\right]^{-1}\left[\mathbf{F}_e^{(\alpha')}\right]^{-1} \qquad (5.32)$$

5.2.3 Governing Equations for Stress

The Cauchy stress and Cauchy stress rate for the overall aggregate are given by

$$\langle\boldsymbol{\sigma}\rangle = \sum_{\alpha=1}^{N_g}\xi^{(\alpha)}\boldsymbol{\sigma}^{(\alpha)} \qquad (5.33)$$

$$\langle\dot{\boldsymbol{\sigma}}\rangle = \sum_{\alpha=1}^{N_g}\xi^{(\alpha)}\dot{\boldsymbol{\sigma}}^{(\alpha)} + \sum_{\alpha'=1}^{N_a}\sum_{\beta=1}^{24}\dot{\xi}^{(\alpha',\beta)}\left[\sum_{i=1}^{2}\lambda^{\left(\zeta_i^\beta\right)}\boldsymbol{\sigma}^{\left(\alpha',\zeta_i^\beta\right)} - \boldsymbol{\sigma}^{(\alpha')}\right] \qquad (5.34)$$

where $\boldsymbol{\sigma}^{(\alpha)}$ and $\dot{\boldsymbol{\sigma}}^{(\alpha)}$ are the volume averaged Cauchy stress and Cauchy stress rate of the grain α, $\boldsymbol{\sigma}^{\left(\alpha',\zeta_i^\beta\right)}$ is the volume averaged Cauchy stress in variant i of martensite plate β transforming from austenite grain α' and $\boldsymbol{\sigma}^{(\alpha')}$ is the volume averaged Cauchy stress in the austenite grain α'. Stress is governed by a hyper-elastic law

$$\mathbf{S}_e^{(\alpha)} = \mathbb{C}^{(\alpha)} : \mathbf{E}_e^{(\alpha)} \qquad (5.35)$$

where $\mathbf{S}^{(\alpha)}$, $\mathbb{C}^{(\alpha)}$ and $\mathbf{E}_e^{(\alpha)}$ are the second Piola-Kirchoff stress, elasticity tensor and the elastic Euler-Green tensor for grain α. In Voigt form, the elasticity tensor is represented as

$$\left\{\mathbb{C}^{(\alpha)}\right\} = \left\{\begin{bmatrix} c_{11}^{(\alpha)} & c_{12}^{(\alpha)} & c_{12}^{(\alpha)} & 0 & 0 & 0 \\ c_{12}^{(\alpha)} & c_{11}^{(\alpha)} & c_{12}^{(\alpha)} & 0 & 0 & 0 \\ c_{12}^{(\alpha)} & c_{12}^{(\alpha)} & c_{11}^{(\alpha)} & 0 & 0 & 0 \\ 0 & 0 & 0 & c_{44}^{(\alpha)} & 0 & 0 \\ 0 & 0 & 0 & 0 & c_{44}^{(\alpha)} & 0 \\ 0 & 0 & 0 & 0 & 0 & c_{44}^{(\alpha)} \end{bmatrix}\right\} \qquad (5.36)$$

where $c_{11}^{(\alpha)}$, $c_{12}^{(\alpha)}$ and $c_{44}^{(\alpha)}$ are the elastic coefficients for grain α.

Since Eq. (5.35) is defined in the thermally deformed configuration, the elastic Jaumann rate of the Cauchy stress can be derived as

$$\overset{\triangledown}{\boldsymbol{\sigma}}{}_e^{(\alpha)} = \dot{\boldsymbol{\sigma}}^{(\alpha)} + \boldsymbol{\sigma}^{(\alpha)}\boldsymbol{\Omega}_e^{(\alpha)} - \boldsymbol{\Omega}_e^{(\alpha)}\boldsymbol{\sigma}^{(\alpha)} = \mathbb{C}_e^{(\alpha)} : \mathbf{D}_e^{(\alpha)} \tag{5.37}$$

where $\mathbf{D}_e^{(\alpha)}$ and $\boldsymbol{\Omega}_e^{(\alpha)}$ are the symmetric and antisymmetric part of the elastic velocity gradient $\mathbf{L}_e^{(\alpha)}$ and $\mathbb{C}_e^{(\alpha)}$ is the elastic tensor in the fully deformed configuration, given by

$$\mathbb{C}_{e(ijkl)}^{(\alpha)} = \mathbf{F}_{e(ia)}^{(\alpha)}\mathbf{F}_{e(jb)}^{(\alpha)}\mathbf{F}_{e(kc)}^{(\alpha)}\mathbf{F}_{e(ld)}^{(\alpha)}\mathbb{C}_{abcd}^{(\alpha)} \tag{5.38}$$

As a result of using the Jaumann rate, it is assumed that $\boldsymbol{\sigma}^{(\alpha)}\mathbf{D}_e^{(\alpha)}$, $\mathbf{D}_e^{(\alpha)}\boldsymbol{\sigma}^{(\alpha)}$ and $\boldsymbol{\sigma}^{(\alpha)}\text{tr}\left(\mathbf{D}_e^{(\alpha)}\right)$ are small relative to $\dot{\boldsymbol{\sigma}}$. The elastic Jaumann rate of the Cauchy stress given in Eq. (5.37) can be related to the total Jaumann rate of the Cauchy stress using

$$\overset{\triangledown}{\boldsymbol{\sigma}}{}^{(\alpha)} = \dot{\boldsymbol{\sigma}}^{(\alpha)} + \boldsymbol{\sigma}^{(\alpha)}\boldsymbol{\Omega}^{(\alpha)} - \boldsymbol{\Omega}^{(\alpha)}\boldsymbol{\sigma}^{(\alpha)} = \overset{\triangledown}{\boldsymbol{\sigma}}{}_e^{(\alpha)} - \sum_{i=1}^{N_p^{(\alpha)}} \mathbf{B}^{(\alpha,i)}\dot{\gamma}^{(\alpha,i)} \tag{5.39}$$

where $\mathbf{B}^{(\alpha,i)}$ represents the plastic rotation in grain α from slip system i. This is given by

$$\mathbf{B}^{(\alpha,i)} = \mathbf{W}^{(\alpha,i)}\boldsymbol{\sigma} - \boldsymbol{\sigma}\mathbf{W}^{(\alpha,i)} \tag{5.40}$$

where $\mathbf{W}^{(\alpha,i)}$ is the antisymmetric part of the slip system matrix given by

$$\mathbf{W}^{(\alpha,i)} = \text{asym}\left(\mathbf{s}_e^{(\alpha,i)} \otimes \mathbf{m}_e^{(\alpha,i)}\right) \tag{5.41}$$

Similar to Eq. (5.37), the Jaumann rate assumes that $\boldsymbol{\sigma}^{(\alpha)}\mathbf{D}^{(\alpha)}$, $\mathbf{D}^{(\alpha)}\boldsymbol{\sigma}^{(\alpha)}$ and $\boldsymbol{\sigma}^{(\alpha)}\text{tr}\left(\mathbf{D}^{(\alpha)}\right)$ are small relative to $\dot{\boldsymbol{\sigma}}$, where $\mathbf{D}^{(\alpha)}$ is the symmetric part of the velocity gradient $\mathbf{L}^{(\alpha)}$. Combining Eqs. (5.15), (5.17), (5.18), (5.37), and (5.39) gives the total Cauchy rate as a function of the symmetric part of the velocity gradient for grain α

$$\overset{\triangledown}{\boldsymbol{\sigma}}{}^{(\alpha)} = \mathbb{C}_e^{(\alpha)} : \mathbf{D}^{(\alpha)} - A^{(\alpha)}\dot{\theta}\left[\mathbb{C}_e^{(\alpha)} : \mathbf{I}\right] - \sum_{i=1}^{N_p^{(\alpha)}} \mathbf{R}^{(\alpha,i)}\dot{\gamma}^{(\alpha,i)} \tag{5.42}$$

where $\mathbf{D}^{(\alpha)}$ is the symmetric part of the velocity gradient for grain α and $\mathbf{R}^{(\alpha,i)}$ is given by

$$\mathbf{R}^{(\alpha,i)} = \mathbb{C}^{(\alpha)} : \mathbf{P}^{(\alpha,i)} + \mathbf{B}^{(\alpha,i)} \tag{5.43}$$

where $\mathbf{P}^{(\alpha,i)}$ is the symmetric part of the slip system matrix. This is given by

$$\mathbf{P}^{(\alpha,i)} = \text{sym}\left(\mathbf{s}_e^{(\alpha,i)} \otimes \mathbf{m}_e^{(\alpha,i)}\right) \tag{5.44}$$

5.2.4 Thermodynamic Equations

The first law of thermodynamics is enforced using the energy balance in the undeformed configuration, given by

$$\rho\langle\dot{e}\rangle + \boldsymbol{\nabla}\cdot\mathbf{q} - \rho\langle r\rangle - \langle\boldsymbol{\sigma}:\mathbf{D}\rangle = 0 \tag{5.45}$$

where ρ is the current material density, $\langle\dot{e}\rangle$ is the current rate of change of the internal energy, $\boldsymbol{\nabla}\cdot\mathbf{q}$ is the divergence of the current heat flux, $\langle r\rangle$ is the energy source per unit mass, $\langle\boldsymbol{\sigma}:\mathbf{D}\rangle$ is the volume averaged external work applied and $\mathbf{D}$ is the symmetric part of the velocity gradient $\mathbf{L}$. In this work, the density ρ is assumed to be constant for all phases. The second law of thermodynamics is enforced through the energy dissipation law

$$\mathcal{D} = -\rho\langle\dot{e}\rangle + \rho\theta\langle\dot{\eta}\rangle + \langle\boldsymbol{\sigma}:\mathbf{D}\rangle - \frac{\boldsymbol{\nabla}\theta\cdot\mathbf{q}}{\theta} \geq 0 \tag{5.46}$$

where $\mathcal{D}$ is the energy dissipation rate which must be greater than 0 and $\langle\dot{\eta}\rangle$ is the volume averaged internal entropy generation rate. The volume averaged entropy can be related to the entropy in each grain through

$$\langle\eta\rangle = \sum_{\alpha=1}^{N_g} \xi^{(\alpha)}\eta^{(\alpha)} \tag{5.47}$$

where $\eta^{(\alpha)}$ is the entropy for grain α. The volume averaged entropy and local grain entropy can be decomposed according to

$$\langle\eta\rangle = \langle\eta_I\rangle + \langle\eta_e\rangle + \langle\eta_m\rangle + \langle\eta_p\rangle \tag{5.48}$$

$$\eta^{(\alpha)} = \eta_I^{(\alpha)} + \eta_e^{(\alpha)} + \eta_m^{(\alpha)} + \eta_p^{(\alpha)} \tag{5.49}$$

where $\langle\eta_I\rangle$ and $\eta_I^{(\alpha)}$ are the average and local grain α entropy associated with the undeformed crystal at reference temperature θ_T, $\langle\eta_e\rangle$ and $\eta_e^{(\alpha)}$ are the average and local grain α reversible entropy due to temperature change from θ_T, $\langle\eta_m\rangle$ and $\eta_m^{(\alpha)}$ are the average and local grain α reversible entropy due to thermo-elastic coupling, and $\langle\eta_p\rangle$ and $\eta_p^{(\alpha)}$ are the average and local grain α entropy generated during plastic slip. For convenience, the

reference temperature θ_T is chosen to be the temperature at which transformation will occur spontaneously without any applied stress or transformation energy barriers.

The volume average and local entropies are related through

$$\langle \eta_I \rangle = \sum_{\alpha=1}^{N_g} \xi^{(\alpha)} \eta_I^{(\alpha)} \tag{5.50}$$

$$\langle \eta_e \rangle = \sum_{\alpha=1}^{N_g} \xi^{(\alpha)} \eta_e^{(\alpha)} \tag{5.51}$$

$$\langle \eta_m \rangle = \sum_{\alpha=1}^{N_g} \xi^{(\alpha)} \eta_m^{(\alpha)} \tag{5.52}$$

$$\langle \eta_p \rangle = \sum_{\alpha=1}^{N_g} \xi^{(\alpha)} \eta_p^{(\alpha)} \tag{5.53}$$

Using Eq. (5.48) and the Legendre transformation between the volume averaged internal energy $\langle e \rangle$ and a volume averaged Helmholtz free energy $\langle \Psi \rangle$, defined by $\langle \Psi \rangle = \langle e \rangle - \theta \langle \eta_e \rangle$, the dissipation rate given in Eq. (5.46) can be rewritten as

$$\mathcal{D} = -\rho \langle \dot{\Psi} \rangle - \rho \dot{\theta} \langle \eta_e \rangle + \rho \theta \langle \dot{\eta}_m \rangle + \rho \theta \langle \dot{\eta}_p \rangle + \rho \theta \langle \dot{\eta}_I \rangle + \langle \boldsymbol{\sigma} : \mathbf{D} \rangle - \frac{\boldsymbol{\nabla} \theta \cdot \mathbf{q}}{\theta} \geq 0 \tag{5.54}$$

where $\langle \dot{\eta}_m \rangle$, $\langle \dot{\eta}_p \rangle$ and $\langle \dot{\eta}_I \rangle$ are the volume averaged rates of change of the thermomechanical coupling part of the reversible entropy density, the plastic slip entropy density, and the initial undeformed crystal entropy density.

The volume-averaged Helmholtz free energy and the rate of change of the Helmholtz free energy are related to the internal variables in grain α through

$$\langle \Psi \rangle = \sum_{\alpha=1}^{N_g} \xi^{(\alpha)} \Psi^{(\alpha)} \tag{5.55}$$

$$\langle \dot{\Psi} \rangle = \sum_{\alpha=1}^{N_g} \dot{\xi}^{(\alpha)} \Psi^{(\alpha)} + \xi^{(\alpha)} \dot{\Psi}^{(\alpha)} \tag{5.56}$$

where $\Psi^{(\alpha)}$ and $\dot{\Psi}^{(\alpha)}$ are the local Helmholtz free energy and rate of change of the Helmholtz free energy for grain α. The local Helmholtz free energy is assumed to follow the form $\Psi^{(\alpha)} \left(\mathbf{E}^{(\alpha)}, \theta, \rho_d^{(\alpha)} \right)$ where $\rho_d^{(\alpha)}$ is the dislocation density for grain α. Since $\Psi^{(\alpha)}$ is independent of the grain volume fractions $\boldsymbol{\xi}$, any changes in the surface energy of grain boundaries is neglected.

The rate of change of the local Helmholtz free energy can then be written as

$$\dot{\Psi}^{(\alpha)} = \frac{\partial \Psi^{(\alpha)}}{\partial \mathbf{E}_e^{(\alpha)}} \dot{\mathbf{E}}_e^{(\alpha)} + \frac{\partial \Psi^{(\alpha)}}{\partial \theta} \dot{\theta} + \frac{\partial \Psi^{(\alpha)}}{\partial \rho_d^{(\alpha)}} \dot{\rho}_d^{(\alpha)} \tag{5.57}$$

For simplicity, the rate of change of the dislocation density is represented as

$$\dot{\rho}_d^{(\alpha)} = \sum_{i=1}^{N_p^{(\alpha)}} \mathrm{w}_p^{(\alpha,i)} \dot{\gamma}^{(\alpha,i)} \tag{5.58}$$

where $\mathrm{w}_p^{(\alpha,i)}$ is the dependence of dislocation density on the plastic slip rates given by

$$\mathrm{w}_p^{(\alpha,i)} = \left[\frac{1}{b^{(\alpha)} k_1^{(\alpha)}} \sqrt{\rho_d^{(\alpha)}} - k_2^{(\alpha)} \rho_d^{(\alpha)} \right] \mathrm{sign}\left(\dot{\gamma}^{(\alpha,i)}\right) \tag{5.59}$$

Using $\dot{\mathbf{E}}_e^{(\alpha)} = \left[\mathbf{F}_e^{(\alpha)}\right]^T \mathbf{D}_e^{(\alpha)} \mathbf{F}_e^{(\alpha)}$ and Eq. (5.58), then Eq. (5.57) can be rewritten as

$$\dot{\Psi}^{(\alpha)} = \mathbf{F}_e^{(\alpha)} \frac{\partial \Psi^{(\alpha)}}{\partial \mathbf{E}_e^{(\alpha)}} \left[\mathbf{F}_e^{(\alpha)}\right]^T : \mathbf{D}_e^{(\alpha)} + \frac{\partial \Psi^{(\alpha)}}{\partial \theta} \dot{\theta} + \frac{\partial \Psi^{(\alpha)}}{\partial \rho_d^{(\alpha)}} \sum_{i=1}^{N_p^{(\alpha)}} \mathrm{w}_p^{(\alpha,i)} \dot{\gamma}^{(\alpha,i)} \tag{5.60}$$

The local thermal component of the reversible entropy density is given by

$$\eta_e^{(\alpha)} = h^{(\alpha)} \ln\left(\frac{\theta}{\theta_T}\right) \tag{5.61}$$

where $h^{(\alpha)}$ is the specific heat capacity of the grain α. The volume averaged rate of change of the thermomechanical coupling part of the reversible entropy density is given by

$$\langle \dot{\eta}_m \rangle = \sum_{\alpha}^{N} \dot{\xi}^{(\alpha)} \eta_m^{(\alpha)} + \xi^{(\alpha)} \dot{\eta}_m^{(\alpha)} \tag{5.62}$$

where the local thermomechanical coupling part of the reversible entropy density for grain α is assumed to take the form

$$\eta_m^{(\alpha)} = \eta_m^{(\alpha)}(\mathbf{E}_e, \eta_e) \tag{5.63}$$

This is congruous with previous work [154] because the dependence of the thermomechanical coupling part of the reversible entropy density in that work arose from homogenization of a multiphase material, whereas here the grain α is a single material. Using $\dot{\mathbf{E}}_e^{(\alpha)} = \left[\mathbf{F}_e^{(\alpha)}\right]^T \mathbf{D}_e^{(\alpha)} \mathbf{F}_e^{(\alpha)}$, the rate of change of the local thermomechanical coupling part of the reversible entropy density can be written as

$$\dot{\eta}_m^{(\alpha)} = \mathbf{F}_e \frac{\partial \eta_m^{(\alpha)}}{\partial \mathbf{E}_e^{(\alpha)}} \mathbf{F}_e^T : \mathbf{D}_e^{(\alpha)} + \frac{\partial \eta_m^{(\alpha)}}{\partial \eta_e^{(\alpha)}} \frac{\partial \eta_e^{(\alpha)}}{\partial \theta} \dot{\theta} \tag{5.64}$$

The volume-averaged rate of change of plastic slip entropy density and undeformed initial crystal entropy density is given by

$$\langle \dot{\eta}_p \rangle = \sum_{\alpha=1}^{N_g} \dot{\xi}^{(\alpha)} \eta_p^{(\alpha)} + \xi^{(\alpha)} \dot{\eta}_p^{(\alpha)} \tag{5.65}$$

$$\langle \dot{\eta}_I \rangle = \sum_{\alpha'=1}^{N_a} \sum_{\beta=1}^{24} \dot{\xi}^{(\alpha',\beta)} \left[\sum_{i=1}^{2} \lambda^{\left(\zeta_i^\beta\right)} \eta_I^{\left(\alpha',\zeta_i^\beta\right)} - \eta^{(\alpha')} \right] \tag{5.66}$$

Since the undeformed initial crystal entropy is defined at the reference temperature θ_T, the jump in initial crystal entropy can be related to the latent heat of transformation through

$$\frac{\lambda_T}{\theta_T} = \frac{\lambda_T^{(\alpha',\beta)}}{\theta_T} = \sum_{i=1}^{2} \lambda^{\left(\zeta_i^\beta\right)} \eta_I^{\left(\alpha',\zeta_i^\beta\right)} - \eta^{(\alpha')} \tag{5.67}$$

where $\lambda_T = \lambda_T^{(\alpha',\beta)}$ is the latent heat of transformation for a martensite plate β transformed from an austenite grain α', which is assumed to be equal for all austenite grains and martensite plates. Combining Eqs. (5.66) and (5.67) gives

$$\langle \dot{\eta}_I \rangle = \sum_{\alpha'=1}^{N_g} \sum_{\beta=1}^{24} \dot{\xi}^{(\alpha',\beta)} \frac{\lambda_T}{\theta_T} \tag{5.68}$$

The local rate of change of entropy generation from plastic slip is given by

$$\dot{\eta}_p^{(\alpha)} = \sum_{i=1}^{N_p^{(\alpha)}} \left| \dot{\gamma}^{(\alpha,i)} \right| \phi^{(\alpha,i)} \tag{5.69}$$

where $\phi^{(\alpha,i)}$ is the rate of entropy generation per unit slip strain in slip system i of grain α.

Following the derivation of Cherkaoui et al. [115], where perfect compatibility is assumed across the transformation surface interface such that $[\![\boldsymbol{\sigma} \cdot \mathbf{n}]\!] = 0$, and using the symmetry of the Cauchy tensor, the volume-averaged external mechanical work can be related to the local grain behaviour through

$$\langle \boldsymbol{\sigma} : \mathbf{D} \rangle = \sum_{\alpha=1}^{N_g} \boldsymbol{\sigma}^{(\alpha)} : \mathbf{D}^{(\alpha)} - \sum_{\alpha'=1}^{N_a} \sum_{\beta=1}^{24} \int_{S^{(\alpha',\beta)}} \boldsymbol{\sigma} : \left[\!\!\left[\frac{\partial \mathbf{u}}{\partial \mathbf{x}} \right]\!\!\right] \mathbf{w} \cdot \mathbf{n} \, \mathrm{d}S^{(\alpha',\beta)} \tag{5.70}$$

Using Eqs. (5.28) and (5.29) and assuming an average stress $\overline{\boldsymbol{\sigma}}^{(\alpha',\beta)}$ along the interface $S^{(\alpha',\beta)}$ given by

$$\overline{\boldsymbol{\sigma}}^{(\alpha',\beta)} = \frac{1}{S^{(\alpha',\beta)}} \int_{S^{(\alpha',\beta)}} \boldsymbol{\sigma} \, \mathrm{d}S^{(\alpha',\beta)} = \frac{1}{2} \left[\sum_{i=1}^{2} \lambda^{\left(\zeta_i^{\beta}\right)} \boldsymbol{\sigma}^{\left(\alpha',\zeta_i^{\beta}\right)} + \boldsymbol{\sigma}^{(\alpha')} \right] \tag{5.71}$$

the volume averaged external mechanical work can be rewritten as

$$\langle \boldsymbol{\sigma} : \mathbf{D} \rangle = \sum_{\alpha=1}^{N_g} \xi^{(\alpha)} \left[\boldsymbol{\sigma}^{(\alpha)} : \mathbf{D}^{(\alpha)} \right] + \sum_{\alpha'=1}^{N_a} \sum_{\beta=1}^{24} \frac{1}{2} \left[\sum_{i=1}^{2} \lambda^{\left(\zeta_i^{\beta}\right)} \boldsymbol{\sigma}^{\left(\alpha',\zeta_i^{\beta}\right)} + \boldsymbol{\sigma}^{(\alpha')} \right] : \mathbf{D}_{tr}^{(\alpha',\beta)} \tag{5.72}$$

where $\mathbf{D}_{tr}^{(\alpha',\beta)}$ is the symmetric part of the transformation velocity gradient $\mathbf{L}_{tr}^{(\alpha',\beta)}$, given by

$$\mathbf{D}_{tr}^{(\alpha',\beta)} = \mathbf{P}_{tr}^{(\alpha',\beta)} \dot{\xi}^{(\alpha',\beta)} \tag{5.73}$$

$$\mathbf{P}_{tr}^{(\alpha',\beta)} = \hat{\gamma}_{tr} \, \mathrm{sym} \left(\mathbf{b}_e^{(\alpha',\beta)} \otimes \mathbf{d}_e^{(\alpha',\beta)} \right) \tag{5.74}$$

where $\mathbf{P}_{tr}^{(\alpha',\beta)}$ is the symmetric part of the transformation deformation. Substituting Eqs. (5.15), (5.17), (5.18), (5.51), (5.56), (5.60) – (5.63), (5.65) – (5.69), and (5.72) into (5.54) and collecting terms gives the expanded dissipation equation

$$\mathcal{D} = \sum_{\alpha=1}^{N_g} \xi^{(\alpha)} \left[\mathcal{D}_e^{(\alpha)} + \mathcal{D}_\theta^{(\alpha)} + \mathcal{D}_p^{(\alpha)} \right] + \sum_{\alpha'=1}^{N_a} \sum_{\beta=1}^{24} \mathcal{D}_{tr}^{(\alpha',\beta)} + \mathcal{D}_\theta \geq 0 \tag{5.75}$$

where $\mathcal{D}_e^{(\alpha)}$, $\mathcal{D}_\theta^{(\alpha)}$ and $\mathcal{D}_p^{(\alpha)}$ are the dissipation associated with elastic strain, temperature change, and dislocation evolution, $\mathcal{D}_{tr}^{(\alpha',\beta)}$ is the dissipation due to transformation into martensite plate orientation β from austenite grain α' and $\mathcal{D}_\theta$ dissipation from heat conduction dissipation. These are given by

$$\mathcal{D}_e^{(\alpha)} = \left[\boldsymbol{\sigma}^{(\alpha)} - \rho \mathbf{F}_e \frac{\partial \Psi^{(\alpha)}}{\partial \mathbf{E}_e^{(\alpha)}} \mathbf{F}_e^T + \rho\theta \mathbf{F}_e \frac{\partial \eta_m^{(\alpha)}}{\partial \mathbf{E}_e^{(\alpha)}} \mathbf{F}_e^T \right] : \mathbf{D}_e^{(\alpha)} \tag{5.76}$$

$$\mathcal{D}_{\theta}^{(\alpha)} = \left[A^{(\alpha)} \left[\boldsymbol{\sigma}^{(\alpha)} : \mathbf{I} \right] - \rho \frac{\partial \Psi^{(\alpha)}}{\partial \theta} - \rho h^{(\alpha)} \ln \left(\frac{\theta}{\theta_T} \right) + \rho \theta \frac{\partial \eta_m^{(\alpha)}}{\partial \eta_e^{(\alpha)}} \frac{\partial \eta_e^{(\alpha)}}{\partial \theta} \right] \dot{\theta} \tag{5.77}$$

$$\mathcal{D}_{p}^{(\alpha)} = \sum_{i=1}^{N_p^{(\alpha)}} \left[\boldsymbol{\sigma}^{(\alpha)} : \mathbf{P}^{(\alpha,i)} - \rho \frac{\partial \Psi^{(\alpha)}}{\partial \rho_d^{(\alpha)}} \mathrm{w}_p^{(\alpha,i)} + \rho \theta \phi^{(\alpha,i)} \mathrm{sign} \left(\dot{\gamma}^{(\alpha,i)} \right) \right] \dot{\gamma}^{(\alpha,i)} \tag{5.78}$$

$$\begin{aligned}
\mathcal{D}_{tr}^{(\alpha',\beta)} =& \rho\theta \left[\sum_{i=1}^{2} \lambda^{\left(\zeta_i^{\beta}\right)} \eta_m^{\left(\alpha',\zeta_i^{\beta}\right)} - \eta_m^{(\alpha')} \right] \dot{\xi}^{(\alpha',\beta)} - \rho \left[\sum_{i=1}^{2} \lambda^{\left(\zeta_i^{\beta}\right)} \Psi^{\left(\alpha',\zeta_i^{\beta}\right)} - \Psi^{(\alpha')} \right] \dot{\xi}^{(\alpha',\beta)} \\
& - \rho \left[\sum_{i=1}^{2} \lambda^{\left(\zeta_i^{\beta}\right)} \xi^{\left(\alpha',\zeta_i^{\beta}\right)} \frac{\partial \Psi^{\left(\alpha',\zeta_i^{\beta}\right)}}{\partial \xi^{\left(\alpha',\zeta_i^{\beta}\right)}} - \xi^{(\alpha')} \frac{\partial \Psi^{(\alpha')}}{\partial \xi^{(\alpha')}} \right] \dot{\xi}^{(\alpha',\beta)} + \rho\theta \left[\frac{\lambda_T}{\theta_T} \right] \dot{\xi}^{(\alpha',\beta)} \\
& + \frac{1}{2} \left[\sum_{i=1}^{2} \lambda^{\left(\zeta_i^{\beta}\right)} \boldsymbol{\sigma}^{\left(\alpha',\zeta_i^{\beta}\right)} + \boldsymbol{\sigma}^{(\alpha')} \right] : \mathbf{P}_{tr}^{(\alpha',\beta)} \dot{\xi}^{(\alpha',\beta)} \\
& + \rho\theta \left[\sum_{i=1}^{2} \lambda^{\left(\zeta_i^{\beta}\right)} \eta_p^{\left(\alpha',\zeta_i^{\beta}\right)} - \eta_p^{(\alpha')} \right] \dot{\xi}^{(\alpha',\beta)}
\end{aligned} \tag{5.79}$$

$$\mathcal{D}_{\theta} = -\frac{\boldsymbol{\nabla}\theta \cdot \mathbf{q}}{\theta} \tag{5.80}$$

In this work, the material is assumed to be strongly dissipative such that

$$\mathcal{D}_{e}^{(\alpha)} \geq 0 \qquad \mathcal{D}_{\theta}^{(\alpha)} \geq 0 \qquad \mathcal{D}_{p}^{(\alpha)} \geq 0 \qquad \mathcal{D}_{tr}^{(\alpha',\beta)} \geq 0 \qquad \mathcal{D}_{\theta} \geq 0 \tag{5.81}$$

The Coleman and Noll [113] procedure then implies that

$$\rho \mathbf{F}_e \frac{\partial \Psi^{(\alpha)}}{\partial \mathbf{E}_e^{(\alpha)}} \mathbf{F}_e^T = \boldsymbol{\sigma}^{(\alpha)} + \rho\theta \mathbf{F}_e \frac{\partial \eta_m^{(\alpha)}}{\partial \mathbf{E}_e^{(\alpha)}} \mathbf{F}_e^T \tag{5.82}$$

$$\rho \frac{\partial \Psi^{(\alpha)}}{\partial \theta} = A^{(\alpha)} \left[\boldsymbol{\sigma}^{(\alpha)} : \mathbf{I} \right] - \rho h^{(\alpha)} \ln \left(\frac{\theta}{\theta_T} \right) + \rho\theta \frac{\partial \eta_m^{(\alpha)}}{\partial \eta_e^{(\alpha)}} \frac{\partial \eta_e^{(\alpha)}}{\partial \theta} \tag{5.83}$$

Integrating Eq. (5.82) with respect to $\mathbf{E}_e$ allows the Helmholtz free energy to be written as

$$\Psi^{(\alpha)} = \frac{1}{2\rho}\mathbb{C}^{(\alpha)} : \left[\mathbf{E}_e^{(\alpha)} \otimes \mathbf{E}_e^{(\alpha)}\right] + \theta\eta_m^{(\alpha)} + \Psi_1^{(\alpha)}\left(\theta, \rho_d^{(\alpha)}\right) \tag{5.84}$$

where $\Psi_1^{(\alpha)}\left(\theta, \rho_d^{(\alpha)}\right)$ is an integration constant representing the dependence of Helmholtz free energy on temperature and dislocation density. Taking the partial derivative of Eq. (5.84) with respect to temperature and substituting into Eq. (5.83) gives

$$\eta_m^{(\alpha)} = \frac{1}{\rho}A^{(\alpha)}\left[\boldsymbol{\sigma}^{(\alpha)} : \mathbf{I}\right] - \left[\frac{\partial\Psi_1^{(\alpha)}}{\partial\theta} + h^{(\alpha)}\ln\left(\frac{\theta}{\theta_T}\right)\right] \tag{5.85}$$

Since η_m should disappear ($\eta_m = 0$) when no stress is applied ($\boldsymbol{\sigma}^{(\alpha)} = \mathbf{0}$), then

$$\eta_m^{(\alpha)} = \frac{1}{\rho}A^{(\alpha)}\left[\boldsymbol{\sigma}^{(\alpha)} : \mathbf{I}\right] \tag{5.86}$$

$$\frac{\partial\Psi_1^{(\alpha)}}{\partial\theta} = -h^{(\alpha)}\ln\left(\frac{\theta}{\theta_T}\right) = -\eta_e^{(\alpha)} \tag{5.87}$$

Integrating Eq. (5.87) with respect to temperature, $\Psi_1^{(\alpha)}$ can be written as

$$\Psi_1^{(\alpha)} = -\eta_e^{(\alpha)}\theta + h^{(\alpha)}\theta + \Psi_2^{(\alpha)}\left(\rho_d^{(\alpha)}\right) \tag{5.88}$$

where $\Psi_2^{(\alpha)}\left(\rho_d^{(\alpha)}\right)$ is a constant of integration representing the dependence of Helmholtz free energy on the dislocation density. Following Tjahjanto et al. [119], this dependence can be written as

$$\Psi_2^{(\alpha)}\left(\rho_d^{(\alpha)}\right) = \Psi_d^{(\alpha)}\left(\rho_d^{(\alpha)}\right) + \Psi_3^{(\alpha)} \tag{5.89}$$

where the change in surface energy due to transformation is neglected, $\Psi_d^{(\alpha)}\left(\rho_d^{(\alpha)}\right)$ represents the dependence of the Helmholtz free energy on dislocation density and $\Psi_3^{(\alpha)}$ is a constant representing the Helmholtz free energy of grain α with no elastic strain or dislocation density and at the reference temperature $\theta = \theta_T$. The dependence of Helmholtz free energy on the dislocation density is then given by

$$\Psi_d^{(\alpha)} = \frac{1}{2\rho}\omega^{(\alpha)}\mu^{(\alpha)}\left[b^{(\alpha)}\right]^2\rho_d^{(\alpha)} \tag{5.90}$$

where $\omega^{(\alpha)}$ is the coefficient representing the impact of dislocation density on energy for grain α, and $\mu^{(\alpha)}$ is the shear modulus for grain α. In this work, it is assumed that $\mu^{(\alpha)} = c_{44}^{(\alpha)}$.

Combining Eqs. (5.84), (5.87), (5.89) and (5.90) gives the Helmholtz free energy as

$$\begin{aligned}\Psi^{(\alpha)} =& \frac{1}{2\rho}\mathbb{C}^{(\alpha)} : \left[\mathbf{E}_e^{(\alpha)} \otimes \mathbf{E}_e^{(\alpha)}\right] + \theta\eta_m^{(\alpha)} - \eta_e^{(\alpha)}\theta + h^{(\alpha)}\theta \\ &+ \frac{1}{2\rho}\omega^{(\alpha)}\mu^{(\alpha)}\left[b^{(\alpha)}\right]^2 \rho_d^{(\alpha)} + \Psi_3^{(\alpha)}\end{aligned} \tag{5.91}$$

Following the terminology of Onsager (see, e.g. Callen [155]), the plastic slip and transformation dissipation can be written as the product of driving forces and the corresponding fluxes, such that

$$\mathcal{D}_p^{(\alpha)} = \sum_{i=1}^{N_p^{(\alpha)}} f_p^{(\alpha,i)}\dot{\gamma}^{(\alpha,i)} \tag{5.92}$$

$$\mathcal{D}_{tr}^{(\alpha',\beta)} = f_{tr}^{(\alpha',\beta)}\dot{\xi}^{(\alpha',\beta)} \tag{5.93}$$

where $f_p^{(\alpha,i)}$ is the driving force of the slip rate $\dot{\gamma}^{(\alpha,i)}$ of slip system i of grain α and $f_{tr}^{(\alpha'\beta)}$ is the driving force of martensitic transformation $\dot{\xi}^{(\alpha',\beta)}$ of martensite plate β transformed from austenite grain α'. Note that the volume fraction rates $\dot{\xi}^{(\alpha',\beta)}$ must be used instead of the rates $\dot{\xi}^{(\alpha',\zeta_i^\beta)}$ because the rates $\dot{\xi}^{(\alpha',\zeta_1^\beta)}$ and $\dot{\xi}^{(\alpha',\zeta_2^\beta)}$ are not independent. The plastic slip driving force $f_p^{(\alpha,i)}$ is given by

$$f_p^{(\alpha,i)} = \underbrace{f_{p,1}^{(\alpha,i)}}_{\text{Resolved Stress}} + \underbrace{f_{p,2}^{(\alpha,i)}}_{\text{Dynamic recovery}} - \underbrace{f_{p,3}^{(\alpha,i)}}_{\text{Dislocation Generation}} + \underbrace{f_{p,4}^{(\alpha,i)}}_{\text{Entropy Generation}} \tag{5.94}$$

where the included terms represent the resolved stress, dynamic recovery, dislocation generation, and entropy generation. In this work, it has been assumed that $\text{sign}\left(\dot{\gamma}^{(\alpha,i)}\right) = \text{sign}\left(f_{p,1}^{(\alpha,i)}\right)$ such that the driving force components are given by

$$f_{p,1}^{(\alpha,i)} = \boldsymbol{\sigma}^{(\alpha)} : \mathbf{P}_p^{(\alpha,i)} \tag{5.95}$$

$$f_{p,2}^{(\alpha,i)} = \frac{1}{2}\omega^{(\alpha)}\mu^{(\alpha)}\left[b^{(\alpha)}\right]^2 k_2^{(\alpha)}\rho_d^{(\alpha)}\text{sign}\left(f_{p,1}^{(\alpha,i)}\right) \tag{5.96}$$

$$f_{p,3}^{(\alpha,i)} = \frac{\omega^{(\alpha)}\mu^{(\alpha)}b^{(\alpha)}}{2k_1^{(\alpha)}}\sqrt{\rho_d^{(\alpha)}}\text{sign}\left(f_{p,1}^{(\alpha,i)}\right) \tag{5.97}$$

$$f_{p,4}^{(\alpha,i)} = \rho\theta\phi^{(\alpha,\beta)}\text{sign}\left(f_{p,1}^{(\alpha,i)}\right) \tag{5.98}$$

The transformation driving force $f_{tr}^{(\alpha',\beta)}$ is given by

$$\begin{aligned} f_{tr}^{(\alpha',\beta)} = & \underbrace{f_{tr,1}^{(\alpha',\beta)}}_{\text{Resolved Stress}} + \underbrace{f_{tr,2}^{(\alpha',\beta)}}_{\text{Latent Heating}} + \underbrace{f_{tr,3}^{(\alpha',\beta)}}_{\substack{\text{Plastic Entropy} \\ \text{Jump}}} \\ & - \underbrace{f_{tr,4}^{(\alpha',\beta)}}_{\substack{\text{Internal Thermal} \\ \text{Energy Jump}}} - \underbrace{f_{tr,5}^{(\alpha',\beta)}}_{\substack{\text{Elastic Distortion} \\ \text{Energy Jump}}} - \underbrace{f_{tr,6}^{(\alpha',\beta)}}_{\substack{\text{Dislocation} \\ \text{Energy Jump}}} \end{aligned} \tag{5.99}$$

where the included terms represent the resolved stress on the transformation system, the latent heating, and the jumps in plastic entropy, internal thermal energy, elastic distortion energy, and stored dislocation energy between the austenite and martensite plate orientation β transformed from austenite grain α'. These terms are then given by

$$f_{tr,1}^{(\alpha',\beta)} = \frac{1}{2}\left[\left[\sum_{i=1}^{2}\lambda^{\left(\zeta_i^\beta\right)}\boldsymbol{\sigma}^{\left(\alpha',\zeta_i^\beta\right)} + \boldsymbol{\sigma}^{(\alpha')}\right] : \mathbf{P}_{tr}^{(\alpha',\beta)}\right] \tag{5.100}$$

$$f_{tr,2}^{(\alpha',\beta)} = \rho\left[\theta\right]\left[\frac{\lambda_T}{\theta_T}\right] \tag{5.101}$$

$$f_{tr,3}^{(\alpha',\beta)} = \rho\left[\sum_{i=1}^{2}\lambda^{\left(\zeta_i^\beta\right)}\eta_p^{\left(\alpha',\zeta_i^\beta\right)} - \eta_p^{(\alpha')}\right]\theta \tag{5.102}$$

$$\begin{aligned} f_{tr,4}^{(\alpha',\beta)} = & \rho\left[\sum_{i=1}^{2}\lambda^{\left(\zeta_i^\beta\right)}h^{\left(\alpha',\zeta_i^\beta\right)} - h^{(\alpha')}\right]\left[\theta - \ln\left(\frac{\theta}{\theta_T}\right)\theta\right] \\ & + \rho\sum_{i=1}^{2}\lambda^{\left(\zeta_i^\beta\right)}\Psi_3^{\left(\alpha',\zeta_i^\beta\right)} - \rho\Psi_3^{(\alpha')} \end{aligned} \tag{5.103}$$

$$f_{tr,5}^{(\alpha',\beta)} = \sum_{i=1}^{2}\frac{1}{2}\lambda^{\left(\zeta_i^\beta\right)}\mathbb{C}^{\left(\alpha',\zeta_i^\beta\right)} : \left[\mathbf{E}_e^{\left(\alpha',\zeta_i^\beta\right)} \otimes \mathbf{E}_e^{\left(\alpha',\zeta_i^\beta\right)}\right] - \frac{1}{2}\mathbb{C}^{(\alpha')} : \left[\mathbf{E}_e^{(\alpha')} \otimes \mathbf{E}_e^{(\alpha')}\right] \tag{5.104}$$

$$f_{tr,6}^{(\alpha',\beta)} = \sum_{i=1}^{2} \lambda^{\left(\zeta_i^{\beta}\right)} \frac{1}{2} \omega^{\left(\alpha',\zeta_i^{\beta}\right)} \mu^{\left(\alpha',\zeta_i^{\beta}\right)} \left[b^{\left(\alpha',\zeta_i^{\beta}\right)}\right]^2 \rho_d^{\left(\alpha',\zeta_i^{\beta}\right)} - \frac{1}{2} \omega^{(\alpha')} \mu^{(\alpha')} \left[b^{(\alpha')}\right]^2 \rho_d^{(\alpha')} \tag{5.105}$$

Since the driving force for transformation should be zero by definition with vanishing dislocation density $\left(\rho_d^{\left(\alpha',\zeta_i^{\beta}\right)} = 0\right)$ and elastic strain $\left(\mathbf{E}_e^{\left(\alpha',\zeta_i^{\beta}\right)} = \mathbf{0}\right)$ at the reference temperature $\theta = \theta_T$, the value of the base Helmholtz free energy $\Psi_3^{(\alpha)}$ can be restricted through

$$f_{tr}^{(\alpha',\beta)} = 0 = \rho \left[h^{(\alpha')}\theta_T + \Psi_3^{(\alpha')}\right] - \rho \sum_{i=1}^{2} \lambda^{\left(\zeta_i^{\beta}\right)} \left[h^{\left(\alpha',\zeta_i^{\beta}\right)}\theta_T + \Psi_3^{\left(\alpha',\zeta_i^{\beta}\right)}\right] + \rho\lambda_T \tag{5.106}$$

which gives a relationship between the base martensite grain α and austenite such that

$$\sum_{i=1}^{2} \lambda^{\left(\zeta_i^{\beta}\right)} \Psi_3^{\left(\alpha',\zeta_i^{\beta}\right)} - \Psi_3^{(\alpha')} = \lambda_T - \sum_{i=1}^{2} \left[\lambda^{\left(\zeta_i^{\beta}\right)} h^{\left(\alpha',\zeta_i^{\beta}\right)} - h^{(\alpha')}\right] \theta_T \qquad \forall\alpha' \quad \forall\beta \tag{5.107}$$

Substituting Eq. (5.107) into Eq. (5.99) and rearranging gives new latent heat and internal thermal energy components of the driving force, given by

$$f_{tr,2}^{(\alpha',\beta)} = \rho \left[\theta - \theta_T\right] \left[\frac{\lambda_T}{\theta_T}\right] \tag{5.108}$$

$$f_{tr,4}^{(\alpha',\beta)} = \rho \left[\sum_{i=1}^{2} \lambda^{\left(\zeta_i^{\beta}\right)} h^{\left(\alpha',\zeta_i^{\beta}\right)} - h^{(\alpha')}\right] \left[\theta - \theta_T - \ln\left(\frac{\theta}{\theta_T}\right)\theta\right] \tag{5.109}$$

Finally, combining Eqs. (5.15), (5.17), (5.18), (5.45), (5.51), (5.52), (5.53), (5.55), (5.61), (5.68), (5.69), (5.72), (5.86), and (5.107) gives the constitutive equation for the evolution of material temperature

$$\rho\left[\sum_{\alpha=1}^{N_g}\xi^{(\alpha)}h^{(\alpha)}\right]\dot{\theta} = -\sum_{\alpha=1}^{N_g}\xi^{(\alpha)}\mathbf{M}_e^{(\alpha)}:\mathbf{D}_e^{(\alpha)} + \sum_{\alpha=1}^{N_g}\sum_{i=1}^{N_p^{(\alpha)}}\xi^{(\alpha)}M_p^{(\alpha,i)}\dot{\gamma}^{(\alpha,i)} + \sum_{\alpha'=1}^{N_a}\sum_{\beta=1}^{24}M_{tr}^{(\alpha',\beta)}\dot{\bar{\xi}}^{(\alpha',\beta)} - \boldsymbol{\nabla}\cdot\mathbf{q} \tag{5.110}$$

where $\mathbf{M}_e^{(\alpha)}$ and $M_p^{(\alpha,i)}$ represent the change in internal energy due to elastic stretching and plastic slip if grain α and $M_{tr}^{(\alpha',\beta)}$ represents the energy dissipated during transformation of martensite plate β form austenite grain α'. These terms are given by

$$\mathbf{M}_e^{(\alpha)} = 4\theta A^{(\alpha)}\boldsymbol{\sigma}^{(\alpha)} + \theta A^{(\alpha)}\mathbf{F}_e^{(\alpha)}\left[\mathbf{I}:\mathbb{C}^{(\alpha)}\right]\left[\mathbf{F}_e^{(\alpha)}\right]^T \tag{5.111}$$

$$M_p^{(\alpha,i)} = f_{p,1}^{(\alpha,i)} + f_{p,2}^{(\alpha,i)} - f_{p,3}^{(\alpha,i)} \tag{5.112}$$

$$M_{tr}^{(\alpha',\beta)} = f_{tr,1}^{(\alpha',\beta)} - f_{tr,5}^{(\alpha',\beta)} - f_{tr,6}^{(\alpha',\beta)} - \rho\lambda_T - \sum_{i=1}^{2}\theta\lambda^{\left(\zeta_i^\beta\right)}A^{\left(\alpha',\zeta_i^\beta\right)}\left[\boldsymbol{\sigma}^{\left(\alpha',\zeta_i^\beta\right)}:\mathbf{I}\right] + \theta A^{(\alpha')}\left[\boldsymbol{\sigma}^{(\alpha')}:\mathbf{I}\right] - \rho\left[\sum_{i=1}^{2}\lambda^{\left(\zeta_i^\beta\right)}h^{\left(\alpha',\zeta_i^\beta\right)} - h^{(\alpha')}\right][\theta-\theta_T] \tag{5.113}$$

5.2.5 Kinetics Relations

Thermodynamic fluxes are related to the driving forces through kinetic relations. For plastic slip, the rate of plastic shearing is related to the plasticity driving force through

$$\dot{\gamma}^{(\alpha,i)} = \begin{cases} a^{(\alpha)}\text{sign}\left(f_{p,1}^{(\alpha,i)}\right)\left|\dfrac{f_p^{(\alpha,i)}}{g_p^{(\alpha)}}\right|^{1/m^{(\alpha)}} & f_{p,1}^{(\alpha,i)} + f_{p,2}^{(\alpha,i)} + f_{p,4}^{(\alpha,i)} > f_{p,3}^{(\alpha,i)} \\ 0 & f_{p,1}^{(\alpha,i)} + f_{p,2}^{(\alpha,i)} + f_{p,4}^{(\alpha,i)} \leq f_{p,3}^{(\alpha,i)} \end{cases} \tag{5.114}$$

where $a^{(\alpha)}$, $m^{(\alpha)}$ and $g_p^{(\alpha)}$ are the reference rate, rate coefficient and critical plastic slip driving force for grain α. The critical plastic slip driving force can be related to the dislocation density in grain α through

$$g_p^{(\alpha)} = g_{p,0}^{(\alpha)} + c^{(\alpha)}\mu^{(\alpha)}b^{(\alpha)}\sqrt{\rho_d^{(\alpha)}} \tag{5.115}$$

where $g_{p,0}^{(\alpha)}$ is the initial critical driving force for grain α and $c^{(\alpha)}$ is the interaction coefficient between dislocation in grain α.

Based on the work of Olson and Cohen [18] and Stringfellow et al. [83], the transformation rate is given by

$$\begin{aligned}\dot{\xi}^{(\alpha',\beta)} &= \xi^{(\alpha')}\nu_m \dot{N}_t^{(\alpha',\beta)} \\ &= \xi^{(\alpha')}\nu_m \Bigg[\underbrace{P_n^{(\alpha',\beta)}\dot{N}_n^{(\alpha')}}_{\substack{\text{Transformation at new} \\ \text{nucleation sites}}} + \underbrace{R\Big(\dot{P}_n^{(\alpha',\beta)}\Big) N_n^{(\alpha')}}_{\substack{\text{Transformation at deformation} \\ \text{induced nucleation sites}}} + \underbrace{R\Big(\dot{P}_o^{(\alpha',\beta)}\Big) N_o}_{\substack{\text{Transformation at original} \\ \text{microstructure nucleation sites}}} \Bigg]\end{aligned} \tag{5.116}$$

where ν_m is the average volume of a newly transformed martensitic unit, $\dot{N}_t^{(\alpha',\beta)}$ is the rate of change of the number of transformed martensite units with orientation β per unit volume of austenite grain α', $P_n^{(\alpha',\beta)}$ is the probability of a strain-induced martensite nucleation site in austenite grain α' transforming into martensite plate orientation β, $N_n^{(\alpha')}$ is the number of strain-induced martensite nucleation sites per unit volume of austenite grain α', $P_o^{(\alpha',\beta)}$ is the probability of a nucleation site in the original microstructure in austenite grain α' transforming into martensite plate orientation β, N_o is the number of martensite nucleation sites in the original microstructure per unit austenite volume (assumed constant for all grains), and $R(\star) = \max(0, \star)$ is a ramp function. The original microstructure and strain-induced martensite nucleation sites are treated separately because the probability of transformation may be different for each type of nucleation site. The first and second terms in Eq. (5.116) represent the transformation due to the formation of strain-induced nucleation sites, and due to the increase in transformation driving force at the existing strain-induced nucleation sites, respectively. The third term represents transformation due to the increase in transformation driving force at martensite nucleation sites in the original microstructure. The number of martensite nucleation sites per unit austenite volume is related to the volume fraction of shear band intersections through

$$N_n^{(\alpha')} = \frac{f_I^{(\alpha')}}{\nu_I} \tag{5.117}$$

where $f_I^{(\alpha')}$ is the volume fraction of shear band intersections in austenite grain α' and

ν_I is the average volume fraction of a shear band intersection site. Following Stringfellow et al. [83], the volume fraction of the shear band intersection sites is related to the volume fraction of shear bands through

$$f_I^{(\alpha')} = \kappa_I \left(f_{sb}^{(\alpha')} \right)^{n_I} \tag{5.118}$$

where κ_I and n_I are power law calibration coefficients and $f_{sb}^{(\alpha')}$ is the volume fraction of shear bands in austenite grain α'. Combining the approach of Stringfellow et al. [83] and Ma and Hartmaier [120], the shear band volume fraction evolution is related to the strain projected onto the shear band systems by

$$\dot{f}_{sb}^{(\alpha')} = \left(1 - f_{sb}^{(\alpha')}\right) a_{sb}^{(\alpha')} \dot{\gamma}_{sb}^{(\alpha')} \tag{5.119}$$

where $\dot{\gamma}_{sb}^{(\alpha')}$ is the total absolute rate of plastic shearing projected on the shear band system i in austenite grain α' and $a_{sb}^{(\alpha')}$ determines the rate of shear band formation in austenite grain α'. Building on the approach of Kohar et al. [9], this coefficient is modelled as a function of the temperature and strain-rate by

$$a_{sb}^{(\alpha')} = \left(a_1 + a_2\theta + a_3\theta^2\right) \left(1 - a_4 \left(\frac{\dot{\gamma}_{sb}^{(\alpha')}}{a^{(\alpha')}}\right)^{a_5}\right) \tag{5.120}$$

where a_1–a_5 are calibration coefficients and $a^{(\alpha')}$ is the reference rate used in the plastic slip kinetics equation for the austenite grain α'.

As in Kim et al. [131] and Zhang et al. [13], the total absolute shear rate on the shear bands is related to the slip rate on the slip systems through the projection

$$\dot{\gamma}_{sb}^{(\alpha')} = \sum_{i=1}^{N_{sb}} \sum_{j=1}^{N_p^{(\alpha')}} H^{(\alpha',i,j)} \left| \dot{\gamma}^{(\alpha',j)} \right| \tag{5.121}$$

where N_{sb} is the number of shear band systems and $\mathbf{H}$ is the absolute value of the projection matrix from the slip systems onto the fault bands in the same plane. In this work, the absolute value of the projection matrix from the slip systems onto the fault bands in the same plane is defined by

$$H^{(\alpha',i,j)} = \begin{cases} \left| \left[\overline{\mathbf{s}}^{(\alpha',i)} \otimes \overline{\mathbf{m}}^{(\alpha',i)} \right] : \left[\mathbf{s}^{(\alpha',j)} \otimes \mathbf{m}^{(\alpha',j)} \right] \right| & \overline{\mathbf{m}}^{(\alpha',i)} = \mathbf{m}^{(\alpha',j)} \\ 0 & \overline{\mathbf{m}}^{(\alpha',i)} \neq \mathbf{m}^{(\alpha',j)} \end{cases} \tag{5.122}$$

where $\overline{\mathbf{s}}^{(\alpha',i)}$ and $\overline{\mathbf{m}}^{(\alpha',i)}$ are the shear band direction and normals related to the cubic axes of austenite grain α' through

$$\overline{\mathbf{s}}^{(\alpha',i)} = \overline{s}_j^{(\alpha',i)} \mathbf{e}_j^{(\alpha')} \tag{5.123}$$

$$\overline{\mathbf{m}}^{(\alpha',i)} = \overline{m}_j^{(\alpha',i)} \mathbf{e}_j^{(\alpha')} \tag{5.124}$$

The shear band systems are defined using the $\langle 211 \rangle \otimes \langle 111 \rangle$ family, enumerated in Table 5.1.

Table 5.1: Shear band systems.

i	$\overline{s}_j^{(\alpha,i)}$	$\overline{m}_j^{(\alpha,i)}$	i	$\overline{s}_j^{(\alpha,i)}$	$\overline{m}_j^{(\alpha,i)}$	i	$\overline{s}_j^{(\alpha,i)}$	$\overline{m}_j^{(\alpha,i)}$	i	$\overline{s}_j^{(\alpha,i)}$	$\overline{m}_j^{(\alpha,i)}$
1	$\langle 211 \rangle$	$\langle 1\bar{1}\bar{1} \rangle$	4	$\langle 2\bar{1}1 \rangle$	$\langle 11\bar{1} \rangle$	7	$\langle 21\bar{1} \rangle$	$\langle 1\bar{1}1 \rangle$	10	$\langle \bar{2}11 \rangle$	$\langle 111 \rangle$
2	$\langle 12\bar{1} \rangle$	$\langle 1\bar{1}\bar{1} \rangle$	5	$\langle \bar{1}21 \rangle$	$\langle 11\bar{1} \rangle$	8	$\langle 121 \rangle$	$\langle 1\bar{1}1 \rangle$	11	$\langle 1\bar{2}1 \rangle$	$\langle 111 \rangle$
3	$\langle 1\bar{1}2 \rangle$	$\langle 1\bar{1}\bar{1} \rangle$	6	$\langle 112 \rangle$	$\langle 11\bar{1} \rangle$	9	$\langle \bar{1}12 \rangle$	$\langle 1\bar{1}1 \rangle$	12	$\langle 11\bar{2} \rangle$	$\langle 111 \rangle$

Using this shear band family, the projection matrix $\mathbf{H}$ is the absolute value of the projection matrix used in Ma and Hartmaier [120], Kim et al. [131] and Zhang et al. [13]. Using this projection matrix, Eq. (5.121) can be rewritten as

$$\dot{\gamma}_{sb}^{(\alpha')} = \sum_{i=1}^{N_{sb}} \sum_{j=1}^{N_p^{(\alpha')}} H^{(\alpha',i,j)} \left| \dot{\gamma}^{(\alpha',j)} \right| = \sqrt{3} \sum_{j=1}^{N_p^{(\alpha')}} \left| \dot{\gamma}^{(\alpha',j)} \right| \tag{5.125}$$

Combining Eqs. (5.116), (5.117), (5.118), (5.119), (5.120), and (5.121) gives the final transformation kinetics equation

$$\begin{aligned} \dot{\xi}^{(\alpha',\beta)} = {} & \sqrt{3} \xi^{(\alpha')} \kappa P_n^{(\alpha',\beta)} n_I \left(f_{sb}^{(\alpha')} \right)^{n_I - 1} \left(1 - f_{sb}^{(\alpha')} \right) a_{sb}^{(\alpha')} \sum_{j=1}^{N_p^{(\alpha')}} \left| \dot{\gamma}^{(\alpha',j)} \right| + \\ & \xi^{(\alpha')} \kappa R \left(\dot{P}_n^{(\alpha',\beta)} \right) \left(f_{sb}^{(\alpha')} \right)^{n_I} + \xi^{(\alpha')} R \left(\dot{P}_o^{(\alpha',\beta)} \right) f_o \end{aligned} \tag{5.126}$$

where without loss of generality, the variables κ_I, ν_m, ν_I and N_o have been replaced with the calibration coefficients κ and f_o such that

$$\kappa = \kappa_I \frac{\nu_m}{\nu_I} \tag{5.127}$$

$$f_o = \frac{\nu_m N_o}{\kappa} = \frac{\nu_I N_o}{\kappa_I} \tag{5.128}$$

The transformation probabilities are calculated as a function of the driving force by assuming the resistance to the transformation of the austenite phase follows a Gaussian distribution [18]. For martensite transformation at strain-induced nucleation sites, this is given by

$$P_n^{(\alpha',\beta)} = \frac{1}{\sqrt{2\pi}\sigma_{tr,n}} \int_{-\infty}^{f_{tr}^{(\alpha',\beta)}} \exp\left(-\frac{g' - g_{tr,n}}{2\sigma_{tr,n}^2}\right) \mathrm{d}g' = \frac{1}{2}\left(1 + \mathrm{erf}\left(\frac{f_{tr}^{(\alpha',\beta)} - g_{tr,n}}{\sqrt{2}\sigma_{tr,n}}\right)\right) \tag{5.129}$$

where $g_{tr,n}$ and $\sigma_{tr,n}$ are the mean and standard deviation of the critical transformation driving force required for transformation in strain-induced nucleation sites. The rate of change of the probability of transformation in the strain-induced and pre-existing nucleation sites are given by

$$\dot{P}_n^{(\alpha',\beta)} = \frac{1}{\sqrt{2\pi}\sigma_{tr,n}} \exp\left[-\left(\frac{f_{tr}^{(\alpha',\beta)} - g_{tr,n}}{\sqrt{2}\sigma_{tr,n}}\right)^2\right] \dot{f}_{tr}^{(\alpha',\beta)} \tag{5.130}$$

$$\dot{P}_o^{(\alpha',\beta)} = \frac{1}{\sqrt{2\pi}\sigma_{tr,o}} \exp\left[-\left(\frac{f_{tr}^{(\alpha',\beta)} - g_{tr,o}}{\sqrt{2}\sigma_{tr,o}}\right)^2\right] \dot{f}_{tr}^{(\alpha',\beta)} \tag{5.131}$$

where $g_{tr,o}$ and $\sigma_{tr,o}$ are the mean and standard deviation of the critical transformation driving force required for transformation of nucleation sites in the original microstructure.

5.3 Numerical Model

This section provides a complete numerical model for simulation of the thermo-mechanical behaviour of steel exhibiting the TRIP effect. Section 5.3.1 gives an overview of the overall thermo-mechanical model boundary conditions used in this model. Section 5.3.2 provides a detailed rate-tangent [141] formulation used to integrate the plastic slip in each crystal for

constitutive model derived in Section 5.2. Finally, Section 5.3.3 provides the overall incremental formulation and an outline of the integration algorithm used to solve the coupled thermo-mechanical problem.

5.3.1 Thermo-Mechanical Model and Boundary Conditions

This work incorporates the constitutive model into a single integration point coupled thermo-mechanical model. If L_{11} is aligned with the loading direction, then uniaxial tension boundary conditions can be summarized by

$$\begin{gathered} \langle L_{11} \rangle = \dot{\varepsilon}_{app} \\ \langle L_{12} \rangle = \langle L_{21} \rangle = \langle L_{13} \rangle = \langle L_{31} \rangle = \langle L_{23} \rangle = \langle L_{32} \rangle = 0 \\ \langle \sigma_{22} \rangle = \langle \sigma_{33} \rangle = 0 \end{gathered} \tag{5.132}$$

where $\dot{\varepsilon}_{app}$ is the applied strain-rate for a simulated case. General biaxial tension boundary conditions are given by

$$\begin{gathered} \langle L_{11} \rangle = \dot{\varepsilon}_{app} \\ \langle L_{22} \rangle = P \langle L_{11} \rangle \\ \langle L_{12} \rangle = \langle L_{21} \rangle = \langle L_{13} \rangle = \langle L_{31} \rangle = \langle L_{23} \rangle = \langle L_{32} \rangle = 0 \\ \langle \sigma_{33} \rangle = 0 \end{gathered} \tag{5.133}$$

where P is a proportionality constant where $P = -0.5$ approximately represents uniaxial tension, $P = 0$ represents plane strain tension and $P = 1$ represents equibiaxial tension. The thermal integration point is defined using a rectangular prismatic control volume, which encloses the entire cross section of the uniaxial tension sample, but only a small portion of the length. Temperature within the control volume is assumed to be approximately spatially invariant (constant throughout the volume at any point in time) such that the thermal boundary conditions are governed by

$$\int_V \rho \left[\sum_{\alpha=1}^{N_g} \xi^{(\alpha)} h^{(\alpha)} \right] \dot{\theta} \mathrm{d}V = w \ell t \rho \left[\sum_{\alpha=1}^{N_g} \xi^{(\alpha)} h^{(\alpha)} \right] \dot{\theta} = Q_{gen} - Q_{bound} \tag{5.134}$$

where w, ℓ and t are the width, length and thickness of the control volume, Q_{gen} is the total volumetric heat generation and Q_{bound} is the heat lost to the thermal boundary. The total heat generation is further decomposed into elastic (Q_e), plastic slip (Q_p) and TRIP (Q_{tr}) components such that

$$Q_{gen} = Q_e + Q_p + Q_{tr} \tag{5.135a}$$

$$Q_e = -\int_V \sum_{\alpha=1}^{N_g} \xi^{(\alpha)} \mathbf{M}_e^{(\alpha)} : \mathbf{D}_e^{(\alpha)} \, \mathrm{d}V = -w\ell t \sum_{\alpha=1}^{N_g} \xi^{(\alpha)} \mathbf{M}_e^{(\alpha)} : \mathbf{D}_e^{(\alpha)} \tag{5.135b}$$

$$Q_p = \int_V \sum_{\alpha=1}^{N_g} \sum_{i=1}^{N_p^{(\alpha)}} \xi^{(\alpha)} M_p^{(\alpha,i)} \dot{\gamma}^{(\alpha,i)} \, \mathrm{d}V = w\ell t \sum_{\alpha=1}^{N_g} \sum_{i=1}^{N_p^{(\alpha)}} \xi^{(\alpha)} M_p^{(\alpha,i)} \dot{\gamma}^{(\alpha,i)} \tag{5.135c}$$

$$Q_{tr} = \int_V \sum_{\alpha'=1}^{N_a} \sum_{\beta=1}^{24} M_{tr}^{(\alpha',\beta)} \dot{\overline{\xi}}^{(\alpha',\beta)} \, \mathrm{d}V = w\ell t \sum_{\alpha'=1}^{N_a} \sum_{\beta=1}^{24} M_{tr}^{(\alpha',\beta)} \dot{\overline{\xi}}^{(\alpha',\beta)} \tag{5.135d}$$

The thermal boundary heat loss per is then decomposed into conduction (Q_{cond}) and convection (Q_{conv}) components, where conduction occurs on the two faces attached to the rest of the uniaxial tension specimen and convection occurs on all surface exposed to air (i.e. all other surfaces). These heat flux components are defined by

$$\begin{aligned} Q_{bound} = \int_V \boldsymbol{\nabla} \cdot \mathbf{q} \, \mathrm{d}V &= Q_{conv} + Q_{cond} \\ Q_{conv} &= 2(w+t)\ell h(\theta - \theta_\infty) \\ Q_{cond} &= 2wtR_{cond}(\theta - \theta_\infty) \end{aligned} \tag{5.136}$$

where h is the convection coefficient between the air and the control volume, R_{cond} is a coefficient governing conduction from the control volume into the rest of the sample, and θ_∞ is the temperature of the thermal boundaries (i.e. the air and the gripping mechanism for the sample). The coefficient R_{cond} includes the effect of conduction into the gripping mechanism as well as convection from the rest of the sample into the air. Since the convection and conduction coefficients are difficult to define and because the thermal boundary temperature for both effects are identical, a single effective heat transfer coefficient can be defined using

$$Q_{bound} = A_{tot} R_{eff} (\theta - \theta_\infty) \tag{5.137}$$

where $A_{tot} = 2(wt + w\ell + \ell t)$ is the total surface area of the control volume and R_{eff} is an effective heat transfer coefficient given by

$$R_{eff} = \frac{2wtR_{cond} + 2(w+t)\ell h}{A_{tot}} \tag{5.138}$$

Due to the difficulty of calculating the effective heat transfer coefficient analytically, it will instead be determined directly from the experiments during model calibration. Directly capturing convection and conduction into the gripping mechanism can be achieved using finite element modelling, which is beyond the scope of this work.

5.3.2 Incremental Constitutive Formulation

This section provides a derivation of a rate-tangent scheme [141, 147] used to integrate the plastic slip rates for each crystal in the polycrystalline aggregate. This algorithm provides a higher-order semi-implicit estimate of the plastic slip vector increment $\Delta\boldsymbol{\gamma}$ to facilitate the use of larger time steps when integrating the polycrystalline aggregate. The change in plastic slip is estimated using

$$\Delta\gamma^{(\alpha,i)} = \left[(1-\Lambda)\dot{\gamma}^{(\alpha,i)}(t) + \Lambda\dot{\gamma}^{(\alpha,i)}(t+\Delta t)\right]\Delta t \tag{5.139}$$

where Λ is an integration parameter determining the dependence on the estimated next timestep. When $\Lambda = 0$, the algorithm becomes a first-order forward Euler method. This work uses $\Lambda = 0.5$, which gives good results in most cases. The rate term at time $t + \Delta t$ is estimated using a Taylor expansion

$$\dot{\gamma}^{(\alpha,i)}(t+\Delta t) = \dot{\gamma}^{(\alpha,i)}(t) + \frac{\partial\dot{\gamma}^{(\alpha,i)}(t)}{\partial f_p^{(\alpha,i)}}\Delta f_p^{(\alpha,i)} + \frac{\partial\dot{\gamma}^{(\alpha,i)}(t)}{\partial g_p^{(\alpha,i)}}\Delta g_p^{(\alpha,i)} \tag{5.140}$$

where the derivatives $\frac{\partial\dot{\gamma}^{(\alpha,i)}(t)}{\partial f_p^{(\alpha,i)}}$ and $\frac{\partial\dot{\gamma}^{(\alpha,i)}(t)}{\partial g_p^{(\alpha,i)}}$ are given by

$$\frac{\partial\dot{\gamma}^{(\alpha,i)}(t)}{\partial f_p^{(\alpha,i)}} = \frac{\dot{\gamma}^{(\alpha,i)}(t)}{f_p^{(\alpha,i)} m^{(\alpha)}} \tag{5.141}$$

$$\frac{\partial\dot{\gamma}^{(\alpha,i)}(t)}{\partial g_p^{(\alpha,i)}} = -\frac{\dot{\gamma}^{(\alpha,i)}(t)}{g_p^{(\alpha,i)} m^{(\alpha)}} \tag{5.142}$$

The increment in the plastic slip driving force is given by

$$\Delta f_p^{(\alpha,i)} \approx \dot{f}_p^{(\alpha,i)} \Delta t = \mathbf{R}_p^{(\alpha,i)} : \mathbf{D}^{(\alpha)} \Delta t + K_c^{(\alpha,i)} \Delta t - \sum_{j=1}^{N_p^{(\alpha)}} K_p^{(\alpha,i,j)} \Delta \gamma^{(\alpha,j)} \tag{5.143}$$

where $K_c^{(\alpha,i)}$ and $K_p^{(\alpha,i,j)}$ are intermediate variables. For non-transforming phases, $K_c^{(\alpha,i)}$ is given by

$$K_c^{(\alpha,i)} = -A^{(\alpha)} \mathbf{R}_p^{(\alpha,i)} : \mathbf{I}\dot{\theta} - \mathbf{R}_p^{(\alpha,i)} : \mathbf{D}_{tr} + \rho \phi^{(\alpha,i)} \text{sign}\left(\tau_p^{(\alpha,i)}\right) \dot{\theta} \tag{5.144}$$

For transforming austenite, $K_c^{(\alpha,i)}$ is given by

$$K_c^{(\alpha,i)} = -A^{(\alpha)} \mathbf{R}_p^{(\alpha,i)} : \mathbf{I}\dot{\theta} - \mathbf{R}_p^{(\alpha,i)} : \mathbf{D}_{tr} - 2\frac{\dot{\xi}^{(\alpha)}}{\xi^{(\alpha)}} \boldsymbol{\sigma}^{(\alpha)} : \mathbf{P}_p^{(\alpha,i)} + \rho \phi^{(\alpha,i)} \text{sign}\left(\tau_p^{(\alpha,i)}\right) \dot{\theta} \tag{5.145}$$

For transforming martensite, $K_c^{(\alpha,i)}$ is given by

$$\begin{aligned} K_c^{(\alpha,i)} = & -A^{(\alpha)} \mathbf{R}_p^{(\alpha,i)} : \mathbf{I}\dot{\theta} - \mathbf{R}_p^{(\alpha,i)} : \mathbf{D}_{tr} - 2\frac{\dot{\xi}^{(\alpha)}}{\xi^{(\alpha)}} \boldsymbol{\sigma}^{(\alpha)} : \mathbf{P}_p^{(\alpha,i)} + \rho \phi^{(\alpha,i)} \text{sign}\left(\tau_p^{(\alpha,i)}\right) \dot{\theta} \\ & + \frac{\dot{\xi}^{(\alpha)}}{\xi^{(\alpha)}} \boldsymbol{\sigma}^{(\alpha)} : \left[\frac{\hat{\mathbf{s}}_e^{(\alpha,i)} \otimes \bar{\mathbf{m}}_e^{(\alpha,i)} + \bar{\mathbf{m}}_e^{(\alpha,i)} \otimes \hat{\mathbf{s}}_e^{(\alpha,i)}}{2} \right] \\ & + \frac{\dot{\xi}^{(\alpha)}}{\xi^{(\alpha)}} \boldsymbol{\sigma}^{(\alpha)} : \left[\frac{\bar{\mathbf{s}}_e^{(\alpha,i)} \otimes \hat{\mathbf{m}}_e^{(\alpha,i)} + \hat{\mathbf{m}}_e^{(\alpha,i)} \otimes \bar{\mathbf{s}}_e^{(\alpha,i)}}{2} \right] \end{aligned} \tag{5.146}$$

For all grains, $K_p^{(\alpha,i)}$ is given by

$$\begin{aligned} K_p^{(\alpha,i,j)} = & \mathbf{R}_p^{(\alpha,i)} : \mathbf{P}^{(\alpha,j)} + \left[\frac{\omega^{(\alpha)} \mu^{(\alpha)} b^{(\alpha)}}{4 k_1^{(\alpha)} \sqrt{\rho_d^{(\alpha)}}} \right] \left[\frac{1}{b^{(\alpha)} k_1^{(\alpha)}} \sqrt{\rho_d^{(\alpha)}} - k_2^{(\alpha)} \rho_d^{(\alpha)} \right] \text{sign}\left(f_{p,1}^{(\alpha,i)} f_{p,1}^{(\alpha,j)} \right) \\ & - \left[\frac{1}{2} \omega^{(\alpha)} \mu^{(\alpha)} \left[b^{(\alpha)} \right]^2 k_2^{(\alpha)} \right] \left[\frac{1}{b^{(\alpha)} k_1^{(\alpha)}} \sqrt{\rho_d^{(\alpha)}} - k_2^{(\alpha)} \rho_d^{(\alpha)} \right] \text{sign}\left(f_{p,1}^{(\alpha,i)} f_{p,1}^{(\alpha,j)} \right) \end{aligned} \tag{5.147}$$

The increment in the critical plastic slip driving force is given by

$$\Delta g_p^{(\alpha,i)} = \sum_{j=1}^{N_p^{(\alpha)}} h_p^{(\alpha,i,j)} \Delta\gamma^{(\alpha,j)} \tag{5.148}$$

where the hardening matrix $h_p^{(\alpha,i,j)}$ is given by

$$h_p^{(\alpha,i,j)} = \frac{c^{(\alpha)}\mu^{(\alpha)}}{2} \sum_{i=1}^{N_p^{(\alpha)}} \left[\frac{1}{k_1^{(\alpha)}} - b^{(\alpha)} k_2^{(\alpha)} \sqrt{\rho_d^{(\alpha)}} \right] \text{sign}\left(\dot{\gamma}^{(\alpha,i)}\right) \tag{5.149}$$

Combining these equations gives

$$\sum_{j=1}^{N_p^{(\alpha)}} G_p^{(\alpha,i,j)} \Delta\gamma^{(\alpha,j)} = \left(G_c^{(\alpha,i)} + \mathbf{Q}^{(\alpha,i)} : \mathbf{D}^{(\alpha)} \right) \Delta t \tag{5.150}$$

where $G_p^{(\alpha,i,j)}$, $G_c^{(\alpha,i)}$ and $\mathbf{Q}^{(\alpha,i)}$ are intermediate derivatives given by

$$G_p^{(\alpha,i,j)} = \delta^{(i,j)} - \Lambda\Delta t \frac{\partial\dot{\gamma}^{(\alpha,i)}(t)}{\partial g_p^{(\alpha,i)}} h_p^{(\alpha,i,j)} \text{sign}\left(f_{p,1}^{(\alpha,i)}\right) + \Lambda\Delta t \frac{\partial\dot{\gamma}^{(\alpha,i)}(t)}{\partial f_p^{(\alpha,i)}} K_p^{(\alpha,i,j)} \tag{5.151}$$

$$G_c^{(\alpha,i)} = \dot{\gamma}^{(\alpha,i)}(t) + \Lambda\Delta t \frac{\partial\dot{\gamma}^{(\alpha,i)}(t)}{\partial f_p^{(\alpha,i)}} K_c^{(\alpha,i)} \tag{5.152}$$

$$\mathbf{Q}^{(\alpha,i)} = \Lambda\Delta t \frac{\partial\dot{\gamma}^{(\alpha,i)}(t)}{\partial f_p^{(\alpha,i)}} \mathbf{R}^{(\alpha,i)} \tag{5.153}$$

Equation (5.150) can then be solved using standard techniques to produce

$$\frac{\Delta\gamma^{(\alpha,i)}}{\Delta t} = y^{(\alpha,i)} + \mathbf{Y}^{(\alpha,i)} : \mathbf{D}^{(\alpha)} \tag{5.154}$$

Finally, $\frac{\Delta\gamma^{(\alpha,i)}}{\Delta t}$ can be substituted in place of $\dot{\boldsymbol{\gamma}}^{(\alpha,i)}$ in Eq. (5.42) to produce the effective Jaumann rate over one timestep

$$\overset{\triangledown}{\boldsymbol{\sigma}}{}^{(\alpha)} = \overline{\mathbb{C}}^{(\alpha)} : \mathbf{D}^{(\alpha)} - \dot{\tilde{\boldsymbol{\sigma}}}^{(\alpha)} \tag{5.155}$$

where the effective stiffness $\overline{\mathbb{C}}^{(\alpha)}$ is given by

$$\overline{\mathbb{C}}^{(\alpha)} = \mathbb{C}_e^{(\alpha)} - \sum_{i=1}^{N_p^{(\alpha)}} \mathbf{R}^{(\alpha,i)} \otimes \mathbf{Y}^{(\alpha,i)} \tag{5.156}$$

and the effective visco-plastic stress $\dot{\bar{\boldsymbol{\sigma}}}^{(\alpha)}$ is

$$\dot{\bar{\boldsymbol{\sigma}}}^{(\alpha)} = A^{(\alpha)}\dot{\theta}\left[\mathbb{C}_e^{(\alpha)} : \mathbf{I}\right] + \sum_{i=1}^{N_p^{(\alpha)}} \mathbf{R}^{(\alpha,i)} y^{(\alpha,i)} \tag{5.157}$$

5.3.3 Numerical Implementation

In this section an overall integration algorithm for solving the coupled thermo-mechanical problem will be outlined. At the beginning of each timestep n the transformation driving forces and transformation rates are calculated as in Eqs. (5.99) and (5.126). However, to simplify the implementation the derivative of the driving force is approximated using a first order approximation:

$$\dot{f}_{tr(n)}^{(\alpha',\beta)} \approx \frac{f_{tr(n)}^{(\alpha',\beta)} - f_{tr(n-1)}^{(\alpha',\beta)}}{\Delta t} \tag{5.158}$$

where $\dot{f}_{tr(n)}^{(\alpha',\beta)}$ is the derivative of the transformation driving force at timestep n, $f_{tr(n)}^{(\alpha',\beta)}$ is the transformation driving force at timestep n, $f_{tr(n-1)}^{(\alpha',\beta)}$ is the transformation driving force at timestep $n-1$ and Δt is the timestep estimated using the method outlined in van der Giessen and Neale [156].

Next, the plastic slip driving forces and plastic slip rates are calculated using Eqs. (5.94) and (5.114). The rate tangent matrices $\mathbf{y}^{(\alpha,i)}$ and $\mathbf{Y}^{(\alpha,i)}$, the effective stiffnesses $\overline{\mathbb{C}}^{(\alpha)}$, and the viscoplastic stresses $\dot{\bar{\boldsymbol{\sigma}}}^{(\alpha)}$ are then calculated using Eqs. (5.150), (5.156) and (4.145). The bulk stress update is derived from Eq. (5.34) using

$$\begin{aligned}\langle \overset{\triangledown}{\boldsymbol{\sigma}}_{(n)} \rangle = &\left[\sum_{\alpha=1}^{N_g} \xi_{(n)}^{(\alpha)} \overline{\mathbb{C}}_{(n)}^{(\alpha)}\right] : \langle \mathbf{D}_{(n)} \rangle - \left[\sum_{\alpha=1}^{N_g} \xi_{(n)}^{(\alpha)} \overline{\mathbb{C}}_{(n)}^{(\alpha)}\right] : \mathbf{D}_{tr(n)} - \sum_{\alpha=1}^{N_g} \xi_{(n)}^{(\alpha)} \dot{\bar{\boldsymbol{\sigma}}}_{(n)}^{(\alpha)} \\ &+ \sum_{\alpha'=1}^{N_a} \sum_{\beta=1}^{24} \dot{\xi}^{(\alpha',\beta)} \left[\sum_{i=1}^{2} \lambda^{\left(\zeta_i^\beta\right)} \boldsymbol{\sigma}^{\left(\alpha',\zeta_i^\beta\right)} - \boldsymbol{\sigma}^{(\alpha')}\right]\end{aligned} \tag{5.159}$$

The bulk stress equation given in Eq. (5.159) is then combined with the boundary conditions outlined in Section 5.3.1 and solved to determine the unknown bulk strain and stress rates. Once

the bulk strain rate tensor $\langle \mathbf{D} \rangle$ is fully known, the individual crystal strain rates $\mathbf{D}^{(\alpha)}$ and the plastic slip increments $\Delta\gamma^{(\alpha,i)}$ can be calculated using Eqs. (5.33) and (5.154). The individual crystal stresses are updated using the incremental form of Eq. (5.155)

$$\boldsymbol{\sigma}^{(\alpha)}_{(n+1)} = \boldsymbol{\sigma}^{(\alpha)}_{(n)} + \boldsymbol{\sigma}^{(\alpha)}_{(n)}\boldsymbol{\Omega}^{(\alpha)}_{(n)} - \boldsymbol{\Omega}^{(\alpha)}_{(n)}\boldsymbol{\sigma}^{(\alpha)}_{(n)} + \overline{\mathbb{C}}^{(\alpha)}_{(n)} : \mathbf{D}^{(\alpha)}_{(n)}\Delta t - \dot{\tilde{\boldsymbol{\sigma}}}^{(\alpha)}_{(n)}\Delta t \tag{5.160}$$

The dislocation density within the crystal is updated using the incremental form of Eq. (5.26)

$$\rho^{(\alpha)}_{d(n+1)} = \rho^{(\alpha)}_{d(n)} + \sum_{i=1}^{N_p^{(\alpha)}} \left[\frac{1}{b^{(\alpha)} k_1^{(\alpha)}} \sqrt{\rho^{(\alpha)}_{d(n)}} - k_2^{(\alpha)} \rho^{(\alpha)}_{d(n)} \right] \left| \Delta\gamma^{(\alpha,i)} \right| \tag{5.161}$$

The lattice orientation update for transforming martensite phases are given by

$$\begin{aligned}
\mathbf{s}^{(\alpha,i)}_{e(n+1)} &= \frac{\xi^{(\alpha)}_{(n)}\mathbf{s}^{(\alpha,i)}_{e(n)} + \Delta\xi^{(\alpha)}\hat{\mathbf{s}}^{(\alpha,i)}_{e(n)} + \xi^{(\alpha)} \left[\mathbf{I} + \mathbf{L}^{(\alpha)}_{(n)}\Delta t - \sum_{i=1}^{N_p^{(\alpha)}} \mathbf{P}^{(\alpha,i)}_{p}\Delta\gamma^{(\alpha,i)} \right] \mathbf{s}^{(\alpha,i)}_{e(n)}}{\xi^{(\alpha)}_{(n)} + \Delta\xi^{(\alpha)}} \\
\mathbf{m}^{(\alpha,i)}_{e(n+1)} &= \frac{\xi^{(\alpha)}_{(n)}\mathbf{m}^{(\alpha,i)}_{e(n)} + \Delta\xi^{(\alpha)}\hat{\mathbf{m}}^{(\alpha,i)}_{e(n)} + \xi^{(\alpha)}\mathbf{m}^{(\alpha,i)}_{e(n)} \left[\mathbf{I} + \mathbf{L}^{(\alpha)}_{(n)}\Delta t - \sum_{i=1}^{N_p^{(\alpha)}} \mathbf{P}^{(\alpha,i)}_{p}\Delta\gamma^{(\alpha,i)} \right]^{-1}}{\xi^{(\alpha)}_{(n)} + \Delta\xi^{(\alpha)}}
\end{aligned} \tag{5.162}$$

The lattice orientation update for all other phases is given by

$$\begin{aligned}
\mathbf{s}^{(\alpha,i)}_{e(n+1)} &= \left[\mathbf{I} + \mathbf{L}^{(\alpha)}_{(n)}\Delta t - \sum_{i=1}^{N_p^{(\alpha)}} \mathbf{P}^{(\alpha,i)}_{p}\Delta\gamma^{(\alpha,i)} \right] \mathbf{s}^{(\alpha,i)}_{e(n)} \\
\mathbf{m}^{(\alpha,i)}_{e(n+1)} &= \mathbf{m}^{(\alpha,i)}_{e(n)} \left[\mathbf{I} + \mathbf{L}^{(\alpha)}_{(n)}\Delta t - \sum_{i=1}^{N_p} \mathbf{P}^{(\alpha,i)}_{p}\Delta\gamma^{(\alpha,i)} \right]^{-1}
\end{aligned} \tag{5.163}$$

For austenite phases, the transformation systems are updated using

$$\begin{aligned}
\mathbf{b}^{(\alpha',i)}_{e(n+1)} &= \left[\mathbf{I} + \mathbf{L}^{(\alpha')}_{(n)}\Delta t - \sum_{i=1}^{N_p^{(\alpha')}} \mathbf{P}^{(\alpha',i)}_{p}\Delta\gamma^{(\alpha',i)} \right] \mathbf{b}^{(\alpha',i)}_{e(n)} \\
\mathbf{d}^{(\alpha',i)}_{e(n+1)} &= \mathbf{d}^{(\alpha',i)}_{e(n)} \left[\mathbf{I} + \mathbf{L}^{(\alpha)}_{(n)}\Delta t - \sum_{i=1}^{N_p} \mathbf{P}^{(\alpha',i)}_{p}\Delta\gamma^{(\alpha',i)} \right]^{-1}
\end{aligned} \tag{5.164}$$

Volume fractions are updated using

$$\boldsymbol{\xi}_{(n+1)}^{(\alpha)} = \boldsymbol{\xi}_{(n)}^{(\alpha)} \dot{\boldsymbol{\xi}}_{(n)}^{(\alpha)} \Delta t \tag{5.165}$$

The temperature is updated using

$$\theta_{(n+1)} = \theta_{(n)} + \frac{Q_{e(n)} + Q_{p(n)} + Q_{tr(n)} - Q_{bound(n)}}{w\ell t\rho \left[\sum_{\alpha=1}^{N_g} h^{(\alpha)}\right]} \Delta t \tag{5.166}$$

where $Q_{e(n)}$, $Q_{tr(n)}$ and $Q_{bound(n)}$ are calculated as in Eqs. (5.135b), (5.135d) and (5.137) and $Q_{p(n)}\Delta t$ is given by

$$Q_{p(n)}\Delta t = w\ell t \sum_{\alpha=1}^{N_g} \sum_{i=1}^{N_p^{(\alpha)}} \xi^{(\alpha)} M_p^{(\alpha,i)} \Delta\gamma^{(\alpha,i)} \tag{5.167}$$

Finally, the total bulk stress is updated using Eq. (5.33). The complete procedure is implemented as in Alg. 2.

Algorithm 2 Constitutive model integration.

procedure INTEGRATE(dt, t_{end}) ▷ Calculate final stress and strain
  INIT VARIABLES()
  while $t \leq t_{end}$ **do**
    $t \leftarrow t + dt$
    for all Austenite crystals α' **do**
      for all Martensite plates β **do**
        $f_{tr(n)}^{(\alpha',\beta)} \leftarrow$ TRIP DRIVING FORCE() ▷ Use Eq. (5.99)
        $\dot{\xi}_{(n)}^{(\alpha',\beta)} \leftarrow$ TRIP RATES() ▷ Use Eq. (5.126)
      end for
    end for
    for all Crystals α **do** ▷ This includes all phases
      for all Slip systems i **do**
        $f_{p(n)}^{(\alpha',\beta)} \leftarrow$ SLIP DRIVING FORCE() ▷ Use Eq. (5.94)
        $\dot{\gamma}^{(\alpha,i)} \leftarrow$ SLIP RATES() ▷ Use Eq. (5.114)
      end for

$y^{(\alpha)}$, $\mathbf{Y}^{(\alpha)} \leftarrow$RATE TANGENT INTER() ▷ Use Eqs. (5.150)
$\overline{\mathbb{C}}^{(\alpha)}$, $\dot{\boldsymbol{\sigma}}^{(\alpha)} \leftarrow$RATE TANGENT STRESS() ▷ Use Eqs. (5.156) and (5.157)
end for
$\langle \mathbf{D} \rangle \leftarrow$MECH BC() ▷ Use Eq. (5.159) and Mech. B.C.s
for all Crystals α **do** ▷ This includes all phases
for all Slip systems i **do**
$\Delta\gamma^{(\alpha,i)} \leftarrow$INCREMENT() ▷ Use Eq. (5.154)
end for
$\rho^{(\alpha)}_{d(n+1)} \leftarrow$UPDATE DISLOCATION DENSITY(α) ▷ Use Eq. (5.26)
$\boldsymbol{\sigma}^{(\alpha)}_{(n+1)} \leftarrow$ UPDATE CRYSTAL STRESS(α) ▷ Use Eq. (5.160)
if Crystal α is Austenite **then**
for all Martensite plates β **do**
$\mathbf{b}^{(\alpha,\beta)}_{e(n+1)}$, $\mathbf{d}^{(\alpha,\beta)}_{e(n+1)} \leftarrow$ UPDATE TRIP SYSTEMS() ▷ Use Eq. (5.164)
end for
end if
for all Slip systems i **do**
if Crystal α is Transforming Martensite **then**
$\mathbf{s}^{(\alpha,i)}_{e(n+1)}$, $\mathbf{m}^{(\alpha,i)}_{e(n+1)} \leftarrow$ UPDATE SLIP SYSTEMS() ▷ Use Eq. (5.162)
else
$\mathbf{s}^{(\alpha,i)}_{e(n+1)}$, $\mathbf{m}^{(\alpha,i)}_{e(n+1)} \leftarrow$ UPDATE SLIP SYSTEMS() ▷ Use Eq. (5.163)
end if
end for
$\boldsymbol{\xi}^{(\alpha)}_{(n+1)} \leftarrow$UPDATE VOLUME FRACTIONS() ▷ Use Eq. (5.165)
end for
$\theta_{(n+1)} \leftarrow$UPDATE TEMPERATURE() ▷ Use Eqs. (5.166) and (5.167)
$\langle \boldsymbol{\sigma}_{(n+1)} \rangle \leftarrow$ UPDATE BULK STRESS() ▷ Use Eq. (5.33)
end while
end procedure

5.4 Results and Discussion

In this section, the provided constitutive model is calibrated, validated, and analyzed for a QP alloy. First, the experimental QP3Mn thermo-mechanical response data presented in Poling [53] is summarized. Next, the simulated conditions and thermal evolution behaviour are described. The model is then calibrated and validated against the reported experimental data. The evolution of the plastic Taylor-Quinney coefficient and the orientation dependence of transformation are

analyzed. The model is then recalibrated without rate-dependent transformation and compared to the complete calibrated model's response to determine the importance of this effect. Finally, the thermo-mechanical response is analyzed for a range of strain paths.

5.4.1 Summary of Experimental Data

In this work, the numerical model is calibrated using the experimental data reported by Poling [53] for a 0.3C-3Mn-1.6Si wt% (QP3Mn) sheet alloy with a thickness of 1.1mm. Details regarding the heat treatment and manufacturing of the QP3Mn alloy are presented in Poling [53]. First, electron backscatter diffraction (EBSD) and X-Ray diffraction (XRD) tests were completed to characterize the material's initial microstructure. It was determined that the material initially consists of approximately 14.5% RA and 85.5% tempered martensite. While the presented constitutive framework can well capture additional phases such as ferrite, none were detected in the QP3Mn alloy. The EBSD results are reported in Fig. 5.3. Pole figures representing the RA and tempered martensite phases are reported in Figs. 5.4 and 5.5, respectively. These textures show a highly anisotropic texture without any symmetry, which is not expected of a rolled sheet material. Nevertheless, this work assumes that the presented EBSD and texture are sufficiently representative for this analysis.

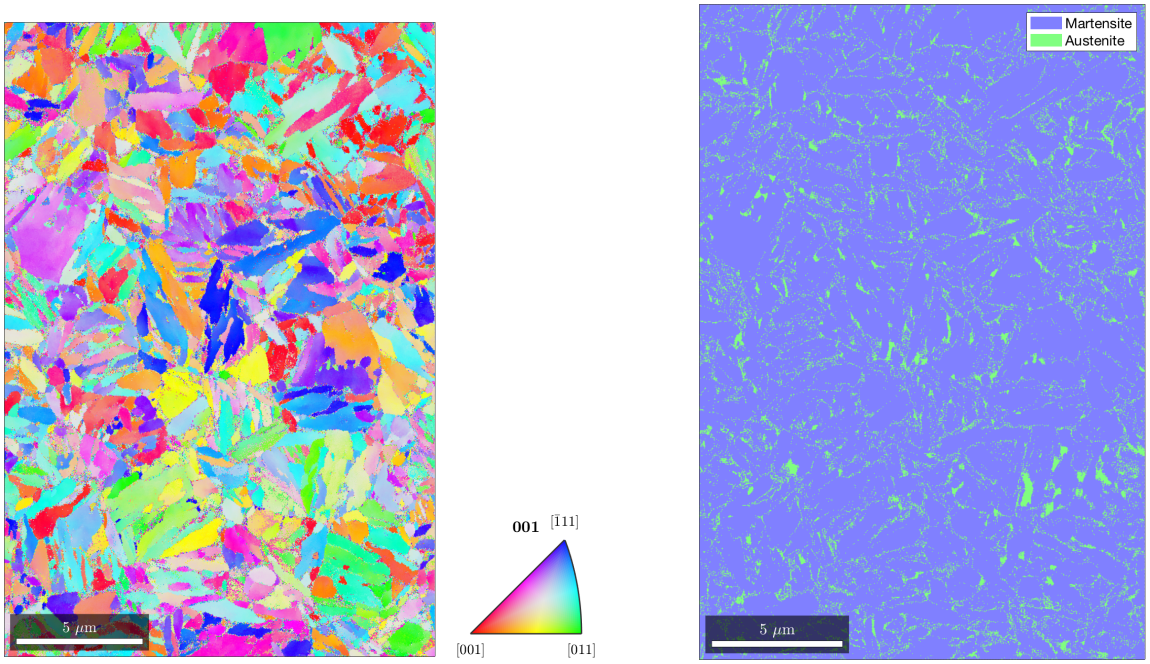

(a) Orientation map (b) Phase map

Fig. 5.3: QP3Mn EBSD from Poling [53].

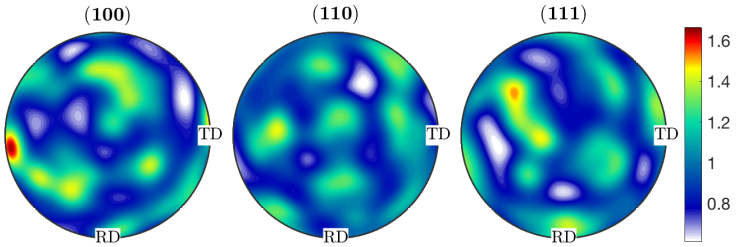

Fig. 5.4: QP3Mn RA texture.

Uniaxial tensile tests were conducted over a wide range of strain-rates and temperatures. A spot cooler and infrared heat lamp was used for reduced and elevated temperature testing, respectively. The temperature was measured using a K-type thermocouple, and the strain was measured using an extensometer. RAVF was measured using XRD at various strain levels. The test matrix representing the tested conditions and recorded data are reported in Table 5.2. This range was chosen by Poling [53] because it well represents the range of temperatures and strain-rates expected in industrial automotive applications [127, 157]. The symbols S, R and T represent

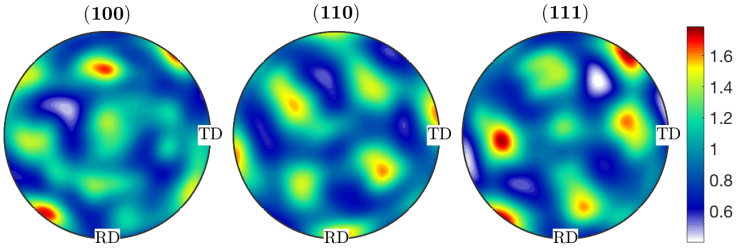

Fig. 5.5: Tempered martensite texture.

Table 5.2: Summary of reported experimental data.

	$T_0 = -10\,°C$	$T_0 = 23\,°C/26\,°C$	$T_0 = 40\,°C$	$T_0 = 55\,°C$	$T_0 = 70\,°C$	$T_0 = 85\,°C$
$\dot{\varepsilon} = 5 \times 10^{-4}\,s^{-1}$	S R	S R T	S R	S R	S R	S R
$\dot{\varepsilon} = 1 \times 10^{-3}\,s^{-1}$		S T				
$\dot{\varepsilon} = 1 \times 10^{-2}\,s^{-1}$		S T				
$\dot{\varepsilon} = 1 \times 10^{-1}\,s^{-1}$		S R T				
$\dot{\varepsilon} = 1 \times 10^{0}\,s^{-1}$		S				
$\dot{\varepsilon} = 1 \times 10^{1}\,s^{-1}$	R	S R			R	
$\dot{\varepsilon} = 1 \times 10^{2}\,s^{-1}$		S R				
$\dot{\varepsilon} = 2 \times 10^{2}\,s^{-1}$		S				

reported stress, RAVF and temperature vs. strain curves at the given testing condition. Only reported data with complete curves are included. Due to differences in room temperature, high strain-rate tests have an initial temperature of $T_0 = 26\,°C$ instead of $T_0 = 23\,°C$. The elevated temperature tests at $\dot{\varepsilon} = 0.0005\,s^{-1}$ are immersed in an oil bath to maintain a high temperature. Low-temperature tests are conducted using a spot cooler, and high-temperature tests with high strain-rates are heated using infrared (IR) heat lamps. All other tests are conducted in room temperature air. Table 5.3 gives a summary of these thermal testing conditions. Fig. 5.6 shows the reported true stress vs. true strain results, which demonstrates low strain-rate and temperature dependence. Fig. 5.7 shows the reported RAVF vs. strain response demonstrating a significant reduction in martensitic transformation with increasing temperature but low strain-rate dependence at any given temperature.

The $T_0 = 85\,°C$, $\dot{\varepsilon} = 5 \cdot 10^{-4} s^{-1}$ experiment in Poling [53] contains a major plateau region, which is attributed to dynamic strain aging (DSA). In high Mn steels (e.g. QP alloys), DSA is frequently attributed to the reorientation of C-Mn couples in dislocation cores resulting in the pinning and unpinning of mobile dislocations [51, 158]. Modelling of DSA requires incorporating C-Mn reorientation physics, the corresponding hardening behaviour and full field modelling of the uniaxial test sample [158, 159]. This is beyond the scope of this work and therefore the $T_0 = 85\,°C$, $\dot{\varepsilon} = 5 \cdot 10^{-4} s^{-1}$ experiment is not used. The $T_0 = 70\,°C$, $\dot{\varepsilon} = 10\,s^{-1}$ experiment seems to exhibit an unusually large experimental error with RAVF increasing by 1% from 2.5% true strain to 4% true strain. Since reverse transformation is not physical for steels near room

Table 5.3: Summary of thermal testing conditions.

	$T_0 = -10\,°C$	$T_0 = 23\,°C/26\,°C$	$T_0 = 40\,°C$	$T_0 = 55\,°C$	$T_0 = 70\,°C$	$T_0 = 85\,°C$
$\dot{\varepsilon} = 5 \times 10^{-4}\,s^{-1}$	Spot Cooler	Air	Oil Bath	Oil Bath	Oil Bath	Oil Bath
$\dot{\varepsilon} = 1 \times 10^{-3}\,s^{-1}$		Air				
$\dot{\varepsilon} = 1 \times 10^{-2}\,s^{-1}$		Air				
$\dot{\varepsilon} = 1 \times 10^{-1}\,s^{-1}$		Air				
$\dot{\varepsilon} = 1 \times 10^{0}\,s^{-1}$		Air				
$\dot{\varepsilon} = 1 \times 10^{1}\,s^{-1}$	Spot Cooler	Air			IR Heater	
$\dot{\varepsilon} = 1 \times 10^{2}\,s^{-1}$		Air				
$\dot{\varepsilon} = 2 \times 10^{2}\,s^{-1}$		Air				

temperature, this results from experimental error or poor repeatability. As such, this experiment will be used only as a validation test.

Fig. 5.8 shows the reported temperature vs. strain results, which shows a significantly higher temperature rise at higher strain-rates. The difference in temperature rise between strain-rates of $\dot{\varepsilon} = 1 \times 10^{-2}\,s^{-1}$ and $\dot{\varepsilon} = 1 \times 10^{-1}\,s^{-1}$ is relatively low, which combined with temperature measurements at the ultimate tensile strength (UTS) indicates that thermal conditions at $1 \times 10^{-1}\,s^{-1}$ is approximately adiabatic (see Poling [53] for details).

The combination of negative temperature sensitivity of transformation and increasing temperature at higher strain-rates suggests that transformation should be suppressed at elevated strain-rates. The absence of observed strain-rate dependence may be due to the concurrent changes in strain-rate and temperature in the conducted experiments. In this case, the negative temperature dependence of transformation is balanced by a positive strain-rate dependence, resulting in zero observed strain-rate dependence in the experimental strain-rate tests (where both temperature and strain-rate change). This hypothesis is tested in Sections 5.4.2 and 5.4.3.

5.4.2 Model Calibration and Validation

Three hundred tempered martensite and retained austenite grains (600 total) are sampled from a uniform orientation distribution, as shown in Figs. 5.9 and 5.10. Using the orientation relationship derived in Appendix B, a total of 14,400 orientations may be generated during the transformation of the austenite grains. Uniaxial tension boundary conditions are applied using a constant strain-rate in the applied loading direction, zero shear strain, and zero transverse and normal stresses using Eq. (5.132). The simulation is continued to a maximum strain of 11.1%, which is slightly larger than the highest strain reported at the UTS over all reported experimental conditions. For all cases submerged in an oil bath, the temperature is assumed to remain constant with time. In all other cases, temperature is modelled as in Section 5.3.1 with $w = 6.35\,mm$, $\ell = 6.35\,mm$ and $t = 1.1\,mm$.

The available experimental data are divided into calibration and validation data sets as shown

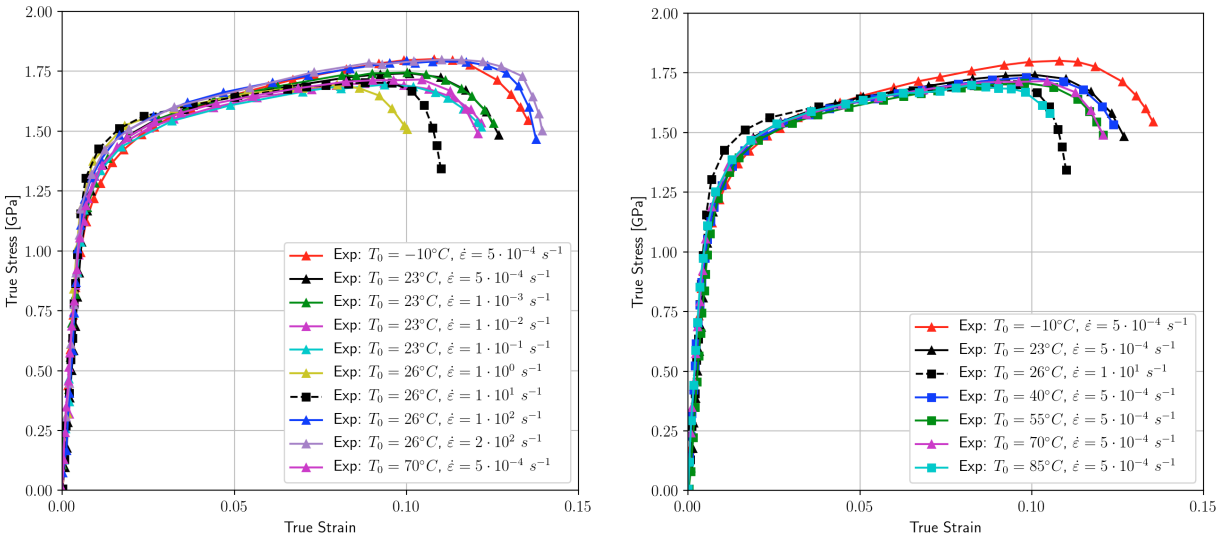

(a) Varying strain-rate (b) Varying temperature

Fig. 5.6: Reported stress vs. strain curves [53].

in Table 5.4. This split uses the minimum number of calibration experiments while maintaining three strain-rates to characterize stress evolution, RAVF and temperature and three initial temperatures to characterize stress evolution and RAVF. Furthermore, the model is only calibrated to the experimental ultimate tensile strength because this model does not incorporate any localization or damage, and therefore, cannot capture strain softening.

Table 5.4: Calibration and validation experimental data set.

Calibration		Validation	
$-10\,°\mathrm{C}$	$5 \times 10^{-4}\,\mathrm{s}^{-1}$	$40\,°\mathrm{C}$	$5 \times 10^{-4}\,\mathrm{s}^{-1}$
$23\,°\mathrm{C}$	$5 \times 10^{-4}\,\mathrm{s}^{-1}$	$55\,°\mathrm{C}$	$5 \times 10^{-4}\,\mathrm{s}^{-1}$
$70\,°\mathrm{C}$	$5 \times 10^{-4}\,\mathrm{s}^{-1}$	$23\,°\mathrm{C}$	$1 \times 10^{-2}\,\mathrm{s}^{-1}$
$23\,°\mathrm{C}$	$1 \times 10^{-3}\,\mathrm{s}^{-1}$	$26\,°\mathrm{C}$	$1 \times 10^{0}\,\mathrm{s}^{-1}$
$23\,°\mathrm{C}$	$1 \times 10^{-1}\,\mathrm{s}^{-1}$	$-10\,°\mathrm{C}$	$1 \times 10^{1}\,\mathrm{s}^{-1}$
$26\,°\mathrm{C}$	$1 \times 10^{2}\,\mathrm{s}^{-1}$	$26\,°\mathrm{C}$	$1 \times 10^{1}\,\mathrm{s}^{-1}$
		$70\,°\mathrm{C}$	$1 \times 10^{1}\,\mathrm{s}^{-1}$
		$26\,°\mathrm{C}$	$2 \times 10^{2}\,\mathrm{s}^{-1}$

The model coefficients are determined through a manual calibration process using a mean squared error (MSE) metric given by

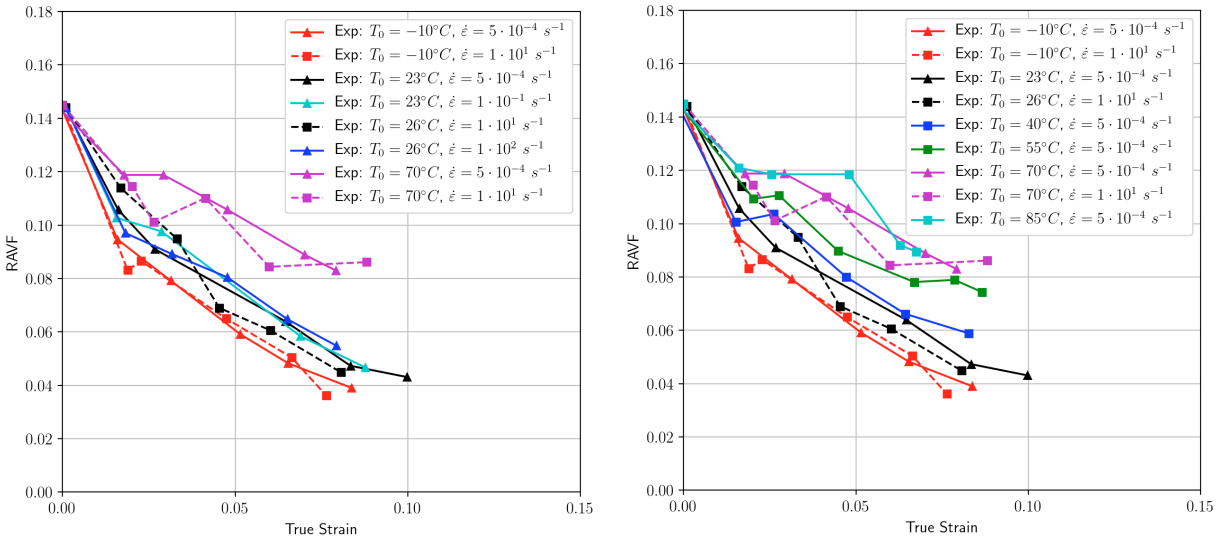

(a) Varying strain-rate (b) Varying temperature

Fig. 5.7: Reported RAVF vs. strain curves [53].

$$MSE = \sum_{i=1}^{N_\sigma} \left(\frac{\sigma_i^{Sim} - \sigma_i^{Exp}}{\sigma_i^{Exp}} \right)^2 + \sum_{i=1}^{N_\theta} \left(\frac{\theta_i^{Sim} - \theta_i^{Exp}}{\theta_i^{Exp}} \right)^2 + \sum_{i=1}^{N_\xi} \left(\frac{\xi_i^{Sim} - \xi_i^{Exp}}{\xi_i^{Exp}} \right)^2 \tag{5.168}$$

where N_σ, N_θ and N_ξ are the number of experimental points for stress, temperature and RAVF evolution respectively, σ_i^{Sim}, θ_i^{Sim} and ξ_i^{Sim} are the simulated stress, temperature and RAVF points, and σ_i^{Exp}, θ_i^{Exp} and ξ_i^{Exp} are the experimental stress, temperature and RAVF points. To reduce the number of calibrated parameters, the coefficients shown in Table 5.5 are taken from literature [154].

The calibrated plasticity and transformation coefficients are summarized in Tables 5.6 and 5.7, respectively. The Burger's vectors for each phase are calculated in Appendix A. The effective heat transfer coefficient is also calibrated to ensure correct temperature evolution and is determined to be $R_{eff} = 25.98\ \frac{\mathrm{W}}{\mathrm{m^2\,K}}$.

Fig. 5.11 compares the calibrated model to the experimental calibration data. Fig. 5.12 compares the calibrated model to the experimental validation data. Figs. 5.11(a) and 5.12(a) show that the low strain-rate and temperature dependence of the stress evolution are well captured. Figs. 5.11(b) and 5.12(b) show that the variation in temperature evolution with strain-rate is well captured. It should be pointed out that even the small decrease in temperature due to elastic cooling is well captured for all strain-rates. Finally, Figs. 5.11(c) and 5.12(c) show that the

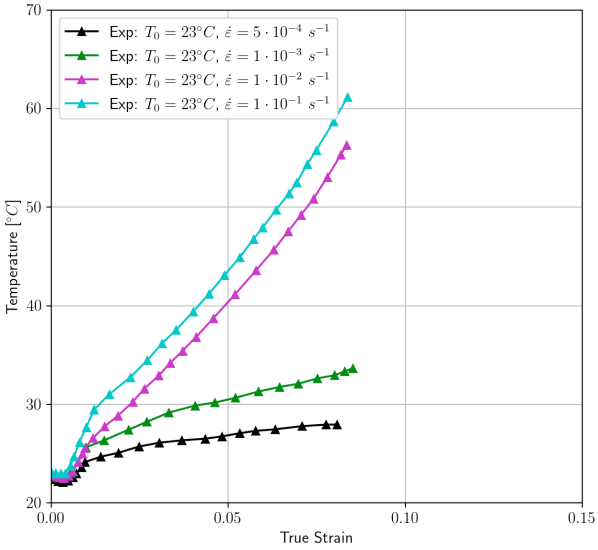

Fig. 5.8: Temperature vs. strain for various strain rates [53].

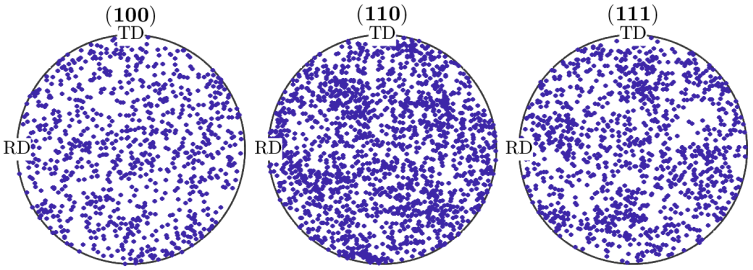

Fig. 5.9: Tempered martensite orientations.

temperature and strain-rate dependence of the RAVF evolution is generally well captured. The RAVF validation case with the highest discrepancy is the $T_0 = 70\,°\mathrm{C}$, $\dot{\varepsilon} = 10\,\mathrm{s}^{-1}$ case where the final RAVF is approximately 1.5% overpredicted. This discrepancy may be a result of the relatively high variance present in this experiment. To the author's knowledge, this is the first time that a crystal plasticity model incorporating the TRIP effect has been calibrated and validated over a wide range of strain-rates and temperatures. Fig. 5.13 shows the evolution of the average plastic Taylor-Quinney coefficient χ, defined by the equation

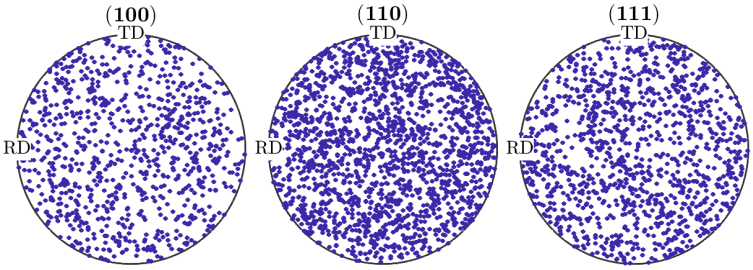

Fig. 5.10: Retained austenite orientations.

Table 5.5: Coefficients obtained from literature.

	Tempered Martensite	Retained Austenite	Transformed Martensite
Elastic Moduli [GPa]	$c_{11} = 233.5$ $c_{12} = 135.5$ $c_{44} = 118$	$c_{11} = 286.8$ $c_{12} = 166.4$ $c_{44} = 145$	$c_{11} = 233.5$ $c_{12} = 135.5$ $c_{44} = 118$
Hardening Law [GPa]	$\mu = 118$	$\mu = 145$	$\mu = 118$
Thermal Parameters	$h = 519\,\frac{\mathrm{J}}{\mathrm{kg\,K}}$ $A = 17 \cdot 10^{-6}\ \mathrm{K}^{-1}$ $\rho = 7.8 \cdot 10^{3}\,\frac{\mathrm{kg}}{\mathrm{m}^3}$	$h = 519\,\frac{\mathrm{J}}{\mathrm{kg\,K}}$ $A = 21 \cdot 10^{-6}\ \mathrm{K}^{-1}$ $\rho = 7.8 \cdot 10^{3}\,\frac{\mathrm{kg}}{\mathrm{m}^3}$	$h = 519\,\frac{\mathrm{J}}{\mathrm{kg\,K}}$ $A = 17 \cdot 10^{-6}\ \mathrm{K}^{-1}$ $\rho = 7.8 \cdot 10^{3}\,\frac{\mathrm{kg}}{\mathrm{m}^3}$
Transformation Parameters		$\lambda_T = -50\,500\,\frac{\mathrm{J}}{\mathrm{kg}}$	

$$\chi = \frac{Q - Q_{tr}}{W_p} = \frac{\sum_{\alpha=1}^{N_g} \sum_{i=1}^{N_p^{(\alpha)}} \xi^{(\alpha)} M_p^{(\alpha,i)} \dot{\gamma}^{(\alpha,i)} - \sum_{\alpha=1}^{N_g} \xi^{(\alpha)} \mathbf{M}_e^{(\alpha)} : \mathbf{D}_e^{(\alpha)}}{\sum_{\alpha=1}^{N_g} \sum_{i=1}^{N_p^{(\alpha)}} \xi^{(\alpha)} \boldsymbol{\sigma}^{(\alpha)} : \mathbf{P}_p^{(\alpha,i)} \dot{\gamma}^{(\alpha,i)}} \tag{5.169}$$

where W_p is the plastic work and Q and Q_{tr} are the total heat generation and the TRIP heat generation, respectively defined by

$$Q = \rho \left[\sum_{\alpha=1}^{N_g} h^{(\alpha)} \right] \dot{\theta} \tag{5.170}$$

$$Q_{tr} = \sum_{\alpha'=1}^{N_a} \sum_{\beta=1}^{24} M_{tr}^{(\alpha',\beta)} \dot{\xi}^{(\alpha',\beta)} \tag{5.171}$$

For low strains (less than 1%), the predicted Taylor-Quinney coefficient is primary driven by the

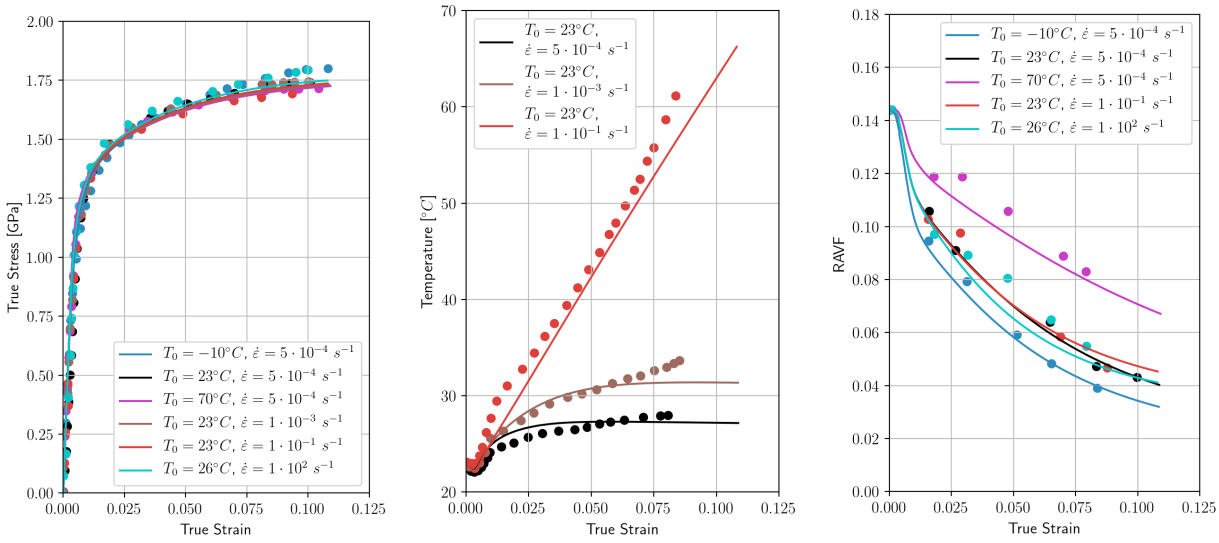

(a) (b) (c)

Fig. 5.11: Comparison of experimental and simulated response for (a) true stress, (b) temperature, and (c) RAVF vs. true strain for the calibration data set.

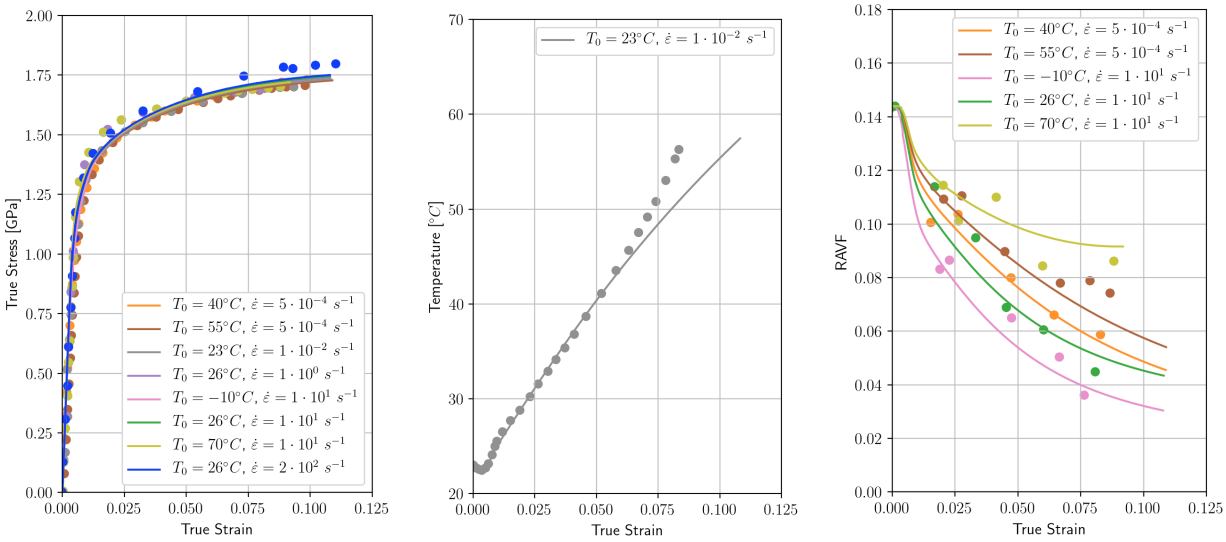

(a) (b) (c)

Fig. 5.12: Comparison of experimental and simulated response for (a) true stress, (b) temperature, and (c) RAVF vs. true strain for the validation data set.

Table 5.6: Calibrated plasticity coefficients.

	Tempered Martensite	Retained Austenite	Transformed Martensite
Hardening	$g_{p,0} = 446\,\mathrm{MPa}$ $c = 0.389$ $k_1 = 37.8$ $k_2 = 8.70$ $\rho_{d,0} = 10.0\,\mathrm{m}^{-2}$	$g_{p,0} = 662\,\mathrm{MPa}$ $c = 0.304$ $k_1 = 54.6$ $k_2 = 38.5$ $\rho_{d,0} = 10.0\,\mathrm{m}^{-2}$	$g_{p,0} = 815\,\mathrm{MPa}$ $c = 0.221$ $k_1 = 33.6$ $k_2 = 49.5$ $\rho_{d,0} = 10.0\,\mathrm{m}^{-2}$
Driving Force	$\omega = 40.0$ $\Phi = 0$	$\omega = 55.0$ $\Phi = 0$	$\omega = 58.2$ $\Phi = 0$
Kinetics	$a = 1 \cdot 10^{-3}\,\mathrm{s}^{-1}$ $m = 1 \cdot 10^{-3}$	$a = 1 \cdot 10^{-3}\,\mathrm{s}^{-1}$ $m = 1 \cdot 10^{-3}$	$a = 1 \cdot 10^{-3}\,\mathrm{s}^{-1}$ $m = 1 \cdot 10^{-3}$

Table 5.7: Calibrated transformation coefficients.

$\theta_T = 650\,\mathrm{K}$	$\kappa = 0.103$	$n_I = 1.39$	$a_1 = -8.29$	$a_2 = 7.79 \cdot 10^{-2}$
$a_3 = -1.49 \cdot 10^{-4}$	$a_4 = -0.150$	$a_5 = 0.100$	$g_{tr,n} = 0\,\mathrm{MPa}$	$\sigma_{tr,n} = 515\,\mathrm{MPa}$
	$f_o = 0.0750$	$g_{tr,o} = 371\,\mathrm{MPa}$	$\sigma_{tr,o} = 40.4\,\mathrm{MPa}$	

elastic cooling and is therefore well below zero. Once plastic slip is initiated, the Taylor-Quinney coefficient increases rapidly to approximately 0.925, further increasing to nearly 0.95 over the rest of the simulation. Despite not being explicitly calibrated, this matches well with the trends found in the existing experimental characterization of TRIP-assisted steels [79], which showed that the Taylor-Quinney coefficient increases from between 0.88 and 0.92 at 2% strain to approximately 0.98 at 10% strain.

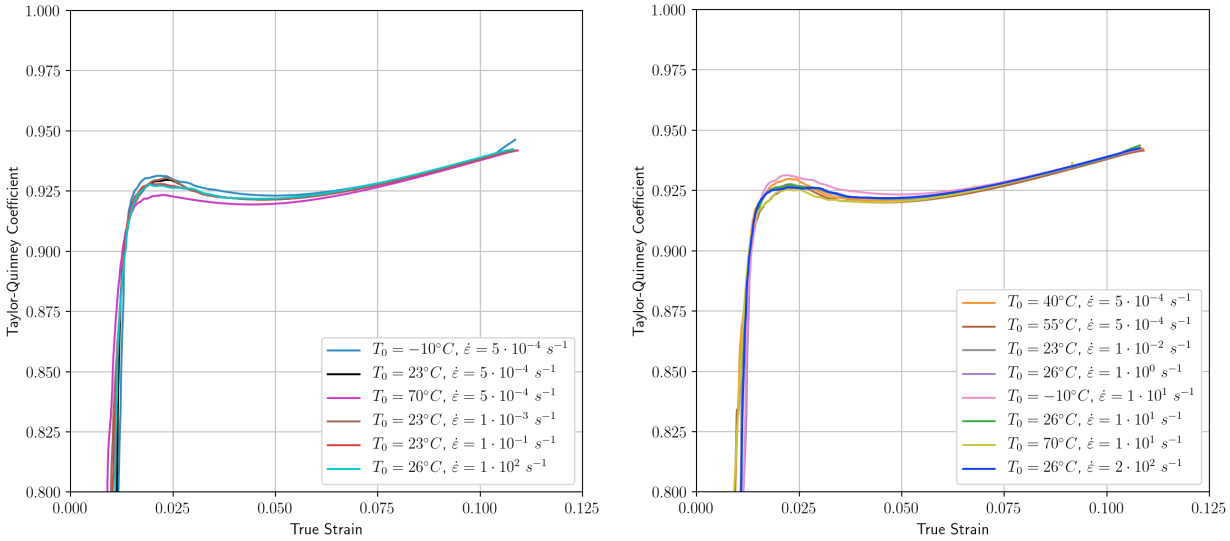

(a) Calibration simulations (b) Validation simulations

Fig. 5.13: Taylor-Quinney coefficient vs. true strain.

Fig. 5.14 shows the final RAVF of each austenite grain for the $T_0 = 23\,°\text{C}$, $\dot{\varepsilon} = 5 \cdot 10^{-4}\ \text{s}^{-1}$ simulation as a function of austenite orientation. This figure shows that transformation occurs preferentially when the austenite $\langle 100 \rangle$ is aligned with the loading axis. This result is representative of all other simulations and matches the existing simulated [154, 160] and experimental results [22, 151].

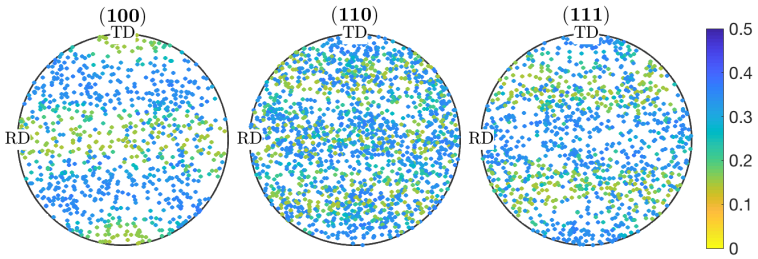

Fig. 5.14: Orientation dependence of final RAVF in 23 °C, $5 \cdot 10^{-4}\ \text{s}^{-1}$ simulation austenite grains.

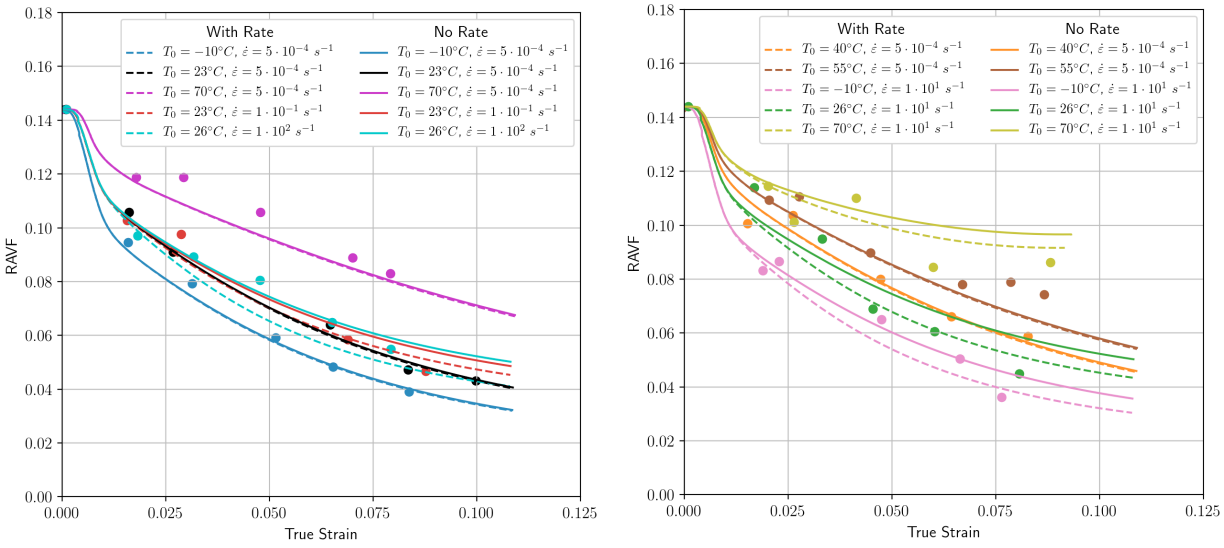

(a) Calibration simulations

(b) Validation simulations

Fig. 5.15: RAVF vs. true strain with (dashed) and without (solid) rate dependence.

5.4.3 Evaluation of Rate-Dependence on Transformation

To test the importance of rate-dependence on the transformation behaviour, the model is recalibrated with strain-rate dependent transformation neglected ($a_4 = 0$). All parameters are left the same, except a_1, a_2, and a_3. These are changed to

$$a_1 = -8.2890, \qquad a_2 = 7.7940 \cdot 10^{-2}, \qquad a_3 = -1.4885 \cdot 10^{-4} \tag{5.172}$$

The stress and temperature evolution were predicted equally well and are not reported here for brevity. Fig. 5.15 compares the RAVF evolution for the simulations with the rate-dependent transformation to the simulation with no rate dependence for the calibration and validation data sets. The conditions with varied temperature at $\dot{\varepsilon} = 5 \cdot 10^{-4}\text{s}^{-1}$ are predicted equally well. However, the elevated strain-rate cases overpredict the final RAVF by 0.5% – 1% relative to the complete calibrated model. Therefore, it is necessary to incorporate strain-rate-dependent transformation even when little strain-rate dependence is observed experimentally. This is necessary to balance with the reduced transformation resulting from increased temperature rise at elevated strain-rates.

5.4.4 Evaluation of Strain-Path Dependence of Transformation

To test the model's ability to capture strain-path dependent transformation, plane strain and equibiaxial tension simulations are conducted and compared to the simulated $T_0 = 23\,^{\circ}\mathrm{C}$, $\dot{\varepsilon} = 5{\cdot}10^{-4}\mathrm{s}^{-1}$ uniaxial tension case. The boundary conditions for the plane strain and equibiaxial tension cases are given by Eq. (5.133) with $P = 0$ for plane strain and $P = 1$ for equibiaxial tension. Both new simulations are continued to a final inelastic work level of $163\,\mathrm{mJ\,mm}^{-3}$, where the inelastic work (W_I) at time t is given by

$$W_I(t) = \sum_{\alpha=1}^{N_g} \int_0^t \xi^{(\alpha)} \left[\boldsymbol{\sigma}^{(\alpha)} : \mathbf{D}_p^{(\alpha)} \right] \mathrm{d}t + \sum_{\alpha'=1}^{N_a} \sum_{\beta=1}^{24} \int_0^t \frac{1}{2} \left[\sum_{i=1}^{2} \lambda^{\left(\zeta_i^{\beta}\right)} \boldsymbol{\sigma}^{\left(\alpha',\zeta_i^{\beta}\right)} + \boldsymbol{\sigma}^{(\alpha')} \right] : \mathbf{D}_{tr}^{(\alpha',\beta)} \mathrm{d}t \tag{5.173}$$

This is equal to the final inelastic work level in the uniaxial tension simulation. The thermal control volume geometries for the plane strain and equibiaxial tension simulations are assumed to be identical to the uniaxial tension simulation, such that identical thermal boundary conditions are applied. The Hosford [161] effective stress is used to compare stresses in each strain path. The yield exponent $a = 6$ was chosen because it follows observations for other existing steels with a predominantly BCC composition [41, 106, 161, 162]. Fig. 5.16 shows the predicted equivalent (Hosford) stress, temperature, and RAVF evolution vs. inelastic work as a function of strain path. Fig. 5.16(a) shows that the equivalent (Hosford) stress well captures all strain paths, with small deviations resulting from the transformation, the multiphase nature of the material and texture evolution. This matches well with existing experimental and numerical analyses [41, 161]. Fig. 5.16(b) shows that the temperature rise increases as the triaxiality increases. This matches expectations because the applied work per unit time is higher for higher triaxialities, resulting in increased heating. Fig. 5.16(c) shows that increasing triaxiality results in increased transformation (reduced final RAVF), despite increased temperatures and having a nearly constant effective strain-rate. This matches well with experimental and numerical results from some steels exhibiting the TRIP effect [9, 13, 120], but conflicts with others [12, 41, 75, 163].

Figs. 5.17 and 5.18 show the final RAVF of each austenite grain for the plane strain and equibiaxial tension cases, respectively. These show reduced orientation dependence of transformation with increasing triaxiality, resulting from better average alignment between grains and the loading stress. This indicates that the orientation dependence of transformation primarily causes the increasing transformation. To capture strain-path dependence of alloys that do not follow the trend predicted by this model, a straightforward modification of Eq. (5.120) can be used to improve predictions. This modified shear band evolution coefficient equation is a common approach in literature [9, 10, 41], and is given by

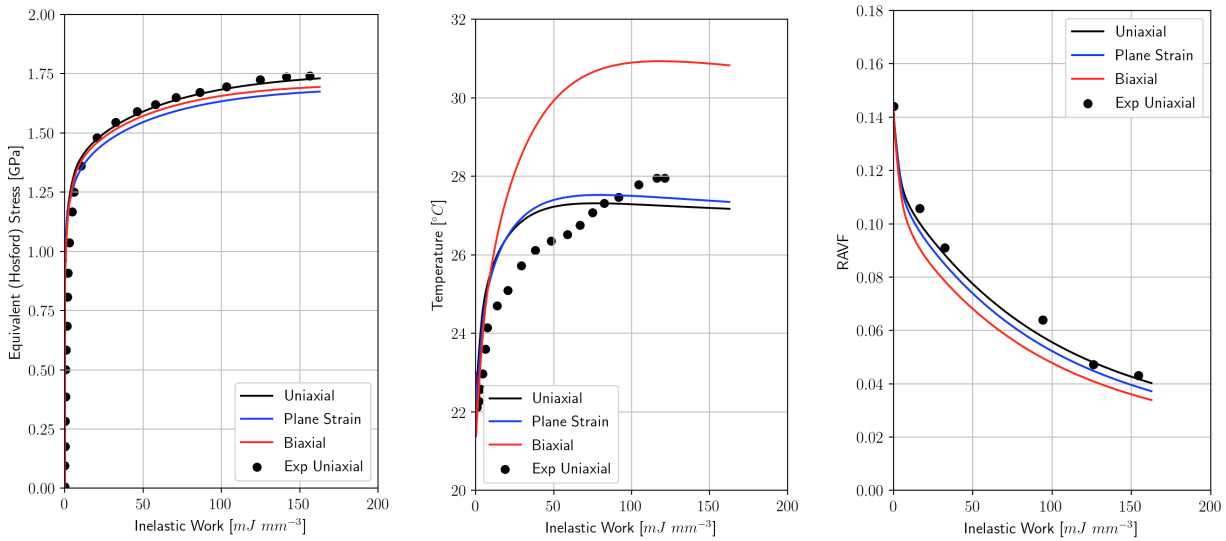

(a) (b) (c)

Fig. 5.16: Simulated strain path dependent (a) stress, (b) temperature and (c) RAVF evolution vs. true strain.

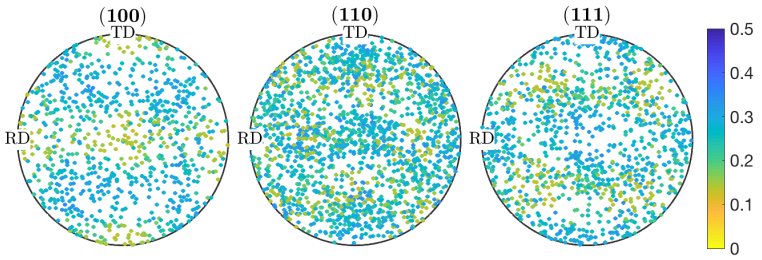

Fig. 5.17: Orientation dependence of final RAVF in plane strain 23 °C, $5 \cdot 10^{-4}$ s^{-1} simulation austenite grains.

$$a_{sb}^{(\alpha')} = \left(a_1 + a_2\theta + a_3\theta^2 + a_4\Sigma\right)\left(1 - a_6\left(\frac{\dot{\gamma}_{sb}^{(\alpha')}}{a^{(\alpha')}}\right)^{a_5}\right) \tag{5.174}$$

where a_4 is a calibrated coefficient and Σ is the triaxiality of the applied loading.

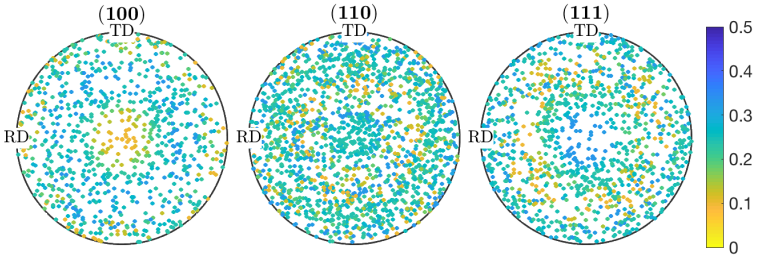

Fig. 5.18: Orientation dependence of final RAVF in equibiaxial tension 23 °C, $5 \cdot 10^{-4}$ s^{-1} simulation austenite grains.

5.4.5 Model Comparison

Table 5.8 shows a comparison between the previously existing works, the constitutive model presented in Chapter 4 and the constitutive model derived in this chapter (referred to as Connolly Model #2). This shows that Connolly Model #2 is the first model to capture all relevant physical mechanisms highlighted in Chapter 3. In particular, Connolly Model #2 can capture the transformation strain-rate sensitivity, temperature evolution, strain-induced transformation and thermal strain that the Cherkaoui model lineage did not. Furthermore, Connolly Model #2 can capture the stress homogenization, transformed martensite plasticity, local plasticity hardening, and strain-induced transformation that were not captured by Connolly Model #1.

To demonstrate the improvements relative to Connolly Model #1, the analysis presented in Section 4.5.4 is completed again using Connolly Model #2 calibrated to QP3Mn. Fig. 5.19 shows the statistical distribution of the variability of σ_{11} using a box and whisker plot as a function of strain. The bounds are defined as in Figs. 4.12 and 4.19, with the limits of each box representing the 25^{th} and 75^{th} percentile data, and the endpoints of the whiskers representing the complete data range. Note that the box and whisker plot does not take the volume fraction of grains into account, and as such is highly biased towards the stress evolution of the martensite phase. The volume-averaged stress at the same strain values is additionally plotted for comparison. This figure shows that the stress variation is much lower than predicted using Connolly Model #1, well within the range expected of a QP steel [15, 41]. Fig. 5.20 presents the evolution of the normalized RA fraction (as defined in Section 4.5.1) at 23 °C with no applied deformation. This shows that no evolution occurs, as expected for athermal martensitic transformation.

Table 5.8: Model comparison chart.

		Stringfellow et al. Model Lineage	Cherkaoui et al. Model Lineage	Lee et al. Model Lineage	Turteltaub et al. Model Lineage	Ma and Hartmaier Model Lineage	Park et al. Model Lineage	Connolly Model #1	Connolly Model # 2
Incorporated Material Behaviours	Transformation temperature sensitivity								
	Transformation strain-rate sensitivity								
	Transformation stress-state dependence								
	Incorporates martensite variants								
	Transformation orientation dependence								
	Hardening due to stress homogenization								
	Plasticity in transformed martensite								
	Hardening due to local plasticity when accommodating transformation strain								
	Temperature evolution								
	Stress-induced transformation								
	Strain-induced transformation								
	Thermodynamically consistent								
	Includes thermal strain								

Aspect present in model

Aspect partially present in model

Aspect not present in model

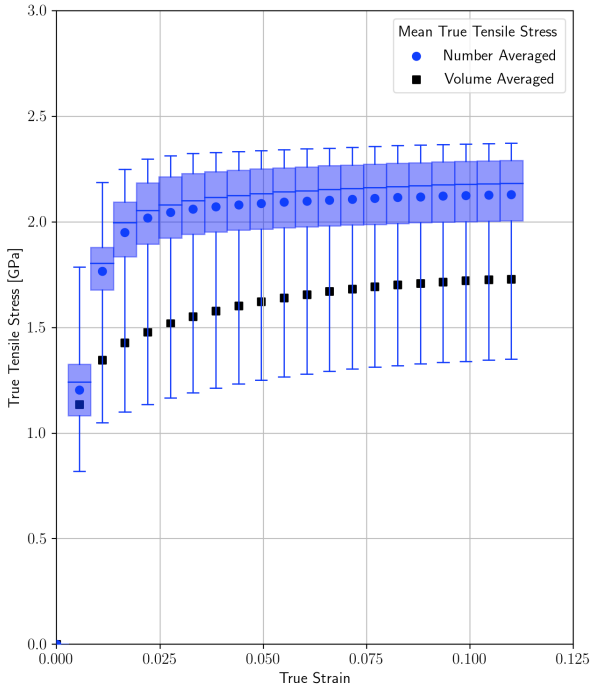

Fig. 5.19: Box and whisker plots of true X stress vs. strain.

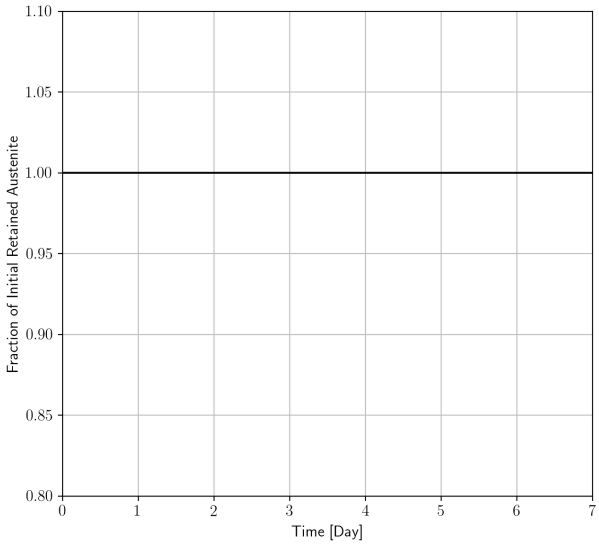

Fig. 5.20: Normalized RA fraction vs. strain at constant temperature without applied deformation over 7 days

5.5 Chapter Conclusions

This chapter presented a novel thermodynamically consistent constitutive model based on rate-dependent crystal plasticity. This model directly homogenized single crystal behaviour of both initially present and transformation generated grains using a modified Taylor-type homogenization law to account for transformation strain. The deformation mechanics of individual grains incorporated plastic slip and thermal deformation. A thermodynamic derivation was used to determine the plastic slip and transformation driving forces. Plastic slip and transformation kinetics laws were proposed to account for the temperature, strain, and orientation-dependent mechanical behaviour. The thermodynamic derivation was additionally used to derive a constitutive equation governing the evolution of temperature. Finally, a thermal numerical model was proposed for a control volume with spatially invariant temperature.

The derived model was then calibrated and validated using available literature data for a QP3Mn alloy. This data included temperature, RAVF, and stress evolution over a wide range of industrially relevant strain-rates and temperatures. Calibration and validation were conducted using six and eight experiments, respectively. Simulated and experimental stress, temperature and RAVF evolution responses exhibited very good agreement for both calibrated and validation cases. To the author's knowledge, this is the first time that a crystal plasticity model incorporating the TRIP effect has been calibrated and validated over a wide range of strain-rates and temperatures. This validated model was then used for several analyses, with the following specific conclusions:

- Despite not being explicitly calibrated, the plastic Taylor-Quinney coefficient matched well with the existing experimental trends.
- Transformation was observed to occur preferentially when the retained austenite $\langle 100 \rangle$ direction is aligned with the loading direction, matching the existing numerical and experimental trends.
- The numerical model was recalibrated assuming no rate-dependence in transformation, producing a significantly higher error for RAVF evolution in high strain-rate cases. This indicates that strain-rate-dependent transformation must be incorporated when the transformation is temperature-dependent, even if no strain-rate dependence is observed experimentally.
- Additional plane strain and equibiaxial tension simulations were conducted at room temperature and the lowest experimental strain-rate using the original calibrated model. This study showed that transformation increases with increasing triaxiality, despite temperature increasing with triaxiality and nearly constant stress evolution.
- It was demonstrated that the increase in transformation occurs due to better alignment between loading and the preferential transformation orientation with increasing triaxiality.

This trend matches some experimental and numerical observations but conflicts with others. For cases with differing trends, a straightforward model extension can better capture strain path dependence.

- The newly developed Connolly Model #2 was compared with Connolly Model #1. This showed that stress homogenization, transformed martensite plasticity, local plasticity hardening, and strain-induced transformation are now fully captured. Furthermore, it was demonstrated that the high stress and transformation without deformation highlighted in Section 4.5.4 are no longer present.

6 Conclusions and Future Work

6.1 Key Conclusions

The objective of this thesis was to develop a crystal plasticity-based constitutive model for steels exhibiting the TRIP effect, suitable for a wide range of strain-rates and temperatures. A baseline model was developed to meet this goal that captured temperature and strain-rate-dependent transformation while also partially capturing local hardening due to plastic deformation when accommodating transformation strain. A new method for incorporating thermal boundary conditions was proposed to simulate the coupled thermo-mechanical behaviour of a CP FEM RVE model. Finally, the baseline model was extended using a modified Taylor homogenization scheme to enable plastic slip in the transformed martensite phase and fully capture hardening due to stress homogenization and local plasticity when accommodating transformation strain. Additionally, the transformation kinetics law in the extended model was modified to incorporate strain-induced transformation to capture the athermal nature of transformation. This extended model was then calibrated and validated against a range of temperatures and strain-rates. To the author's knowledge, this is the first time that a crystal plasticity model incorporating the TRIP effect has been calibrated and validated over a range of strain-rates and temperatures. The key conclusions from the work presented in this thesis are as follows:

6.1.1 A Coupled Thermomechanical Crystal Plasticity Model Applied to Quenched and Partitioned Steel

- Simulation of non-interrupted vs. interrupted conditions predicted 16.7% less martensitic transformation in the interrupted condition, despite little difference in stress vs. strain curve. This suggests that there may be unexpected differences in RA evolution between in-situ uniaxial tension HEXRD and standard uniaxial tension experiments.
- Neither isothermal nor adiabatic conditions accurately captured room-temperature quasi-static behaviour, as predicted using the interrupted general thermal conditions.
- Increased initial temperature decreased both the amount of transformation and the bulk stress, which matches the majority of literature for steels exhibiting the TRIP effect.
- Predicted temperature evolution for non-interrupted general, and adiabatic cases are nearly identical for a strain-rate of $8 \times 10^{-2}\,\mathrm{s}^{-1}$.

6.1.2 A Novel Crystal Plasticity Model Incorporating Transformation Induced Plasticity for a Wide Range of Temperatures

- A crystal plasticity model incorporating the TRIP effect was calibrated and validated over a range of temperatures ($-10\,^{\circ}\mathrm{C}$ – $70\,^{\circ}\mathrm{C}$) and strain-rates ($5 \times 10^{-4}\,\mathrm{s}^{-1}$ – $200\,\mathrm{s}^{-1}$) for the first time.
- Despite not being explicitly calibrated, the plastic Taylor-Quinney coefficient matched well with the existing experimental trends.
- The numerical model was calibrated with and without transformation rate-dependence, demonstrating that it must be incorporated when the transformation is temperature-dependent, even if no strain-rate dependence is observed experimentally.
- Additional plane strain and equibiaxial tension simulations were conducted, demonstrating that predicted transformation increases with increasing triaxiality. For cases with differing trends, a straightforward model extension can better capture strain path dependence.

6.2 Future Work

In Section 3.3, several limitations of the proposed model are highlighted. A logical extension to the current thesis would be to address these limitations:

- Incorporate DSA and modelling of propagative instabilities to enable modelling of higher elevated temperatures (e.g. QP3Mn at $85\,^{\circ}\mathrm{C}$).
- Incorporate ϵ-martensite transformation mechanics to improve the range of materials the model can capture.
- Incorporate strain-gradient plasticity into the crystal plasticity mechanics to better capture the impact of small grain size in QP steel.
- Incorporate initial internal stresses due to QP heat treatment process to capture the impact of backstress on transformation, particularly for comparing austenite morphologies.
- Model film and block austenite separately to capture statistical differences in chemistry and transformation behaviour.

Additional extensions to the constitutive model beyond those highlighted in the limitations section include:

- Develop modified VPSC homogenization model to more accurately account for strain partitioning between grains while still capturing transformation strain.
- Calibrate and validate the model using all the above data and individual phase lattices strain to ensure local deformation behaviour is fully captured.
- Calibrate and validate using all the above data and non-uniaxial (e.g. shear, plane strain, equibiaxial tension) and non-linear strain-paths, modifying the model as necessary to capture the material behaviour.

Finally, the developed constitutive model can be used to provide direct insight into improving the design of lab-scale components. Several avenues exist for exploring engineering applications:

- Apply the model to formability prediction applications as in Connolly et al. [10].
- Apply the model to a lab-scale component, either directly or with multi-scale modelling, to study differential transformation throughout a component during forming or crash applications.
- Use the constitutive model in conjunction with fracture modelling to study the impact of transformation on component fracture.

References

[1] U.S.E.P.A., Draft Technical Assessment Report: Midterm Evaluation of Light-Duty Vehicle Greenhouse Gas Emission Standards and Corporate Average Fuel Economy Standards for Model Years 2022-2025, U.S. Environmental Protection Agency, 2016.

[2] C. P. Kohar, M. Mohammadi, R. K. Mishra, K. Inal, Effects of elastic–plastic behaviour on the axial crush response of square tubes, Thin-Walled Structures 93 (2015) 64–87. doi:10.1016/j.tws.2015.02.023.

[3] C. P. Kohar, A. Zhumagulov, A. Brahme, M. J. Worswick, R. K. Mishra, K. Inal, Development of high crush efficient, extrudable aluminium front rails for vehicle lightweighting, International Journal of Impact Engineering 95 (2016) 17–34. doi:10.1016/j.ijimpeng.2016.04.004.

[4] C. P. Kohar, A. Brahme, J. Imbert, R. K. Mishra, K. Inal, Effects of coupling anisotropic yield functions with the optimization process of extruded aluminum front rail geometries in crashworthiness, International Journal of Solids and Structures 128 (2017) 174–198. doi:10.1016/j.ijsolstr.2017.08.026.

[5] Y. L. Li, C. P. Kohar, R. K. Mishra, K. Inal, A new crystal plasticity constitutive model for simulating precipitation-hardenable aluminum alloys, International Journal of Plasticity 132 (2020) 102759. doi:10.1016/j.ijplas.2020.102759.

[6] A. Iftikhar, L. Li, C. Kohar, K. Inal, A. Khan, Evolution of subsequent yield surfaces with plastic deformation along proportional and non-proportional loading paths on annealed aa6061 alloy: Experiments and crystal plasticity finite element modeling, International Journal of Plasticity (2021).

[7] J. Rossiter, K. Inal, R. Mishra, Numerical modeling of the failure of magnesium tubes under compressive loading, Journal of Engineering Materials and Technology 134 (2012) 021008–021008–9. doi:10.1115/1.4005918.

[8] T. M. Pollock, Weight loss with magnesium alloys, Science 328 (2010) 986–987. doi:10.1126/science.1182848.

[9] C. P. Kohar, M. Cherkaoui, H. El Kadiri, K. Inal, Numerical modeling of trip steel in axial crashworthiness, International Journal of Plasticity 84 (2016) 224–254. doi:10.1016/j.ijplas.2016.05.010.

[10] D. S. Connolly, C. P. Kohar, R. K. Mishra, K. Inal, A new coupled thermomechanical framework for modeling formability in transformation induced plasticity steels, International Journal of Plasticity 103 (2018) 39–66. doi:10.1016/j.ijplas.2017.12.008.

[11] P. Zhang, C. P. Kohar, A. Brahme, S.-H. Choi, R. K. Mishra, K. Inal, Crystal plasticity based transformation induced plasticity formulation for predictions of forming limit diagrams, IOP Conference Series: Materials Science and Engineering 418 (2018) 012002. doi:10.1088/1757-899X/418/1/012002.

[12] W. Wu, Y.-W. Wang, P. Makrygiannis, F. Zhu, G. A. Thomas, L. G. Hector, X. Hu, X. Sun, Y. Ren, Deformation mode and strain path dependence of martensite phase transformation in a medium manganese trip steel, Materials Science and Engineering: A 711 (2018) 611–623. doi:10.1016/j.msea.2017.11.008.

[13] P. Zhang, C. P. Kohar, A. P. Brahme, S.-H. Choi, R. K. Mishra, K. Inal, A crystal plasticity formulation for simulating the formability of a transformation induced plasticity steel, Journal of Materials Processing Technology (2019) 116493. doi:10.1016/j.jmatprotec.2019.116493.

[14] R. Wu, W. Li, S. Zhou, Y. Zhong, L. Wang, X. Jin, Effect of retained austenite on the fracture toughness of quenching and partitioning (q&p)-treated sheet steels, Metallurgical and Materials Transactions A 45 (2014) 1892–1902. doi:10.1007/s11661-013-2113-0.

[15] X. Hu, K. S. Choi, X. Sun, Y. Ren, Y. Wang, Determining individual phase flow properties in a quench and partitioning steel with in situ high-energy x-ray diffraction and multiphase elasto-plastic self-consistent method, Metallurgical and Materials Transactions A 47 (2016) 5733–5749. doi:10.1007/s11661-016-3373-2.

[16] J. G. Speer, A. M. Streicher, D. K. Matlock, F. Rizzo, G. Krauss, Quenching and partitioning: a fundamentally new process to create high strength trip sheet microstructures., in: Symposium on the Thermodynamics, Kinetics, Characterization and Modeling of: Austenite Formation and Decomposition, 2003, p. 221–248.

[17] D. K. Matlock, J. G. Speer, E. De Moor, P. J. Gibbs, Recent developments in advanced high strength sheet steels for automotive applications: an overview, Jestech 15 (2012) 1–12.

[18] G. B. Olson, M. Cohen, Kinetics of strain-induced martensitic nucleation, Metallurgical Transactions A 6 (1975) 791. doi:10.1007/BF02672301.

[19] T. Iwamoto, T. Tsuta, Y. Tomita, Investigation on deformation mode dependence of strain-induced martensitic transformation in trip steels and modelling of transformation kinetics, International Journal of Mechanical Sciences 40 (1998) 173–182. doi:10.1016/S0020-7403(97)00047-7.

[20] A. M. Beese, D. Mohr, Anisotropic plasticity model coupled with lode angle dependent strain-induced transformation kinetics law, Journal of the Mechanics and Physics of Solids 60 (2012) 1922–1940. doi:10.1016/j.jmps.2012.06.009.

[21] Y. Tomita, T. Iwamoto, Constitutive modeling of trip steel and its application to the improvement of mechanical properties, International Journal of Mechanical Sciences 37 (1995) 1295–1305. doi:10.1016/0020-7403(95)00039-Z.

[22] E. C. Oliver, P. J. Withers, M. R. Daymond, S. Ueta, T. Mori, Neutron-diffraction study of stress-induced martensitic transformation in trip steel, Applied Physics A 74 (2002) s1143–s1145. doi:10.1007/s003390201555.

[23] S. S. Hecker, M. G. Stout, K. P. Staudhammer, J. L. Smith, Effects of strain state and strain rate on deformation-induced transformation in 304 stainless steel: Part i. magnetic measurements and mechanical behavior, Metallurgical Transactions A 13 (1982) 619–626. doi:10.1007/BF02644427.

[24] N. Abedrabbo, F. Pourboghrat, J. Carsley, Forming of aa5182-o and aa5754-o at elevated temperatures using coupled thermo-mechanical finite element models, International Journal of Plasticity 23 (2007) 841–875. doi:10.1016/j.ijplas.2006.10.005.

[25] Y. Li, M. Luo, J. Gerlach, T. Wierzbicki, Prediction of shear-induced fracture in sheet metal forming, Journal of Materials Processing Technology 210 (2010) 1858–1869. doi:10.1016/j.jmatprotec.2010.06.021.

[26] C. P. Kohar, A. Brahme, F. Hekmat, R. K. Mishra, K. Inal, A computational mechanics engineering framework for predicting the axial crush response of aluminum extrusions, Thin-Walled Structures 140 (2019) 516–532. doi:10.1016/j.tws.2019.02.007.

[27] W. Muhammad, A. P. Brahme, U. Ali, J. Hirsch, O. Engler, H. Aretz, J. Kang, R. K. Mishra, K. Inal, Bendability enhancement of an age-hardenable aluminum alloy: Part ii — multiscale numerical modeling of shear banding and fracture, Materials Science and Engineering: A 754 (2019) 161–177. doi:10.1016/j.msea.2019.03.050.

[28] F. Roters, P. Eisenlohr, L. Hantcherli, D. D. Tjahjanto, T. R. Bieler, D. Raabe, Overview of constitutive laws, kinematics, homogenization and multiscale methods in crystal plasticity finite-element modeling: Theory, experiments, applications, Acta Materialia 58 (2010) 1152–1211. doi:10.1016/j.actamat.2009.10.058.

[29] C. P. Kohar, J. L. Bassani, A. Brahme, W. Muhammad, R. K. Mishra, K. Inal, A new multi-scale framework to incorporate microstructure evolution in phenomenological plasticity: Theory, explicit finite element formulation, implementation and validation, International Journal of Plasticity 117 (2019) 122–156. doi:10.1016/j.ijplas.2017.08.006.

[30] A. Streicher, J. Speer, D. Matlock, B. De Cooman, Quenching and partitioning response of a si-added trip sheet steel, in: Proceedings of the International Conference on Advanced

High-Strength Sheet Steels for Automotive Applications, Warrendale, PA: AIST, 2004, p. 51–62.

[31] O. Matsumura, Y. Sakuma, H. TakeChi, Enhancement of elongation by retained austenite in intercritical annealed 0.4 c-1.5 si-o. 8mn steel, Transactions of the Iron and Steel Institute of Japan 27 (1987) 570–579.

[32] G. Krauss, Steels: processing, structure, and performance, Asm International, 2015.

[33] J. Speer, D. K. Matlock, B. C. De Cooman, J. G. Schroth, Carbon partitioning into austenite after martensite transformation, Acta Materialia 51 (2003) 2611–2622. doi:10.1016/S1359-6454(03)00059-4.

[34] E. De Moor, J. Penning, C. Föjer, A. Clarke, J. Speer, Alloy design for enhanced austenite stabilization via quenching and partitioning, in: Proceedings of the International Conference on New Developments in Advanced High-Strength Sheet Steels, AIST Warrendale, PA, 2008, p. 199–207.

[35] M. J. Santofimia, L. Zhao, R. Petrov, C. Kwakernaak, W. G. Sloof, J. Sietsma, Microstructural development during the quenching and partitioning process in a newly designed low-carbon steel, Acta Materialia 59 (2011) 6059–6068. doi:10.1016/j.actamat.2011.06.014.

[36] L. Wang, J. G. Speer, Quenching and partitioning steel heat treatment, Metallography, Microstructure, and Analysis 2 (2013) 268–281. doi:10.1007/s13632-013-0082-8.

[37] D. C. Pagan, P. A. Shade, N. R. Barton, J.-S. Park, P. Kenesei, D. B. Menasche, J. V. Bernier, Modeling slip system strength evolution in ti-7al informed by in-situ grain stress measurements, Acta Materialia 128 (2017) 406–417. doi:10.1016/j.actamat.2017.02.042.

[38] J. A. Venables, C. J. Harland, Electron back-scattering patterns—a new technique for obtaining crystallographic information in the scanning electron microscope, The Philosophical Magazine: A Journal of Theoretical Experimental and Applied Physics 27 (1973) 1193–1200. doi:10.1080/14786437308225827.

[39] Y. Staraselski, A. Brahme, R. K. Mishra, K. Inal, Reconstruction of the 3d representative volume element from the generalized two-point correlation function, Modelling and Simulation in Materials Science and Engineering 23 (2014) 015007. doi:10.1088/0965-0393/23/1/015007.

[40] X. H. Hu, X. Sun, L. G. Hector Jr., Y. Ren, Individual phase constitutive properties of a trip-assisted qp980 steel from a combined synchrotron x-ray diffraction and crystal plasticity approach, Acta Materialia 132 (2017) 230–244. doi:10.1016/j.actamat.2017.04.028.

[41] T. Park, L. G. Hector, X. Hu, F. Abu-Farha, M. R. Fellinger, H. Kim, R. Esmaeilpour, F. Pourboghrat, Crystal plasticity modeling of 3rd generation multi-phase ahss with martensitic transformation, International Journal of Plasticity (2019). URL: http://www.sciencedirect.com/science/article/pii/S0749641918304790. doi:10.1016/j.ijplas.2019.03.010.

[42] B. Petit, N. Gey, M. Cherkaoui, B. Bolle, M. Humbert, Deformation behavior and microstructure/texture evolution of an annealed 304 aisi stainless steel sheet. experimental and micromechanical modeling, International Journal of Plasticity 23 (2007) 323–341. doi:10.1016/j.ijplas.2006.07.002.

[43] X. C. Xiong, B. Chen, M. X. Huang, J. F. Wang, L. Wang, The effect of morphology on the stability of retained austenite in a quenched and partitioned steel, Scripta Materialia 68 (2013) 321–324. doi:10.1016/j.scriptamat.2012.11.003.

[44] W. Commons, Hexagonal close packed lattice cell, front view, 2013. URL: https://en.wikipedia.org/wiki/File:Hexagonal_latticeFRONT.svg.

[45] W. Commons, Face centered cubic lattice cell, front view, 2007. URL: https://en.wikipedia.org/wiki/File:Cubic-face-centered.svg.

[46] W. Commons, Body centered cubic lattice cell, front view, 2007. URL: https://en.wikipedia.org/wiki/File:Cubic-body-centered.svg.

[47] W. Commons, Body centered tetragonal lattice cell, front view, 2007. URL: https://en.wikipedia.org/wiki/File:Tetragonal-body-centered.svg.

[48] D. R. Askeland, P. P. Phule, The science and engineering of materials, Springer, 2003.

[49] D. Caillard, J.-L. Martin, Thermally activated mechanisms in crystal plasticity, Elsevier, 2003.

[50] G. T. (Rusty) Gray, High-strain-rate deformation: Mechanical behavior and deformation substructures induced, Annual Review of Materials Research 42 (2012) 285–303. doi:10.1146/annurev-matsci-070511-155034.

[51] Y. N. Dastur, W. C. Leslie, Mechanism of work hardening in hadfield manganese steel, Metallurgical Transactions A 12 (1981) 749–759. doi:10.1007/BF02648339.

[52] D. Canadinc, C. Efstathiou, H. Sehitoglu, On the negative strain rate sensitivity of hadfield steel, Scripta Materialia 59 (2008) 1103–1106. doi:10.1016/j.scriptamat.2008.07.027.

[53] W. A. Poling, Tensile Deformation of Third Generation Advanced High Strength Sheet Steels Under High Strain Rates, Ph.D. thesis, Colorado School of Mines, 2016.

[54] T. G. Langdon, Grain boundary sliding as a deformation mechanism during creep, The Philosophical Magazine: A Journal of Theoretical Experimental and Applied Physics 22 (1970) 689–700. doi:10.1080/14786437008220939.

[55] B. Mintz, R. Abu-Shosha, M. Shaker, Influence of deformation induced ferrite, grain boundary sliding, and dynamic recrystallisation on hot ductility of 0·1–0·75%c steels, Materials Science and Technology 9 (1993) 907–914. doi:10.1179/mst.1993.9.10.907.

[56] N. A. Fleck, G. M. Muller, M. F. Ashby, J. W. Hutchinson, Strain gradient plasticity: Theory and experiment, Acta Metallurgica et Materialia 42 (1994) 475–487. doi:10.1016/0956-7151(94)90502-9.

[57] W. Commons, Dislocation illustration, 2008. URL: https://en.wikipedia.org/wiki/File:Vector_de_Burgers.PNG.

[58] G. Subhash, Y. J. Lee, G. Ravichandran, Plastic deformation of cvd textured tungsten—i. constitutive response, Acta Metallurgica et Materialia 42 (1994) 319–330. doi:10.1016/0956-7151(94)90074-4.

[59] Y. Guan, B. Chen, J. Zou, T. B. Britton, J. Jiang, F. P. E. Dunne, Crystal plasticity modelling and hr-dic measurement of slip activation and strain localization in single and oligo-crystal ni alloys under fatigue, International Journal of Plasticity 88 (2017) 70–88. doi:10.1016/j.ijplas.2016.10.001.

[60] C. S. Kaira, S. S. Singh, A. Kirubanandham, N. Chawla, Microscale deformation behavior of bicrystal boundaries in pure tin (sn) using micropillar compression, Acta Materialia 120 (2016) 56–67. doi:10.1016/j.actamat.2016.08.030.

[61] S. Curtze, V. T. Kuokkala, M. Hokka, P. Peura, Deformation behavior of trip and dp steels in tension at different temperatures over a wide range of strain rates, Materials Science and Engineering: A 507 (2009) 124–131. doi:10.1016/j.msea.2008.11.050.

[62] K. Bhattacharya, et al., Microstructure of martensite: why it forms and how it gives rise to the shape-memory effect, volume 2, Oxford University Press, 2003.

[63] R. Richman, Plastic deformation modes in fe-ni-c martensites, TRANSACTIONS OF THE METALLURGICAL SOCIETY OF AIME 227 (1963) 159.

[64] M. Roberts, W. Owen, Physical properties of martensite and bainite, Iron and Steel Institute Special Report 93 (1965) 171.

[65] J. Min, L. G. Hector, L. Zhang, J. Lin, J. E. Carsley, L. Sun, Elevated-temperature mechanical stability and transformation behavior of retained austenite in a quenching and

partitioning steel, Materials Science and Engineering: A 673 (2016) 423–429. doi:10.1016/j.msea.2016.07.090.

[66] E. C. Bain, N. Dunkirk, The nature of martensite, trans. AIME 70 (1924) 25–47.

[67] G. Kurdjumov, G. Sachs, Over the mechanisms of steel hardening, Z. Phys 64 (1930) 325–343.

[68] Z. Nishiyama, X-ray investigation of the mechanism of the transformation from face centered cubic lattice to body centered cubic, Sci. Rep. Tohoku Univ. 23 (1934) 637.

[69] G. Wassermann, Einfluss der umwandlung eines irreversiblen nickelstahls auf kristallorientierung und zugfestigkeit, Archiv fr das Eisenhttenwesen 6 (1933) 347–351.

[70] W. Pitsch, Der orientierungszusammenhang zwischen zementit und austenit, Acta Metallurgica 10 (1962) 897–900. doi:10.1016/0001-6160(62)90108-6.

[71] Y. He, S. Godet, J. J. Jonas, Representation of misorientations in rodrigues–frank space: application to the bain, kurdjumov–sachs, nishiyama–wassermann and pitsch orientation relationships in the gibeon meteorite, Acta Materialia 53 (2005) 1179–1190. doi:10.1016/j.actamat.2004.11.021.

[72] G. W. Greenwood, R. H. Johnson, The deformation of metals under small stresses during phase transformations, Proc. R. Soc. Lond. A 283 (1965) 403–422. doi:10.1098/rspa.1965.0029.

[73] P. J. Jacques, F. Delannay, J. Ladrière, On the influence of interactions between phases on the mechanical stability of retained austenite in transformation-induced plasticity multiphase steels, Metallurgical and Materials Transactions A 32 (2001) 2759–2768. doi:10.1007/s11661-001-1027-4.

[74] J. Cramer, D. Adams, M. P. Miles, D. T. Fullwood, E. R. Homer, T. Brown, R. Misha, A. Sachdev, Effect of strain path on forming limits and retained austenite transformation in q&p 1180 steel, Materials Science and Engineering: A 734 (2018) 192–199. doi:10.1016/j.msea.2018.07.062.

[75] J. Serri, Caractérisation expérimentale et modélisation du comportement plastique d'aciers à transformation martensitique: applications à la mise en forme, University of Metz, 2006.

[76] H.-S. Yang, H. K. D. H. Bhadeshia, Austenite grain size and the martensite-start temperature, Scripta Materialia 60 (2009) 493–495. doi:10.1016/j.scriptamat.2008.11.043.

[77] W. J. Dan, W. G. Zhang, S. H. Li, Z. Q. Lin, A model for strain-induced martensitic transformation of trip steel with strain rate, Computational Materials Science 40 (2007) 101–107. doi:10.1016/j.commatsci.2006.11.006.

[78] L. Durrenberger, J. R. Klepaczko, A. Rusinek, Constitutive modeling of metals based on the evolution of the strain-hardening rate, Journal of Engineering Materials and Technology 129 (2007) 550–558. doi:10.1115/1.2772327.

[79] A. Rusinek, J. R. Klepaczko, Experiments on heat generated during plastic deformation and stored energy for trip steels, Materials & Design 30 (2009) 35–48. doi:10.1016/j.matdes.2008.04.048.

[80] T. Iwamoto, T. Sawa, M. Cherkaoui, A study on impact deformation and transformation behavior of trip steel by finite element simulation and experiment, International Journal of Modern Physics B 22 (2008) 5985–5990. doi:10.1142/S0217979208051479.

[81] A. S. Khan, M. Baig, S.-H. Choi, H.-S. Yang, X. Sun, Quasi-static and dynamic responses of advanced high strength steels: Experiments and modeling, International Journal of Plasticity 30–31 (2012) 1–17. doi:10.1016/j.ijplas.2011.08.004.

[82] Y. Tomita, T. Iwamoto, Computational prediction of deformation behavior of trip steels under cyclic loading, International Journal of Mechanical Sciences 43 (2001) 2017–2034. doi:10.1016/S0020-7403(01)00026-1.

[83] R. G. Stringfellow, D. M. Parks, G. B. Olson, A constitutive model for transformation plasticity accompanying strain-induced martensitic transformations in metastable austenitic steels, Acta Metallurgica et Materialia 40 (1992) 1703–1716. doi:10.1016/0956-7151(92)90114-T.

[84] J. Serri, M. Martiny, G. Ferron, Finite element analysis of the effects of martensitic phase transformation in trip steel sheet forming, International Journal of Mechanical Sciences 47 (2005) 884–901. doi:10.1016/j.ijmecsci.2005.02.001.

[85] J. Serri, M. Cherkaoui, Constitutive modeling and finite element analysis of the formability of trip steels, Journal of Engineering Materials and Technology 130 (2008) 031009–031009–13. doi:10.1115/1.2931146.

[86] J. Krauer, P. Hora, Enhanced material models for the process design of the temperature dependent forming behavior of metastable steels, International Journal of Material Forming 5 (2012) 361–370. doi:10.1007/s12289-011-1057-4.

[87] L. Durrenberger, Analyse de la pré-deformation plastique sur la tenue au crash d'une structure crash-box par approaches expérimentale et numérique, University of Metz, 2007.

[88] P. Dasappa, K. Inal, R. Mishra, The effects of anisotropic yield functions and their material parameters on prediction of forming limit diagrams, International Journal of Solids and Structures 49 (2012) 3528–3550. doi:10.1016/j.ijsolstr.2012.04.021.

[89] C. P. Kohar, M. Mohammadi, R. K. Mishra, K. Inal, The effects of the yield surface curvature and anisotropy constants on the axial crush response of circular crush tubes, Thin-Walled Structures 106 (2016) 28–50. doi:10.1016/j.tws.2016.04.021.

[90] K. Zhang, B. Holmedal, O. S. Hopperstad, S. Dumoulin, J. Gawad, A. Van Bael, P. Van Houtte, Multi-level modelling of mechanical anisotropy of commercial pure aluminium plate: Crystal plasticity models, advanced yield functions and parameter identification, International Journal of Plasticity 66 (2015) 3–30. doi:10.1016/j.ijplas.2014.02.003.

[91] C. W. Sinclair, R. G. Hoagland, A molecular dynamics study of the fcc→bcc transformation at fault intersections, Acta Materialia 56 (2008) 4160–4171. doi:10.1016/j.actamat.2008.04.043.

[92] O. Cazacu, Multiscale Modeling of Heterogenous Materials: From Microstructure to Macroscale Properties, John Wiley & Sons, 2013.

[93] S. R. Kalidindi, C. A. Bronkhorst, L. Anand, Crystallographic texture evolution in bulk deformation processing of fcc metals, Journal of the Mechanics and Physics of Solids 40 (1992) 537–569. doi:10.1016/0022-5096(92)80003-9.

[94] R. A. Lebensohn, A. K. Kanjarla, P. Eisenlohr, An elasto-viscoplastic formulation based on fast fourier transforms for the prediction of micromechanical fields in polycrystalline materials, International Journal of Plasticity 32–33 (2012) 59–69. doi:10.1016/j.ijplas.2011.12.005.

[95] M.-G. Lee, S.-J. Kim, H. N. Han, Crystal plasticity finite element modeling of mechanically induced martensitic transformation (mimt) in metastable austenite, International Journal of Plasticity 26 (2010) 688–710. doi:10.1016/j.ijplas.2009.10.001.

[96] G. I. Taylor, Plastic strain in metals, J. Inst. Metals 62 (1938) 307–324.

[97] G. Sachs, Z. Ver. Dtsch. Ing. 72 (1928) 734.

[98] K. Inal, P. D. Wu, K. W. Neale, Instability and localized deformation in polycrystalline solids under plane-strain tension, International Journal of Solids and Structures 39 (2002) 983–1002. doi:10.1016/S0020-7683(01)00246-3.

[99] J. Lévesque, M. Mohammadi, R. K. Mishra, K. Inal, An extended taylor model to simulate localized deformation phenomena in magnesium alloys, International Journal of Plasticity 78 (2016) 203–222. doi:10.1016/j.ijplas.2015.10.012.

[100] T. P. Van, K. Jöchen, T. Böhlke, Simulation of sheet metal forming incorporating ebsd data, Journal of Materials Processing Technology 212 (2012) 2659–2668. doi:10.1016/j.jmatprotec.2012.07.015.

[101] J. D. Eshelby, The determination of the elastic field of an ellipsoidal inclusion, and related problems, Proceedings of the Royal Society of London. Series A, Mathematical and Physical Sciences 241 (1957) 376–396.

[102] R. Hill, Continuum micro-mechanics of elastoplastic polycrystals, Journal of the Mechanics and Physics of Solids 13 (1965) 89–101. doi:10.1016/0022-5096(65)90023-2.

[103] A. Molinari, G. R. Canova, S. Ahzi, A self consistent approach of the large deformation polycrystal viscoplasticity, Acta Metallurgica 35 (1987) 2983–2994. doi:10.1016/0001-6160(87)90297-5.

[104] R. A. Lebensohn, C. N. Tomé, P. P. CastaÑeda, Self-consistent modelling of the mechanical behaviour of viscoplastic polycrystals incorporating intragranular field fluctuations, Philosophical Magazine 87 (2007) 4287–4322. doi:10.1080/14786430701432619.

[105] R. J. Asaro, J. R. Rice, Strain localization in ductile single crystals, Journal of the Mechanics and Physics of Solids 25 (1977) 309–338. doi:10.1016/0022-5096(77)90001-1.

[106] J. F. W. Bishop, R. Hill, Cxxviii. a theoretical derivation of the plastic properties of a polycrystalline face-centred metal, The London, Edinburgh, and Dublin Philosophical Magazine and Journal of Science 42 (1951) 1298–1307. doi:10.1080/14786444108561385.

[107] R. J. Asaro, A. Needleman, Overview no. 42 texture development and strain hardening in rate dependent polycrystals, Acta Metallurgica 33 (1985) 923–953. doi:10.1016/0001-6160(85)90188-9.

[108] J. D. Clayton, Dynamic plasticity and fracture in high density polycrystals: constitutive modeling and numerical simulation, Journal of the Mechanics and Physics of Solids 53 (2005) 261–301. doi:10.1016/j.jmps.2004.06.009.

[109] S. Yadegari, S. Turteltaub, A. S. J. Suiker, Coupled thermomechanical analysis of transformation-induced plasticity in multiphase steels, Mechanics of Materials 53 (2012) 1–14. doi:10.1016/j.mechmat.2012.05.002.

[110] S. Turteltaub, A. S. J. Suiker, A multiscale thermomechanical model for cubic to tetragonal martensitic phase transformations, International Journal of Solids and Structures 43 (2006) 4509–4545. doi:10.1016/j.ijsolstr.2005.06.065.

[111] G. R. Weber, S. Ghosh, Thermo-mechanical deformation evolution in polycrystalline ni-based superalloys by a hierarchical crystal plasticity model, Materials at High Temperatures 33 (2016) 401–411. doi:10.1080/09603409.2016.1190147.

[112] Y. W. Chang, R. J. Asaro, An experimental study of shear localization in aluminum-copper single crystals, Acta Metallurgica 29 (1981) 241–257. doi:10.1016/0001-6160(81)90103-6.

[113] B. D. Coleman, W. Noll, The thermodynamics of elastic materials with heat conduction and viscosity, Archive for Rational Mechanics and Analysis 13 (1963) 167–178.

[114] J. L. Raphanel, G. Ravichandran, Y. M. Leroy, Three-dimensional rate-dependent crystal plasticity based on runge–kutta algorithms for update and consistent linearization, International Journal of Solids and Structures 41 (2004) 5995–6021. doi:10.1016/j.ijsolstr.2004.05.027.

[115] M. Cherkaoui, M. Berveiller, H. Sabar, Micromechanical modeling of martensitic transformation induced plasticity (trip) in austenitic single crystals, International Journal of Plasticity 14 (1998) 597–626. doi:10.1016/S0749-6419(99)80000-X.

[116] M. Cherkaoui, M. Berveiller, X. Lemoine, Couplings between plasticity and martensitic phase transformation: overall behavior of polycrystalline trip steels, International Journal of Plasticity 16 (2000) 1215–1241. doi:10.1016/S0749-6419(00)00008-5.

[117] R. Kubler, M. Berveiller, M. Cherkaoui, K. Inal, Transformation textures in unstable austenitic steel, Journal of Engineering Materials and Technology 125 (2002) 12–17. doi:10.1115/1.1525249.

[118] S. Turteltaub, A. S. J. Suiker, Transformation-induced plasticity in ferrous alloys, Journal of the Mechanics and Physics of Solids 53 (2005) 1747–1788. doi:10.1016/j.jmps.2005.03.004.

[119] D. D. Tjahjanto, S. Turteltaub, A. S. J. Suiker, S. van der Zwaag, Transformation-induced plasticity in multiphase steels subjected to thermomechanical loading, Philosophical Magazine 88 (2008) 3369–3387. doi:10.1080/14786430802438150.

[120] A. Ma, A. Hartmaier, A study of deformation and phase transformation coupling for trip-assisted steels, International Journal of Plasticity 64 (2015) 40–55. doi:10.1016/j.ijplas.2014.07.008.

[121] G. B. Olson, M. Cohen, A mechanism for the strain-induced nucleation of martensitic transformations, Journal of the Less Common Metals 28 (1972) 107–118. doi:10.1016/0022-5088(72)90173-7.

[122] A. R. Zamiri, F. Pourboghrat, A novel yield function for single crystals based on combined constraints optimization, International Journal of Plasticity 26 (2010) 731–746. doi:10.1016/j.ijplas.2009.10.004.

[123] A. M. Beese, D. Mohr, Effect of stress triaxiality and lode angle on the kinetics of strain-induced austenite-to-martensite transformation, Acta Materialia 59 (2011) 2589–2600. doi:10.1016/j.actamat.2010.12.040.

[124] K. Chung, O. Richmond, A deformation theory of plasticity based on minimum work paths, International Journal of Plasticity 9 (1993) 907–920. doi:10.1016/0749-6419(93)90057-W.

[125] J.-W. Yoon, F. Barlat, R. E. Dick, K. Chung, T. J. Kang, Plane stress yield function for aluminum alloy sheets—part ii: Fe formulation and its implementation, International Journal of Plasticity 20 (2004) 495–522. doi:10.1016/S0749-6419(03)00099-8.

[126] N. Gey, B. Petit, M. Humbert, Electron backscattered diffraction study of ε/α' martensitic variants induced by plastic deformation in 304 stainless steel, Metallurgical and Materials Transactions A 36 (2005) 3291–3299.

[127] R. Johnson, J. Evans, P. Jacobsen, J. Thompson, M. Christopher, The changing automotive environment: high-temperature electronics, IEEE Transactions on Electronics Packaging Manufacturing 27 (2004) 164–176. doi:10.1109/TEPM.2004.843109.

[128] D. D. Tjahjanto, S. Turteltaub, A. S. J. Suiker, S. van der Zwaag, Modelling of the effects of grain orientation on transformation-induced plasticity in multiphase carbon steels, Modelling and Simulation in Materials Science and Engineering 14 (2006) 617. doi:10.1088/0965-0393/14/4/006.

[129] C. U. Jeong, W. Woo, J. Y. Choi, S. H. Choi, Effect of kinematic stability of initial orientation on deformation heterogeneity and ductile failure in duplex stainless steel during uniaxial tension, Acta Materialia 67 (2014) 21–31. doi:10.1016/j.actamat.2013.12.020.

[130] C. U. Jeong, Y. U. Heo, J. Y. Choi, W. Woo, S. H. Choi, A study on the micromechanical behaviors of duplex stainless steel under uniaxial tension using ex-situ experimentation and the crystal plasticity finite element method, International Journal of Plasticity 75 (2015) 22–38. doi:10.1016/j.ijplas.2015.07.005.

[131] E.-Y. Kim, W. Woo, Y.-U. Heo, B. Seong, J. Choi, S.-H. Choi, Effect of kinematic stability of the austenite phase on phase transformation behavior and deformation heterogeneity

in duplex stainless steel using the crystal plasticity finite element method, International Journal of Plasticity 79 (2016) 48–67. doi:10.1016/j.ijplas.2015.12.009.

[132] M. Madrid, Hole Expansion Performance and the Resistance to Crack Propagation in High Strength DP and QP Steels, Ph.D. thesis, Colorado School of Mines, 2018.

[133] F. Bachmann, R. Hielscher, H. Schaeben, Texture analysis with mtex – free and open source software toolbox, 2010. URL: https://www.scientific.net/SSP.160.63. doi:10.4028/www.scientific.net/SSP.160.63.

[134] Z. Wang, Z. C. Luo, M. X. Huang, Revealing hydrogen-induced delayed fracture in ferrite-containing quenching and partitioning steels, Materialia 4 (2018) 260–267. doi:10.1016/j.mtla.2018.09.022.

[135] R. Petrov, L. Kestens, A. Wasilkowska, Y. Houbaert, Microstructure and texture of a lightly deformed trip-assisted steel characterized by means of the ebsd technique, Materials Science and Engineering: A 447 (2007) 285–297. doi:10.1016/j.msea.2006.10.023.

[136] M. J. Santofimia, L. Zhao, R. Petrov, J. Sietsma, Characterization of the microstructure obtained by the quenching and partitioning process in a low-carbon steel, Materials Characterization 59 (2008) 1758–1764. doi:10.1016/j.matchar.2008.04.004.

[137] T. J. Vogler, J. D. Clayton, Heterogeneous deformation and spall of an extruded tungsten alloy: plate impact experiments and crystal plasticity modeling, Journal of the Mechanics and Physics of Solids 56 (2008) 297–335. doi:10.1016/j.jmps.2007.06.013.

[138] L. Anand, M. E. Gurtin, B. D. Reddy, The stored energy of cold work, thermal annealing, and other thermodynamic issues in single crystal plasticity at small length scales, International Journal of Plasticity 64 (2015) 1–25. doi:10.1016/j.ijplas.2014.07.009.

[139] D. D. Tjahjanto, P. Eisenlohr, F. Roters, Multiscale deep drawing analysis of dual-phase steels using grain cluster-based rgc scheme, Modelling and Simulation in Materials Science and Engineering 23 (2015) 045005. doi:10.1088/0965-0393/23/4/045005.

[140] B. Mohammed, T. Park, F. Pourboghrat, J. Hu, R. Esmaeilpour, F. Abu-Farha, Multiscale crystal plasticity modeling of multiphase advanced high strength steel, International Journal of Solids and Structures 151 (2018) 57–75. doi:10.1016/j.ijsolstr.2017.05.007.

[141] D. Peirce, C. F. Shih, A. Needleman, A tangent modulus method for rate dependent solids, Computers & Structures 18 (1984) 875–887. doi:10.1016/0045-7949(84)90033-6.

[142] S. R. Kalidindi, Incorporation of deformation twinning in crystal plasticity models, Journal of the Mechanics and Physics of Solids 46 (1998) 267–290. doi:10.1016/S0022-5096(97)00051-3.

[143] J. M. Ball, R. D. James, Fine phase mixtures as minimizers of energy, Archive for Rational Mechanics and Analysis 100 (1987) 13–52.

[144] K. F. Hane, T. W. Shield, Symmetry and microstructure in martensites, Philosophical Magazine A 78 (1998) 1215–1252. doi:10.1080/01418619808239984.

[145] H. J. Woodside, H. Robert, Bounds and self-consistent estimates for creep of polycrystalline materials, Proceedings of the Royal Society of London. A. Mathematical and Physical Sciences 348 (1976) 101–127. doi:10.1098/rspa.1976.0027.

[146] D. Peirce, R. J. Asaro, A. Needleman, An analysis of nonuniform and localized deformation in ductile single crystals, Acta Metallurgica 30 (1982) 1087–1119. doi:10.1016/0001-6160(82)90005-0.

[147] D. Peirce, R. J. Asaro, A. Needleman, Material rate dependence and localized deformation in crystalline solids, Acta Metallurgica 31 (1983) 1951–1976. doi:10.1016/0001-6160(83)90014-7.

[148] J. Hallquist, LS-Dyna Manual R8.0, volume I, Livermore Software Technology Corporation, 2015.

[149] A. Devaraj, Z. Xu, F. Abu-Farha, X. Sun, L. G. Hector, Nanoscale solute partitioning and carbide precipitation in a multiphase trip steel analyzed by atom probe tomography, JOM 70 (2018) 1752–1757. doi:10.1007/s11837-018-2974-1.

[150] S. M. C. Van Bohemen, An acoustic emission study of martensitic and bainitic transformations in carbon steel, Ph.D. thesis, Technical University of Delft, 2004. URL: http://resolver.tudelft.nl/uuid:e7dec82c-83be-4e7a-8dc9-60401b32a53b.

[151] S. Kruijver, L. Zhao, J. Sietsma, E. Offerman, N. van Dijk, L. Margulies, E. Lauridsen, S. Grigull, H. Poulsen, S. van der Zwaag, In situ observations on the austenite stability in trip-steel during tensile testing, Steel Research 73 (2002) 236–241. doi:10.1002/srin.200200202.

[152] C. Enloe, V. Savic, W. Poling, L. Hector, R. Alturk, Strain rate effect on martensitic transformation in a trip steel containing carbide-free bainite, SAE Papers (2019). URL: https://www.sae.org/content/2019-01-0521/. doi:10.4271/2019-01-0521.

[153] Q. Lai, L. Brassart, O. Bouaziz, M. Gouné, M. Verdier, G. Parry, A. Perlade, Y. Bréchet, T. Pardoen, Influence of martensite volume fraction and hardness on the plastic behavior of dual-phase steels: Experiments and micromechanical modeling, International Journal of Plasticity 80 (2016) 187–203. doi:10.1016/j.ijplas.2015.09.006.

[154] D. Connolly, C. Kohar, W. Muhammad, L. G. Hector, R. K. Mishra, K. Inal, A coupled thermomechanical crystal plasticity model applied to quenched and partitioned steel, International Journal of Plasticity In Press (2020).

[155] H. B. Callen, Thermodynamics and an Introduction to Thermostatistics, AAPT, 1998.

[156] E. van der Giessen, K. W. Neale, Analysis of the inverse swift effect using a rate-sensitive polycrystal model, Computer Methods in Applied Mechanics and Engineering 103 (1993) 291–313. doi:10.1016/0045-7825(93)90050-8.

[157] S. Hiermaier, Structures Under Crash and Impact: Continuum Mechanics, Discretization and Experimental Characterization, New York: Springer Science+Business Media, LLC, 2008.

[158] T.-K. Lee, W. Xie, B. Zhou, T. Bieler, K.-C. Liu, Impact of isothermal aging on long-term reliability of fine-pitch ball grid array packages with sn-ag-cu solder interconnects: Die size effects, Journal of Electronic Materials 40 (2011) 1967–1976. doi:10.1007/s11664-011-1702-1.

[159] J. G. Kim, S. Hong, N. Anjabin, B. H. Park, S. K. Kim, K. G. Chin, S. Lee, H. S. Kim, Dynamic strain aging of twinning-induced plasticity (twip) steel in tensile testing and deep drawing, Materials Science and Engineering: A 633 (2015) 136–143. doi:10.1016/j.msea.2015.03.008.

[160] M. Dakshinamurthy, A. Ma, Crack propagation in trip assisted steels modeled by crystal plasticity and cohesive zone method, Theoretical and Applied Fracture Mechanics 96 (2018) 545–555. doi:10.1016/j.tafmec.2018.06.005.

[161] W. F. Hosford, A generalized isotropic yield criterion, Journal of Applied Mechanics 39 (1972) 607–609. doi:10.1115/1.3422732.

[162] J. W. Hutchinson, Plastic deformation of b.c.c. polycrystals, Journal of the Mechanics and Physics of Solids 12 (1964) 25–33. doi:10.1016/0022-5096(64)90004-3.

[163] S. Cluff, M. Knezevic, M. P. Miles, D. T. Fullwood, R. K. Mishra, A. K. Sachdev, T. Brown, E. R. Homer, Coupling kinetic monte carlo and finite element methods to model the strain path sensitivity of the isothermal stress-assisted martensite nucleation in trip-assisted steels, Mechanics of Materials 154 (2021) 103707. doi:10.1016/j.mechmat.2020.103707.

[164] C. P. Kohar, Multi-scale Modeling and Optimization of Energy Absorption and Anisotropy in Aluminum Alloys, Ph.D. thesis, Waterloo University, 2017.

[165] K. Inal, K. W. Neale, A. Aboutajeddine, Forming limit comparisons for fcc and bcc sheets, International Journal of Plasticity 21 (2005) 1255–1266. doi:10.1016/j.ijplas.2004.08.001.

Appendices

Appendix A Model Slip Systems

In this work, austenite and ferrite have FCC and BCC lattice structures, and martensite is assumed to be BCC for the purposes of plastic slip [154]. Fig. A.1 illustrates the FCC and BCC lattices and example slip systems.

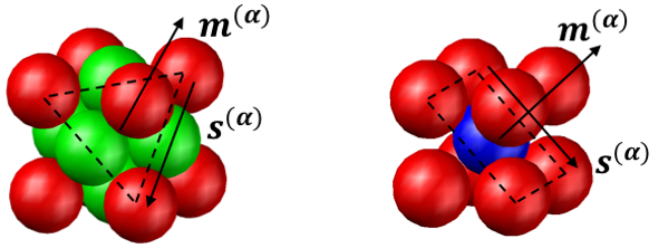

(a) (b)

Fig. A.1: (a) FCC and (b) BCC Crystal Latices (Modified from Kohar [164]).

For FCC phases, this work assumes that dislocation motion is solely accommodated via the $\langle 011\rangle \otimes \langle 111\rangle$ family of slip systems [95, 131, 140, 165]. The Burger's vector associated with this slip system is $b = \frac{a^A}{2}\sqrt{1^2+1^2+0^2} = 2.507\,\text{Å}$. The $\langle 011\rangle \otimes \langle 111\rangle$ slip family is enumerated in Table A.1.

Table A.1: FCC slip systems.

i	$s_j^{(i)}$	$m_j^{(i)}$	i	$s_j^{(i)}$	$m_j^{(i)}$	i	$s_j^{(i)}$	$m_j^{(i)}$	i	$s_j^{(i)}$	$m_j^{(i)}$
1	$\langle 01\bar{1}\rangle$	$\langle 1\bar{1}\bar{1}\rangle$	4	$\langle 011\rangle$	$\langle 11\bar{1}\rangle$	7	$\langle 011\rangle$	$\langle 1\bar{1}1\rangle$	10	$\langle 01\bar{1}\rangle$	$\langle 111\rangle$
2	$\langle 101\rangle$	$\langle 1\bar{1}\bar{1}\rangle$	5	$\langle 101\rangle$	$\langle 11\bar{1}\rangle$	8	$\langle 10\bar{1}\rangle$	$\langle 1\bar{1}1\rangle$	11	$\langle 10\bar{1}\rangle$	$\langle 111\rangle$
3	$\langle 110\rangle$	$\langle 1\bar{1}\bar{1}\rangle$	6	$\langle 1\bar{1}0\rangle$	$\langle 11\bar{1}\rangle$	9	$\langle 110\rangle$	$\langle 1\bar{1}1\rangle$	12	$\langle 1\bar{1}0\rangle$	$\langle 111\rangle$

For BCC phases, this work assumes that dislocation motion is solely accommodated via the $\langle 111\rangle\otimes\langle 110\rangle$ and $\langle 111\rangle\otimes\langle 211\rangle$ families of slip systems. For tempered martensite, it is assumed that the carbon content is approximately 0 [149], giving lattice parameters of $a^M = c^M = 2.861\,\text{Å}$. This gives a Burger's vector of $b = \frac{a^M}{2}\sqrt{1^2+1^2+1^2} = 2.477\,\text{Å}$. For freshly transformed martensite, the Burger's vector is given by $b = \frac{1}{2}\sqrt{(a^M)^2+(a^M)^2+(c^M)^2} = 2.507$. These $\langle 111\rangle \otimes \langle 110\rangle$ and $\langle 111\rangle \otimes \langle 211\rangle$ slip families are enumerated in Table A.2.

Table A.2: BCC slip systems.

i	$s_j^{(i)}$	$m_j^{(i)}$	i	$s_j^{(i)}$	$m_j^{(i)}$	i	$s_j^{(i)}$	$m_j^{(i)}$	i	$s_j^{(i)}$	$m_j^{(i)}$
1	$\langle 11\bar{1}\rangle$	$\langle 011\rangle$	7	$\langle 1\bar{1}1\rangle$	$\langle 011\rangle$	13	$\langle 11\bar{1}\rangle$	$\langle 2\bar{1}1\rangle$	19	$\langle 1\bar{1}1\rangle$	$\langle 21\bar{1}\rangle$
2	$\langle 11\bar{1}\rangle$	$\langle 101\rangle$	8	$\langle 1\bar{1}1\rangle$	$\langle 10\bar{1}\rangle$	14	$\langle 11\bar{1}\rangle$	$\langle 1\bar{2}1\rangle$	20	$\langle 1\bar{1}1\rangle$	$\langle 121\rangle$
3	$\langle 11\bar{1}\rangle$	$\langle 1\bar{1}0\rangle$	9	$\langle 1\bar{1}1\rangle$	$\langle 110\rangle$	15	$\langle 11\bar{1}\rangle$	$\langle 112\rangle$	21	$\langle 1\bar{1}1\rangle$	$\langle 1\bar{1}\bar{2}\rangle$
4	$\langle 1\bar{1}\bar{1}\rangle$	$\langle 01\bar{1}\rangle$	10	$\langle 111\rangle$	$\langle 01\bar{1}\rangle$	16	$\langle 1\bar{1}\bar{1}\rangle$	$\langle 211\rangle$	22	$\langle 111\rangle$	$\langle 2\bar{1}\bar{1}\rangle$
5	$\langle 1\bar{1}\bar{1}\rangle$	$\langle 101\rangle$	11	$\langle 111\rangle$	$\langle 10\bar{1}\rangle$	17	$\langle 1\bar{1}\bar{1}\rangle$	$\langle 12\bar{1}\rangle$	23	$\langle 111\rangle$	$\langle 1\bar{2}1\rangle$
6	$\langle 1\bar{1}\bar{1}\rangle$	$\langle 110\rangle$	18	$\langle 1\bar{1}\bar{1}\rangle$	$\langle 1\bar{1}2\rangle$	12	$\langle 111\rangle$	$\langle 1\bar{1}0\rangle$	24	$\langle 111\rangle$	$\langle 11\bar{2}\rangle$

Appendix B Transformation Kinematic Properties

B.1 QP1180 Properties

Following Turteltaub and Suiker [118], QP1180 is assumed to have a carbon concentration of 1.4wt%. For completeness, the kinematic properties presented in Turteltaub and Suiker [118] are repeated here. The austenite and transformed martensite lattice parameters are calculated from the carbon concentration using [118]

$$c^M = 2.861 + 0.116(p_c) = 3.0233\,\text{Å} \tag{B.1}$$

$$a^M = 2.861 - 0.013(p_c) = 2.8428\,\text{Å} \tag{B.2}$$

$$a^A = 3.548 + 0.044(p_c) = 3.6096\,\text{Å} \tag{B.3}$$

Using these lattice parameters and the analytic approach presented in Hane and Shield [144], the compatibility Eqs. (5.4) and (5.5) are solved to give the transformation shear magnitude, transformation systems, internal twin and martensite plate rotation matrices, and martensite variant volume fractions.

The transformation shear magnitude is

$$\hat{\gamma}_{tr} = 0.1809 \tag{B.4}$$

Table B.1 presents the martensite variants ζ_1^β and ζ_2^β, martensite variant 1 volume fraction $\lambda^{(\zeta_1^\beta)}$, and the transformation direction $b_i^{(\beta)}$ and normal components $d_i^{(\beta)}$ for martensite plate orientation β.

Table B.1: QP1180 transformation systems.

β	$(\zeta_1^\beta, \zeta_2^\beta)$	$\lambda^{(\zeta_1^\beta)}$	$b_i^{(\beta)}$			$d_i^{(\beta)}$		
1	(1,2)	0.3998	−0.1906	−0.6311	−0.7520	0.1711	0.5666	−0.8060
2	(1,2)	0.3998	0.1906	0.6311	−0.7520	−0.1711	−0.5666	−0.8060
3	(1,2)	0.6002	−0.6311	−0.1906	−0.7520	0.5666	0.1711	−0.8060
4	(1,2)	0.6002	0.6311	0.1906	−0.7520	−0.5666	−0.1711	−0.8060
5	(1,2)	0.3998	0.1906	−0.6311	−0.7520	−0.1711	0.5666	−0.8060
6	(1,2)	0.3998	−0.1906	0.6311	−0.7520	0.1711	−0.5666	−0.8060
7	(1,2)	0.6002	−0.6311	0.1906	−0.7520	0.5666	−0.1711	−0.8060
8	(1,2)	0.6002	0.6311	−0.1906	−0.7520	−0.5666	0.1711	−0.8060
9	(1,3)	0.3998	0.1906	0.7520	−0.6311	−0.1711	0.8060	0.5666

Table B.1 (*Continued*)

β	$(\zeta_1^\beta, \zeta_2^\beta)$	$\lambda^{(\zeta_1^\beta)}$	$b_i^{(\beta)}$			$d_i^{(\beta)}$		
10	(1,3)	0.3998	−0.1906	0.7520	0.6311	0.1711	0.8060	−0.5666
11	(1,3)	0.6002	−0.6311	0.7520	0.1906	0.5666	0.8060	−0.1711
12	(1,3)	0.6002	0.6311	0.7520	−0.1906	−0.5666	0.8060	0.1711
13	(1,3)	0.3998	0.1906	−0.7520	0.6311	−0.1711	−0.8060	−0.5666
14	(1,3)	0.3998	−0.1906	−0.7520	−0.6311	0.1711	−0.8060	0.5666
15	(1,3)	0.6002	−0.6311	−0.7520	−0.1906	0.5666	−0.8060	0.1711
16	(1,3)	0.6002	0.6311	−0.7520	0.1906	−0.5666	−0.8060	−0.1711
17	(2,3)	0.3998	−0.7520	−0.1906	0.6311	−0.8060	0.1711	−0.5666
18	(2,3)	0.3998	−0.7520	0.1906	−0.6311	−0.8060	−0.1711	0.5666
19	(2,3)	0.6002	−0.7520	0.6311	−0.1906	−0.8060	−0.5666	0.1711
20	(2,3)	0.6002	−0.7520	−0.6311	0.1906	−0.8060	0.5666	−0.1711
21	(2,3)	0.3998	−0.7520	0.1906	0.6311	−0.8060	−0.1711	−0.5666
22	(2,3)	0.3998	−0.7520	−0.1906	−0.6311	−0.8060	0.1711	0.5666
23	(2,3)	0.6002	−0.7520	0.6311	0.1906	−0.8060	−0.5666	−0.1711
24	(2,3)	0.6002	−0.7520	−0.6311	−0.1906	−0.8060	0.5666	0.1711

Table B.2 presents the rotation matrix between martensite variants 1 (ζ_1^β) and 2 (ζ_2^β) of martensite plate orientation β.

Table B.2: QP1180 rotation between twinned martensite variant ζ_1^β and ζ_1^β.

β	$\overline{\mathbf{R}}^{(\beta)}$	β	$\overline{\mathbf{R}}^{(\beta)}$
1	$\begin{bmatrix} 0.9607 & -0.2775 & 0 \\ 0.2775 & 0.9607 & 0 \\ 0 & 0 & 1 \end{bmatrix}$	13	$\begin{bmatrix} 0.9607 & 0 & -0.2775 \\ 0 & 1 & 0 \\ 0.2775 & 0 & 0.9607 \end{bmatrix}$
2	$\begin{bmatrix} 0.9607 & -0.2775 & 0 \\ 0.2775 & 0.9607 & 0 \\ 0 & 0 & 1 \end{bmatrix}$	14	$\begin{bmatrix} 0.9607 & 0 & -0.2775 \\ 0 & 1 & 0 \\ 0.2775 & 0 & 0.9607 \end{bmatrix}$
3	$\begin{bmatrix} 0.9607 & -0.2775 & 0 \\ 0.2775 & 0.9607 & 0 \\ 0 & 0 & 1 \end{bmatrix}$	15	$\begin{bmatrix} 0.9607 & 0 & -0.2775 \\ 0 & 1 & 0 \\ 0.2775 & 0 & 0.9607 \end{bmatrix}$
4	$\begin{bmatrix} 0.9607 & -0.2775 & 0 \\ 0.2775 & 0.9607 & 0 \\ 0 & 0 & 1 \end{bmatrix}$	16	$\begin{bmatrix} 0.9607 & 0 & -0.2775 \\ 0 & 1 & 0 \\ 0.2775 & 0 & 0.9607 \end{bmatrix}$

Table B.2 (*Continued*)

β	$\overline{\mathbf{R}}^{(\beta)}$	β	$\overline{\mathbf{R}}^{(\beta)}$
5	$\begin{bmatrix} 0.9607 & 0.2775 & 0 \\ -0.2775 & 0.9607 & 0 \\ 0 & 0 & 1 \end{bmatrix}$	17	$\begin{bmatrix} 1 & 0 & 0 \\ 0 & 0.9607 & 0.2775 \\ 0 & -0.2775 & 0.9607 \end{bmatrix}$
6	$\begin{bmatrix} 0.9607 & 0.2775 & 0 \\ -0.2775 & 0.9607 & 0 \\ 0 & 0 & 1 \end{bmatrix}$	18	$\begin{bmatrix} 1 & 0 & 0 \\ 0 & 0.9607 & 0.2775 \\ 0 & -0.2775 & 0.9607 \end{bmatrix}$
7	$\begin{bmatrix} 0.9607 & 0.2775 & 0 \\ -0.2775 & 0.9607 & 0 \\ 0 & 0 & 1 \end{bmatrix}$	19	$\begin{bmatrix} 1 & 0 & 0 \\ 0 & 0.9607 & 0.2775 \\ 0 & -0.2775 & 0.9607 \end{bmatrix}$
8	$\begin{bmatrix} 0.9607 & 0.2775 & 0 \\ -0.2775 & 0.9607 & 0 \\ 0 & 0 & 1 \end{bmatrix}$	20	$\begin{bmatrix} 1 & 0 & 0 \\ 0 & 0.9607 & 0.2775 \\ 0 & -0.2775 & 0.9607 \end{bmatrix}$
9	$\begin{bmatrix} 0.9607 & 0 & 0.2775 \\ 0 & 1 & 0 \\ -0.2775 & 0 & 0.9607 \end{bmatrix}$	21	$\begin{bmatrix} 1 & 0 & 0 \\ 0 & 0.9607 & -0.2775 \\ 0 & 0.2775 & 0.9607 \end{bmatrix}$
10	$\begin{bmatrix} 0.9607 & 0 & 0.2775 \\ 0 & 1 & 0 \\ -0.2775 & 0 & 0.9607 \end{bmatrix}$	22	$\begin{bmatrix} 1 & 0 & 0 \\ 0 & 0.9607 & -0.2775 \\ 0 & 0.2775 & 0.9607 \end{bmatrix}$
11	$\begin{bmatrix} 0.9607 & 0 & 0.2775 \\ 0 & 1 & 0 \\ -0.2775 & 0 & 0.9607 \end{bmatrix}$	23	$\begin{bmatrix} 1 & 0 & 0 \\ 0 & 0.9607 & -0.2775 \\ 0 & 0.2775 & 0.9607 \end{bmatrix}$
12	$\begin{bmatrix} 0.9607 & 0 & 0.2775 \\ 0 & 1 & 0 \\ -0.2775 & 0 & 0.9607 \end{bmatrix}$	24	$\begin{bmatrix} 1 & 0 & 0 \\ 0 & 0.9607 & -0.2775 \\ 0 & 0.2775 & 0.9607 \end{bmatrix}$

Table B.3 presents the rotation matrix between austenite and the aggregate martensite plate orientation β, in the martensite variant 2 (ζ_2^β) basis.

Table B.3: QP1180 rotation between austenite and martensite plate β in martensite variant basis.

β	$\widehat{\mathbf{R}}^{(\beta)}$	β	$\widehat{\mathbf{R}}^{(\beta)}$
1	$\begin{bmatrix} 0.9935 & 0.1109 & 0.0249 \\ -0.1127 & 0.9902 & 0.0826 \\ -0.0155 & -0.0849 & 0.9963 \end{bmatrix}$	13	$\begin{bmatrix} 0.9935 & -0.0249 & 0.1109 \\ 0.0155 & 0.9963 & 0.0849 \\ -0.1127 & -0.0826 & 0.9902 \end{bmatrix}$
2	$\begin{bmatrix} 0.9935 & 0.1109 & -0.0249 \\ -0.1127 & 0.9902 & -0.0826 \\ 0.0155 & 0.0849 & 0.9963 \end{bmatrix}$	14	$\begin{bmatrix} 0.9935 & 0.0249 & 0.1109 \\ -0.0155 & 0.9963 & -0.0849 \\ -0.1127 & 0.0826 & 0.9902 \end{bmatrix}$
3	$\begin{bmatrix} 0.9826 & 0.1666 & 0.0826 \\ -0.1691 & 0.9853 & 0.0249 \\ -0.0772 & -0.0385 & 0.9963 \end{bmatrix}$	15	$\begin{bmatrix} 0.9826 & 0.0826 & 0.1666 \\ -0.0772 & 0.9963 & -0.0385 \\ -0.1691 & 0.0249 & 0.9853 \end{bmatrix}$
4	$\begin{bmatrix} 0.9826 & 0.1666 & -0.0826 \\ -0.1691 & 0.9853 & -0.0249 \\ 0.0772 & 0.0385 & 0.9963 \end{bmatrix}$	16	$\begin{bmatrix} 0.9826 & -0.0826 & 0.1666 \\ 0.0772 & 0.9963 & 0.0385 \\ -0.1691 & -0.0249 & 0.9853 \end{bmatrix}$
5	$\begin{bmatrix} 0.9935 & -0.1109 & -0.0249 \\ 0.1127 & 0.9902 & 0.0826 \\ 0.0155 & -0.0849 & 0.9963 \end{bmatrix}$	17	$\begin{bmatrix} 0.9963 & -0.0155 & 0.0849 \\ 0.0249 & 0.9935 & -0.1109 \\ -0.0826 & 0.1127 & 0.9902 \end{bmatrix}$
6	$\begin{bmatrix} 0.9935 & -0.1109 & 0.0249 \\ 0.1127 & 0.9902 & -0.0826 \\ -0.0155 & 0.0849 & 0.9963 \end{bmatrix}$	18	$\begin{bmatrix} 0.9963 & 0.0155 & -0.0849 \\ -0.0249 & 0.9935 & -0.1109 \\ 0.0826 & 0.1127 & 0.9902 \end{bmatrix}$
7	$\begin{bmatrix} 0.9826 & -0.1666 & 0.0826 \\ 0.1691 & 0.9853 & -0.0249 \\ -0.0772 & 0.0385 & 0.9963 \end{bmatrix}$	19	$\begin{bmatrix} 0.9963 & 0.0772 & -0.0385 \\ -0.0826 & 0.9826 & -0.1666 \\ 0.0249 & 0.1691 & 0.9853 \end{bmatrix}$
8	$\begin{bmatrix} 0.9826 & -0.1666 & -0.0826 \\ 0.1691 & 0.9853 & 0.0249 \\ 0.0772 & -0.0385 & 0.9963 \end{bmatrix}$	20	$\begin{bmatrix} 0.9963 & -0.0772 & 0.0385 \\ 0.0826 & 0.9826 & -0.1666 \\ -0.0249 & 0.1691 & 0.9853 \end{bmatrix}$
9	$\begin{bmatrix} 0.9935 & 0.0249 & -0.1109 \\ -0.0155 & 0.9963 & 0.0849 \\ 0.1127 & -0.0826 & 0.9902 \end{bmatrix}$	21	$\begin{bmatrix} 0.9963 & 0.0155 & 0.0849 \\ -0.0249 & 0.9935 & 0.1109 \\ -0.0826 & -0.1127 & 0.9902 \end{bmatrix}$
10	$\begin{bmatrix} 0.9935 & -0.0249 & -0.1109 \\ 0.0155 & 0.9963 & -0.0849 \\ 0.1127 & 0.0826 & 0.9902 \end{bmatrix}$	22	$\begin{bmatrix} 0.9963 & -0.0155 & -0.0849 \\ 0.0249 & 0.9935 & 0.1109 \\ 0.0826 & -0.1127 & 0.9902 \end{bmatrix}$
11	$\begin{bmatrix} 0.9826 & -0.0826 & -0.1666 \\ 0.0772 & 0.9963 & -0.0385 \\ 0.1691 & 0.0249 & 0.9853 \end{bmatrix}$	23	$\begin{bmatrix} 0.9963 & 0.0772 & 0.0385 \\ -0.0826 & 0.9826 & 0.1666 \\ -0.0249 & -0.1691 & 0.9853 \end{bmatrix}$

Table B.3 (*Continued*)

β	$\overline{\mathbf{R}}^{(\beta)}$	β	$\overline{\mathbf{R}}^{(\beta)}$
12	$\begin{bmatrix} 0.9826 & 0.0826 & -0.1666 \\ -0.0772 & 0.9963 & 0.0385 \\ 0.1691 & -0.0249 & 0.9853 \end{bmatrix}$	24	$\begin{bmatrix} 0.9963 & -0.0772 & -0.0385 \\ 0.0826 & 0.9826 & 0.1666 \\ 0.0249 & -0.1691 & 0.9853 \end{bmatrix}$

B.2 QP3Mn Properties

Recent atom probe tomography [149] results for a quenched and partition (QP980) indicate RA carbon concentration of 1.12wt%. The austenite and transformed martensite lattice parameters are calculated from the carbon concentration using [118]

$$c^M = 2.861 + 0.116(p_c) = 2.990\,92\,\text{Å} \tag{B.5}$$
$$a^M = 2.861 - 0.013(p_c) = 2.846\,44\,\text{Å} \tag{B.6}$$
$$a^A = 3.548 + 0.044(p_c) = 3.597\,28\,\text{Å} \tag{B.7}$$

Using these lattice parameters and the analytic approach presented in Hane and Shield [144], the compatibility Eqs. (5.4) and (5.5) are solved to give the transformation shear magnitude, transformation systems, internal twin and martensite plate rotation matrices, and martensite variant volume fractions.

The transformation shear magnitude is

$$\hat{\gamma}_{tr} = 0.1886 \tag{B.8}$$

Table B.4 presents the martensite variants ζ_1^β and ζ_2^β, martensite variant 1 volume fraction $\lambda^{(\zeta_1^\beta)}$, and the transformation direction $b_i^{(\beta)}$ and normal components $d_i^{(\beta)}$ for martensite plate orientation β.

Table B.4: QP3Mn transformation systems.

β	$(\zeta_1^\beta, \zeta_2^\beta)$	$\lambda^{(\zeta_1^\beta)}$	$b_i^{(\beta)}$	$d_i^{(\beta)}$
1	(1,2)	0.4024	$[-0.2011 \quad -0.6286 \quad -0.7523]$	$[0.1793 \quad 0.5616 \quad -0.8078]$
2	(1,2)	0.4024	$[0.2011 \quad 0.6286 \quad -0.7523]$	$[-0.1793 \quad -0.5616 \quad -0.8078]$
3	(1,2)	0.5976	$[-0.6286 \quad -0.2011 \quad -0.7523]$	$[0.5616 \quad 0.1793 \quad -0.8078]$

Table B.4 (*Continued*)

β	$(\zeta_1^\beta, \zeta_2^\beta)$	$\lambda^{(\zeta_1^\beta)}$	$b_i^{(\beta)}$			$d_i^{(\beta)}$		
4	(1,2)	0.5976	0.6286	0.2011	−0.7523	−0.5616	−0.1793	−0.8078
5	(1,2)	0.4024	0.2011	−0.6286	−0.7523	−0.1793	0.5616	−0.8078
6	(1,2)	0.4024	−0.2011	0.6286	−0.7523	0.1793	−0.5616	−0.8078
7	(1,2)	0.5976	−0.6286	0.2011	−0.7523	0.5616	−0.1793	−0.8078
8	(1,2)	0.5976	0.6286	−0.2011	−0.7523	−0.5616	0.1793	−0.8078
9	(1,3)	0.4024	0.2011	0.7523	−0.6286	−0.1793	0.8078	0.5616
10	(1,3)	0.4024	−0.2011	0.7523	0.6286	0.1793	0.8078	−0.5616
11	(1,3)	0.5976	−0.6286	0.7523	0.2011	0.5616	0.8078	−0.1793
12	(1,3)	0.5976	0.6286	0.7523	−0.2011	−0.5616	0.8078	0.1793
13	(1,3)	0.4024	0.2011	−0.7523	0.6286	−0.1793	−0.8078	−0.5616
14	(1,3)	0.4024	−0.2011	−0.7523	−0.6286	0.1793	−0.8078	0.5616
15	(1,3)	0.5976	−0.6286	−0.7523	−0.2011	0.5616	−0.8078	0.1793
16	(1,3)	0.5976	0.6286	−0.7523	0.2011	−0.5616	−0.8078	−0.1793
17	(2,3)	0.4024	−0.7523	−0.2011	0.6286	−0.8078	0.1793	−0.5616
18	(2,3)	0.4024	−0.7523	0.2011	−0.6286	−0.8078	−0.1793	0.5616
19	(2,3)	0.5976	−0.7523	0.6286	−0.2011	−0.8078	−0.5616	0.1793
20	(2,3)	0.5976	−0.7523	−0.6286	0.2011	−0.8078	0.5616	−0.1793
21	(2,3)	0.4024	−0.7523	0.2011	0.6286	−0.8078	−0.1793	−0.5616
22	(2,3)	0.4024	−0.7523	−0.2011	−0.6286	−0.8078	0.1793	0.5616
23	(2,3)	0.5976	−0.7523	0.6286	0.2011	−0.8078	−0.5616	−0.1793
24	(2,3)	0.5976	−0.7523	−0.6286	−0.2011	−0.8078	0.5616	0.1793

Table B.5 presents the rotation matrix between martensite variants 1 (ζ_1^β) and 2 (ζ_2^β) of martensite plate orientation β.

Table B.5: QP3Mn rotation between twinned martensite variant ζ_1^β and ζ_1^β.

β	$\overline{\mathbf{R}}^{(\beta)}$	β	$\overline{\mathbf{R}}^{(\beta)}$
1	$\begin{bmatrix} 0.95744 & -0.28862 & 0 \\ 0.28862 & 0.95744 & 0 \\ 0 & 0 & 1 \end{bmatrix}$	13	$\begin{bmatrix} 0.95744 & 0 & -0.28862 \\ 0 & 1 & 0 \\ 0.28862 & 0 & 0.95744 \end{bmatrix}$

Table B.5 (*Continued*)

β	$\overline{\mathbf{R}}^{(\beta)}$	β	$\overline{\mathbf{R}}^{(\beta)}$
2	$\begin{bmatrix} 0.95744 & -0.28862 & 0 \\ 0.28862 & 0.95744 & 0 \\ 0 & 0 & 1 \end{bmatrix}$	14	$\begin{bmatrix} 0.95744 & 0 & -0.28862 \\ 0 & 1 & 0 \\ 0.28862 & 0 & 0.95744 \end{bmatrix}$
3	$\begin{bmatrix} 0.95744 & -0.28862 & 0 \\ 0.28862 & 0.95744 & 0 \\ 0 & 0 & 1 \end{bmatrix}$	15	$\begin{bmatrix} 0.95744 & 0 & -0.28862 \\ 0 & 1 & 0 \\ 0.28862 & 0 & 0.95744 \end{bmatrix}$
4	$\begin{bmatrix} 0.95744 & -0.28862 & 0 \\ 0.28862 & 0.95744 & 0 \\ 0 & 0 & 1 \end{bmatrix}$	16	$\begin{bmatrix} 0.95744 & 0 & -0.28862 \\ 0 & 1 & 0 \\ 0.28862 & 0 & 0.95744 \end{bmatrix}$
5	$\begin{bmatrix} 0.95744 & 0.28862 & 0 \\ -0.28862 & 0.95744 & 0 \\ 0 & 0 & 1 \end{bmatrix}$	17	$\begin{bmatrix} 1 & 0 & 0 \\ 0 & 0.95744 & 0.28862 \\ 0 & -0.28862 & 0.95744 \end{bmatrix}$
6	$\begin{bmatrix} 0.95744 & 0.28862 & 0 \\ -0.28862 & 0.95744 & 0 \\ 0 & 0 & 1 \end{bmatrix}$	18	$\begin{bmatrix} 1 & 0 & 0 \\ 0 & 0.95744 & 0.28862 \\ 0 & -0.28862 & 0.95744 \end{bmatrix}$
7	$\begin{bmatrix} 0.95744 & 0.28862 & 0 \\ -0.28862 & 0.95744 & 0 \\ 0 & 0 & 1 \end{bmatrix}$	19	$\begin{bmatrix} 1 & 0 & 0 \\ 0 & 0.95744 & 0.28862 \\ 0 & -0.28862 & 0.95744 \end{bmatrix}$
8	$\begin{bmatrix} 0.95744 & 0.28862 & 0 \\ -0.28862 & 0.95744 & 0 \\ 0 & 0 & 1 \end{bmatrix}$	20	$\begin{bmatrix} 1 & 0 & 0 \\ 0 & 0.95744 & 0.28862 \\ 0 & -0.28862 & 0.95744 \end{bmatrix}$
9	$\begin{bmatrix} 0.95744 & 0 & 0.28862 \\ 0 & 1 & 0 \\ -0.28862 & 0 & 0.95744 \end{bmatrix}$	21	$\begin{bmatrix} 1 & 0 & 0 \\ 0 & 0.95744 & -0.28862 \\ 0 & 0.28862 & 0.95744 \end{bmatrix}$
10	$\begin{bmatrix} 0.95744 & 0 & 0.28862 \\ 0 & 1 & 0 \\ -0.28862 & 0 & 0.95744 \end{bmatrix}$	22	$\begin{bmatrix} 1 & 0 & 0 \\ 0 & 0.95744 & -0.28862 \\ 0 & 0.28862 & 0.95744 \end{bmatrix}$
11	$\begin{bmatrix} 0.95744 & 0 & 0.28862 \\ 0 & 1 & 0 \\ -0.28862 & 0 & 0.95744 \end{bmatrix}$	23	$\begin{bmatrix} 1 & 0 & 0 \\ 0 & 0.95744 & -0.28862 \\ 0 & 0.28862 & 0.95744 \end{bmatrix}$
12	$\begin{bmatrix} 0.95744 & 0 & 0.28862 \\ 0 & 1 & 0 \\ -0.28862 & 0 & 0.95744 \end{bmatrix}$	24	$\begin{bmatrix} 1 & 0 & 0 \\ 0 & 0.95744 & -0.28862 \\ 0 & 0.28862 & 0.95744 \end{bmatrix}$

Table B.6 presents the rotation matrix between austenite and the aggregate martensite plate orientation β, in the martensite variant 2 (ζ_2^β) basis.

Table B.6: QP3Mn rotation between Austenite and Martensite plate β in Martensite variant basis.

β	$\widehat{\mathbf{R}}^{(\beta)}$	β	$\widehat{\mathbf{R}}^{(\beta)}$
1	$\begin{bmatrix} 0.9929 & 0.1161 & 0.0273 \\ -0.1181 & 0.9893 & 0.0856 \\ -0.0171 & -0.0882 & 0.9960 \end{bmatrix}$	13	$\begin{bmatrix} 0.9929 & -0.0273 & 0.1161 \\ 0.0171 & 0.9960 & 0.0882 \\ -0.1181 & -0.0856 & 0.9893 \end{bmatrix}$
2	$\begin{bmatrix} 0.9929 & 0.1161 & -0.0273 \\ -0.1181 & 0.9893 & -0.0856 \\ 0.0171 & 0.0882 & 0.9960 \end{bmatrix}$	14	$\begin{bmatrix} 0.9929 & 0.0273 & 0.1161 \\ -0.0171 & 0.9960 & -0.0882 \\ -0.1181 & 0.0856 & 0.9893 \end{bmatrix}$
3	$\begin{bmatrix} 0.9813 & 0.1725 & 0.0856 \\ -0.1754 & 0.9841 & 0.0273 \\ -0.0795 & -0.0418 & 0.9960 \end{bmatrix}$	15	$\begin{bmatrix} 0.9813 & 0.0856 & 0.1725 \\ -0.0795 & 0.9960 & -0.0418 \\ -0.1754 & 0.0273 & 0.9841 \end{bmatrix}$
4	$\begin{bmatrix} 0.9813 & 0.1725 & -0.0856 \\ -0.1754 & 0.9841 & -0.0273 \\ 0.0795 & 0.0418 & 0.9960 \end{bmatrix}$	16	$\begin{bmatrix} 0.9813 & -0.0856 & 0.1725 \\ 0.0795 & 0.9960 & 0.0418 \\ -0.1754 & -0.0273 & 0.9841 \end{bmatrix}$
5	$\begin{bmatrix} 0.9929 & -0.1161 & -0.0273 \\ 0.1181 & 0.9893 & 0.0856 \\ 0.0171 & -0.0882 & 0.9960 \end{bmatrix}$	17	$\begin{bmatrix} 0.9960 & -0.0171 & 0.0882 \\ 0.0273 & 0.9929 & -0.1161 \\ -0.0856 & 0.1181 & 0.9893 \end{bmatrix}$
6	$\begin{bmatrix} 0.9929 & -0.1161 & 0.0273 \\ 0.1181 & 0.9893 & -0.0856 \\ -0.0171 & 0.0882 & 0.9960 \end{bmatrix}$	18	$\begin{bmatrix} 0.9960 & 0.0171 & -0.0882 \\ -0.0273 & 0.9929 & -0.1161 \\ 0.0856 & 0.1181 & 0.9893 \end{bmatrix}$
7	$\begin{bmatrix} 0.9813 & -0.1725 & 0.0856 \\ 0.1754 & 0.9841 & -0.0273 \\ -0.0795 & 0.0418 & 0.9960 \end{bmatrix}$	19	$\begin{bmatrix} 0.9960 & 0.0795 & -0.0418 \\ -0.0856 & 0.9813 & -0.1725 \\ 0.0273 & 0.1754 & 0.9841 \end{bmatrix}$
8	$\begin{bmatrix} 0.9813 & -0.1725 & -0.0856 \\ 0.1754 & 0.9841 & 0.0273 \\ 0.0795 & -0.0418 & 0.9960 \end{bmatrix}$	20	$\begin{bmatrix} 0.9960 & -0.0795 & 0.0418 \\ 0.0856 & 0.9813 & -0.1725 \\ -0.0273 & 0.1754 & 0.9841 \end{bmatrix}$
9	$\begin{bmatrix} 0.9929 & 0.0273 & -0.1161 \\ -0.0171 & 0.996 & 0.0882 \\ 0.1181 & -0.0856 & 0.9893 \end{bmatrix}$	21	$\begin{bmatrix} 0.9960 & 0.0171 & 0.0882 \\ -0.0273 & 0.9929 & 0.1161 \\ -0.0856 & -0.1181 & 0.9893 \end{bmatrix}$
10	$\begin{bmatrix} 0.9929 & -0.0273 & -0.1161 \\ 0.0171 & 0.996 & -0.0882 \\ 0.1181 & 0.0856 & 0.9893 \end{bmatrix}$	22	$\begin{bmatrix} 0.9960 & -0.0171 & -0.0882 \\ 0.0273 & 0.9929 & 0.1161 \\ 0.0856 & -0.1181 & 0.9893 \end{bmatrix}$

Table B.6 (*Continued*)

β	$\overline{\mathbf{R}}^{(\beta)}$	β	$\overline{\mathbf{R}}^{(\beta)}$
11	$\begin{bmatrix} 0.9813 & -0.0856 & -0.1725 \\ 0.0795 & 0.996 & -0.0418 \\ 0.1754 & 0.0273 & 0.9841 \end{bmatrix}$	23	$\begin{bmatrix} 0.9960 & 0.0795 & 0.0418 \\ -0.0856 & 0.9813 & 0.1725 \\ -0.0273 & -0.1754 & 0.9841 \end{bmatrix}$
12	$\begin{bmatrix} 0.9813 & 0.0856 & -0.1725 \\ -0.0795 & 0.996 & 0.0418 \\ 0.1754 & -0.0273 & 0.9841 \end{bmatrix}$	24	$\begin{bmatrix} 0.9960 & -0.0795 & -0.0418 \\ 0.0856 & 0.9813 & 0.1725 \\ 0.0273 & -0.1754 & 0.9841 \end{bmatrix}$